Compaction and Cure of Resin Film Infusion Prepregs

Joseph Earl Thompson

Thesis submitted to the faculty of the Virginia Polytechnic Institute and State University
in partial fulfillment of the requirements for the degree of

Masters of Science
In
Engineering Mechanics

Romesh C. Batra, Chairman
Scott W. Case
Alfred C. Loos
Saad A. Ragab

December 22, 2004
Blacksburg, Virginia

Keywords: resin film infusion (RFI), fiber compaction, kinetics, viscosity, Cytec 754

© 2004 Joseph Earl Thompson

Compaction and Cure of Resin Film Infusion Prepregs

Joseph Earl Thompson

(ABSTRACT)

Gutowski *et al.*'s model has been employed to describe the cure and consolidation of prepregs used for resin film infusion. Resin kinetics, rheology, flow and fiber deformation are considered. Resin kinetics are simulated with an isothermal autocatalytic-1 type relation. The non-Newtonian viscosity of the Cytec™ 754 resin is represented with a gel type expression. The one dimensional flow of resin through a deformable, partially saturated porous medium is studied. A nonlinear partial differential equation describing the spatial and temporal variation of the fiber volume fraction combining the continuity equation, Darcy's Law, and mat compressibility has been derived and solved numerically. Resin is assumed to be incompressible and inertial effects are neglected. Based on the resin content of regions where resin and fiber coexist, expressions for tracking resin flow through fully and partially saturated regions of fiber are given. Values of material parameters for the E-QX 3600-5 glass fabric are estimated from literature data involving compression of similar dry fabrics and through comparison of computed results with the experimental data. Results for the final thickness of the consolidated part agree with the experimental values, but those for the mass loss do not.

Acknowledgements

I would like to thank my current advisor, Dr. Romesh C. Batra, for his guidance and support. I would also like to thank my past advisor, Dr. Alfred C. Loos, for his guidance in graduate and undergraduate studies and for financial support. I would also like to thank the other members of my committee, Dr. Scott W. Case and Dr. Saad A. Ragab.

Many others have made invaluable contributions to this work. Many thanks are due to Dr. Todd A. Bullions, Aaron Caba, Danny Reed, Joe Price-O'Brien, Dr. Donald G. Baird, Dr. Micheal Bortner, Dr. David Dillard, David Simmons and Robert Simonds. I extend my thanks to the U.S. Navy for the material and the financial support. I would also like to thank Joyce Smith who has been an immense help in administrative matters.

Of course, none of this would have been possible without the lifetime, unflagging, and unwavering support of my family and friends. To them I extend the deepest thanks of all.

Table of Contents

List of Figures

List of Tables

Chapter 1

1.1 Introduction

Manufacturing processes for fiber reinforced polymer matrix composites include pultrusion, resin transfer molding (RTM), compression molding, fiber placement, filament winding, structural reaction injection molding (SRIM), vacuum assisted resin transfer molding (VARTM), resin film infusion (RFI), and less sophisticated methods such as hand layup [1]. The process to be used for a given application depends on many factors, the most important of which are often cost, performance, and production process safety.

Some of these processes use prepregs, which are materials with the resin and the fiber mixed together prior to placement in a mold. Typically provided as tapes or sheets, they are used to fabricate high performance parts and are more costly than other production techniques. Parts made from prepregs in general have high fiber volume content, low volume fraction of voids, high strength-to-weight ratio and are employed in demanding applications. Fiber placement and filament winding are examples of processes which commonly use prepregs.

Other methods, such as VARTM and hand layup, use initially dry (resin free), fibrous cloths. These cloths are composed of fiber bundles, called tows, which are arranged in specific patterns, allowing the fibers to be oriented at desired angles. The cloths are laid into a mold of the desired final shape, and then impregnated with resin. These processes, especially VARTM, are useful for manufacturing larger parts and

structures where the cost of prepregs becomes prohibitive. Examples of such parts include boat hulls or large blades for wind turbines.

RFI is a manufacturing process wherein the resin and the fiber are laid together into the mold but are not initially combined. In some applications [2] the reinforcement and the resin film are placed in the mold in separate steps and are combined by applying pressure. In the present application, resin and fiber are contained in each ply of a type of prepreg prior to placement in a mold. This prepreg is one in which a resin film is placed on one or both sides of a sheet of dry fibers. These prepregs are commercially known as Sprint® (SP, Isle of Wight, UK), or Cycom™ (Cytec Engineered Materials, Tempe, AZ). In these prepregs the majority of the fiber stays dry while most of the resin stays outside the cloth. A small region exists through the thickness of the prepreg where the resin and fibers mix.

These prepregs have many advantages. They can be used in manufacturing processes in the same manner as dry reinforcement, but without a complex resin infusion process. This allows simple and efficient assembly practices to be maintained without the fear of having dry or resin rich areas after infusion of a complex part. Expensive resin distribution networks are not needed. The resin film exhibits a light tack at room temperature which allows adhesion to curved surfaces. Extra adhesives, which may introduce defects in a finished laminate, are not required for support before infusion. High quality parts can be obtained using vacuum pressure only; external application of pressure is not required. Styrene emissions of processes involving styrenated resins are reduced, and handling of bulk resin is eliminated. In many cases, production costs can be brought down while product quality is maintained or improved. This process has special

significance for large one-off structures: There is no possibility of an incomplete infusion. The elimination of dry spots in infusion processes may lessen the need for secondary bonding in complex parts, owing to the fact that larger and more complex sections can be fabricated in a single step versus multiple steps. A schematic of this prepreg is shown in Figure 1.1.1.

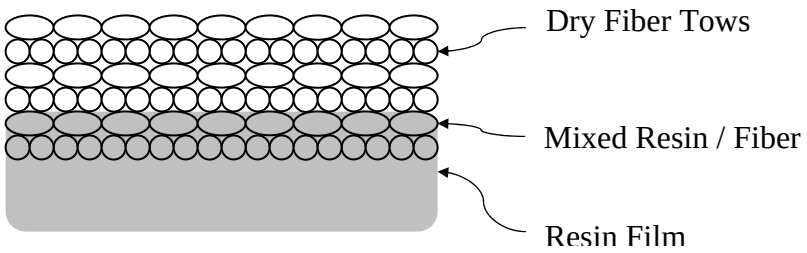

Figure 1.1.1. Schematic of a Typical RFI Prepreg

Stored in refrigeration, the resin retains low-tack properties at room temperature. Some resins used with this prepreg, designed to allow out-of-autoclave manufacture of large parts that previously required autoclaving, cure at temperatures as low as 70^{o}C. The resins typically maintain their handling properties for nearly a month of intermittent exposure to ambient temperatures (1 month out-life).

The goal of the present research was to develop a cure and consolidation model for this prepreg system. Of critical importance was the capability to predict resin flow and laminate compaction during cure. Such a model could be used to determine optimum cure cycles without a need for experimental trial and error. The overall model is composed of three main parts: a kinetics expression, a viscosity relation, and a flow model. The kinetics expression predicts how the resin will cure, the viscosity relation

predicts what the viscosity of the resin will be during cure, and the flow model predicts how the resin will flow through the laminate and how the laminate will deform. These models are inter-related since the viscosity relation requires information from the kinetics expression, and the flow model requires information from the viscosity relation. Both the kinetics and viscosity expressions are fits to experimental data.

The material system used for experiments in this study was a combination of Cytec™ 754 resin film and E-QX 3600-5, a non-woven, quasi-isotropic E-glass fabric. Available in many varieties, the product is commercially known as Cycom™ 754.

A review of previous work in the area is presented in Section 1.2. Chapter 2 presents the results of experiments using the Cycom™ 754 material system. Chapter 3 describes the flow model. Experimental results, curve fits to kinetics and rheology test data and verification of supplemental relations are presented in Chapter 4. Chapter 5 details the numerical evaluation of the flow model and presents observations and comparisons with experimental findings. Conclusions and recommendations for future work are given in Chapter 6.

1.2 Literature Review

Many models to simulate resin flow through fibrous preforms have been proposed, but few account for the motion of fibers. We review those that do, however we also mention some historical models that do not.

Loos and Springer's [3] work on the compaction of laminated composites formed a baseline for future efforts. They modeled the flow of Hercules 3501-6 resin through

multiple layers of unidirectional carbon fiber, and experimentally and analytically investigated the mechanisms of consolidation. They combined Darcy's Law, the balance of linear momentum equation, and the conservation of mass to obtain equations governing the resin flow. However, they did not account for fiber deformation during consolidation, but considered laminate compaction resulting from resin loss.

A necessary ingredient for any model allowing deformation of the fibrous reinforcement is a relation between fiber deformation and permeability. The fiber volume fraction, porosity, and permeability of the reinforcement change as fibers deform. Relations between these properties and the applied pressure or deformation of a laminate are needed. A frequently employed expression to model permeability is due to Carman and Kozeny [4-6]. Loos and MacRae [2] and Song [1] have used empirical relations with good results. Some researchers [7-9] have developed dual scale analytical models that account for the variation in permeability between the fiber tows and the spaces between them in a reinforcement fabric.

The Carman-Kozeny [4] permeability Equation 1.2.1 is based on the concept of hydraulic radius. It gives the permeability of an array of aligned cylinders based on the volume fraction, the cylinder radius, and a single constant. It has been criticized for ambiguity regarding the constant but has been shown to adequately predict the in-plane permeability of aligned fibers [10]. However, it does not predict well the permeability in the transverse direction. Gutowski *et al.* [11, 12] have proposed its generalization, given below as Equation 1.2.2. Equation 1.2.2 predicts better the transverse permeability, although modern works tend to favor using permeability relations determined from experimental data. Gutowski *et al*. [11, 12] introduced the flow limiting volume fraction

parameter. This is defined as the volume fraction at which all flow paths are cut off due to the motion of fibers and is less than the maximum attainable volume fraction. A major difference between Equations 1.2.1 and 1.2.2 is that the latter allows permeability to significantly decrease before the maximum attainable volume fraction is approached, which agrees with experimental results. Equation 1.2.1 does not predict a significant decrease in permeability until the available volume fraction is nearly realized. The available volume fraction is the maximum volume fraction attainable under any compaction pressure.

$$S_{ij} = \frac{r_f^2}{4k_{ij}} \frac{(1-V_f)^3}{V_f^2}, \quad i, j = 1,2,3 \tag{1.2.1}$$

$$S_{ij} = \frac{r_f^2}{4k_{ij}} \frac{\left(\sqrt{\frac{V_a^{'}}{V_f}} - 1\right)^3}{\frac{V_a^{'}}{V_f} + 1}, \quad i, j = 1,2,3 \tag{1.2.2}$$

Here

S_{ij}	=	Permeability, m^2
k_{ij}	=	Carman-Kozeny constant
r_f	=	Fiber radius, m
V_f	=	Fiber volume fraction
$V_a^{'}$	=	Flow-limiting volume fraction

Another essential element of a model that accounts for fiber deformation is a constitutive relation for the fibers. An early investigation by Van Wyk [13] explored

fiber compaction in the compressibility of wool. He treated fibers as Kirchhoff beams, and assumed that no twisting, slipping, or extension occurred.

Gutowski *et al.* [11, 12, 14-18] account for fiber deformation by assuming that fibers exhibit a mathematically characterizable periodic waviness and that their compressive behavior can be approximated by a network of Kirchhoff beams between multiple contact points. Given as Equation 1.2.3, Gutowski *et al.*'s expression is simpler than that of Van Wyk. Its use in the linear momentum equation gives a nonlinear equation governing the fiber volume fraction as a function of space and time. Straightforward expressions for resin velocity, permeability, and other pertinent quantities are given in terms of the volume fraction. Analytically complete and experimentally verified by Wineman [19], Kingery [20] and others, this model has been developed over time and has been employed by other researchers [21, 22].

$$P = A_s \frac{\sqrt{\frac{V_f}{V_o}} - 1}{\left(\sqrt{\frac{V_a}{V_f}} - 1\right)^4} \tag{1.2.3}$$

Where:

A_s = Spring constant, Pa

P = Supported pressure, Pa

V_o = Initial fiber volume fraction

V_a = Available volume fraction

Advani *et al*. [22] applied Equation 1.2.3 to a dual scale porous medium in a RTM application and obtained good agreement with experimental results for some cases but recognized a need to modify the equation for complex geometries and/or varying levels of compaction. Chen and Chou [7, 8] used the concept of Kirchhoff beams to describe three dimensional deformations in woven fibrous preforms. Robitaille and Gauvin [23] used it to predict repeated compaction and relaxation behavior in both dry and wet preforms.

Chen *et al*. [9] later proposed a simple relation for dry compressibility of woven fiber preforms. They define a bulk modulus as an analytical function of volume fraction and five parameters. The bulk modulus is called a bulk compressibility modulus in [9]. The parameters for the bulk modulus can be determined in experiment. The modulus has been specified for limited material systems and has been shown to correlate well with experimental results. Its major limitation is its restriction to dry preforms.

Loos *et al*. [24] analyzed the fiber deformation by assuming a standard continuum constitutive relation for homogeneous elastic orthotropic materials, and used the rule of mixtures to determine the necessary elastic and thermal properties. Combining the continuity equation, Darcy's law, and the balance of linear momentum equation, they described the deformation and saturation of a multiaxial warp knit (MAWK) stitched carbon preform in an RFI application. They used a finite element / control volume method to find an approximate solution of the governing equations. The model included a partially saturated porous medium, aluminum tooling, bleeder plies, and other materials necessary for their RTM application. Their constitutive relation is given below as Equation 1.2.4, in which the Einstein summation convention applies and the range of

indices is three. The fluid pressure in this relation pertains only to the fluid pressure in Loos *et al*.'s model.

$$\sigma_{ij} = C_{ijkl}(e_{kl} - \alpha_{kl}(T - T_0)) - f\bar{\phi}p\delta_{ij} \tag{1.2.4}$$

Where:

σ_{ij}	=	Stress tensor
C_{ijkl}	=	Elastic constants
e_{kl}	=	Infinitesimal strain tensor
α_{kl}	=	Coefficient of thermal expansion tensor
T, T_0	=	Current and reference temperatures respectively
f	=	Volume fraction of a pore occupied by fluid
$\bar{\phi}$	=	Porosity of the preform
p	=	Fluid pressure

Each analytical expression requires a set of parameters to be determined for a given material. In most cases, this involves laboratory experiments and data reduction, each of which is time consuming and expensive. To date, there is no model available which can describe composites consolidation solely on the basis of easily found material parameters such as fiber density, modulus and diameter.

Faced with the need to conduct experiments, many researchers elect to employ empirical [1, 2, 23-26] or statistical [10] relations to describe deformations of fibers under applied loads and the corresponding changes in permeability. It has been shown that a power law expression, such as Equation 1.2.5, can be made to fit compression versus pressure curves for a wide variety of fabrics [25]. A power law expression has

also been used to describe changes in permeability with volume fraction [1, 24]. Experimental data for fiber relaxation under constant deformation has been fit to Equations 1.2.6 [25] and 1.2.8 [1].

$$V_f = A \cdot P^B \tag{1.2.5}$$

$$\frac{P}{P_0} = 1 - C \cdot t^{1/D} \tag{1.2.6}$$

$$V_f = a(1 - e^{b \cdot P}) \tag{1.2.7}$$

$$V_f = c + d\frac{P}{f - P} \tag{1.2.8}$$

where:

P_0	=	Initial relaxation pressure, Pa
$A, B, C, D, a, b, c, d, f$	=	Constants determined from experimental data
t	=	Time elapsed from a reference time, s

Song [1] gave an empirical relation that described fiber motion in a vacuum infusion process. An initially dry preform, sealed under flexible tooling, is infused with resin with the aid of a vacuum (VARTM). Experimental data for dry fiber compaction, wet fiber compaction and wet fiber recovery were fitted by Equations 1.2.7 and 1.2.8. The variation of permeability with volume fraction was accounted for by Equation 1.2.9. The VARTM process was analyzed using a finite element / control volume method and good agreement between computed results and experimental findings was obtained.

$$S = gV_f^{\ h} \tag{1.2.9}$$

Where:

S = Permeability, m^2

V_f = Volume fraction

g, h = Constants to be determined from experimental data.

Verijenko *et al*. [27] numerically studied the resin film infusion process by treating it as a moving boundary problem. A continuum approach is used to describe stresses and strains in the fibrous preforms.

Chapter 2

Experiments

An experimental parametric study has been carried out to determine the effects of cure temperature and consolidation pressure on the void content of parts manufactured from the Cycom™ 754 / E-QX 3600-5 prepreg. Changes in mass and thickness of the test specimens were measured. Values of consolidation pressure and cure temperature used in these tests are shown in Figure 2.1 and are tabulated in Table 2.1. The pressure values were chosen to span the range of pressures encountered in manufacturing practice, from nearly no pressure to almost a full atmosphere. The temperature values spanned the manufacturers recommended processing temperatures.

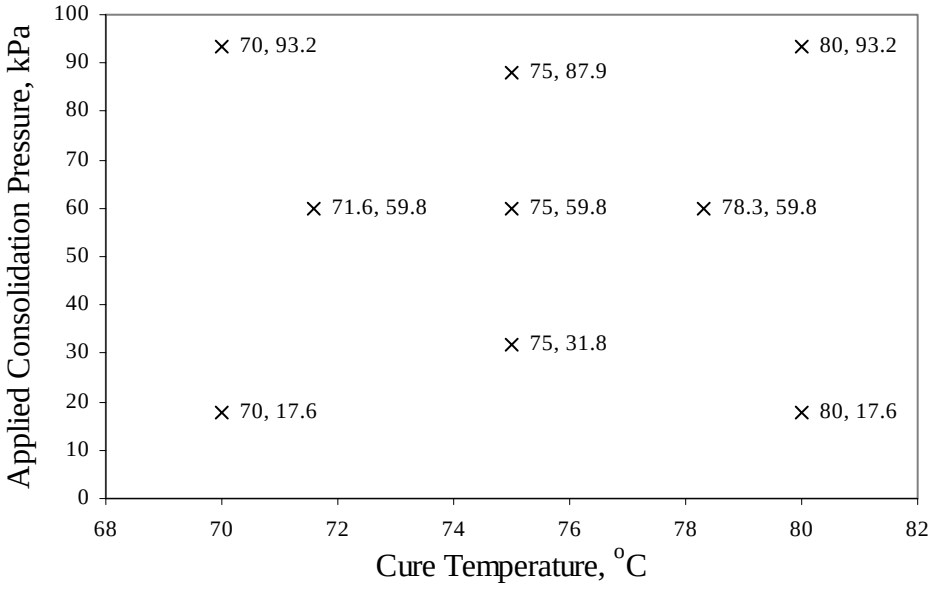

Figure 2.1. Test Points for Experimental Parametric Study

Table 2.1. Test Points for Experimental Study

Test ID	Specimen ID	Temperature ^{o}C	Pressure kPa	Cure Time (hrs)
1	506-1	70.0	17.5	8
2	508-1	80.0	17.5	5
5	509-1	75.0	59.4	6
6	509-2	78.3	59.4	6
7	510-1	71.6	59.4	8
9	514-1	75.0	31.5	6

The cure time was varied according to the manufacturer's recommendations [28]. Each specimen carries both a test ID and a specimen ID. The test ID indicates the grid point of the parametric study, and the specimen ID serves to identify physical samples and to carry labels forward into other tests such as the void content determination.

Each specimen was a 152.4 mm square panel. This size was deemed large enough to render edge flow insignificant. Each panel was composed of eight layers of prepreg, placed with their resin rich faces down, and was consolidated in a standard vacuum bag layup as schematically shown in Figure 2.2. The warp of each layer of the E-QX 3600-5 fabric was aligned with that of every other. The cure cycle for each part was a 45 minute linear ramp from room temperature to the cure temperature, followed by a dwell at the prescribed temperature for the prescribed time, concluded by a 45 minute linear ramp back to room temperature. A sample cure cycle, that for test 5, is given in Figure 2.3. These cure cycles were automatically controlled in a programmable forced convection oven.

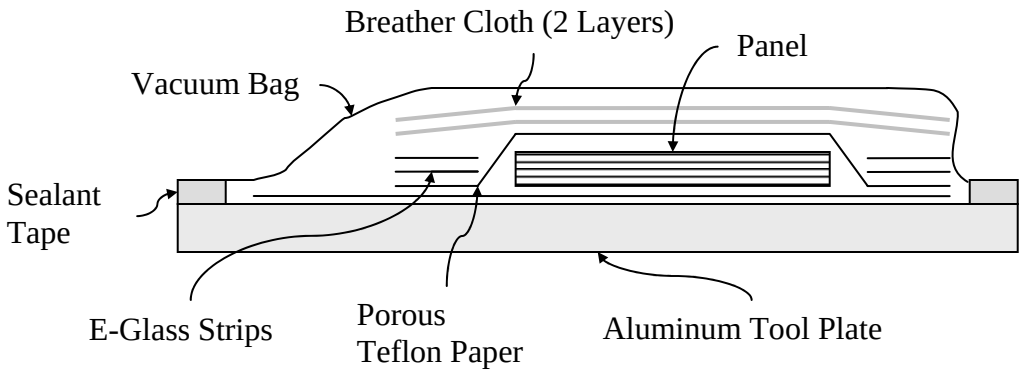

Figure 2.2. Schematic of Typical Vacuum Bag Layup

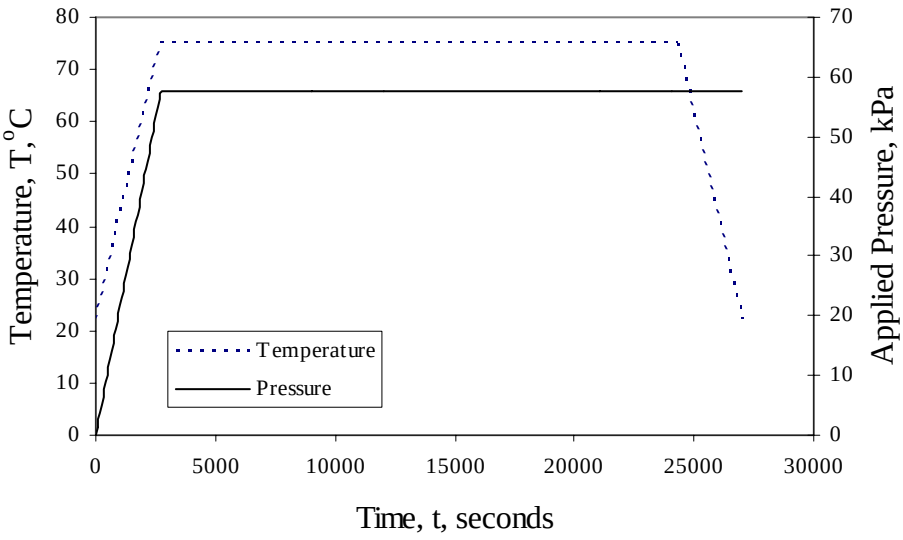

Figure 2.3. Sample Cure Cycle from Experiments

In Figure 2.2, the E-Glass strips assist the function of the breather and have no other bearing on the panel. The 8 layers of prepreg are contained in the panel or part, which is the object of interest. Two layers of breather cloth were used to ensure that enough was available so as not to restrict the flow of resin. Not shown in Figure 2.2 is the vacuum port. In each test, the vacuum port was placed in contact with the breather but away from the panel. A vacuum port contacting the breather allows the consolidation

pressure to be evenly distributed, and one away from the panel assures that there will be no stress concentrations on the panel due to the physical presence of the vacuum port.

The following data was taken: Initial and final thickness, initial and final mass, and void content. The final mass was measured before trimming the fine edges of the finished plate, a necessary safety precaution. Void contents were determined using the standard burn off technique (ASTM D2734-94(2003)). All masses were measured on a calibrated digital scale, thicknesses were taken as the average of 5 micrometer measurements; one in the center and one in each corner, 1 inch away from both sides of the plate. The data are summarized in Figures 2.4-2.6 and Table 2.2. Figure 2.4 shows the void content of each plate over the range of test parameters, Figure 2.5 shows the mass loss, and Figure 2.6 shows the thickness loss. It can be seen from these figures and Table 2.2 that more scatter is present in the mass loss data than for the thickness loss, and both data sets show increasing levels of consolidation with increasing pressure and temperature

Some of the intial and final masses presented in Table 2.2 (Test 1, 2, and 5) add to a number greater than the initial mass; this can be attributed to experimental error in the determination of the initial and final masses. The large changes in thickness presented in Table 2.2 are due to compaction of the composite. Also, any mass loss by the panel is assumed to correspond to a mass gain in the bleeder. The uniform mixing of resin and fiber, along with an increase in volume fraction and cure of the resin are the goals of the consolidation process. A marked reduction in thickness is a by-product of these goals.

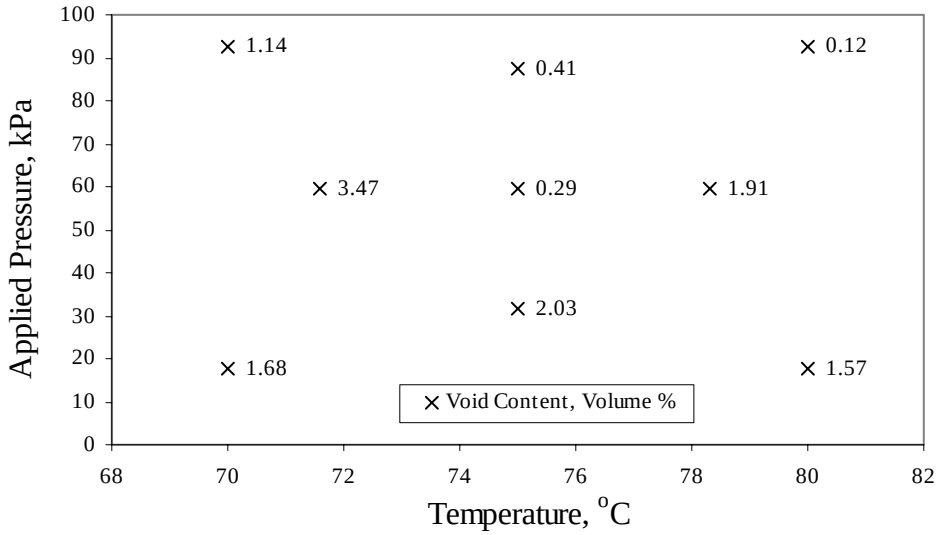

Figure 2.4. Void Content versus Cure Temperature and Consolidation Pressure

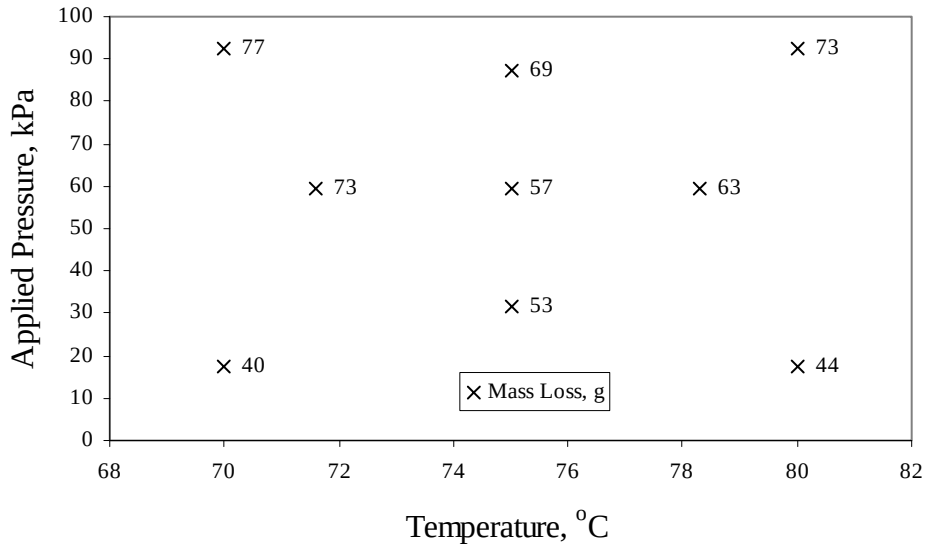

Figure 2.5. Mass Loss versus Cure Temperature and Consolidation Pressure

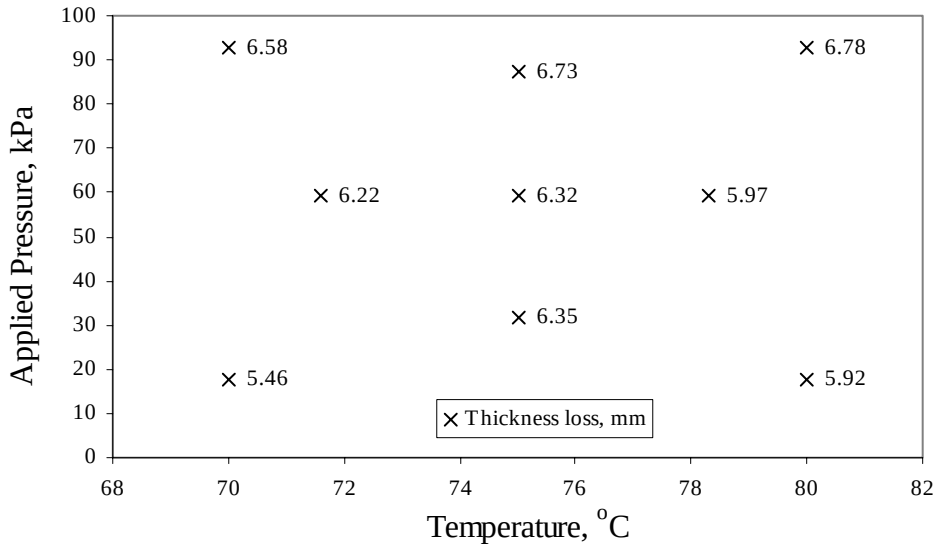

Figure 2.6. Thickness Loss versus Cure Temperature and Consolidation Pressure

Table 2.2. Results of Experimental Study

	Thickness (mm)			Mass (g)			Void Content
Test ID	Initial	Final	Δ	Initial	Final	Δ	Volume %
1	13.21	7.75	5.461 (41.0%)	362	323	40 (10.9%)	1.68
2	13.49	7.57	5.918 (43.9%)	366	323	44 (11.9%)	1.57
3	13.56	6.78	6.782 (50.0%)	371	298	73 (19.6%)	0.12
4	13.31	6.73	6.579 (49.4%)	372	295	77 (20.7%)	1.14
5	13.39	7.06	6.325 (47.3%)	365	309	57 (15.5%)	0.29
6	12.83	6.86	5.969 (46.5%)	361	298	63 (17.3%)	1.91
7	13.23	7.01	6.223 (47.0%)	370	297	73 (19.7%)	3.47
8	13.61	6.88	6.731 (49.4%)	368	299	69 (18.8%)	0.41
9	13.74	7.39	6.350 (46.2%)	369	316	53 (14.4%)	2.03

Chapter 3

Model Development

The flow and compaction model is based on the work of Gutowski *et al.* [14-18]. Its formulation is modified or extended where necessary to fit the requirements of this application.

The following assumptions are made in the formulation of the flow model. The resin is assumed to be incompressible and Newtonian. Capillary, gravitational and surface tension effects are neglected. Flow is assumed to be quasi-steady and inertial effects are judged insignificant. The fibers are assumed to be incompressible. Though the fibers are incompressible, the mat they combine to form is not. Because the laminate is thin and large, flow is only considered in the thickness direction. It is also assumed that the entire laminate uniformly heats and cools with the prescribed cure temperatures. The thermal effects of chemical reactions are neglected. The fibers are assumed to be uniformly distributed in the prepreg, as opposed to being organized into tows or bundles. The deformation of dry fibers is assumed to be elastic.

3.1 Flow Model Formulation

The composite is represented as a porous and nonlinear elastic medium which is either dry, partially saturated, or completely saturated with the resin. The application of consolidation pressure, concurrent with the presence of a reservoir into which the resin

can flow, is the sole cause of resin flow and laminate consolidation. Support of this load is shared by the resin and the fiber structure throughout the consolidation process. Because the fibers are assumed to initially exist in their unloaded or natural state, the initial application of load is solely supported by the resin in resin-containing regions in the same manner as it would be at all times if there was no reservoir into which the resin could flow. If this reservoir is present and a resin-containing region exists with a favorable pressure gradient at the boundary between the composite and the reservoir, the resin will flow from the composite into the reservoir. The loss of resin from the resin-containing region aids consolidation of the laminate, transferring an increasing portion of the load to the fibers. This continues until the fibers support the entire applied load and maximum consolidation has been reached or until the viscosity of the resin increases to a point where flow no longer occurs.

The concept is similar to a spring-supported piston filled with water [1]. A schematic of this system is shown in Figure 3.1.1. In part (a) of Figure 3.1.1, the spring is in its natural state. Before the valve on the piston is opened (a), the water, assumed to be incompressible, supports the entire applied load. After the valve is opened (b) and water flows out, the spring begins to deform and carries an increasing portion of the load until it carries the entire load (c) and the water supports none. In Gutowski's model, the load supported by the spring corresponds to the load supported by the fibers (See Equations 3.1.5 and 3.1.10), and the load supported by the water is that supported by the resin. The increasing load carried by the spring corresponds directly to the increasing load carried by the fibers and increased consolidation. The water which comes to reside on top of the piston can be said to have flowed into the bleeder, and the water remaining

in the lower section of the piston can be said to have remained in the panel; this is the only mechanism for mass loss of the panel, resin flow into the bleeder. The sum of the masses of the panel and the bleeder is assumed to be constant.

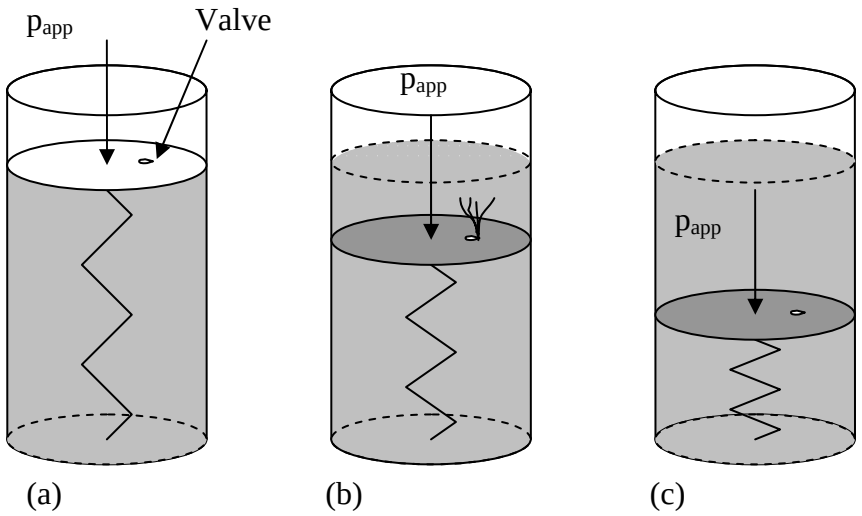

Figure 3.1.1. Schematic of Piston Containing Spring and Incompressible Fluid

Some unique aspects of Gutowski's model are that the fibers are assumed to exhibit an initial periodic waviness which can be mathematically characterized and a fiber between two consecutive contact points is modeled as a Kirchhoff beam. Because there are many fibers that may initially be near each other but not in contact, the number of contact points increases as the fiber network is compressed, and the resulting compressive behavior is strongly nonlinear. The reader is referred to [11, 14, 17] for an in-depth discussion of this concept.

An example laminate is shown in Figure 3.1.2. It has dimensions $a \times b \times h_0$ and is composed of aligned fibers. It is not necessary that the fibers be unidirectional, but for this formulation the distribution of fibers should be uniform.

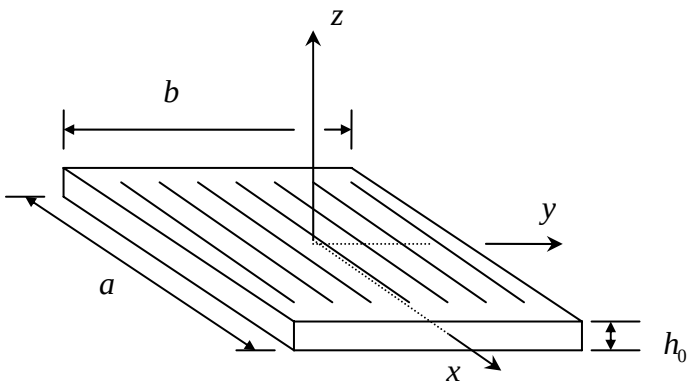

Figure 3.1.2. Orientation and Dimensions of Composite Laminate

The axes in Figure 3.1.2 are aligned with the principal axes of the laminate. The x axis is aligned with the warp, y is with the weft, and z is perpendicular to the plane of the laminate. Pressure is evenly applied in the $-z$ direction and the laminate is uniformly supported underneath. The model is one dimensional as stated earlier.

Shown in Figure 3.1.3 is a representative volume element of the composite.

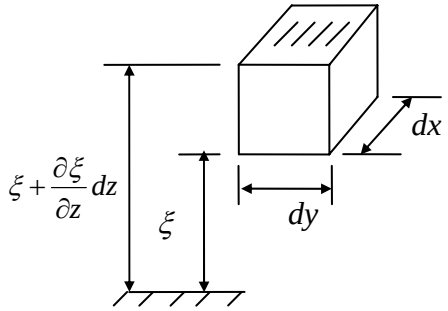

Figure 3.1.3. Representative Composite Element

It is useful to introduce a filter velocity for tracking resin flow through the composite. First proposed by Scheidegger [29], it is the ratio of the volume flow rate relative to the fibers and the cross sectional area perpendicular to the flow direction. The filter velocity has units of length per time; its components are given in Equations 3.1.2-3.1.3. The velocity of the fiber bed, $\partial\xi/\partial t$, is taken into account in the z component of the filter velocity in Equation 3.1.3.

$$q_x = \frac{Q_x}{A_x} \tag{3.1.1}$$

$$q_y = \frac{Q_y}{A_y} \tag{3.1.2}$$

$$q_z = (1 - V_f)(u_z - \frac{\partial \xi}{\partial t}) \tag{3.1.3}$$

where:

Q_x, Q_y = Volume flow rate along x or y axis, m^3/s

A_x, A_y = Cross-sectional area normal to x or y axis, m^2

q_x, q_y, q_z = Filter velocity in x, y, or z direction

u_z = Resin velocity in the z direction, m/s

It is important to note that the volume fractions of the resin, V_r, and of fiber, V_f, always add to one, as per Equation 3.1.4.

$$V_r + V_f = 1 \tag{3.1.4}$$

Also, both the resin and fibers are incompressible, that is, $\rho_r = const.$ and $\rho_f = const.$ Note that while the fibers are in this sense incompressible, the mat, which is composed of multiple curved and interlaced fibers, is compressible.

In order to account for the balance of forces in the composite, it is necessary to consider the linear momentum equation. If inertial forces are small and gravitational effects are neglected, the external applied load must be balanced by the loads supported by the resin and the fiber. Expressed in terms of the applied pressure, p, the average resin pressure, $\overline{p}_r$, and the average fiber pressure, $\overline{p}_f$;

$$p = \overline{p}_f V_f + \overline{p}_r P_r \tag{3.1.5}$$

where the product $\overline{p}_f V_f$ is termed the 'fiber effective stress', and is the portion of the applied pressure supported by the fibers. P_r is a parameter that takes on a value of 0 when no resin is present and 1 when it is. Also, $\overline{p}_r P_r = p_r$. Equation 3.1.5 states that the applied pressure is shared by the fiber and the resin. The portion borne by the fiber varies with the fiber volume fraction. Though it is intuitive, it may prove useful to draw attention to the following: This relation also states that if there is no resin in a given region, the fiber must solely support the applied pressure. Similarly, if there is no fiber in a region, the resin alone supports the applied pressure.

The volume of fibers in the representative element in Figure 3.1.3 is assumed to be constant. Therefore, fiber continuity can be expressed as:

$$V_o = V_f \frac{\partial \xi}{\partial z}, \tag{3.1.6}$$

where V_o is the initial volume fraction. The continuity equation accounting for mat compressibility can be written as:

$$\frac{\partial}{\partial x}(q_x \frac{\partial \xi}{\partial z}) + \frac{\partial}{\partial y}(q_y \frac{\partial \xi}{\partial z}) + \frac{\partial}{\partial z}(q_z) + \frac{\partial}{\partial t}[(1-V_f)\frac{\partial \xi}{\partial z}] = 0 \tag{3.1.7}$$

Because the problem involves fluid flow through a porous medium, Darcy's Law [11], is employed as given below in Equation 3.1.8 where the variable thickness in the z direction is taken into account.

$$\begin{Bmatrix} q_x \\ q_y \\ q_z \end{Bmatrix} = -\frac{1}{\mu}\begin{bmatrix} S_{xx} & 0 & 0 \\ 0 & S_{yy} & 0 \\ 0 & 0 & S_{zz} \end{bmatrix}\begin{Bmatrix} \partial p_r / \partial x \\ \partial p_r / \partial y \\ \partial p_r / \partial \xi \end{Bmatrix} \tag{3.1.8}$$

Here μ is the resin viscosity, and S_{xx}, S_{yy}, and S_{zz} are the permeabilities in the principal material directions.

Under the assumptions that S_{xx} and S_{yy} are functions of V_f only, that V_f is a function of z and t only, and that μ is a function of t only, Equations 3.1.6-3.1.8 reduce to the following:

$$\frac{S_{xx}}{V_f}\frac{\partial^2 p_r}{\partial x^2} + \frac{S_{yy}}{V_f}\frac{\partial^2 p_r}{\partial y^2} + \frac{1}{V_0^2}\frac{\partial}{\partial z}(V_f S_{zz}\frac{\partial p_r}{\partial z}) = \mu \frac{\partial}{\partial t}(\frac{1-V_f}{V_f}) \tag{3.1.9}$$

Equation 3.1.9 is a three dimensional, nonlinear governing equation relating resin pressure to the volume fraction of the fibers. With proper boundary and initial conditions, and expressions for S_{xx}, S_{yy}, S_{zz}, V_f and μ, it can be solved numerically for p_r. For the present application, further simplifications are made.

We adopt the following expression proposed by Gutowski *et al*. [11] for the stress in the fibers.

$$\sigma(V_f) = A_s \frac{\sqrt{\frac{V_f}{V_o}} - 1}{\left(\sqrt{\frac{V_a}{V_f}} - 1\right)^4} \tag{3.1.10}$$

where:

$\sigma(V_f)$ = Fiber effective stress, Pa

V_a = Available volume fraction

A_s = Spring constant, Pa

The fiber effective stress σ in Equation 3.1.10 equals $\bar{p}_f V_f$ in Equation 3.1.5, so that it becomes:

$$p = \sigma(V_f) + \bar{p}_r P_r \tag{3.1.11}$$

A relation between the permeability and the volume fraction of fibers is also needed. Tabulated values of permeability, while convenient, are obtained through a test

on a material in which V_f does not change, or if it does, the variation of V_f is unaccounted for. Because of this, tabulated values have limited applicability. Here we use Equation 1.2.2 proposed by Gutowski *et al*. [11].

Neglecting flow in the x and y directions, Equation 3.1.9 becomes:

$$\frac{1}{V_o^2}\frac{\partial}{\partial z}\left(V_f S_{zz}\frac{\partial p_r}{\partial z}\right)=\mu\frac{\partial}{\partial t}\left(\frac{1-V_f}{V_f}\right). \tag{3.1.12}$$

Carrying out the differentiation in 3.1.12 and rearranging gives:

$$\frac{1}{\mu}\frac{V_f^2}{V_o^2}\left[\frac{\partial\left(V_f S_{zz}\right)}{\partial z}\frac{\partial p_r}{\partial z}+V_f S_{zz}\frac{\partial^2 p_r}{\partial z^2}\right]=V_f\frac{\partial}{\partial t}(1-V_f)-(1-V_f)\frac{\partial V_f}{\partial t}. \tag{3.1.13}$$

Using $p=\sigma(V_f)+\bar{p}_r P_r$, the fact that the applied pressure does not change with respect to z ($\partial p/\partial z = 0$), and rearranging, Equation 3.1.13 becomes:

$$\frac{1}{\mu}\frac{V_f^2}{V_o^2}\left[\frac{\partial\left(V_f S_{zz}\right)}{\partial z}\frac{\partial\sigma}{\partial z}+V_f S_{zz}\frac{\partial^2\sigma}{\partial z^2}\right]=\frac{\partial V_f}{\partial t}. \tag{3.1.14}$$

The use of the chain rule of Calculus on the first term inside the brackets gives:

$$\frac{\partial\left(V_f S_{zz}\right)}{\partial z}=\frac{\partial\left(V_f S_{zz}\right)}{\partial V_f}\frac{\partial V_f}{\partial\sigma}\frac{\partial\sigma}{\partial z}. \tag{3.1.15}$$

Substituting 3.1.15 into 3.1.14 we obtain:

$$\frac{1}{\mu}\frac{V_f^2}{V_o^2}\left[\frac{\dfrac{\partial\left(V_f S_{zz}\right)}{\partial V_f}}{\dfrac{\partial\sigma}{\partial V_f}}\left(\frac{\partial\sigma}{\partial z}\right)^2 + V_f S_{zz}\left(\frac{\partial^2\sigma}{\partial z^2}\right)\right] = \frac{\partial V_f}{\partial t}. \tag{3.1.16}$$

This form of the governing equation is useful for comparison with experimental data because quantities involved, fiber volume fraction, permeability, and fiber effective stress (the difference between applied and resin pressure) are easily measured. However, for numerical evaluation it is useful to obtain an equation where all differentiation is on $V_f(z,t)$, not $\sigma(V_f)$. With this in mind:

$$\frac{\partial\sigma}{\partial z} = \frac{\partial\sigma}{\partial V_f}\frac{\partial V_f}{\partial z} \tag{3.1.17}$$

allows the first derivative with respect to z to be carried out on V_f. It should be noted that differentiations with respect to V_f can be carried out analytically on Equation 3.1.10. Differentiating Equation 3.1.17 with respect to z gives:

$$\frac{\partial^2\sigma}{\partial z^2} = \frac{\partial}{\partial z}\left(\frac{\partial\sigma}{\partial V_f}\frac{\partial V_f}{\partial z}\right) = \frac{\partial^2\sigma}{\partial {V_f}^2}\left(\frac{\partial V_f}{\partial z}\right)^2 + \frac{\partial\sigma}{\partial V_f}\frac{\partial^2 V_f}{\partial z^2} \tag{3.1.18}$$

An additional chain rule has been used in the first term on the right hand side of Equation 3.1.18. Substituting the results of Equations 3.1.17 and 3.1.18 into Equation 3.1.16 and rearranging yields:

$$\frac{\partial V_f}{\partial t} = \frac{1}{\mu}\frac{V_f^2}{V_o^2}\left[C_{zz}\left(\frac{\partial^2 \sigma}{\partial V_f^2}\left(\frac{\partial V_f}{\partial z} \right)^2 + \frac{\partial \sigma}{\partial V_f}\frac{\partial^2 V_f}{\partial z^2} \right) + \frac{C_{zz}^{'}}{\sigma^{'}}\left(\frac{\partial \sigma}{\partial V_f}\frac{\partial V_f}{\partial z} \right)^2 \right] \quad (3.1.19)$$

where $C_{zz} = V_f S_{zz}$ and the prime denotes differentiation with respect to V_f. Rearranging Equation 3.1.19 gives:

$$\frac{\partial V_f}{\partial t} = A(V_f)\frac{\partial^2 V_f}{\partial z^2} + B(V_f)\left(\frac{\partial V_f}{\partial z} \right)^2, \quad (3.1.20)$$

where:

$$A(V_f) = \frac{1}{\mu}\frac{V_f^2}{V_o^2} C_{zz}\frac{\partial \sigma}{\partial V_f} \quad (3.1.21)$$

$$B(V_f) = \frac{1}{\mu}\frac{V_f^2}{V_o^2}\left[C_{zz}\frac{\partial^2 \sigma}{\partial V_f^2} + \frac{C_{zz}^{'}}{\sigma^{'}}\left(\frac{\partial \sigma}{\partial V_f} \right)^2 \right]. \quad (3.1.22)$$

Equation 3.1.20 is solved numerically for V_f as a function of z and t. Fiber and resin velocities at any point in a mixed fiber/resin region can be obtained from the following relations [14]:

$$\frac{\partial \xi}{\partial t} = -\frac{S_{zz}}{\mu}\frac{V_f}{V_o}\frac{\partial \sigma}{\partial V_f}\frac{\partial V_f}{\partial z} \quad (3.1.23)$$

$$u_z = \frac{S_{zz}}{\mu}\frac{V_f^{\,2}}{(1-V_f)V_o}\frac{\partial \sigma}{\partial V_f}\frac{\partial V_f}{\partial z}. \quad (3.1.24)$$

Here $\partial\xi/\partial t$ is the fiber velocity, and u_z is the resin velocity, both being in the z direction.

3.2 Boundary and Initial Conditions

At an interface between a region of mixed fiber and resin and a dry fiber region, the fibers support all of the applied pressure.

$$\sigma(V_f) = p \tag{3.2.1}$$

At an interface between a mixed region and a resin only region, the resin supports all of the pressure.

$$\sigma(V_f) = 0 \tag{3.2.2}$$

Equation 3.2.1 specifies a value of V_f between V_o and V_a. Equation 3.2.2 specifies that $V_f = V_o$.

Another boundary condition is that which occurs when a mixed region meets another mixed region. The two regions are distinguished by their initial and time-dependent positions and thicknesses. Resin and fiber continuity require that V_f be smooth and continuous across the boundary. The consequences of this are that all other calculated quantities will be continuous across the boundary, conservation of linear

momentum and conservation of mass (to be presented in Equations 3.3.6-3.3.11) remain satisfied, in addition to the condition on V_f. This can be expressed as follows:

$$V_f\ |_+ = V_f\ |_- \tag{3.2.3}$$

$$\frac{\partial V_f}{\partial z}|_+ = \frac{\partial V_f}{\partial z}|_- \tag{3.2.4}$$

where the subscripts '+' and '-' indicate evaluation from the upper and lower side of the boundary respectively.

At the interface between a mixed fiber-resin region and a solid surface, we have $u_z = 0$ and $\partial\xi/\partial t = 0$ which are simultaneously satisfied (see Equations 3.1.23 and 3.1.24) if:

$$\frac{\partial V_f}{\partial z} = 0\,. \tag{3.2.5}$$

The initial condition for all regions containing fiber is as follows:

$$V_f = V_o \text{ at } t = 0 \tag{3.2.6}$$

3.3 Flow Front Tracking

In its initial state, the prepreg can be divided into three regions in the thickness direction. On one side is neat resin, in the middle is a region of mixed fiber and resin,

and on the other side is a region of dry fiber. A single layer of prepreg under pressure is shown in Figure 3.3.1.

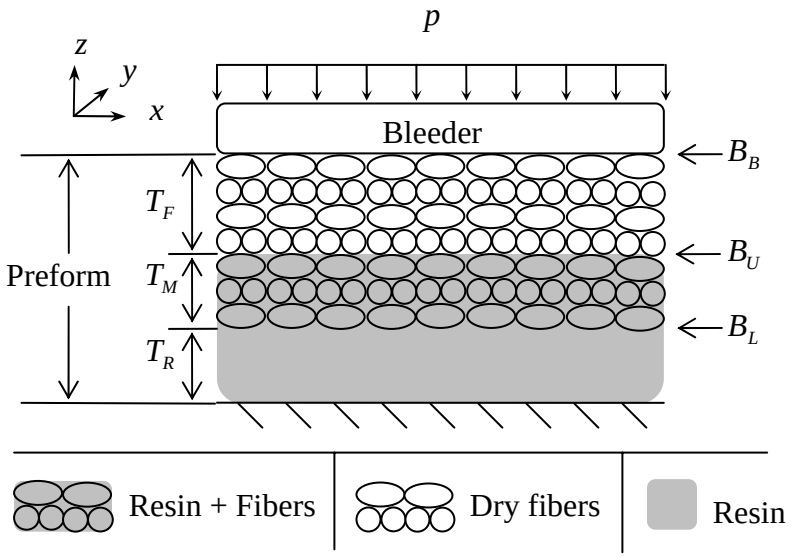

Figure 3.3.1. Schematic of a Single Layer Preform Under Pressure

At the top of the laminate in Figure 3.3.1 is the bleeder into which excess resin can flow. Underneath the bleeder is a region of dry fiber, described by the thickness dimension T_F. Below this is the region of mixed fiber and resin, of thickness T_M. At the bottom is a region of neat resin, of thickness T_R. The boundaries between the bleeder, the dry fiber, the mixed fiber / resin, and the neat resin regions are denoted by B_B, B_U, and B_L, respectively. Finally, p is the pressure applied on the topmost surface of the assembly.

The bleeder is made of a porous material which provides both a region into which resin can flow with negligible resistance and a structure capable of transferring the applied load to the laminate. It is separated from the underlying, initially dry fiber by a

sheet of porous cloth, which allows the bleeder to be separated from the part once the cure reaction is complete. This is called the porous release paper in Figure 2.2. Both the bleeder and the release paper are assumed to be much more porous than the fibers. The bleeder is also assumed to be of adequate capacity to accept all resin that flows into it, and along with the release paper is otherwise neglected in the analysis. The entire assembly rests on the surface of a rigid, fixed, and impenetrable tool.

All regions in the preform must satisfy Equation 3.1.11. Because there is no resin in the dry fiber region, the fiber supports the applied load there, and Equation 3.2.1 holds.

The dry fiber will deform to a volume fraction sufficient to support the applied pressure as required by Equations 3.1.10 and 3.1.11. Because the fibers are assumed to be elastic, the deformation of the dry fiber region occurs instantaneously upon the application of pressure.

The thickness of the dry fiber region after deformation due to the application of pressure is calculated from the following relation:

$$T_F = \left(T_F \mid_{t_t}\right)\frac{V_i}{V_f} \tag{3.3.1}$$

$T_F\big|_{t_i}$ is the thickness of the dry fiber region and V_i the fiber volume fraction prior to the application of load, and V_f in Equation 3.3.1 is the fiber volume fraction which solves Equation 3.2.1. If $t_i = 0$, $V_i = V_o$.

The thicknesses of the regions that contain resin are tracked by their resin content. The resin content of a region is the product of its thickness, its average porosity and its degree of saturation. The degree of saturation of any region defined thus far is either zero

or one: It is either saturated or not saturated. The initial resin contents are computed using the initial volume fraction of the fibers which is assumed uniform across all fiber containing regions. The filter velocity, q_z, defined in Equation 3.1.3, is evaluated at the boundaries of the regions and used to track resin flow there. The region thicknesses are obtained by dividing their resin contents by their average porosities. Average fiber volume fractions and porosities are determined using the mean value theorem. The dry fiber regions contain no resin by definition, and must be tracked by their absolute thicknesses using Equation 3.3.1.

Until either T_R or T_F becomes zero or the resin gels, the flow can be discretized in time and tracked as follows:

$$T_R^{t+\Delta t} = T_R^t - q_z\,|_{B_L}\,\Delta t \tag{3.3.2}$$

$$RC_M^{t+\Delta t} = RC_M^t + q_z\big|_{B_L}\,\Delta t \tag{3.3.3}$$

$$T_F^{t+\Delta t} = T_F^t\,\frac{V_f^t}{V_f^{t+\Delta t}} - \frac{q_z\,|_{B_U}}{V_f^t}\Delta t \tag{3.3.4}$$

where deformation of the dry fiber region in response to the applied pressure has been taken into account in Equation 3.3.4. The term RC_M is the resin content of the mixed region. Because the fiber volume fraction of the resin region is by definition zero, and because resin content is being tracked in units of length, the thickness of the resin region, T_R, is synonymous with its resin content. If T_F becomes zero, the dry region has been saturated, the resin flow has reached the bleeder, and B_U will coincide with B_B. In this situation, the change in resin content of the mixed region in contact with the bleeder through time is no longer given by Equation 3.3.3 but by the following relation:

$$RC_M^{t+\Delta t} = RC_M^t + \left(q_z\big|_{B_L} - q_z\big|_{B_U} \right)\Delta t \tag{3.3.5}$$

The filter velocity given by Equation 3.1.3 is used to calculate the amount of resin flowing into the bleeder and is evaluated at B_U.

If T_R becomes zero, the resin tracking expressions do not change other than T_R being zero. B_L will coincide with the tool plate, and the existing boundary condition will change to $q_z = 0$ which is equivalent to Equation 3.2.5. It is assumed that a region whose thickness has reached zero cannot regain thickness regardless of future variations in pressure.

Some additional possibilities must be considered in the case of a laminate composed of multiple layers. At the interfaces between layers, the neat resin region from an upper layer of prepreg will be in direct contact with the dry fiber region of the layer directly underneath. There is no barrier to prevent resin flow across this boundary, and a second mixed region results. This second mixed fiber and resin region will have different boundaries, a different thickness, different position, and a different resin content than the mixed region for a preform composed of a single layer but is treated much the same. The second mixed region will exist in every layer except the top layer. The possibility exists that mixed regions may meet; therefore, resin flow expressions accounting for this are necessary. A multiple layer situation is schematically shown in Figure 3.3.2. Commas in subscripts do not imply differentiation here.

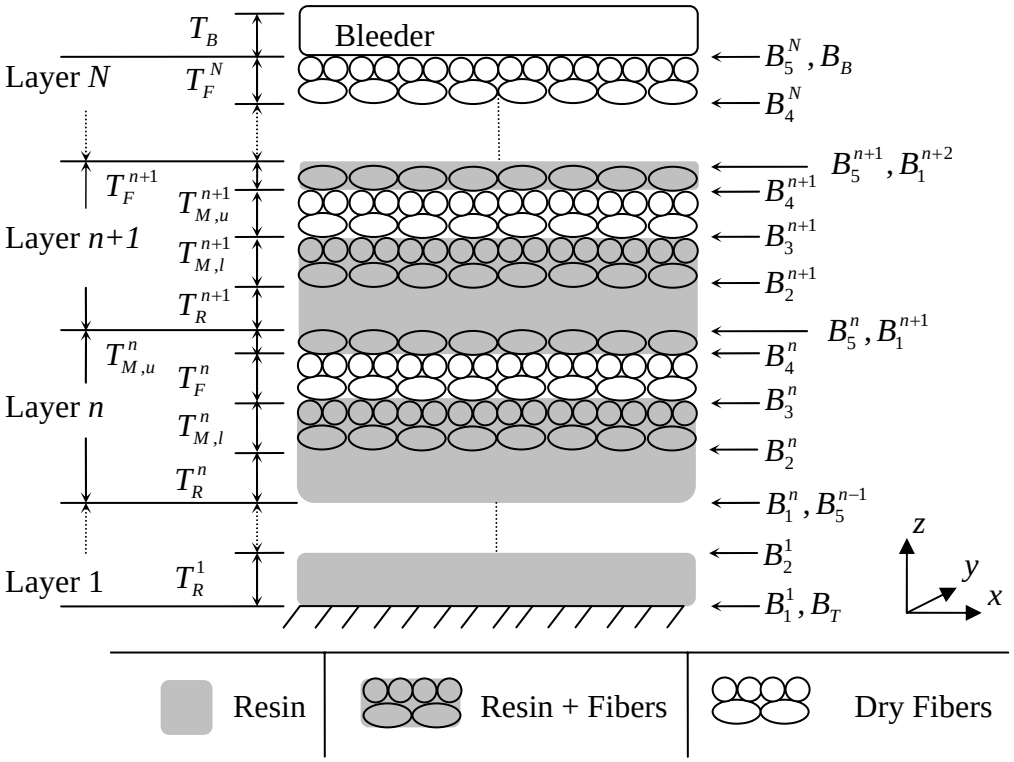

Figure 3.3.2. Schematic of a Multi-Layer Laminate

The superscript n denotes the layer number and the subscripts l and u (following a comma) denote lower and upper respectively. The dots imply that the stacking sequence repeats.

The layer under consideration is now composed of the following four regions: (1) A region of neat resin; (2) A region of mixed fiber and resin, now the lower mixed region; (3) A region of dry fiber; and (4) An upper mixed region. Two layers, the top and the bottom, will have different surroundings. The top layer will be bounded on its upper surface by the bleeder and will have no upper mixed region. The bottom layer will be bounded on its lower surface by the tool and will lose no resin to a lower layer. The

flow tracking expressions in Equations 3.3.2-3.3.5 are extended to take into account the upper mixed region:

$$RC_{M,u}^{t+\Delta t} = RC_{M,u}^{t} + q_z\big|_{B_5^n}\,\Delta t \tag{3.3.6}$$

$$T_F^{t+\Delta t} = T_F^{t}\,\frac{V_f^t}{V_f^{t+\Delta t}} + \left(\frac{q_z\,|_{B_4^n} - q_z\,|_{B_3^n}}{V_f^t}\right)\Delta t \tag{3.3.7}$$

$$RC_{M,l}^{t+\Delta t} = RC_{M,l}^{t} + q_z\,|_{B_2^n}\,\Delta t \tag{3.3.8}$$

$$T_R^{t+\Delta t} = T_R^{t} + \left(q_z\,|_{B_1^n} - q_z\,|_{B_2^n}\right)\Delta t \tag{3.3.9}$$

These relations hold for every layer in a multi-layered laminate if one considers that the thickness of the upper mixed region in the top-most layer is always zero, and that q_z evaluated at B_1^n is zero for the bottom-most layer.

An additional consideration is the intersection of two mixed regions, which can meet in two ways: (a) through a dry fiber region and (b) through a neat resin region. Regardless, the volume fraction at the flow fronts must be that which satisfies Equation 3.1.11. In the case of a meeting through a dry fiber region, the pressure supported by the resin at the flow front will be zero by Equation 3.2.1. In the case of a meeting through a neat resin region, the fiber effective stress at the flow front will be zero by Equation 3.2.2. The situation of two mixed regions meeting is schematically shown in Figure 3.3.3.

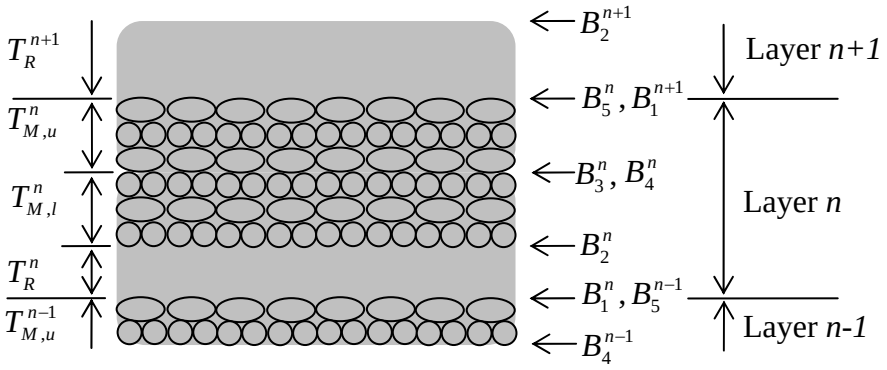

Figure 3.3.3. Schematic of Two Mixed Regions Intersecting

After the meeting, the term on the right hand side of Equation 3.1.11 which was zero before the meeting begins to increase. Neither of these terms can now be specified, and the appropriate boundary conditions are those given by Equations 3.2.3 and 3.2.4. The flow tracking expressions for the mixed regions, Equations 3.3.6 and 3.3.8, are modified as follows:

$$RC_{M,u}^{t+\Delta t} = RC_{M,u}^{t} + \left(q_z\big|_{B_5^n} - q_z\big|_{B_4^n}\right)\Delta t \tag{3.3.10}$$

$$RC_{M,l}^{t+\Delta t} = RC_{M,l}^{t} + \left(q_z\big|_{B_3^n} - q_z\big|_{B_2^n}\right)\Delta t \tag{3.3.11}$$

In summary, we solve Equation 3.1.20 under initial conditions (Equation 3.2.6) and the pertinent boundary conditions. However, it requires that the viscosity μ be known as a function of V_f. We address this next.

Chapter 4

Supplemental Relations

In addition to the flow model, it is necessary to incorporate a relation for resin viscosity. The expression for resin viscosity requires information about the degree of cure of the resin, so resin kinetics must also be accounted for. These are derived by fitting curves to the test data and are presented below, we also estimate values of the constants appearing in Equations 3.1.10 and 1.2.2.

4.1 Resin Viscosity Relation for the Cytec™ 754 Resin

Steady shear isothermal viscosity measurements on the resin were conducted at 70-95^{o}C in 5 degree increments. Each test was carried out until a sharp increase in resin viscosity was encountered, indicating that the resin was beginning to gel. It was necessary to terminate the tests before the resin fully gelled to avoid damage to the rheometer. Tests were conducted on a Rheometrics RMS-800 parallel plate rheometer in a nitrogen atmosphere. Samples of neat resin were approximately 1 mm thick and were placed between 40 mm diameter disposable aluminum disks.

Data from each test gave the viscosity of the resin as the cure reaction progressed under isothermal conditions. A sample data set is shown in Figure 4.1.1. Degree of cure for this and similar tests was obtained with the resin kinetics relation detailed in section 4.2.

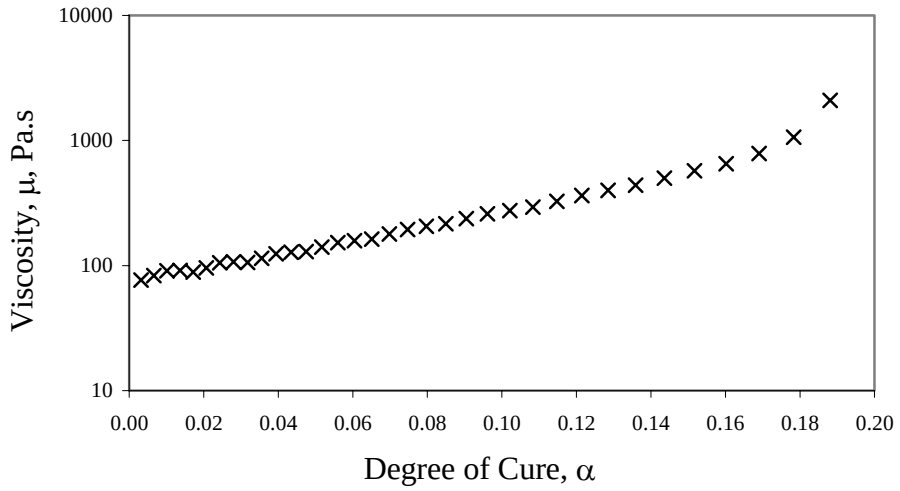

Figure 4.1.1. Viscosity versus Degree of Cure for 70°C Isothermal Test

Typical of all tests, Figure 4.1.1 shows that viscosity increases with the degree of cure, due to the progressive cross linking of polymer chains in the thermosetting resin. The onset of gel is indicated by a sharp increase in viscosity, heralding the end of the test. In the case of the 70°C isotherm shown in Figure 4.1.1, gel was reached at a degree of cure of approximately 20%. The determination of the degree of cure is described in the following section.

An expression for the viscosity as a function of degree of cure is sought in the following form [30, 31]:

$$\mu = K_\mu \left(\frac{\alpha_g}{\alpha_g - \alpha} \right)^{A+B\alpha} \tag{4.1.1}$$

$$K_\mu = A_\mu e^{Ea_\mu / R \cdot T} \tag{4.1.2}$$

where:

μ	=	Viscosity, $Pa\ s$
K_μ	=	Coefficient of viscosity, s^{-1}
α_g	=	Degree of cure at gel
A, B	=	Exponential coefficients
A_μ	=	Arrhenius pre-exponential viscosity coefficient, s^{-1}
Ea_μ	=	Arrhenius activation energy for viscosity, s^{-1}
R	=	Universal gas constant, $J / mol\ K$
T	=	Temperature, K

The Arrhenius coefficients A_μ and Ea_μ depend on temperature as follows:

$T \le 358.15\ K$:

$$A_\mu = 2.6418 \times 10^9\ \ s^{-1} \tag{4.1.3}$$

$$Ea_\mu = 4.6209 \times 10^4\ \ s^{-1} \tag{4.1.4}$$

$T > 358.15\ K$:

$$A_\mu = 6.0597\ \ s^{-1} \tag{4.1.5}$$

$$Ea_\mu = 1.0545 \times 10^5\ \ s^{-1} \tag{4.1.6}$$

A break point of 358.15 K was chosen to follow a trend exhibited by the data, as shown in Figure 4.1.2. The following expressions for the coefficients A, B, and α_g were found from best fits to the experimental data:

$$A = a_1 T^2 + a_2 T + a_3 \tag{4.1.7}$$

$$B = b_1 T^2 + b_2 T + b_3 \tag{4.1.8}$$

$$\alpha_g = \alpha_1 T^2 + \alpha_2 T + \alpha_3 \tag{4.1.9}$$

Values of the coefficients a_i, b_i, and α_i are given in Table 4.1.1.

Table 4.1.1. Values of a_i, b_i, and α_i

Constant	Value	Units	Constant	Value	Units	Constant	Value	Units
a_1	1.84320E-03	K^{-2}	b_1	1.94318E-03	K^{-2}	α_1	1.82938E-04	*unitless*
a_2	-0.344526	K^{-1}	b_2	6.28418E-03	K^{-1}	α_2	-3.25384E-02	*unitless*
a_3	18.0722	*unitless*	b_3	-20.5750	*unitless*	α_3	1.57533	*unitless*

Values of constants in Equations 4.1.1 and 4.1.2 were obtained using a recursive least squares method. The procedure for this was as follows: (a) The values of the coefficients that gave the best fit to the test data at each isothermal temperature were determined by the least squares method. (b) The coefficients for these individual fits were plotted over the range of tests, versus temperature or inverse temperature as applicable. (c) Numerical fits were made where variation of a coefficient was seen to occur over the range of test temperatures. The Arrhenius coefficients were fit to their prescribed relations.

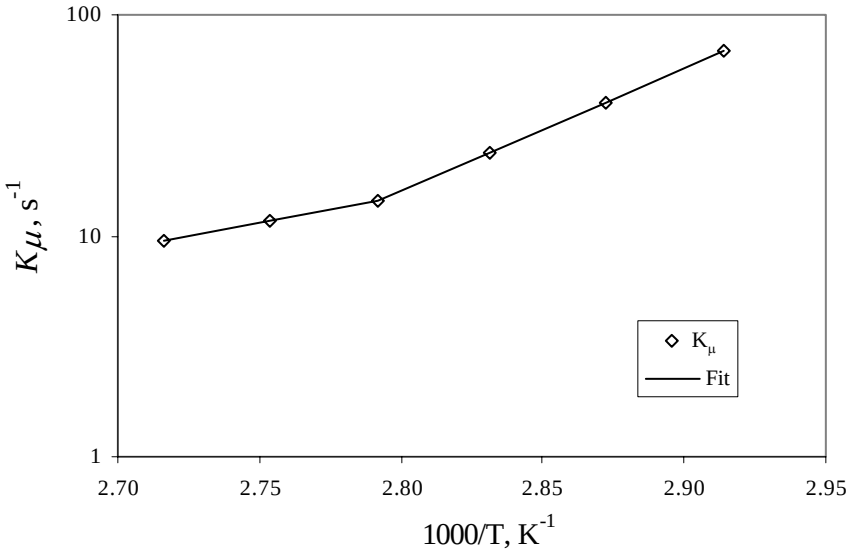

Figure 4.1.2. Arrhenius Pre-Exponential Coefficient K_μ versus Inverse Temperature

Variations from the individually determined values of the coefficients, encountered in curve fitting, caused excessive overall deviations from experimental data at many temperatures. Thus, a recursive fitting method was used. Once an overall fit for one coefficient was determined, the values for that coefficient were held fixed while values of the other coefficients were adjusted to improve the overall fit to the test data. Next, two coefficients were held fixed while others were adjusted to improve the overall fit to the data. In this manner it was possible to obtain acceptable values of all constants.

Shown in Figures 4.1.2-4.1.5 are the results of this process. It was found that the quality of the overall fit was affected by the order in which the constants were determined. The optimum sequence, determined by trial and error, is to determine K_μ first, then A and finally B. The two temperature ranges of K_μ are clearly seen in Figure 4.1.2, with a split at 80^oC (358.15 K). This temperature was chosen for the split because it allowed the best fit to experimental data. Shown in Figure 4.1.3 is the variation of the coefficient A with temperature, from which it can be seen that A follows a quadratic fit. Shown in Figure 4.1.4 is the variation of the coefficient B with temperature. Shown in Figure 4.1.5 is the variation of the degree of cure at gel (gelpoint) with temperature.

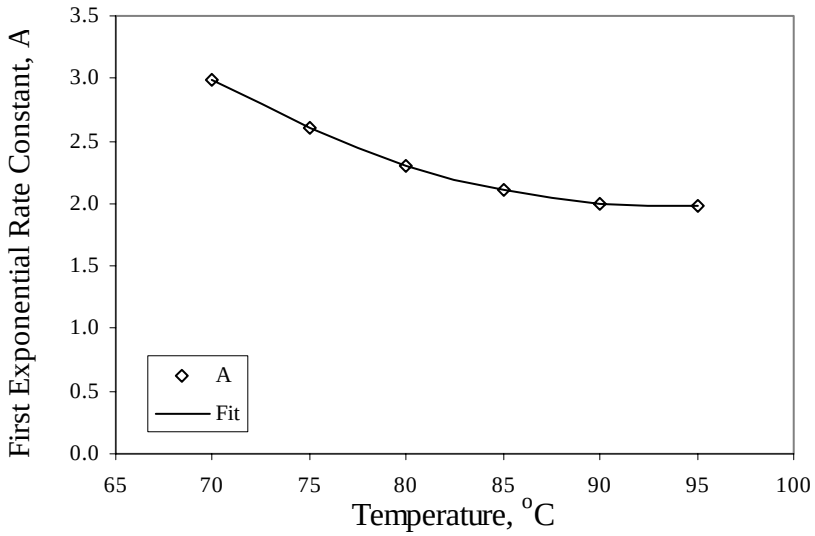

Figure 4.1.3. First Exponential Rate Constant *A* versus T

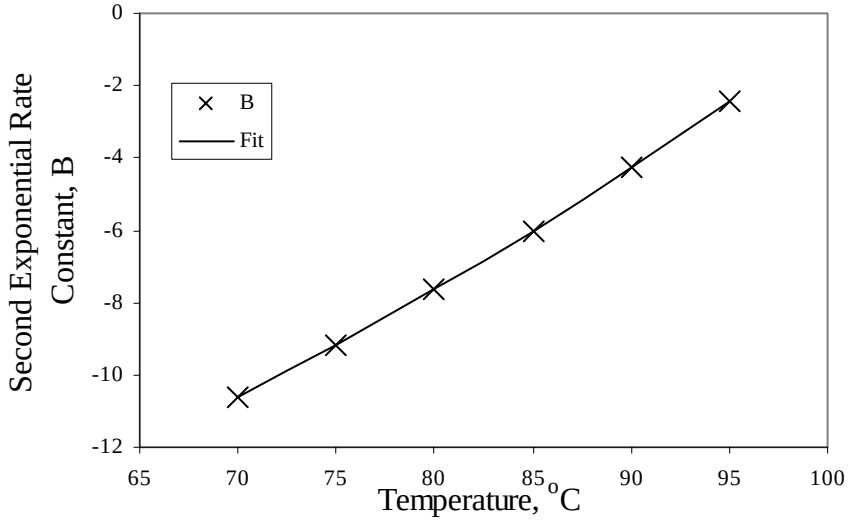

Figure 4.1.4. Second Exponential Rate Constant *B* versus T

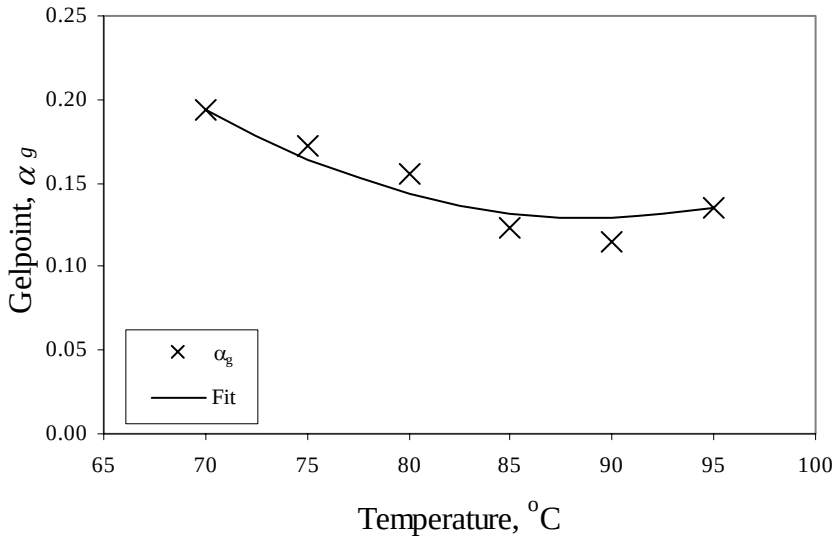

Figure 4.1.5. Degree of cure at gel, α_G, versus T

The complete set of experimental data and fits to that data determined by the recursive least squares method are given in Appendix A.

4.2 Resin Kinetics Relation

Differential scanning calorimetry (DSC) was used to determine the reactive characteristics of the resin. DSC is an experimental method of measuring the amount and the rate of heat absorbed or emitted by a substance as it is exposed to prescribed thermal conditions. It is carried out in an inert environment, so only matter within the substance is involved. Using information obtained with DSC, it was possible to determine the coefficients necessary to allow an empirical relation to represent the reactive characteristics of the Cytec™ 754 resin.

Two types of DSC tests were performed: dynamic and isothermal. In a dynamic test a sample of resin is heated from room temperature to a substantially higher temperature at a prescribed constant rate. This type of test allows for nearly complete

cure of the resin so that the amount of heat given off by a complete reaction can be measured. This amount of heat is approximately the ultimate heat of reaction. Slower heating rates give higher heats of reaction as they allow for more complete polymerization.

An isothermal scan consists of rapidly heating a sample from room temperature to some prescribed temperature which is maintained until the sample ceases to produce or absorb heat. At this point, the isothermal reaction is judged complete, although an additional exotherm of a thermosetting sample can usually be observed if a subsequent dynamic scan is carried out on the specimen; this subsequent dynamic scan is called a residual scan. The isothermal test is an effective simulation of the temperature dwells commonly used in cure cycles for the fabrication of composites. By carrying out both isothermal and dynamic tests at many temperatures and heating rates, it is possible to completely characterize the kinetics of the resin under consideration.

Tests were carried out on a TA Instruments Differential Scanning Calorimeter. Samples were prepared in hermetic aluminum pans with each sample of neat resin having a mass of 10-20 mg.

To obtain the ultimate heat of reaction of Cytec™ 754 resin, a series of dynamic tests were carried out at heating rates of 5, 2.5, and 1^{o}C/min. Three tests were carried out at 2.5^{o}C/min, three at 5^{o}C/min and one at 1^{o}C/min. A sample result, from a test with heating rate of 2.5^{o}C/min, is shown in Figure 4.2.1. The heat of reaction is determined as the area enclosed by the large peak and the curved baseline. The large peak is a measure of the heat given off by the sample as it reacts. The baseline is an estimate of the heat flow of a non reacting sample. Another line shown in Figures 4.2.1 and 4.2.2 is an

inclined straight line commingled with the peak. This is the maximum rate of change of heat flow as determined automatically by the TA DSC software. The average heat of reaction from the three 2.5°C/min tests was taken to be the ultimate heat of reaction.

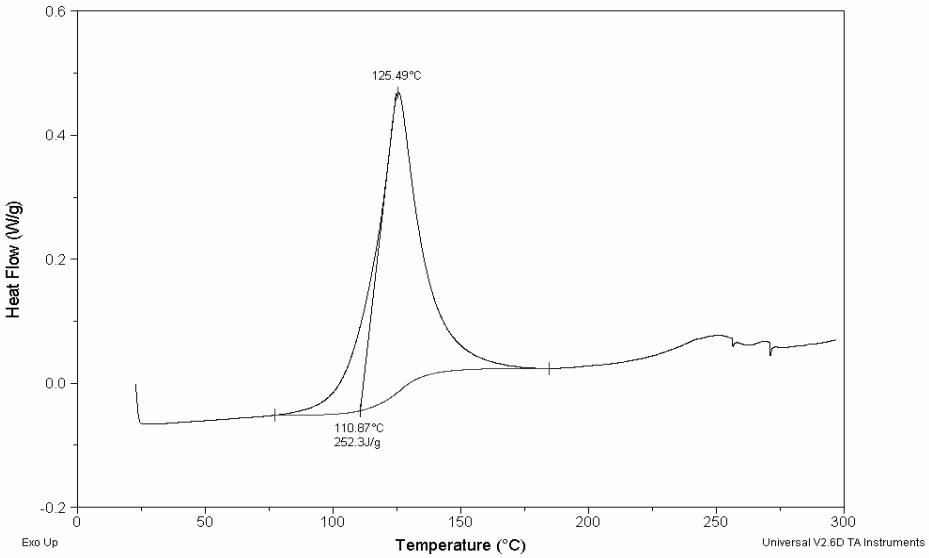

Figure 4.2.1. Heat Flow versus Temperature for Dynamic DSC at 2.5°C/min

Following the determination of the ultimate heat of reaction, isothermal tests were carried out at 70-95°C in 5 degree increments and at 110-130°C in 10 degree increments. Each test was allowed to proceed until no exotherm was observed, which assured as complete a reaction as possible. The result of an isothermal test at 70°C is shown in Figure 4.2.2.

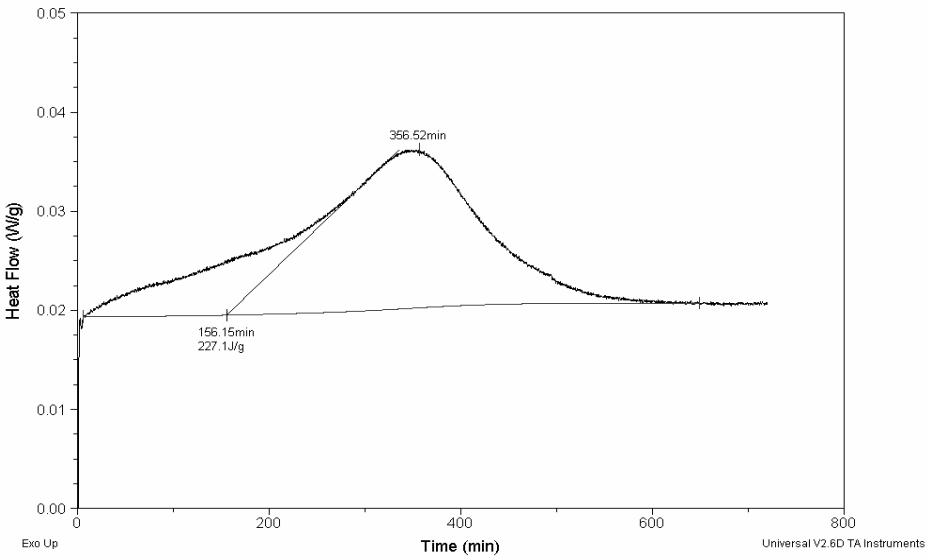

Figure 4.2.2. Heat Flow versus Time for Isothermal DSC at 70^{o}C

From each isothermal test, an isothermal heat of reaction was calculated. The heat of reaction obtained from an isothermal test may differ from that obtained from dynamic tests because the sample may not completely cure during an isothermal test. This phenomenon is exacerbated at lower temperatures. The isothermal degree of cure for a given test is calculated as the ratio of the isothermal heat of reaction determined from the present test to the ultimate heat of reaction. Additionally, the rates of cure were determined for the duration of each test from the heat flow data and used to determine the coefficients which fit the empirical kinetics relation to the experimental DSC data [32].

The primary function of the empirical kinetics equation is to explicitly and independently provide the degree of cure at any time. Both isothermal and non-isothermal autocatalytic and combination Arrhenius type relations were evaluated; however, a reasonable fit to experimental data was only obtained with an isothermal implementation of an autocatalytic-1 type relation [32]. The form is as follows:

$$\frac{d\beta}{dt} = (K_1 + K_2\beta^m)(1-\beta)^n \tag{4.2.1}$$

$$\frac{d\alpha}{dt} = \frac{H_T}{H_U}\frac{d\beta}{dt} \tag{4.2.2}$$

Where:

β	=	Isothermal degree of cure
K_1, K_2	=	Rate constants
m	=	First kinetic exponent
n	=	Second kinetic exponent
H_T	=	Isothermal heat of reaction, J/g
H_U	=	Ultimate heat of reaction, J/g
α	=	Ultimate degree of cure

The first term on the right hand side of Equation 4.2.1 represents the contribution of the unreacted portion of the resin to the reaction rate. The second term represents the contribution of that portion which has reacted.

The constants K_1 and K_2 are given by the following Arrhenius relations:

$T \leq 368.15\ K$:

$$K_{1,Low} = A_1 \exp\left(-Ea_1 \diagup RT\right) \tag{4.2.3}$$

$$K_{2,Low} = A_2 \exp\left(-Ea_2 \diagup RT\right) \tag{4.2.4}$$

$T > 368.15\ K$:

$$K_{1,High} = A_3 \exp\left(-Ea_3 \diagup RT\right) \tag{4.2.5}$$

$$K_{2,High} = A_4 \exp\left(-Ea_4 / RT\right) \tag{4.2.6}$$

Where:

A_i	=	Arrhenius pre-exponential factors, min^{-1}
Ea_i	=	Arrhenius activation energies, J/mol
R	=	Universal gas constant, $J/mol \cdot K$
T	=	Temperature, K

A break point of 368.15 K was chosen based on a transition in the slopes of the Arrhenius relations exhibited by curve fits to the experimental data, which can be seen in Figure 4.2.3. It should be noted that m, n, and H_T are functions of temperature and H_U, A_3, A_4, Ea_3, and Ea_4 are functions of the time rate of change of temperature. These dependencies are given below:

$$A_3 = a_1\dot{T}^2 + a_2\dot{T} + a_3 \tag{4.2.7}$$
$$Ea_3 = e_1\dot{T}^3 + e_2\dot{T}^2 + e_3\dot{T} + e_4 \tag{4.2.8}$$
$$A_4 = a_4\dot{T}^3 + a_5\dot{T}^2 + a_6\dot{T} + a_7 \tag{4.2.9}$$
$$Ea_4 = e_5\dot{T}^3 + e_6\dot{T}^2 + e_7\dot{T} + e_8 \tag{4.2.10}$$
$$T \le 363.15\ K,\ m = 1.7167 \tag{4.2.11}$$
$$T > 363.15\ K,\ m = m_1T + m_2 \tag{4.2.12}$$
$$n = n_1T + n_2 \tag{4.2.13}$$
$$H_T = H_1T^2 + H_2T + H_3 \tag{4.2.14}$$
$$H_U = H_4\dot{T}^2 + H_5\dot{T} + H_6 \tag{4.2.15}$$

Where $\dot{T}$ is expressed in K/min. The linear and constant portions of the fit for m were joined at 363.15 K to follow the trend exhibited by the experimental data, which can

be seen in Figure 4.2.4. The coefficients A_i, Ea_i, a_i, e_i, m_i, n_i, and H_i are given in Table 4.2.1.

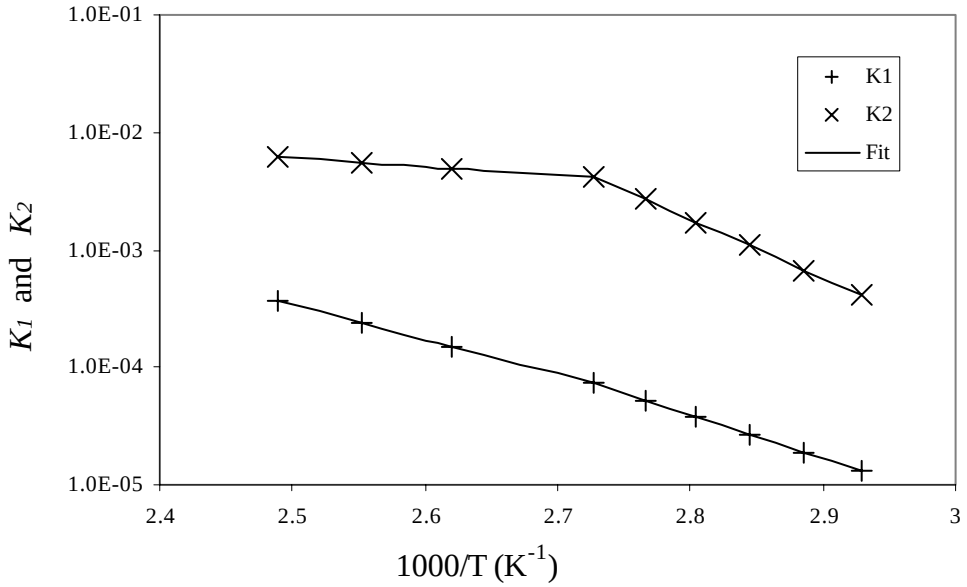

Figure 4.2.3. Variation of K_1 and K_2 with Inverse Temperature

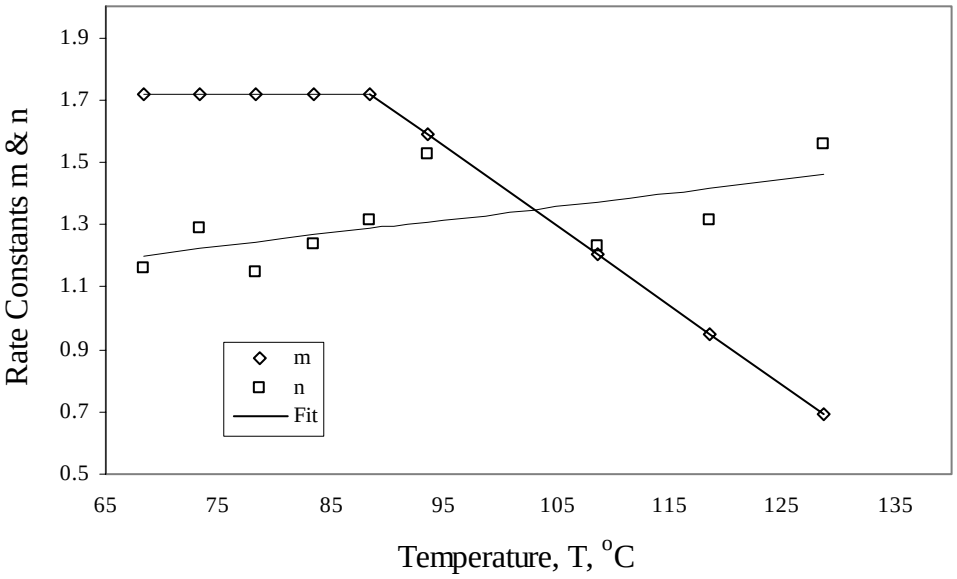

Figure 4.2.4. Variation of Rate Constants *m* and *n* with Temperature

Table 4.2.1. Values of Coefficients in the Kinetics Equation

Constant	Value	Units	Constant	Value	Units
e_1	1419.9	$J \cdot \min^3 / mol \cdot K^3$	a_1	2.6144E+08	$\min^2 / K^2$
e_2	-13139	$J \cdot \min^2 / mol \cdot K^2$	a_2	-1.9705E+08	min/ K
e_3	38797	$J \cdot \min / mol \cdot K$	a_3	8662.5	$\min^{-1}$
e_4	56681	J / mol	a_4	-7.1991E-03	$\min^3 / K^3$
e_5	-105.80	$J \cdot \min^3 / mol \cdot K^3$	a_5	6.1398E-02	$\min^2 / K^2$
e_6	487.04	$J \cdot \min^2 / mol \cdot K^2$	a_6	-0.19577	min/ K
e_7	-1788.9	$J \cdot \min / mol \cdot K$	a_7	0.36056	$\min^{-1}$
e_8	13606	J / mol			
Constant	Value	Units	Constant	Value	Units
A_1	1.4657E+06	$\min^{-1}$	h_1	0.0056568	$J / g \cdot K^2$
A_2	1.9474E+10	$\min^{-1}$	h_2	0.31232	$J / g \cdot K$
Ea_1	2.3315E+05	J / mol	h_3	197.07	J / g
Ea_2	2.7124E+06	J / mol	h_4	0.91895	$J \cdot \min^2 / g \cdot K^2$
n_1	0.0043100	K^{-1}	h_5	-19.371	$J \cdot \min / g \cdot K$
n_2	0.90695	*unitless*	h_6	333.89	J / g
m_1	-0.025479	K^{-1}			
m_2	3.9697	*unitless*	m	1.7167	*unitless*

A recursive least squares method similar to that used with the viscosity relation 4.1.1 and 4.1.2 was used here to determine the values of the coefficients given in Table 4.2.1.

As can be seen in Equations 4.2.7-4.2.10 and Equation 4.2.15, the parameters A_3, Ea_3, A_4, Ea_4, and H_U are allowed to change with the time rate of change of temperature. Plots of these variations are given in Figures 4.2.5-4.2.8.

Note that A_3 and Ea_3, shown respectively in Figures 4.2.5 and 4.2.6, which pertain to the upper temperature range of K_1, increase with heating rate, and that A_4 and Ea_4, shown respectively in Figures 4.2.7 and 4.2.8, which pertain to the upper

temperature range of K_2, decrease with heating rate. One can infer that for higher heating rates, the values of K_1 are higher than those at lower heating rates. The slopes of the curves in Figures 4.2.5 and 4.2.6 seem to diminish to zero as heating rates increase, so A_3 and Ea_3 seem to approach steady values at higher heating rates. From Figures 4.2.7 and 4.2.8 we conclude that for high heating rates and higher temperatures, K_2 takes on lower values than those for low temperatures and low heating rates.

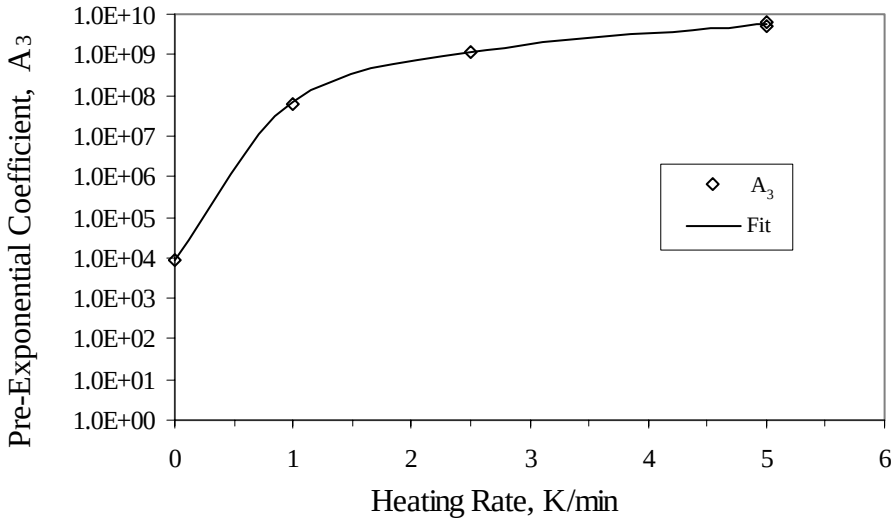

Figure 4.2.5. A_3 versus dT/dt

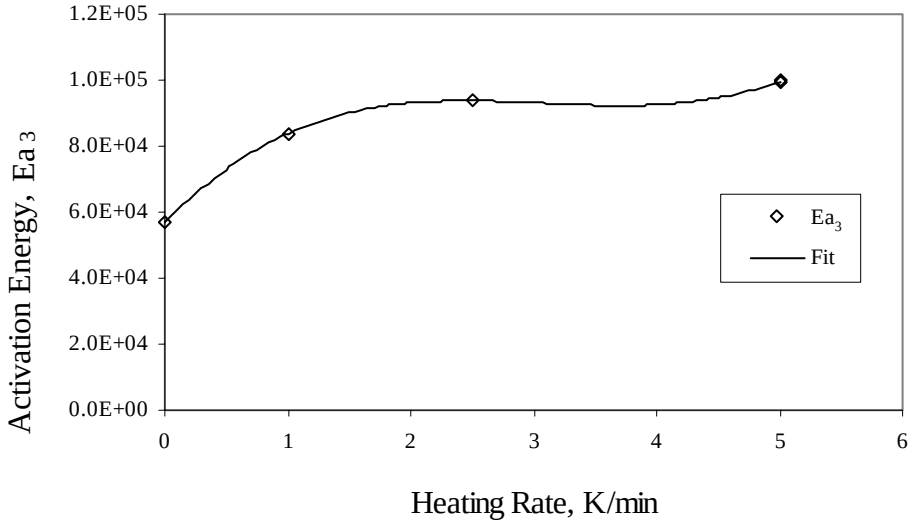

Figure 4.2.6. Ea_3 versus dT/dt

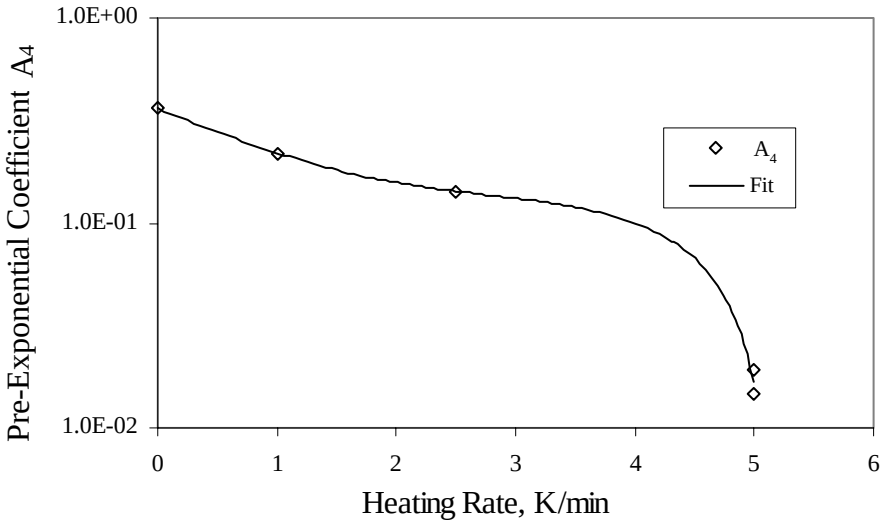

Figure 4.2.7. A_4 versus dT/dt

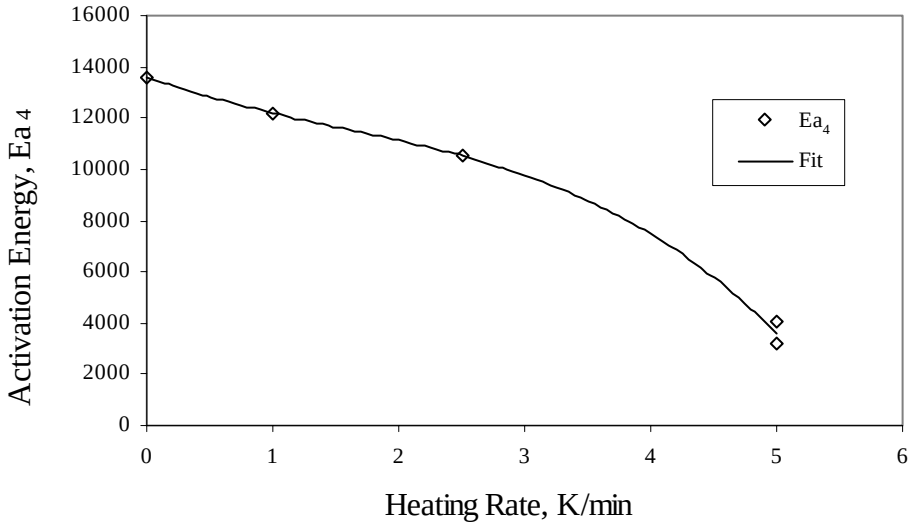

Figure 4.2.8. Ea_4 versus dT/dt

If one considers Equation 4.2.1 in an expanded form, given below as Equation 4.2.17, some additional implications of the changes in K_1 and K_2 with heating rate become clear:

$$\frac{d\beta}{dt} = K_1(1-\beta)^n + K_2\beta^m(1-\beta)^n \qquad (4.2.16)$$

An increase in K_1 implies that the contribution of the unreacted portion of the resin, represented by the first term on the right hand side of Equation 4.2.16, becomes larger with increased heating rate. The decrease in K_2 at high temperatures and increased heating rates implies that the portion of the resin which has reacted, represented by the second term on the right hand side of Equation 4.2.16, contributes less to the total reaction in those situations. Overall, this indicates a shift in the reactive characteristics of the resin at high temperatures and high heating rates.

For the problem studied herein, the implications of this trend are small. Cure cycles for large parts generally involve low heating rates because parts, ovens, and corresponding thermal masses and energy requirements are large. During a temperature dwell, the heating rate is zero. Also, product literature for the Cytec™ 754 resin states that it is intended for low temperature cures [28], so the characteristics of the resin at high temperatures are less significant to a manufacturing situation.

Shown in Figure 4.2.9 is the ultimate heat of reaction versus the heating rate. It shows that the ultimate heat of reaction decreases with heating rate. This is to be expected, as lower heating rates allow for more complete polymerization of the resin.

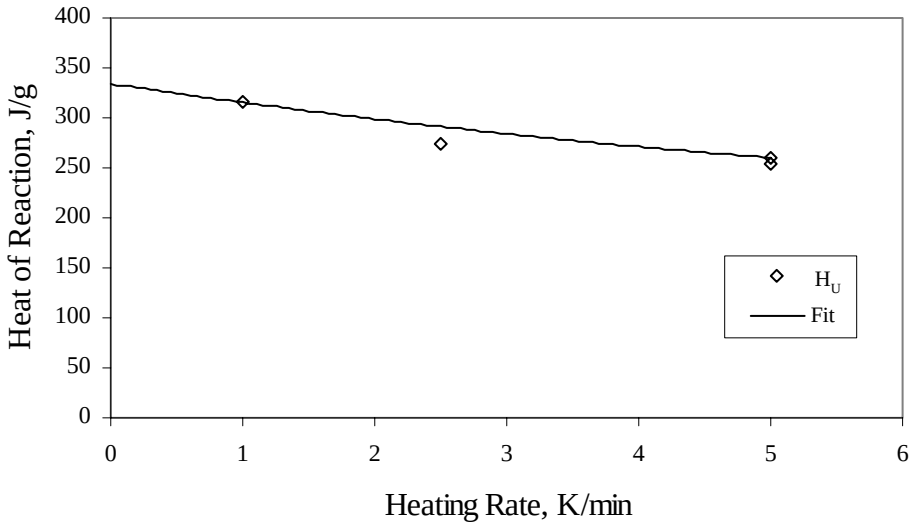

Figure 4.2.9. H_U versus dT/dt

The complete set of experimental data and the fit of the empirical kinetics relations 4.2.1 and 4.2.2 over the range of tested temperatures are included in Appendix B.

A final test was carried out to verify both the kinetic and the rheology relations. The gelpoint must be precisely predicted if the viscosity expression is to give good values, which requires that the kinetics relation be precise. Therefore, a verification of the viscosity expression is also a verification of the kinetics equation. To this end, a steady shear viscosity test was carried out with a temperature ramp, contrasting the isothermal viscosity tests. This was simulated with the two empirical expressions, and good correlation between the test data and values from these expressions was found. The comparisons are shown in Figures 4.2.10 and 4.2.11, giving viscosity versus degree of cure and temperature, respectively.

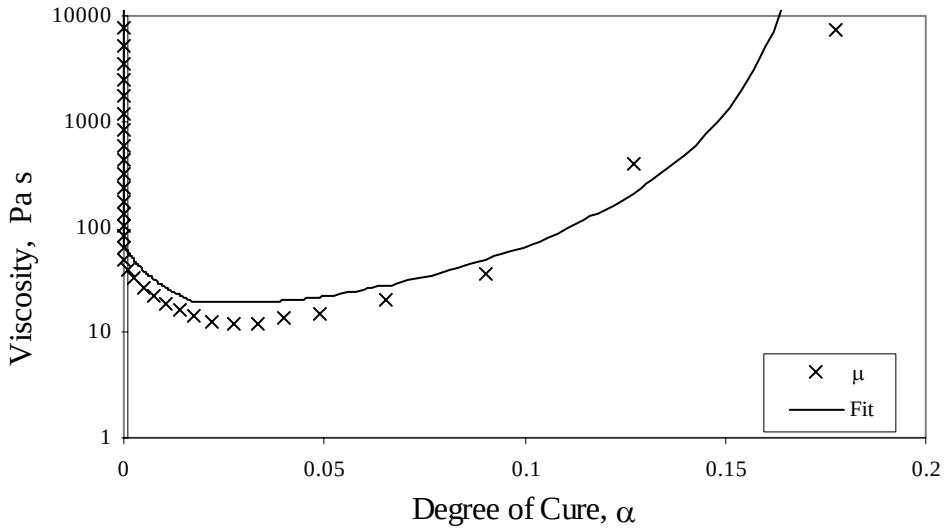

Figure 4.2.10. Viscosity versus Degree of Cure for Steady Shear Thermal Ramp Viscosity Test

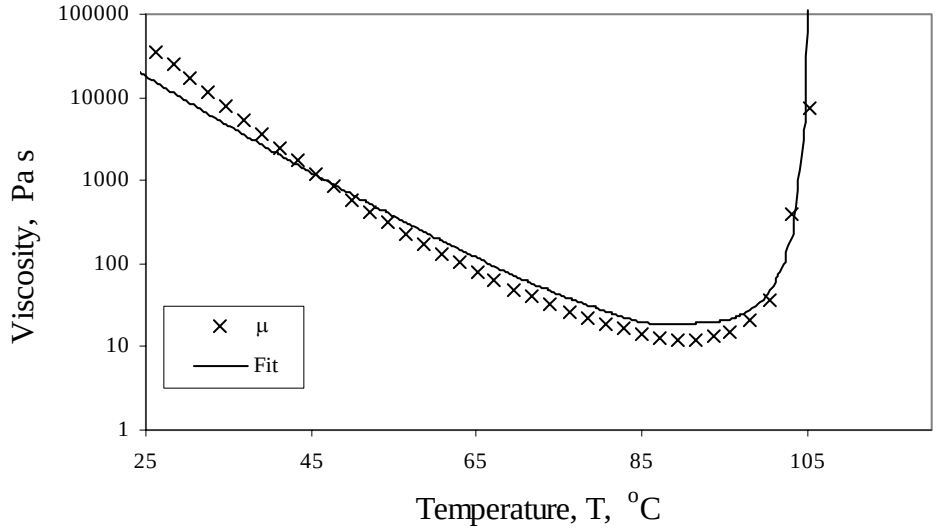

Figure 4.2.11. Viscosity versus Temperature for Steady Shear Thermal Ramp Viscosity Test

4.3 Preform Compressibility and Permeability

It was necessary to determine values of parameters in the flow model for describing the Cycom™ 754 / E-QX 3600-5 material. The non-woven glass fabric, E-

QX 3600-5, is considered here as a glass preform. A list of the parameters involved is given in Table 4.3.1. Some parameters such as the fiber radius, are tabulated in the literature or are easily measured. Other parameters such as the Carman-Kozeny flow constant, could not be found in the literature for this particular material and are not easily measured. Inferences to their proper values, or ranges of reasonable values, can be found in the previous work of Gutowski *et al*. [11, 12], Kingery [20] and Wineman [19].

Table 4.3.1. Material Parameters, Names and Units

Symbol	Name	Units
V_o	Initial Volume Fraction	None
V_a	Available Volume Fraction	None
$V_a^{'}$	Flow Limiting Volume Fractio	None
A_s	Spring Constant	Pressure
k_{zz}	Carman-Kozeny Constant	None
r_f	Fiber Radius	Length

Experimental data regarding the compression of glass fabrics at pressures on the order of one atmosphere were gathered from the literature [10, 21, 24-26, 33]. Unfortunately, no studies were found which tested the variation of the permeability of glass fabric under compression at less than one atmosphere pressure. Furthermore, only one study [24] was found which tested the permeability variation of glass fabric with respect to compaction pressure in any pressure range. It was employed as a basis from which to estimate values in the equation for permeability. A summary of the fabrics found in the literature is given in Table 4.3.2. The values of parameters A_s, V_o, and V_f determined from the literature data are given in Table 4.3.3. k_{zz} and $V_a^{'}$ were determined

by a fit to permeability data presented in Figure 4.3.2; the fiber radius was taken from the literature to be 49.824 μm.

Table 4.3.2. Fabric Types and Information Gathered from the Literature

Fabric Type	Description	Layers	Basis Weight (g/m^2)	Reference
DeBold L900-E11	Unidirectional	10	884	10
NCS 81053	Non-Crimped Bidirectional	3	618	21
NCS 82675	Non-Crimped Bidirectional	6	315	21
WR 24	Woven Bidirectional	3	814	21
BTI C24	Non-Crimped Bidirectional	3	814	21
EB 315 E02 F120	Unbalanced Bidirectional	3	315	21
EBX 936	Non-Crimped Bidirectional	3	1000	21
BM 196	Double Twill Woven Bidirectional	---	1048	21
BM 154	Plain Woven Bidirectional	---	312	21
JBM 82001	Non-Crimped Bidirectional	---	306	21
Cotech ETLX583	Triaxial, 0,+/-45, 50% of fiber on warp	2	584	33
EQX1168	Quadraxial, 0/90/+45/-45	2	1230	33
UTE250	Unidirectional	8	234	33
7544	Bidirectional Woven	---	618	24

Table 4.3.3. Values of Parameters from Literature

Fabric Type	A_s (Pa)	V_o	V_a
DeBold L900-E11	2467	0.241	0.892
NCS 81053	2354	0.064	1.000
NCS 82675	3944	0.066	1.000
WR 24	3758	0.075	0.989
BTI C24	2283	0.091	0.910
EB 315 E02 F120	9616	0.010	1.000
EBX 936	1206	0.131	1.000
BM 196	230	0.185	0.663
BM 154	149	0.201	0.623
JBM 82001	780	0.136	0.796
Cotech ETLX583	4255	0.307	0.839
EQX1168	2866	0.360	0.886
UTE250	3371	0.383	1.000
7544	85161	0.413	1.000

Test data for the fabrics listed in Tables 4.3.2 and 4.3.3 were given as curve fits, of the form of Equation 1.2.5. All tests were conducted on dry fiber cloths, and no consistent relaxation, springback, or wet fabric tests were found.

Gutowski's Equation 3.1.10 was fit to these data by a least squares technique similar to that used for the kinetics and the viscosity expressions. The recursive method described in Section 4.1 was not required as good fits were readily obtained. A sample fit is given in Figure 4.3.1. Fits for all fabrics can be found in Appendix C.

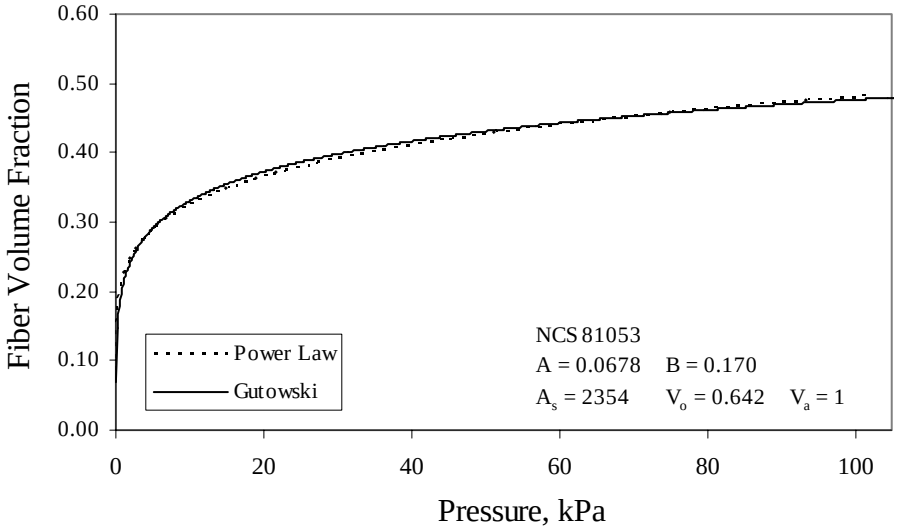

Figure 4.3.1. Volume Fraction versus Pressure for Fabric NCS 81053

Figure 4.3.1, typical of all of the data fits, shows that the Gutowski relation can very closely approximate the power law relation with which the experimental data was represented. Hammami and Gebart [10] did not use a power law relation to represent their data for DeBold L900-E11 fabric, choosing instead to use a statistically based

Kriging equation. Gutowski's equation was able to fit this data as well. The form of the Kriging equation is given in Appendix C.

The experimental data for transverse permeability of a glass fabric as a function of the volume fraction was used to evaluate parameters both in the original and in the modified Carman-Kozeny expressions for permeability. These are given as Equations 1.2.1 and 1.2.2 respectively. Again, the least squares method was used to find a best fit of the expressions to the data and the recursive method was not required. The results are shown in Figure 4.3.2.

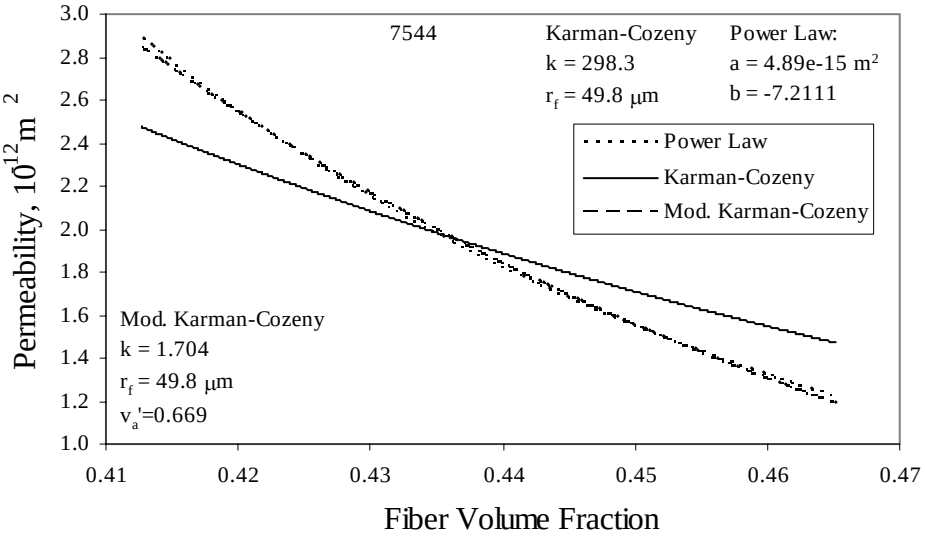

Figure 4.3.2. Fits of Original and Modified Carman-Kozeny Relations to Data for 7544 Glass Fabric

Figure 4.3.2 shows that the original Carman-Kozeny Equation 1.2.1 could not be made to fit the power law representation of experimental data for 7544 glass fabric in Figure 4.3.2; however, a good fit could be determined for the modified relation 1.2.2. The radius of E-glass fiber was taken to be $49.824\ \mu m$. Because only one test of one

type of fabric could be found, this fit does not conclusively support the modified Carman-Kozeny Equation. However, if one considers the support lent to it by Gutowski *et al*. [11, 12], the fit to the literature data does imply viability of the modified Carman-Kozeny expression.

E-QX 3600-5 is a nonwoven, quasi-isotropic fabric with a basis weight of approximately 1230 g/m^2. Fabrics were selected from those in the literature based on their weave, fiber structure and basis weight. The average values for A_s, V_o and V_a appearing in Equation 3.1.10 for these fabrics are shown in Figures 4.3.3-4.3.5. Standard deviations of the averaged quantities in Figures 4.3.3-4.3.5 are represented as bars surrounding the average value.

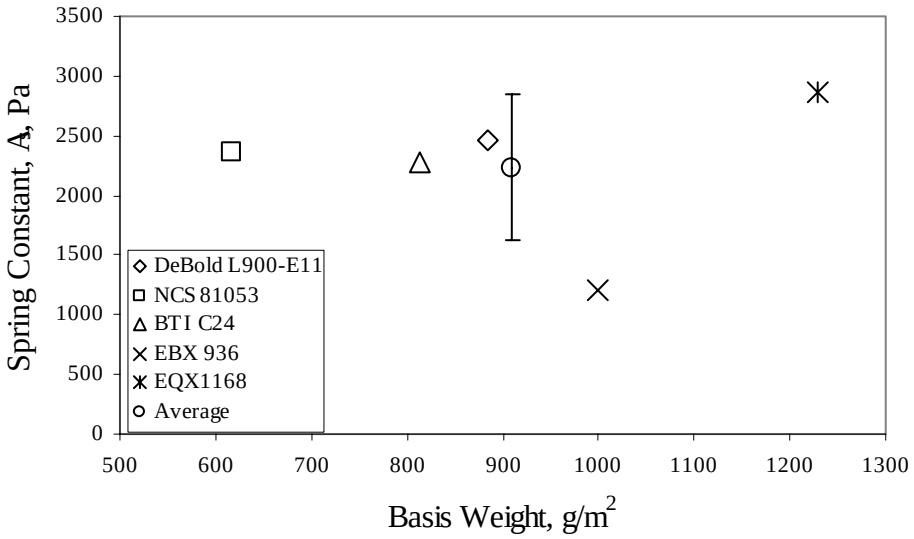

Figure 4.3.3. Spring Constant versus Basis Weight for Similar Fabric Types

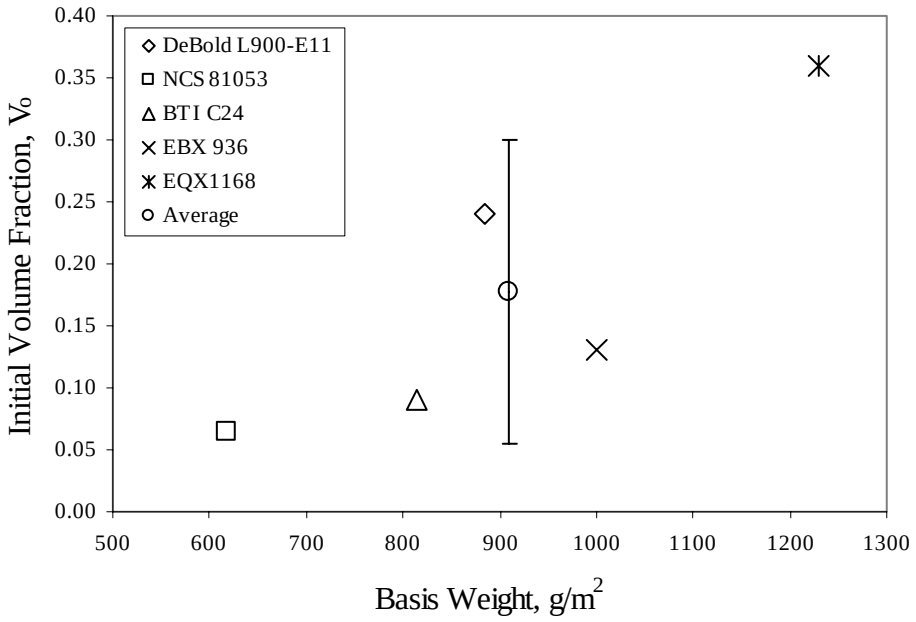

Figure 4.3.4. Initial Volume Fraction versus Basis Weight for Similar Fabric Types

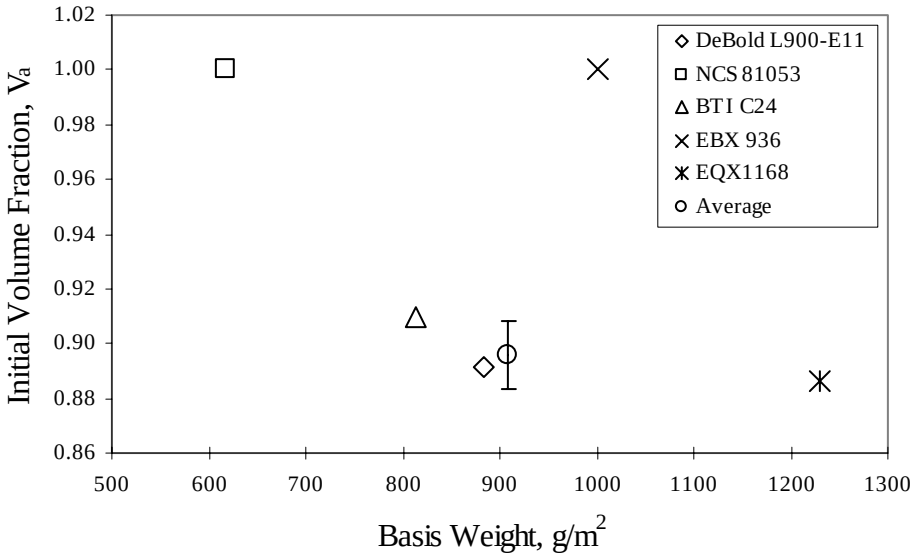

Figure 4.3.5. Available Volume Fraction versus Basis Weight for Similar Fabric Types

In Figure 4.3.5, the values for NCS81053 and EBX 936 are neglected in the computations of the average and the standard deviation because the value which gave

best fits to the Gutowski relation for these materials, unity, is not realistic as an available volume fraction. The values of these averages are given in Table 4.3.4. Unless stated otherwise, these values were used for runs simulating the E-QX 3600-5 material.

Table 4.3.4. Values of Model Parameters for E-QX 3600-5 Glass

A_s (Pa)	V_o	V_a	$K_{modified}$	V_a'
2865	0.360	0.886	1.704	0.669

4.4 Initial Thicknesses of Different Regions

The determination of the initial thicknesses of the regions depicted in Figure 3.3.1 was necessary. To this end, a small piece of Cycom™ 754 prepreg was cured at a low temperature and micrographed. The low temperature cure attempted to avoid any resin motion by keeping the viscosity high. One of the many micrographs that were obtained is shown in Figure 4.4.1. It should be noted that Figure 4.4.1 is a photo of a darkfield micrograph, as opposed to the standard brightfield micrograph. This is due to the fact that it was very difficult to discern any boundary between the resin contained in the prepreg and the potting resin used to create the micrograph in a photo of a brightfield micrograph, because the two resins were very nearly of the same color. In a darkfield micrograph, the luminosity of the two resins is clearly different and the boundary is readily seen. From this collection of micrographs, of which an example is shown in Figure 4.4.1, the initial thickness of the neat resin region was determined to be 37.5% of the initial prepreg thickness. The mixed region and dry regions were determined to account for 30% and 28.5% of the initial thickness respectively. A value of 4% of the

initial prepreg thickness was assumed for the thickness of the upper mixed region, as it is plainly difficult to measure. The initial thickness of one ply of prepreg was measured as 1.67 mm. The initial prepreg areal mass was found to be 1.978 kg/m^2, which includes both the fiber and the resin.

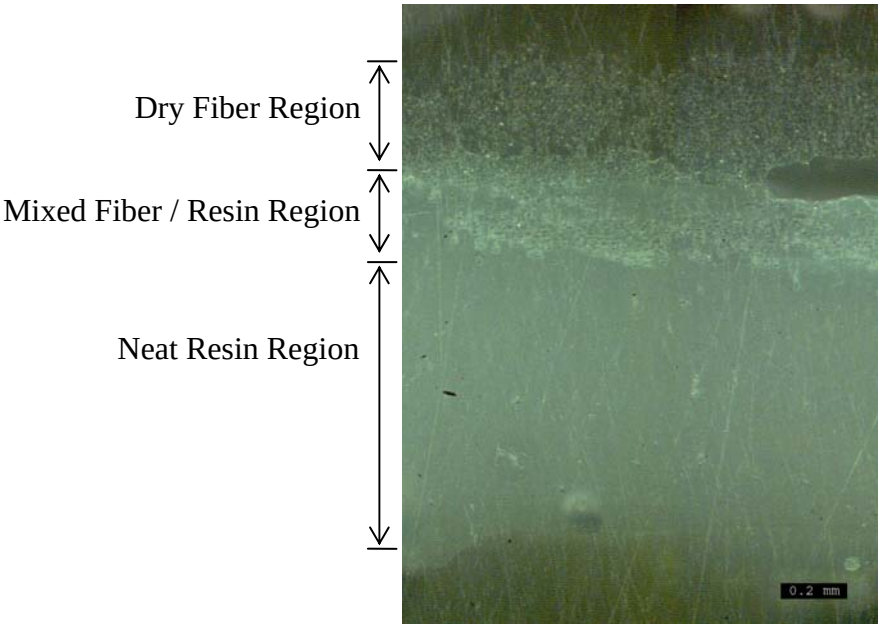

Figure 4.4.1. Sample Micrograph of Unconsolidated Prepreg

Chapter 5

Model Evaluation and Verification

5.1 Numerical Implementation

The governing Equation 3.1.20 must be solved with the appropriate initial and boundary conditions. It is desirable to employ a method that is precise and well tested. Previous researchers have used a finite element / control volume technique for multi-dimensional problems with good results [1, 2, 24]. Others [3] have used finite difference techniques for multi-dimensional problems with good results. In particular, Gutowski *et al*. [17] have obtained an accurate solution of a one-dimensional problem very similar to the one studied here with the explicit finite difference method. The solution presented here also uses the explicit finite difference method.

The spatial derivatives in Equation 3.1.20 are evaluated by the central difference method, and the time derivative is evaluated by the forward difference method. The expressions for the spatial and time derivatives are as follows:

$$\frac{\partial V_f}{\partial t} = \frac{V_f\Big|_z^{t+\Delta t} - V_f\Big|_z^{t}}{\Delta t} \tag{5.1.1}$$

$$\frac{\partial V_f}{\partial z} = \frac{V_f\ |_{z+\Delta z}^{t} - V_f\ |_{z-\Delta z}^{t}}{2\Delta z} \tag{5.1.2}$$

$$\frac{\partial^2 V_f}{\partial z^2} = \frac{V_f\ |_{z+\Delta z}^{t} - 2V_f\ |_{z}^{t} + V_f\ |_{z-\Delta z}^{t}}{\Delta z^2} \tag{5.1.3}$$

where Δz is the current spatial step and Δt is the current time step. Substitution of these relations in the governing Equation 3.1.20 gives the following discretized governing relation:

$$\frac{V_f\Big|_z^{t+\Delta t} - V_f\Big|_z^t}{\Delta t} = A(V_f)\Big|_z^t \left(\frac{V_f\,|_{z+\Delta z}^t - 2V_f\,|_z^t + V_f\,|_{z-\Delta z}^t}{\Delta z^2} \right) + B(V_f)\Big|_z^t \left(\frac{V_f\,|_{z+\Delta z}^t - V_f\,|_{z-\Delta z}^t}{2\Delta z} \right)^2 \quad (5.1.4)$$

An advantage of explicit evaluation is its simplicity. A disadvantage is its lack of unconditional stability and the corresponding high computational cost. In order for the explicit evaluation to remain precise, both Δt and Δz must be sufficiently small. Once a satisfactory Δz was determined through a convergence study (to be detailed in Section 5.1.1), the following stability criterion was employed to determine Δt:

$$\max\left\{ \frac{A(V_f)\Big|_z^t \Delta t}{\Delta z^2} \right\} < \frac{1}{2} \quad (5.1.5)$$

where $A(V_f)\Big|_z^t$ given by Equation 3.1.21 is evaluated at every node and at each time. At every instant in time, Equation 5.1.5 is used to find the smallest Δt required by any node. This procedure results in an adaptive time step which can greatly reduce computational time without sacrificing precision in calculations as compared to the use of a constant but very small time step. However, the kinetics relation requires a time step less than one

second to maintain its convergence, though this is only important at the end of the cure cycle where Δt allowed by Equation 5.1.5 becomes large due to the high viscosity of the gelled resin. Shown in Figure 5.1.1 is a flow diagram of the computer code.

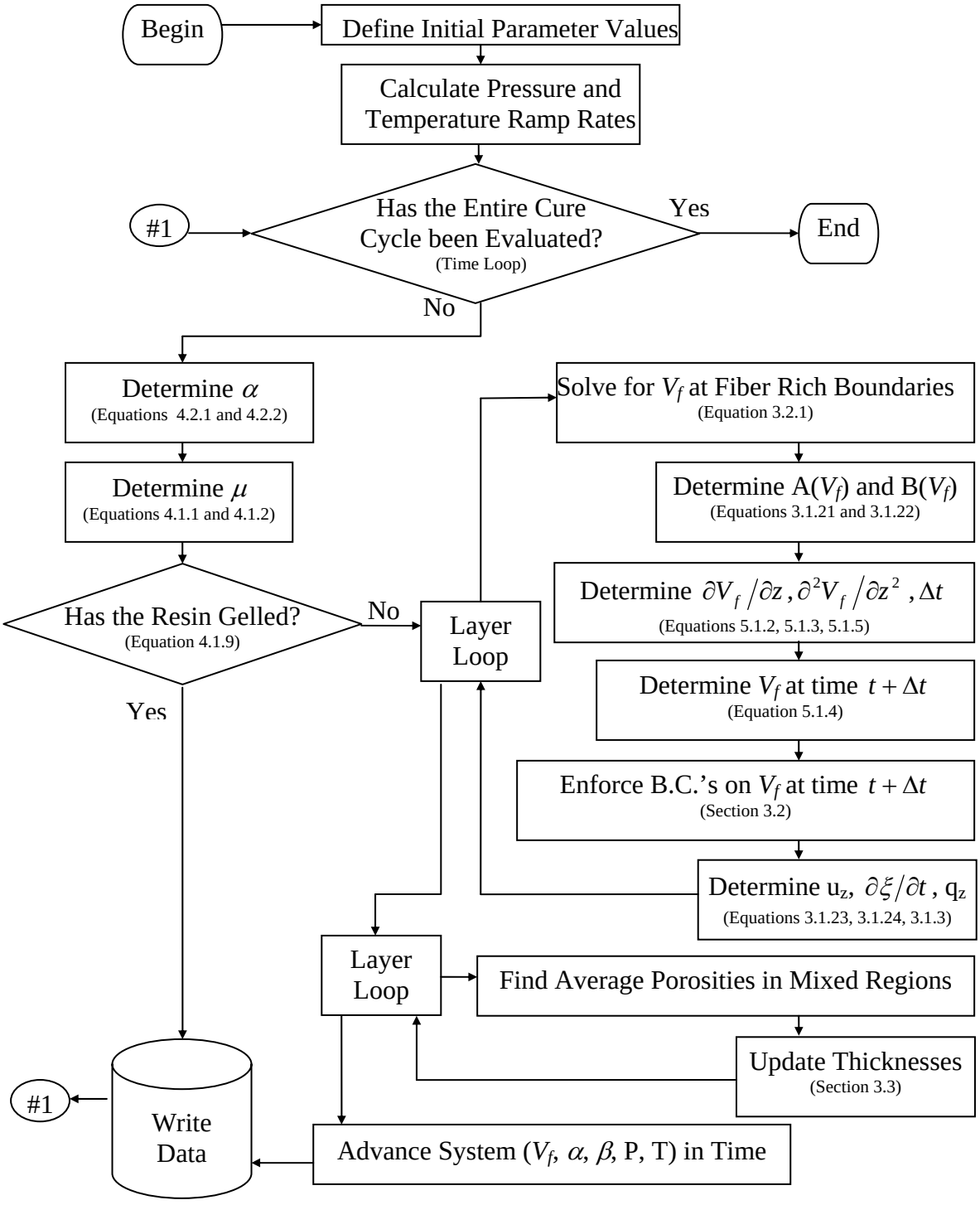

Figure 5.1.1. Flow Diagram of Computer Code

5.1.1 Convergence

Convergence of the numerical solution was determined by increasing the spatial density of the uniform finite difference grid until no significant change in the solution was observed. Using a solution computed for comparison to literature results, a maximum difference at any node of 0.19% was observed between the solution computed with 104 and 208 nodes, so a 104 node grid was judged sufficient. This grid density was used for all subsequent calculations. Higher grid densities were tested; however, computational cost became prohibitive and significant increases in accuracy were not obtained. The results for grids of 208 nodes and less are shown in Figure 5.1.1.1. The data shown in Figure 5.1.1.1 is an approximation of literature results in the following section, a single layer problem consisting of a single mixed region, at $t^* = 0.01$.

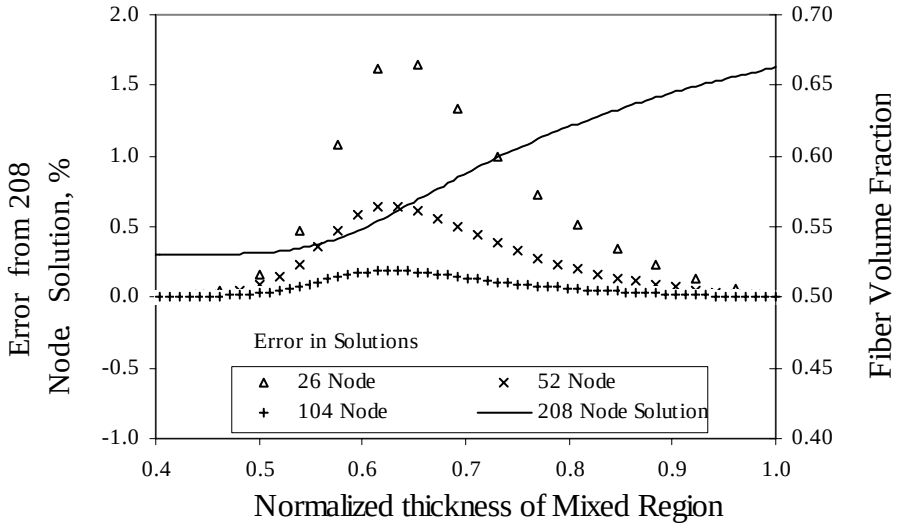

Figure 5.1.1.1. Convergence of the Numerical Solution

5.1.2 Verification

Two methods were used to verify that the numerical solution to Equation 3.1.20 was correct. The first verification was a comparison to data in the literature. The numerical solution of Equation 3.1.16 has been published by Gutowski *et al*. [17] for a similar problem with similar boundary conditions. A second verification of the method of solution was performed with the fictitious body force method [34].

A solution to a problem similar to that of Figure 3.3.1 was published by Gutowski *et al*. Shown in Figure 5.1.2.1, the problem includes a mixed region, a bleeder, and a tool plate. The governing equation for Gutowski's problem, Equation 3.1.17, is solved with the boundary and initial conditions given by Equations 3.2.1, 3.2.5, and 3.2.6. Resin flow is tracked using the expressions 3.1.23 and 3.1.24, and only a single layer is accounted for. Gutowski's solution was carried out in terms of the following non-dimensional variables:

$$z^* = \frac{z}{h_o} \tag{5.1.2.1}$$

$$\sigma^* = \frac{\sigma}{A_s} \tag{5.1.2.2}$$

$$t^* = \int_0^t \frac{dt}{\tau(t)} \tag{5.1.2.3}$$

$$\tau(t) = \frac{4k_{zz}\mu(t)}{A_s}\left(\frac{h_o}{r_f}\right)^2 \tag{5.1.2.4}$$

$$p^* = \frac{p}{A_s} \tag{5.1.2.5}$$

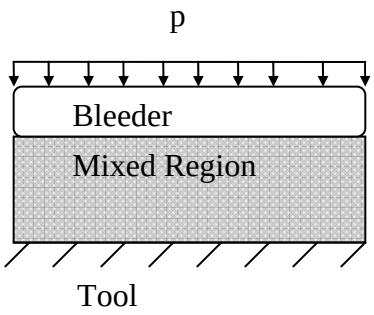

Figure 5.1.2.1. Schematic of Gutowski *et al.*'s Problem

The applied pressure was ramped at a constant rate of $\Delta p^* / \Delta t^* = 10^3$ (where Δp^* is the discrete change in non-dimensional applied pressure), V_o was 0.53, and V_a was 0.9. A survey of Gutowski's other works [14-18] gave $A_s = 0.023$ and $k_{zz} = 0.8$. Values for initial thickness (h_o) of the mixed region and viscosity were not found in the literature. A value of unity was assumed for the initial thickness, and $\mu = 0.019\ Pa\ s$ was found to approximate the published results. Although Equations 5.1.2.3 and 5.1.2.4 allow for a time varying viscosity, it was stated by Gutowski *et al*. [14] that a constant viscosity was employed.

While Gutowski's solution does not involve all physical situations that are encountered in the present problem, it provides a reference for comparison. The results of this verification follow. The resin pressure in Figure 5.1.2.2 is seen to drop to zero near the end of the test because the fibers reach their peak consolidation and have begun to carry most of the applied load, as can be seen in Figure 5.1.2.4. This implies that the term $\bar{p}_r P_r$ in Equation 3.1.5 has begun to approach zero.

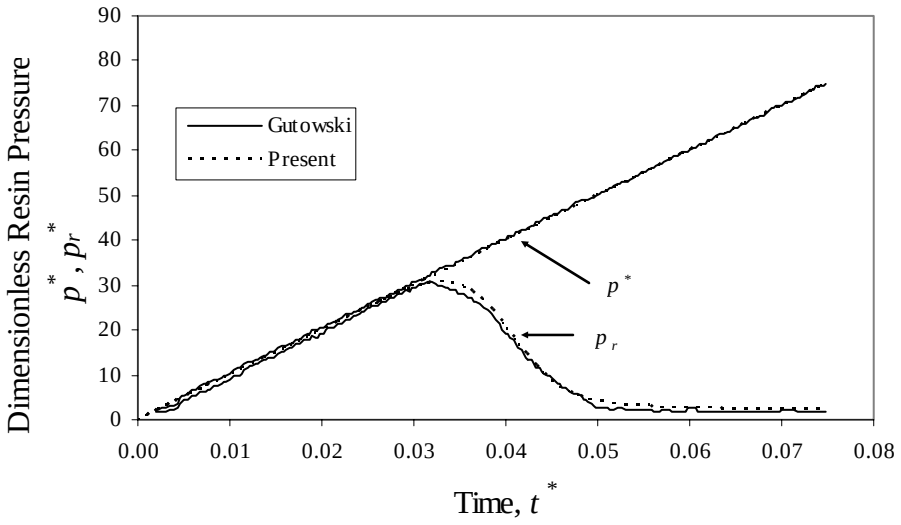

Figure 5.1.2.2. p^* and p_r^* at the Tool Surface for $\Delta p^* / \Delta t^* = 10^3$

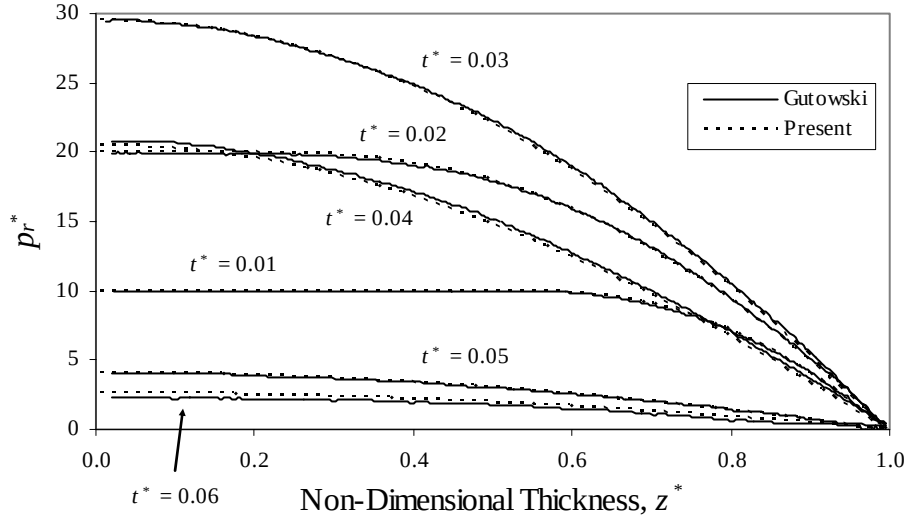

Figure 5.1.2.3. p_r^* Through the Thickness of the Composite for $\Delta p^* / \Delta t^* = 10^3$

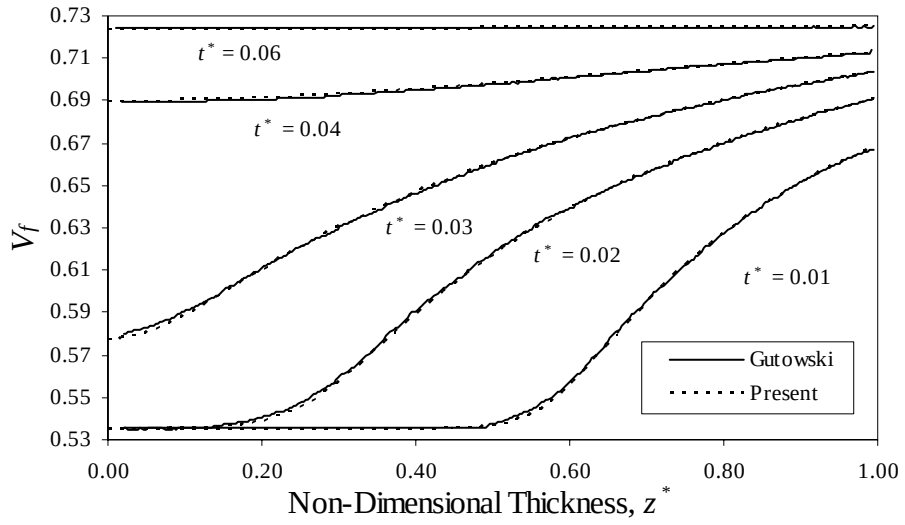

Figure 5.1.2.4. Variation of V_f Through the Thickness of the Composite for $\Delta p^* / \Delta t^* = 10^3$

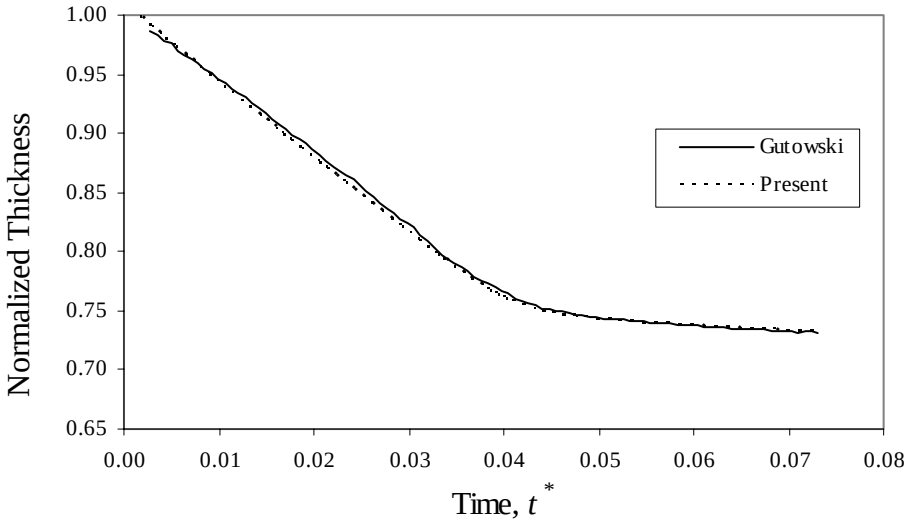

Figure 5.1.2.5. Normalized Composite Thickness as a Function of t^* for $\Delta p^* / \Delta t^* = 10^3$

A small amount of error can be attributed to the method with which the numerical values of the literature data were obtained. A program was developed which extracted numerical values from digital images of the appropriate graphs. Limitations on

resolution and definition in the original images in turn placed limits on the precision with which the literature data could be extracted.

Considering that error was introduced in the acquisition of the literature results, and that some error may have resulted from inferring and assuming values of the related constants, Figures 5.1.2.2-5.1.2.5 show good agreement with published results.

The fictitious body force method [34] was used to verify that the governing equation was being solved correctly. The method is implemented by assuming an analytical function for V_f, which satisfies all requirements for differentiability imposed by the governing equation. Because this assumed function in all likelihood will not solve the governing equation, it is necessary to add a fictitious body force, Q, as shown in Equation 5.1.2.6:

$$\frac{\partial V_f}{\partial t} = A(V_f)\frac{\partial^2 V_f}{\partial z^2} + B(V_f)\left(\frac{\partial V_f}{\partial z}\right)^2 + Q \qquad (5.1.2.6)$$

The assumed function for V_f is substituted in Equation 5.1.2.6, and Q is analytically determined. This modified governing equation is then solved numerically by the present code. A correct numerical solution will agree with the assumed analytical solution. It is necessary that the boundary and initial conditions correspond to the assumed analytical solution. Two assumed solutions were used:

$$V_f(z^*, t^*) = \left(t^*\right)^2 \left(z^*\right)^3 + 0.53 \qquad (5.1.2.7)$$

$$V_f(z^*, t^*) = \left(t^*\right)^6 \sin(\pi z^*) + 0.53\,. \qquad (5.1.2.8)$$

The results of these verifications are given in Figures 5.1.2.6 and 5.1.2.7. The low percent error of the numerical solution is taken as verification of the numerical method and the code.

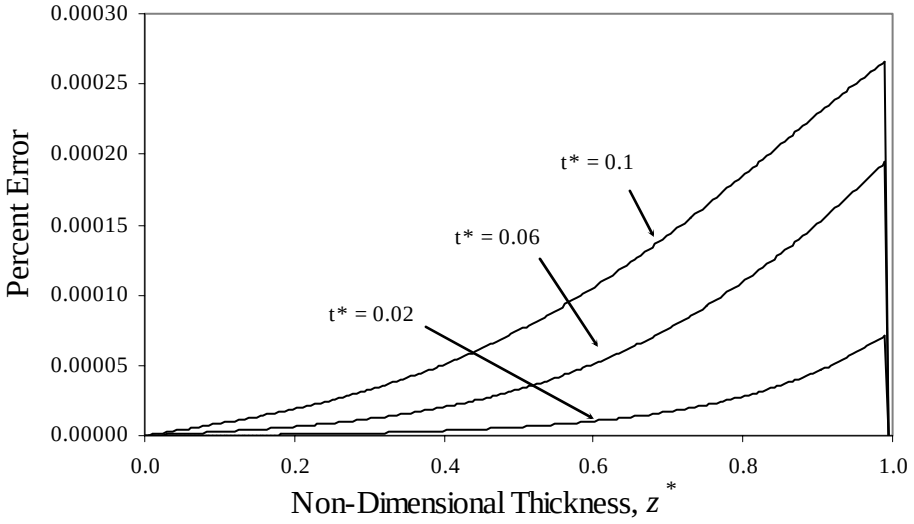

Figure 5.1.2.6. Percent Error versus z^* for Assumed Solution 5.1.2.6

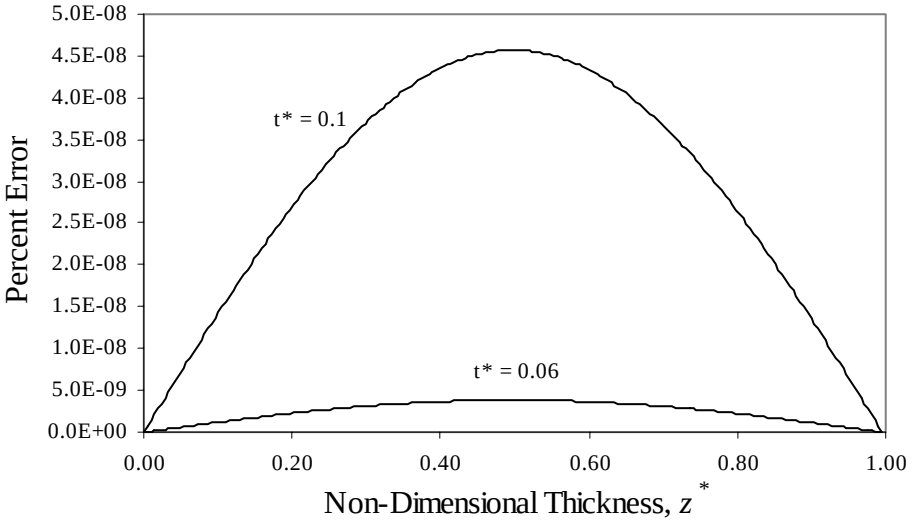

Figure 5.1.2.7. Percent Error versus z^* for Assumed Solution 5.1.2.7

5.2 Comparison to Experimental Results

Using the values of constants given in Table 4.3.4 as a starting point, a series of computational parametric studies were undertaken to determine values of the parameters yielding results which matched the experimental data given in Chapter 2. Each run was a numerical simulation of those experiments, simulating an 8 layer, 152.4 mm square plate as described in Chapter 2 and depicted in Figures 3.3.2 and 3.3.3, surrounded on the top and bottom by a bleeder and tool respectively, as shown in Figure 3.3.1. Each study aimed to replicate the results of the center point of the experimental study, Test 5 as given in Table 2.1. Each numerical simulation in the series of computational studies used the cure cycle given in Figure 2.3. Resin viscosity, required by Equation 3.1.21, was evaluated with Equations 4.1.1 and 4.1.2, and the parameter values given in Table 4.1.1 and Equations 4.1.3-4.1.6. Resin kinetics was evaluated using Equations 4.2.1 and 4.2.2, and the values given in Equations 4.2.7-4.2.15 and Table 4.2.1. Layer and region initial thicknesses were taken as described in Section 4.3, and each layer was identical except for the top-most and bottom-most layers, where the 4% initial thickness of the upper mixed region does not exist (in the top-most layer) or resin is not lost to create a second mixed region (in the bottom-most layer). Values of $A(V_f)$ and $B(V_f)$ were evaluated at the present time in the explicit numerical solution, as shown in Figure 5.1.1. Each computational study was a three dimensional Box-Behnkin design [35], the structure of which is shown in Figure 5.2.1.

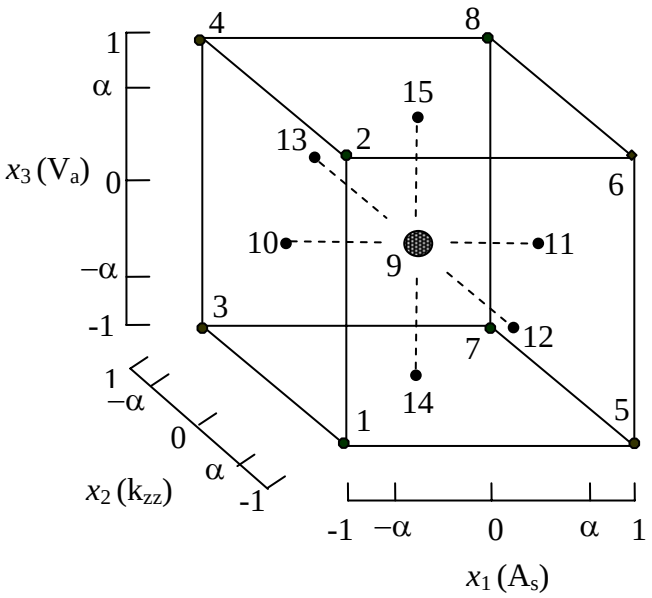

Figure 5.2.1. Structure of Box-Behnkin Experimental Design

The Box-Behnkin design aims to test the response of a system to variation of a number of parameters. The parameters chosen for variation were the spring constant (A_s), the Carman-Kozeny constant ($k_{\mathrm{mod}\,ified}$), and the flow limiting volume fraction ($V_a^{'}$). They were selected because very little definite information about their proper values was available in comparison to that for the initial and available volume fractions. Other parameters, such as the fiber radius and the viscosity, are not open to arbitrary variation. r_f was taken to be 49.824 μm, V_a was taken to be 0.886, and V_o was taken as 0.36.

Tests were conducted at each numbered point in Figure 5.2.1. These are the center point (#9), the eight corners of the unit cube (#'s 1-8), and the six star points (#'s 11-15). The range of the coordinates x_1, x_2, and x_3 from -1 to 1 implies that the variation is uniform in each dimension x_i. The star points, which are tests conducted at

$x_i = \pm\alpha$ add additional information to the study. The dimensions x_i are related to A_s, $k_{\mathrm{mod}ified}$, and $V_a^{'}$ by linear transformations as follows:

$$x_1 = \frac{A_s - [c.p.]_{A_s}}{[\mathrm{var}]_{A_s}} \tag{5.2.1}$$

$$x_2 = \frac{k_{zz} - [c.p.]_{k_{zz}}}{[\mathrm{var}]_{k_{zz}}} \tag{5.2.2}$$

$$x_1 = \frac{V_a^{'} - [c.p.]_{V_a^{'}}}{[\mathrm{var}]_{V_a^{'}}} \tag{5.2.3}$$

where *c.p.* is the center point of the indicated parameter and var is its variation. The center point is that point corresponding to $x_i = 0$ through the transformation, and the variation is the absolute value of the difference between the value corresponding to the center point and those values that correspond to $x_i = \pm 1$. For instance, referring to Table 5.2.1 which gives the values of A_s, $k_{\mathrm{mod}ified}$, and $V_a^{'}$ used in each study, the center point for A_s in Study 1 would be 2865, and the variation would be 40. For the present studies, a value of 0.75 was chosen for α.

Table 5.2.1. Progression of Model Parameters in Parametric Studies

Parameter	-1	-α	0	α	1	
A_s	2825	2835	2865	2895	2905	
$k_{modified}$	1.6	1.625	1.7	1.775	1.8	Study 1
V_a'	0.659	0.6615	0.669	0.6765	0.679	
A_s	2765	2775	2805	2835	2845	
$k_{modified}$	1.75	1.775	1.85	1.925	1.95	Study 2
V_a'	0.66	0.6625	0.67	0.6775	0.68	
A_s	2705	2715	2745	2775	2785	
$k_{modified}$	1.95	1.975	2.05	2.125	2.15	Study 3
V_a'	0.66	0.66125	0.665	0.66875	0.67	
A_s	2665	2675	2705	2735	2745	
$k_{modified}$	2.15	2.175	2.25	2.325	2.35	Study 4
V_a'	0.655	0.65625	0.66	0.66375	0.665	
A_s	2605	2630	2705	2780	2805	
$k_{modified}$	2.35	2.3875	2.5	2.6125	2.65	Study 5
V_a'	0.6625	0.663125	0.665	0.666875	0.6675	
A_s	2550	2575	2650	2725	2750	
$k_{modified}$	2.75	2.8125	3	3.1875	3.25	Study 6
V_a'	0.6635	0.664125	0.666	0.667875	0.6685	
A_s	2600	2625	2700	2775	2800	
$k_{modified}$	3.25	3.3125	3.5	3.6875	3.75	Study 7
V_a'	0.6645	0.665125	0.667	0.668875	0.6695	
A_s	2150	2175	2250	2325	2350	
$k_{modified}$	3.55	3.6	3.75	3.9	3.95	Study 8
V_a'	0.664	0.6645	0.666	0.6675	0.668	

The results of study 7, given below in Table 5.2.2, indicate that the thickness change of test 5 (the center panel) in the experimental study detailed in Chapter 2 had been matched. Results for all computational studies (1-8) can be found in Appendix D.

Table 5.2.2 Results of Computational Parametric Study 7

	Computed Results				% Diff. from Experiment		Consolidation	
	Δ Mass, g (%)		Δ Thickness, mm (%)		Mass	Thickness	y / n	Uncons. Layers
1	92.8	(25.3)	6.41	(49.0)	64.1	1.8	n	2
2	93.4	(25.4)	6.33	(48.4)	65.1	0.5	n	2
3	86.5	(23.5)	6.22	(47.5)	53.0	-1.3	n	3
4	86.9	(23.6)	6.13	(46.8)	53.7	-2.7	n	2
5	93.1	(25.3)	6.35	(48.5)	64.6	0.9	n	2
6	95.0	(25.8)	6.35	(48.5)	68.0	0.7	n	2
7	86.7	(23.6)	6.16	(47.0)	53.3	-2.3	n	2
8	88.4	(24.1)	6.13	(46.8)	56.3	-2.7	n	2
9	89.9	(24.4)	6.23	(47.6)	58.9	-1.1	n	2
10	89.5	(24.4)	6.25	(47.7)	58.3	-0.9	n	2
11	90.2	(24.6)	6.23	(47.6)	59.6	-1.2	n	2
12	92.3	(25.1)	6.31	(48.2)	63.3	0.2	n	2
13	87.5	(23.8)	6.16	(47.1)	54.7	-2.2	n	2
14	89.6	(24.4)	6.26	(47.8)	58.4	-0.6	n	2
15	90.5	(24.6)	6.22	(47.5)	60.0	-1.2	n	2

The presence of a match to the experimental data for thickness change is indicated by the sign-changing nature of the '% Difference from Experiment of Thickness' column in Table 5.2.2. If the percent difference changes from positive to negative, and it is assumed that percent difference can be represented by a continuous function, there must be at least one point in the parameter space where the difference is equal to zero. To find this point, a complete characteristic polynomial of the percent difference between the computational and experimental thickness changes must be constructed. In matrix notation,

$$y = c_0 + \mathbf{x}'\mathbf{c} + \mathbf{x}'C\mathbf{x} \tag{5.2.4}$$

where:

$$\mathbf{x} = \begin{bmatrix} x_1 \\ x_2 \\ x_3 \end{bmatrix}, \quad \mathbf{c} = \begin{bmatrix} c_1 \\ c_2 \\ \cdots \\ c_k \end{bmatrix}, \text{ and } C = \begin{bmatrix} c_{11} & c_{12}/2 & \cdots & c_{1k}/2 \\ & c_{22} & \cdots & \cdots \\ & & \cdots & c_{k-1,k}/2 \\ sym. & & & c_{kk} \end{bmatrix}$$

The vector $\mathbf{x}$ contains the design space variables. The quantities c_o, $\mathbf{c}$ and C are coefficients of the fitted response polynomial. The $\mathbf{x}'\mathbf{c}$ portion in (5.2.4) gives the first order terms and the $\mathbf{x}'C\mathbf{x}$ portion gives the quadratic contribution. The index k for the present studies has a value of three, and repeated indices do not imply summation.

It is necessary to determine the coefficients of the fitted response surface: c_o, $\mathbf{c}$, and C. This is done using a least squares method. What is known after computation is the design matrix (shown in Table 5.2.3), D, and the response vector, $\mathbf{y}$. For the present study, $\mathbf{y}$ consists of the percent thickness changes determined in each of the fifteen tests specified by D. The coefficients are placed in a vector $\hat{\mathbf{C}}$, and determined by solving the following relation:

$$(X'X)\hat{\mathbf{C}} = X'\mathbf{y} \tag{5.2.5}$$

where:

$$X = \left[\begin{array}{c|ccc|cccccc} & x_1 & x_2 & x_3 & x_1^2 & x_2^2 & x_3^2 & x_1x_2 & x_1x_3 & x_2x_3 \\ 1 & & & & 1 & 1 & 1 & 1 & 1 & 1 \\ 1 & & & & 1 & 1 & 1 & -1 & -1 & 1 \\ 1 & & & & 1 & 1 & 1 & -1 & 1 & -1 \\ 1 & & & & 1 & 1 & 1 & 1 & -1 & -1 \\ 1 & & & & 1 & 1 & 1 & 1 & -1 & -1 \\ 1 & & & & 1 & 1 & 1 & -1 & 1 & -1 \\ 1 & & D & & 1 & 1 & 1 & -1 & -1 & 1 \\ 1 & & & & 1 & 1 & 1 & 1 & 1 & 1 \\ 1 & & & & 0 & 0 & 0 & 0 & 0 & 0 \\ 1 & & & & \alpha^2 & 0 & 0 & 0 & 0 & 0 \\ 1 & & & & \alpha^2 & 0 & 0 & 0 & 0 & 0 \\ 1 & & & & 0 & \alpha^2 & 0 & 0 & 0 & 0 \\ 1 & & & & 0 & \alpha^2 & 0 & 0 & 0 & 0 \\ 1 & & & & 0 & 0 & \alpha^2 & 0 & 0 & 0 \\ 1 & & & & 0 & 0 & \alpha^2 & 0 & 0 & 0 \end{array}\right], \text{ and } \quad \hat{\mathbf{C}} = \begin{bmatrix} c_0 \\ c_1 \\ c_2 \\ c_3 \\ c_{11} \\ c_{22} \\ c_{33} \\ c_{12} \\ c_{13} \\ c_{23} \end{bmatrix}$$

Table 5.2.3. Test Sequence for Box-Behnken Design

Test #	$(x_1)\ A_s$	$(x_2)\ k_{modified}$	$(x_3)\ V_a'$
1	-1	-1	-1
2	-1	-1	1
3	-1	1	-1
4	-1	1	1
5	1	-1	-1
6	1	-1	1
7	1	1	-1
8	1	1	1
9	0	0	0
10	$-\alpha$	0	0
11	α	0	0
12	0	$-\alpha$	0
13	0	α	0
14	0	0	$-\alpha$
15	0	0	α

$= D$

It is desired to find at least one point in the domain of the study where the characteristic polynomial, Equation 5.2.4, is equal to zero. The results of this analysis are given in Table 5.2.4.

Table 5.2.4. Parameter Values for Zero Percent Difference

A_s	V_a'	$k_{modified}$
2700	0.667	3.341

It may be noted from Table 5.2.2 that the percent differences between the computational and experimental mass changes are far from zero and do not change sign. This indicates that there is still significant error in the calculation of mass change for that

given range of parameters. While the values given in Table 5.2.4 are taken to give zero error for thickness change, they still yield significant error for mass change. It was known, as can be seen in Figures 5.2.2 through 5.2.4, that variations in the parameters A_s, $V_a^{'}$, and $k_{modified}$ sometimes have opposite effects on mass loss and thickness loss.

Considering Figure 5.2.4, it can be seen that an increase in $k_{modified}$ decreases both the mass change and the thickness change. Figure 5.2.3 shows that an increase in $V_a^{'}$ increases the mass change while decreasing the change in thickness. Figure 5.2.2 shows a similar trend for A_s. It should be noted that the influence of $k_{modified}$ is much greater than that of $V_a^{'}$ or A_s.

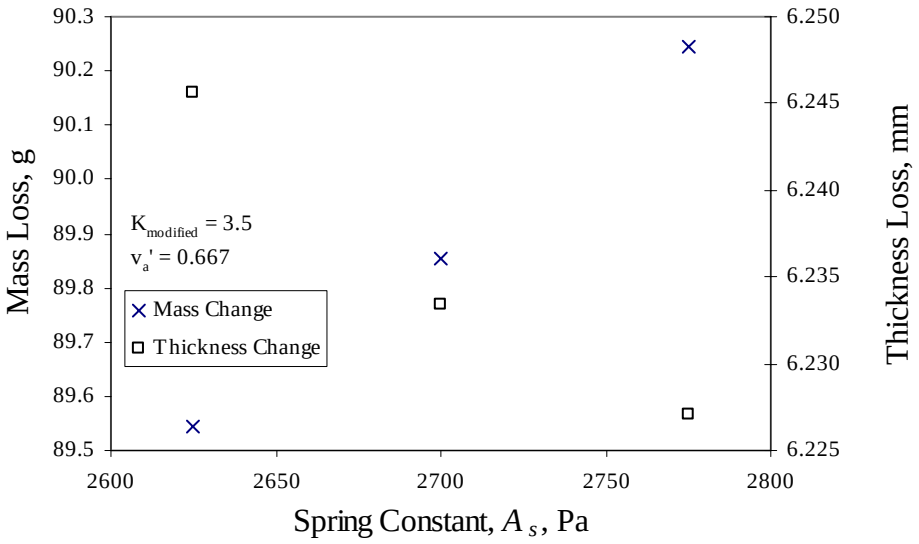

Figure 5.2.2. Mass and Thickness Change versus A_s

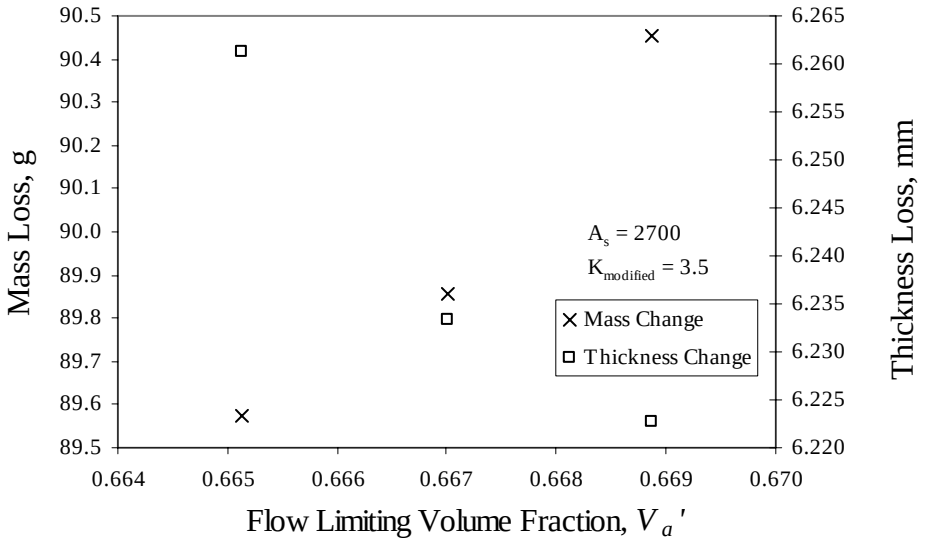

Figure 5.2.3. Mass and Thickness Change versus $V_a^{'}$

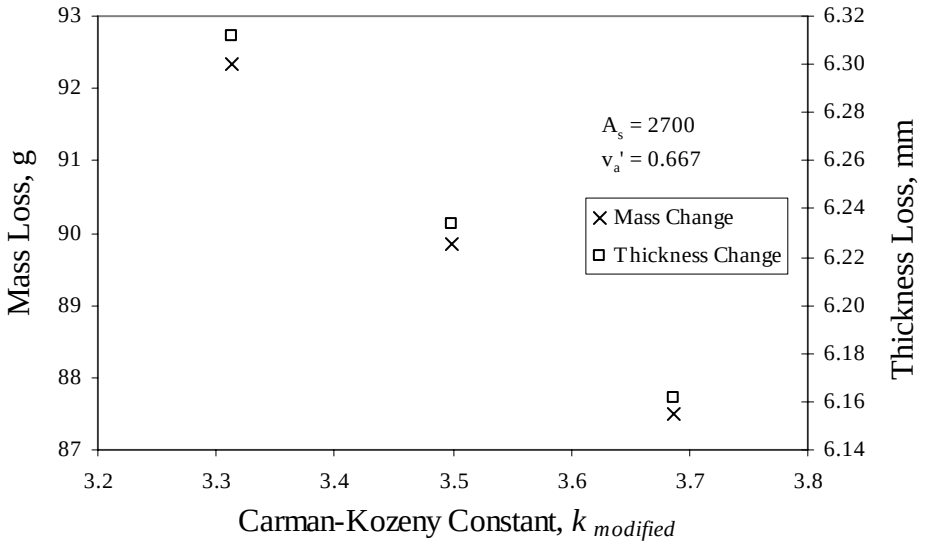

Figure 5.2.4. Mass and Thickness Change versus $k_{modified}$

On the basis of these observations, a further parametric study (Study 8) was undertaken in an attempt to lower the error for mass change while maintaining agreement on thickness change. This was Study 8 as described in Table 5.2.1. The results of this study are given in Table 5.2.5 and Figures 5.2.5-5.2.7 below.

Table 5.2.5 Results of Computational Parametric Study 8

	Computed Results				% Diff. from Experiment		Consolidation	
	Δ Mass, g (%)		Δ Thickness, mm (%)		Mass	Thickness	y / n	Uncons. Layers
1	89.6	(24.4)	6.52	(49.8)	58.4	3.5	n	3
2	89.3	(24.3)	6.42	(49.0)	58.0	1.9	n	3
3	85.5	(23.3)	6.38	(48.8)	51.2	1.3	n	4
4	85.0	(23.1)	6.27	(47.9)	50.4	-0.4	n	4
5	89.9	(24.5)	6.45	(49.3)	59.0	2.3	n	3
6	88.6	(24.1)	6.30	(48.1)	56.7	0.0	n	3
7	85.6	(23.3)	6.30	(48.2)	51.3	0.1	n	4
8	84.1	(22.9)	6.15	(47.0)	48.7	-2.4	n	4
9	87.4	(23.8)	6.36	(48.6)	54.5	0.9	n	4
10	87.6	(23.8)	6.40	(48.9)	55.0	1.6	n	4
11	87.0	(23.7)	6.31	(48.2)	53.8	0.2	n	4
12	89.0	(24.2)	6.41	(49.0)	57.5	1.8	n	3
13	85.8	(23.3)	6.30	(48.2)	51.7	0.1	n	4
14	87.8	(23.9)	6.41	(49.0)	55.3	1.8	n	4
15	86.8	(23.6)	6.30	(48.1)	53.4	0.0	n	4

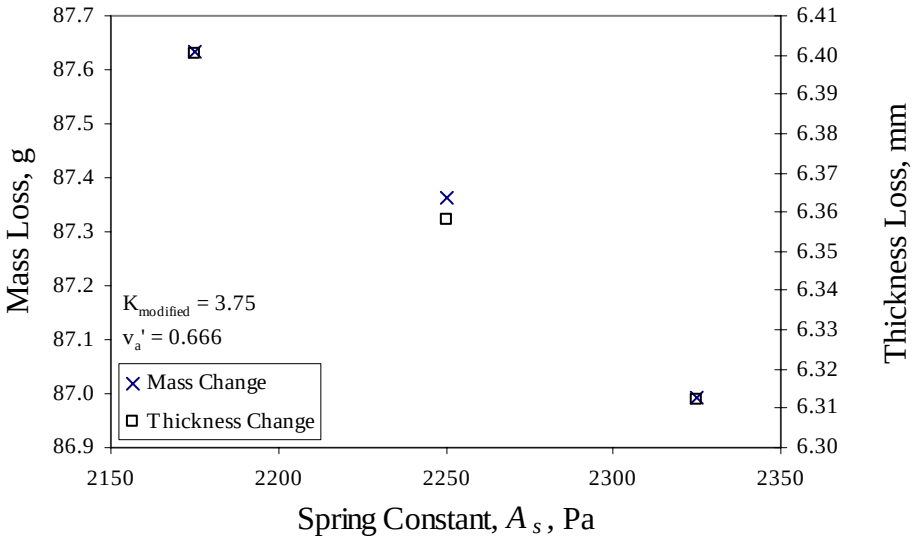

Figure 5.2.5. Computational Mass and Thickness Loss versus A_s for Study 8

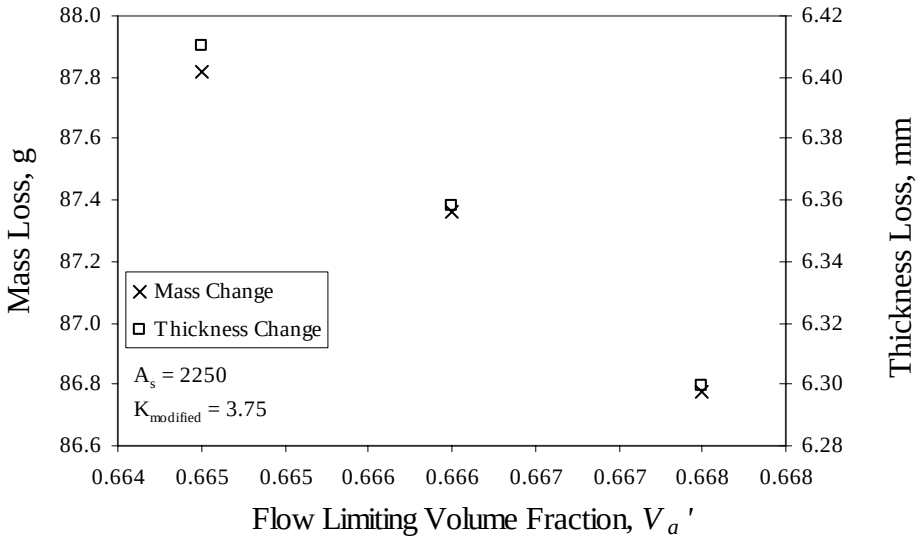

Figure 5.2.6. Computational Mass and Thickness Loss versus $V_a^{'}$ for Study 8

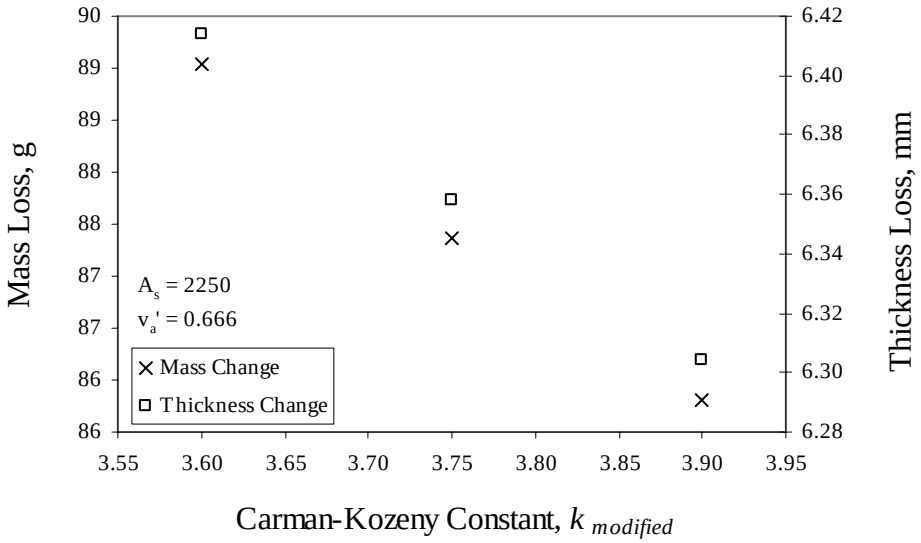

Figure 5.2.7. Computational Mass and Thickness Loss versus $k_{modified}$ for Study 8

It can be seen from Table 5.2.5 that while a match for thickness loss (though possibly at different parameter values) has been preserved as indicated by the changes in sign of the % Difference from Experiment of Thickness column, the mass loss has been reduced at the majority of the test points. While this is encouraging, the information in

Figures 5.2.5-5.2.7 is not. It is plainly seen that within this range of parameter test values, there is no parameter that has opposing effects on mass loss versus thickness loss. Hence, a change in any parameter will affect both mass loss and thickness loss in the same manner. It is not clear which direction is best to pursue to achieve the goal of reducing the error on mass loss while preserving the low error on thickness loss at this point in the series of parametric studies.

Using the values of A_s, $V_a^{'}$, and k_{modified} from Study 7, given in Table 5.2.4, $V_o = 0.36$ and $V_a = 0.886$, a computational simulation of the experimental parametric study discussed in Chapter 2 was undertaken. Each of the 9 tests were simulated using the experimental test parameters for applied pressure, cure temperature, and cure cycle duration as given in Table 2.1. The results of the computational study are given in Table 5.2.6. Note that Tests 3, 4, and 8 did not complete due to excessive computational time (>30 days).

Table 5.2.6. Comparison of Numerical and Experimental Results

	Thickness Loss			Mass Loss		
Test	Experimental	Numerical	% Difference	Experimental	Numerical	% Difference
1	5.46	5.49	0.51	39.6	73.9	86.7
2	5.92	5.79	-2.11	43.5	83.4	91.6
5	6.32	6.30	-0.40	56.6	91.9	62.6
6	5.97	6.40	7.24	62.6	95.2	52.0
7	6.22	6.22	-0.02	72.8	89.3	22.6
9	6.35	5.86	-7.78	53.1	83.4	56.9

Considering the existence of experimental error in any physical study, the computational results compare well with those of experimental thickness loss, which they

were intended to match with the given parameter set from computational Study 7. As previously discussed, the computational results for mass loss did not match experimental results using the parameters in Table 5.2.4, and it was not expected that any improved correspondence would be seen in a simulation of the experimental parametric study. Results in Table 5.2.6 confirm this. Figures 5.2.8 and 5.2.9 show the percent difference between experimental and computational thickness and mass loss through the center and star points of the studies, tests 5-9 as given in Table 2.1. Test 1-4 will not appear in these figures because they are not the center or star points.

Figure 5.2.8 shows low percent error for both thickness and mass loss at the low temperature, reasonable error for thickness loss at the center temperature, and higher error for mass loss at both the center and higher cure temperatures as well as higher error for thickness loss at the higher cure temperature. Figure 5.2.9 shows high error for mass loss at low pressure, with lesser error at the center pressure. Thickness loss in Figure 5.2.9 shows very little error at the center with higher error at the low pressure point.

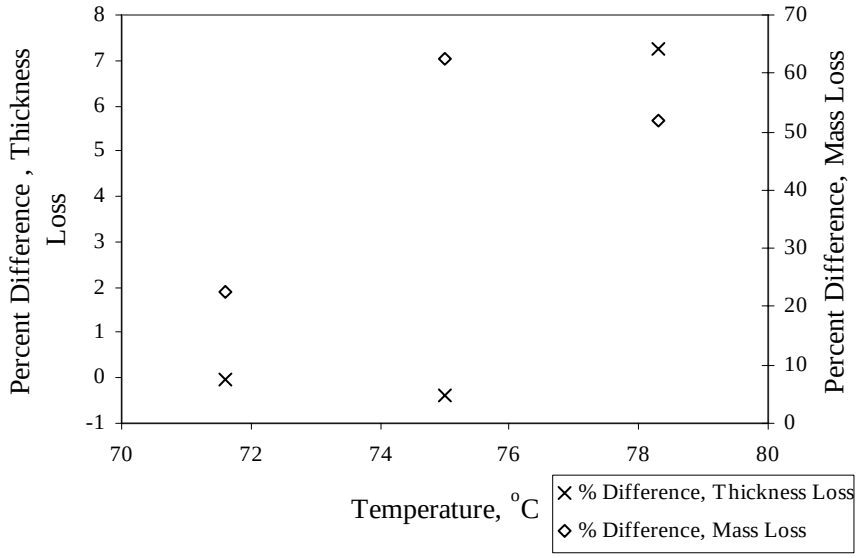

Figure 5.2.8. Percent Difference Between Experimental and Numerical Mass and Thickness Loss versus Temperature

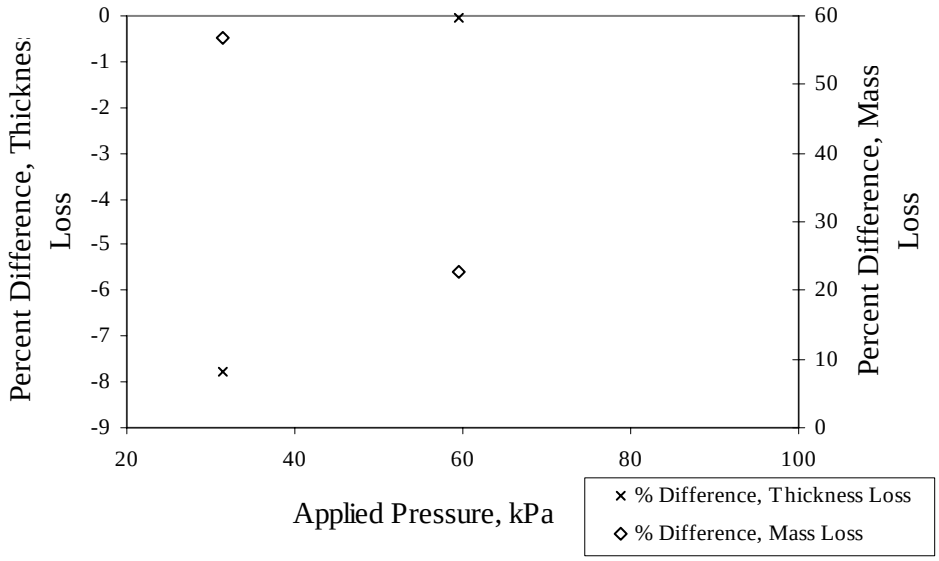

Figure 5.2.9. Percent Difference Between Experimental and Numerical Mass and Thickness Loss versus Applied Pressure

5.3 Observations

Test 2 of study 1 of the computational parametric studies previously detailed in Tables 5.2.1 and 5.2.3, a simulation of test 5 of the experimental study provides an example of how the model demonstrates the mechanism of multi-layer consolidation for the laminate. As pointed out by Loos and Springer [3], laminated composites composed of sheets of prepreg and cured under pressure consolidate in a specific order. The sheet of prepreg next to the bleeder consolidates first, followed by the layer adjoining it, and so on until the layer next to the tool is consolidated. This mechanism is demonstrated by the present model. The initial state of the laminate is shown in Figure 5.3.1. The fiber volume fraction is equal to the initial fiber volume fraction as required by Equation 3.2.6 everywhere except in the neat resin regions, where the volume fraction is zero. A

sequence of the consolidation process demonstrated by the model during test 2 of study 1 in the computational parametric studies is shown in Figures 5.3.1-5.3.8. The parameters used for the test and its supporting viscosity and kinetics relations are the same as those detailed early in Section 5.2. The laminate is composed of 8 layers and is 152.4 mm square.

As pressure is applied, the dry fiber regions compress and their fiber volume fractions increase uniformly. The volume fraction along the boundaries of the mixed regions increases as the boundary condition in Equation 3.2.1 requires, followed by V_f in the adjacent mixed regions. This is shown in Figure 5.3.2. The total thickness begins to decrease mostly due to compaction of the dry fiber regions and, to a lesser extent because the viscosity is still high, to a reduction in thickness of the neat resin and mixed regions.

At some point in time during a reasonable cure cycle, the thickness of the dry fiber regions will likely decrease to zero. When this occurs, the volume fraction of the mixed regions in every layer except the top layer will decrease because the presence of a neat resin region in the top layer requires all of the flow into the bleeder to originate from the mixed region in the top layer. This is due to the fact that one side of the mixed region in the top layer, in contact with a neat resin region, is constrained to V_o as required by Equation 3.2.2 and the other, in contact with the bleeder, is constrained by Equation 3.2.1. This situation is shown in Figure 5.3.3.

In order for the consolidation pressure to affect the inner layers, the thickness of the neat resin layer between the top layer and the one immediately beneath it must decrease to zero. This is the mechanism described by Loos and Springer [3], shown in Figure 5.3.4 and clearly seen in Figure 5.3.8. The fiber volume fraction of the lower

layers is held low because there is yet a neat resin region of nonzero thickness above them, therefore their boundaries have been held at a low volume fraction as per Equation 3.2.2, and they have not yet consolidated.

Once the neat resin region in the lowermost layer has vanished, the boundary condition given by Equation 3.2.5 is applied at the bottom of the laminate and the final phase of consolidation can begin. Because the lowermost boundary of the laminate is no longer constrained to V_o, the volume fraction through the thickness of the laminate can increase. This is when the fibers begin to support the applied pressure through the thickness of the laminate and the volume fraction of all regions approaches the solution of Equation 3.3.1.

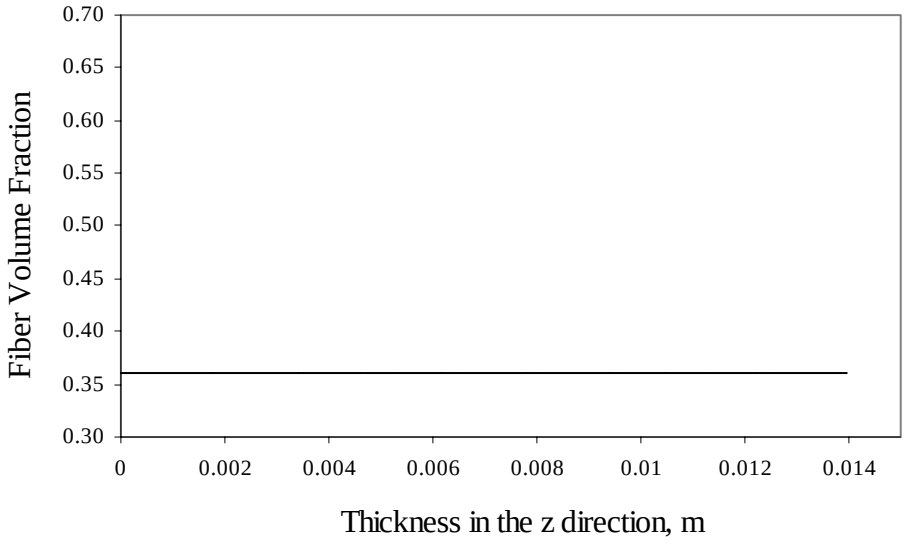

Figure 5.3.1. Fiber Volume Fraction Variation Through the Thickness of the Composite at 0 seconds

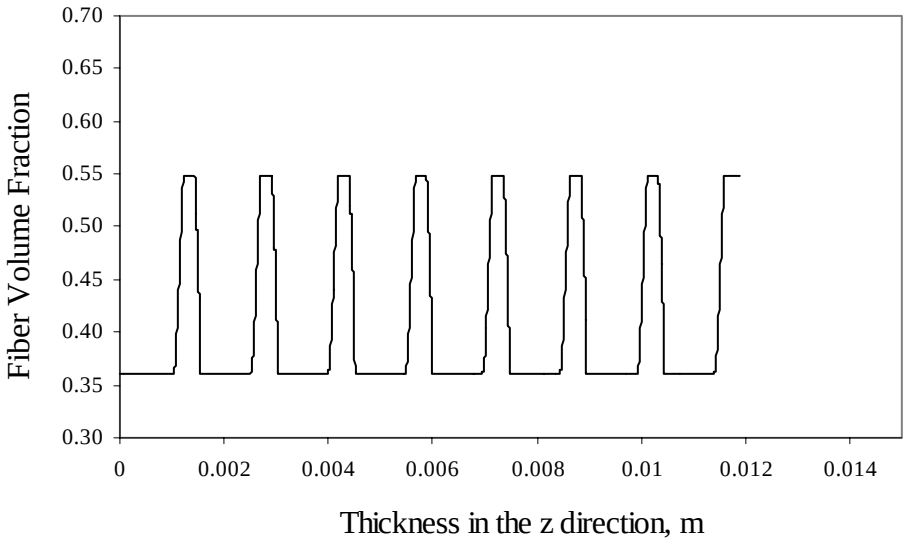

Figure 5.3.2. Fiber Volume Fraction Variation Through the Thickness of the Composite at 300 seconds

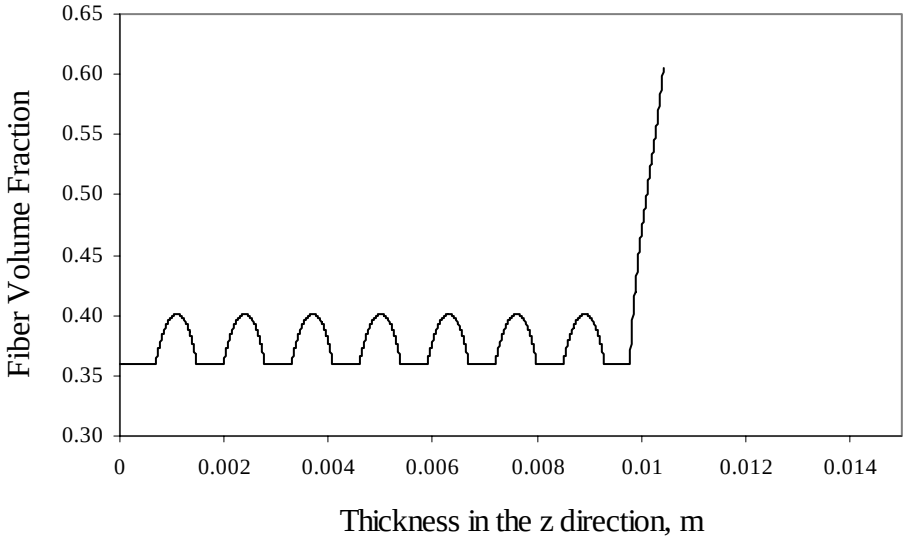

Figure 5.3.3. Fiber Volume Fraction Variation Through the Thickness of the Composite at 1200 seconds

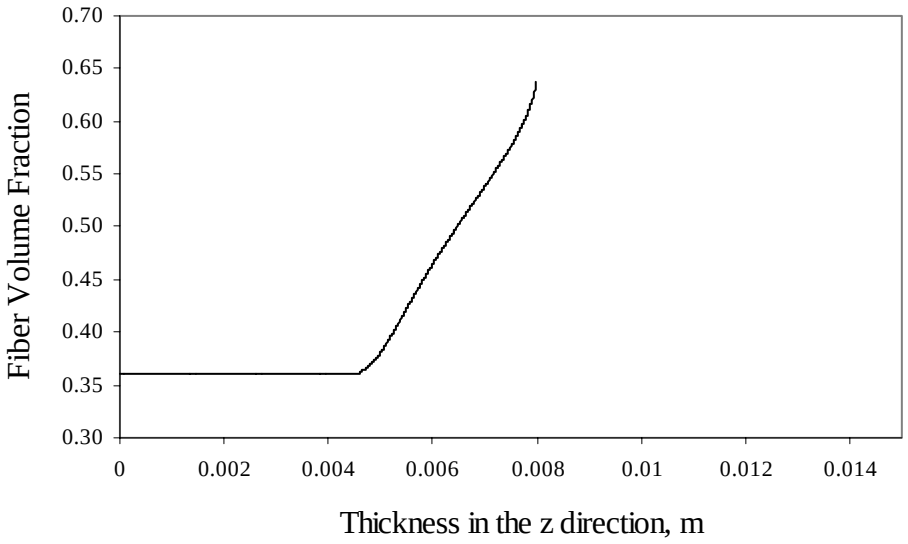

Figure 5.3.4. Fiber Volume Fraction Variation Through the Thickness of the Composite at 3000 seconds

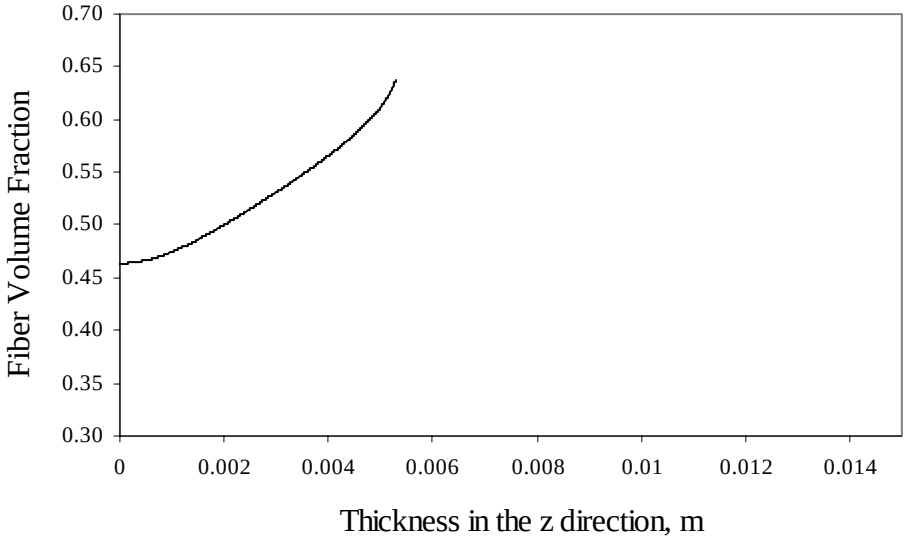

Figure 5.3.5. Fiber Volume Fraction Variation Through the Thickness of the Composite at 7020 seconds

The mass and thickness changes of the composite over time reveal further information about the consolidation process. Shown in Figures 5.3.6 and 5.3.7 are the mass and thickness changes of test 2 of study 1 in the numerical parametric study

discussed in the previous section. An overall representation of the consolidation process is shown in Figure 5.3.8.

Figure 5.3.6 shows that the laminate does not immediately begin to lose mass. This is because the dry fiber region in the top layer must saturate before resin can flow through it and into the bleeder. Mass loss then falls into a nearly linear progression until the lower layers begin to saturate and viscosity begins to increase. Once the resin gels, indicated both by a flattening of both curves slightly before 9000 seconds and by a sharp increase in the computed resin viscosity, no more mass change is observed.

The thickness change as shown in Figure 5.3.7, is initially rapid due to the compaction and saturation of the dry fiber regions. The rate of thickness change drops sharply once the dry fiber regions saturate, occurring in Figure 5.3.7 at approximately 1000 seconds. The thickness continues to fall as the composite consolidates, ceasing to change when the resin gels. The slope of the thickness curve during the period of time between saturation of the dry regions and gel of the resin is governed by the consolidation of the neat resin regions and the viscosity of the resin. The presence of a neat resin region in each layer speeds the thickness change, because the thickness of the mixed region that is consolidating on top of the uppermost neat resin region is small. As more neat resin regions disappear, the rate of thickness change decreases. An increase in resin viscosity initially slows consolidation, then brings it to a halt.

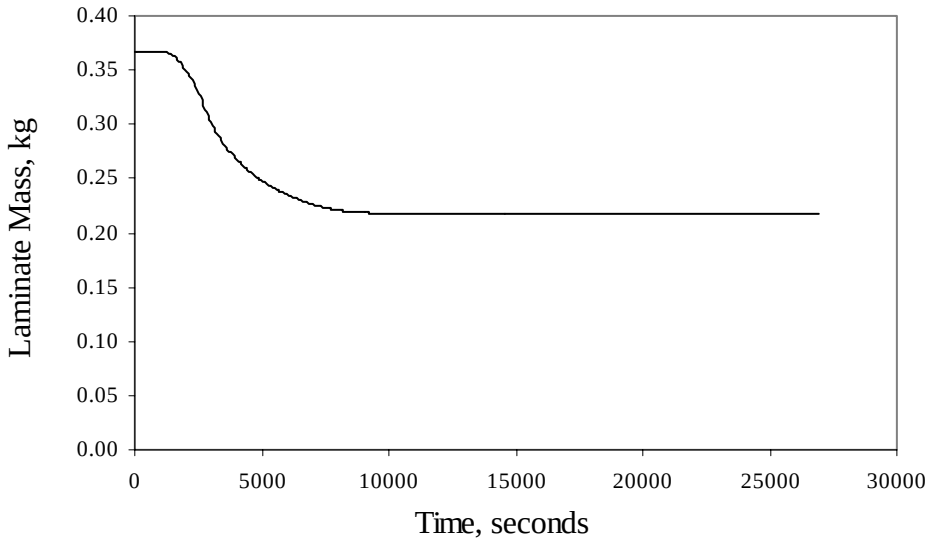

Figure 5.3.6. Laminate Mass versus Time for Parametric Study Trial Two

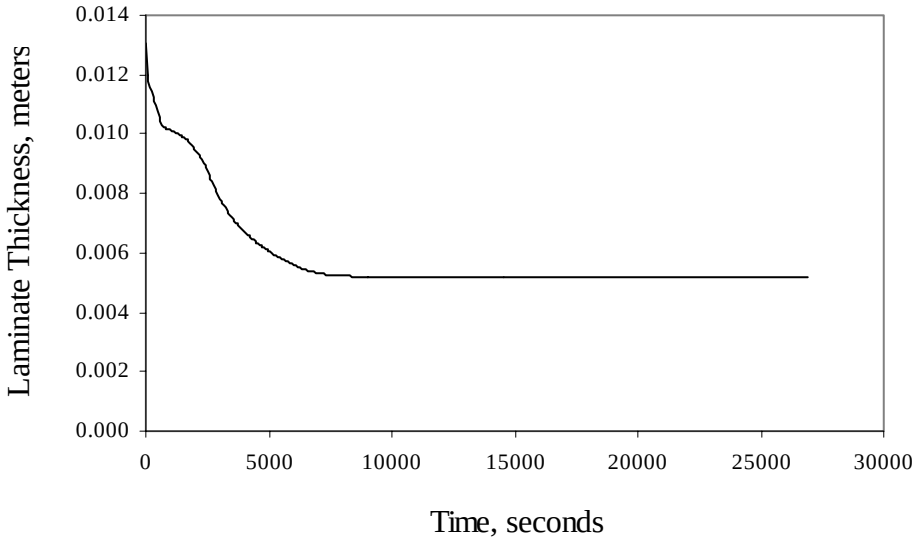

Figure 5.3.7. Laminate Thickness versus Time for Parametric Study Trial Two

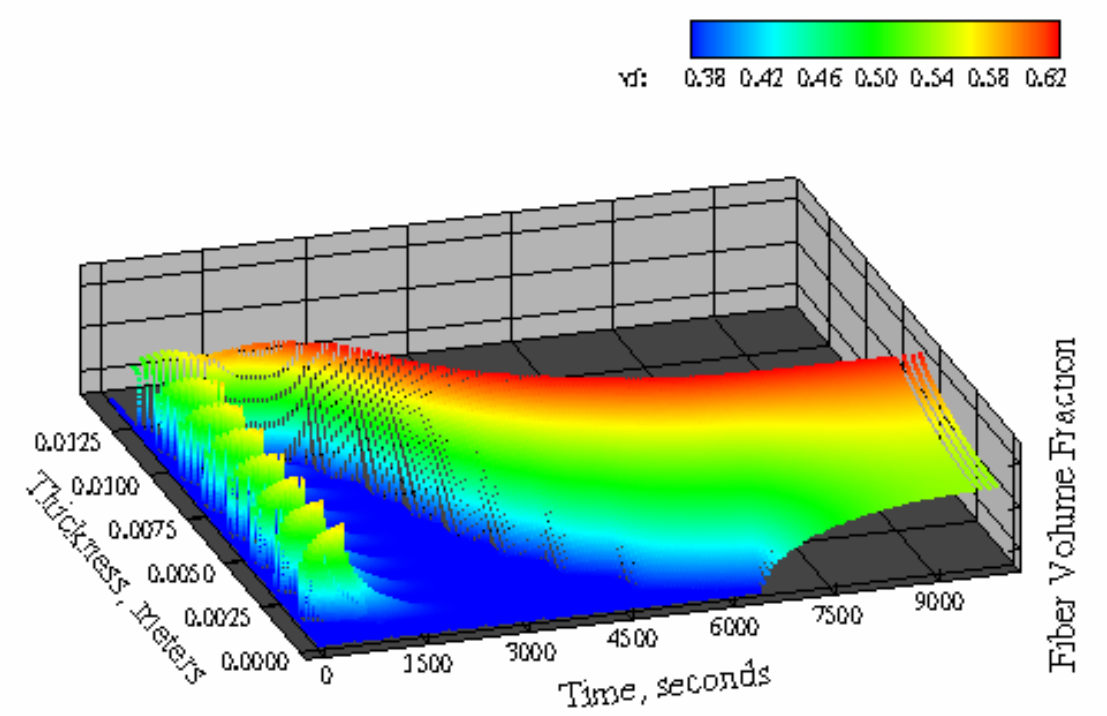

Figure 5.3.8. Overall Representation of the Consolidation Process

Chapter 6

Conclusions

A model of consolidation in the multi-layered resin film infusion process has been studied. It is capable of accounting for both fiber and resin motion within a partially saturated, deformable and porous reinforcement. It assumes one dimensional, isothermal flow and has boundary conditions based on pressure equilibrium. The governing equation is expressed in terms of the fiber volume fraction as a function of space and time. Once the volume fraction is determined, the fiber velocity, resin velocity, fiber permeabilities, and resin volume flow rates can be calculated as functions of space and time for the duration of consolidation. Flow front tracking expressions have been proposed which take into account the multiple layer and partially saturated nature of the laminate. The model accounts for changing boundary conditions as dry regions saturate and fiber-free regions diminish. Additionally, kinetics and viscosity relations of the Cytec™ 754 epoxy resin system have been fitted and verified.

An attempt to estimate values of material parameters in the model has been made; however, a targeted experimental verification should be carried out in which the detailed predictions of the model, such as volume fraction and resin pressure through the thickness of the composite during and after cure, are tested. In addition, the model parameters should be determined by experiment. For extended cure cycles or thick parts, a less computationally expensive implicit formulation of the model may be desirable. A comparison of computed and experimental results has shown a general agreement

between the two for the thickness loss, but not for the mass loss. The explicit formulation was found to be computationally expensive.

We note that parameters involved in the model have not been determined for a wide range of fabrics and cannot be estimated from widely tabulated data. For the present problem, further parameter determination and model verification employing these parameters should be undertaken.

Bibliography

[1] Song, X. (2003) Vacuum Assisted Resin Transfer Molding (VARTM): Model Development and Verification. Ph.D. Dissertation. Virginia Polytechnic Institute and State University

[2] Loos, A.C. and J.D. Macrae. (1996) A Process Simulation Model for the Manufacture of a Blade Stiffened Panel by the Resin Film Infusion Process. Composites Science and Technology, 56, 273-289

[3] Loos, A.C. and G.S. Springer. (1983) Curing of Epoxy Matrix Composites. Journal of Composite Materials, 17, 135-169

[4] Carman, P.C. (1939) Fluid Flow Through Aligned Fiber Beds. Journal of Agricultural Science, 29, 262-273

[5] Costa, V.A.F. and A.C.M. Sousa. (2002) Modeling of Flow and Thermo-Kinetics during the Cure of Thick Laminated Composites. International Journal of Thermal Sciences, 42, 15-22

[6] Rahatekar, S.S. and J.A. Roux. (2002) Numerical Simulation of Pressure Variation and Resin Flow in Injection Pultrusion. Journal of Composite Materials, 37(12), 1067-1082

[7] Chou, T.W. and B. Chen. (2000) Compaction of Woven Fabric Preforms: Nesting and Multi-Layer Deformation. Composites Science and Technology, 60, 2223-2231

[8] Chou, T.W. and B. Chen. (1999) Compaction of Woven Fabric Preforms in Liquid Composite Molding Processes: Single Layer Deformation. Composites Science and Technology, 59, 1519-1526

[9] Chen, B., Cheng, A.H.-D. and T.-W. Chou. (2001) A Nonlinear Compaction Model for Fibrous Preforms. Composites Part A: Applied Science and Manufacturing, 32, 701-707

[10] Hammami, A. and B. R. Gebart. (2000) Analysis of the Vacuum Infusion Molding Process. Polymer Composites, 21(1), 28-40

[11] Gutowski, T.G., Cai, Z., Bauer, S., Boucher, D., Kingery, J. and S. Wineman. (1986) Consolidation Experiments for Laminate Composites. Journal of Composite Materials, 21, 650-669

[12] Gutowski, T.G., Ed., (1997) Advanced Composites Manufacturing. John Wiley and Sons, New York

[13] Van Wyk, C.M. (1946) Notes on the Compressibility of Wool. Journal of Textile Inst., 37, T285-292

[14] Gutowski, T.G., Morigaki, T. and Z. Cai. (1987) The Consolidation of Laminate Composites. Journal of Composite Materials, 21, 172-188

[15] Gutowski, T.G. (1985) A Resin Flow / Fiber Deformation Model for Composites. SAMPE Quarterly, 16(4), 58-64

[16] Gutowski, T.G., Cai, Z., Kingery, J. and S. J. Wineman. (1986) Resin Flow / Fiber Deformation Experiments. SAMPE Quarterly, 17(4), 54-58

[17] Gutowski, T.G., Kingery, J. and D. Boucher. (1986) Experiments in Composites Consolidation: Fiber Deformation. Proceedings of the SPE Annual Technical Conference, Boston, 1316-1320

[18] Gutowski, T.G., Wineman, S. J. and Z. Cai. (1986) Applications of the Resin Flow / Fiber Deformation Model. 31st International SAMPE Symposium, April 7 – 10. 245-254

[19] Wineman, S. J. (1985) Viscous Flow Through Aligned Graphite Fibers in Compression. S. B. Thesis, MIT

[20] Kingery, J. C. (1985) Composite Process Modeling: Consolidation of Aligned Fiber Assemblies. M. S. Thesis, MIT

[21] Gauvin, R., Clerk, P., Lemenn, Y. and F. Trochu. (1994) Compaction and Creep Behavior of Glass Reinforcement for Liquid Composite Molding. Proceedings of the 10th Annual ASM / ESD Advanced Composites Conference, Dearborn, Michigan. November 7-10. 357-367

[22] Advani, S.G., Simacek, P. and J.A. Acheson. (2003) The Implications of Fiber Compaction and Saturation on Fully Coupled VARTM Simulation. Composites Part A: Applied Science and Manufacturing, 35, 159-169

[23] Robitaille, F. and R. Gauvin. (1999) Compaction of Textile Reinforcements for Composites Manufacturing. III: Reorganization of the Fiber Network. Polymer Composites, 20(1), 48-61

[24] Loos, A.C., Batra, R.C., Rattazzi, D., Caba, A.C. and T. Knott. (1998) Process Model Development / Residual Stress Model Development. Final Report.

Prepared for The Boeing Company, Long Beach, CA. Prime Contract Number NAS1-20546. Purchase Order Number 5XY070866

[25] Robitaille, F. and R. Gauvin. (1998) Compaction of Textile Reinforcements for Composites Manufacturing. I: Review of Experimental Results. Polymer Composites, 19(2), 198-216

[26] Robitaille, F. and R. Gauvin. (1998) Compaction of Textile Reinforcements for Composites Manufacturing. II: Compaction and Relaxation of Dry and H_2O Saturated Woven Reinforcements. Polymer Composites, 19(5), 543-557

[27] Verijenko, V.E., Sevostianov, I.B., von Klemperer, C.J. and B. Chevallereau. (1999) Mathematical Model of Stress Formation During Vacuum Resin Infusion Process. Composites Part B: Engineering, 30, 513-521

[28] Cytec Industries, Inc. (2003) Cytec Engineered Materials CYCOM ®754 Marine Product Range. Last Accessed October 26, 2004 at http://www.cytec.com/ business/EngineeredMaterials/Cycom%20754.shtm

[29] Scheidegger, A.E. (1974) The Physics of Flow Through Porous Media. University of Toronto Press, Toronto, ON. 3rd Edition

[30] Halley, P.J. and M.E. Mackay. (1996) Chemorheology of Thermosets – An Overview. Polymer Engineering and Science, 36(5), 593-609

[31] Perry, M.J. (1993) Analysis of resin transfer molding: material characterization, molding and simulation. Ph.D. Dissertation, Ohio State University

[32] Dupuy, J.D. Leroy, E. and A. Maazouz. (2000) Determination of Activation Energy and Preexponential Factor of Thermoset Reaction Kinetics Using Differential Scanning Calorimetry in Scanning Mode: Influence of Baseline

Shape on Different Calculation Methods. Journal of Applied Polymer Science, 78, 2262-2271

[33] Liu, X.L., Falzon, P.J., Sweeting, R. and R. Paton. (2004) Effective Compressibility and Permeability of Multi-Layer Non-Crimp Fiberglass Reinforcements. Journal of Reinforced Plastics and Composites, 23(8), 861-879

[34] Batra, R.C. and Q. C. Liang. (1997) Finite Dynamic Deformations of Smart Structures. Computational Mechanics, 20, 427-438

[35] Myers, R.H. (1971) Response Surface Methodology. Allyn & Bacon Inc., Boston, MA. 68-80

Appendix A

Experimental Data and Least Squares Fits for the Empirical Viscosity Relation

Contained in this appendix are the overall and individual fits at each test temperature for the viscosity model. The form of and process for fitting the viscosity model are detailed in Section 4.1. Overall fits are the comparison of the overall model to individual test data. Individual fits are the fits used to determine the forms of the coefficient fits for the overall model, also given in Section 4.1. The overall and individual fits follow.

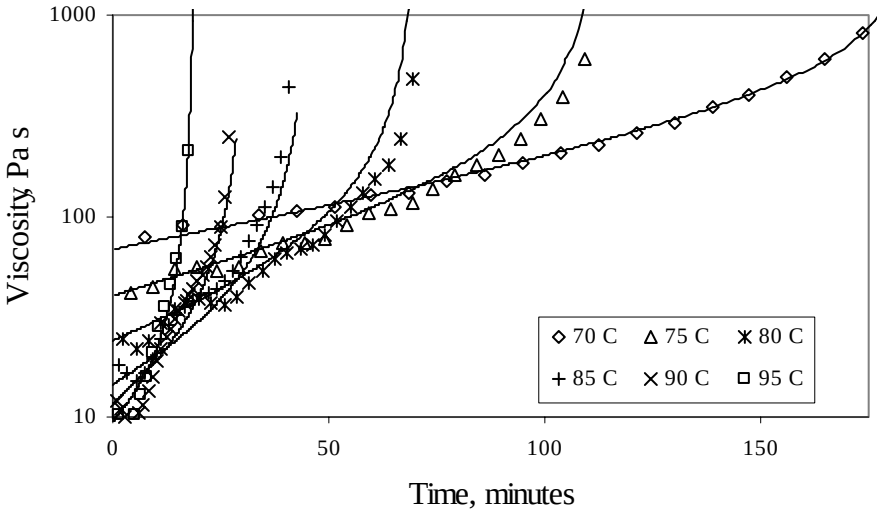

Figure A.1. Viscosity versus Time for Overall Model at all Test Temperatures

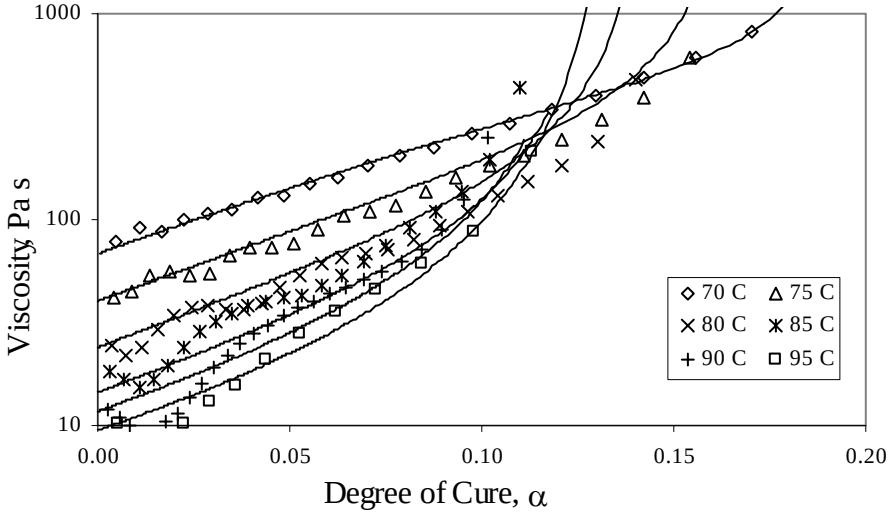

Figure A.2. Viscosity versus Degree of Cure for Overall Fit at all Test Temperatures

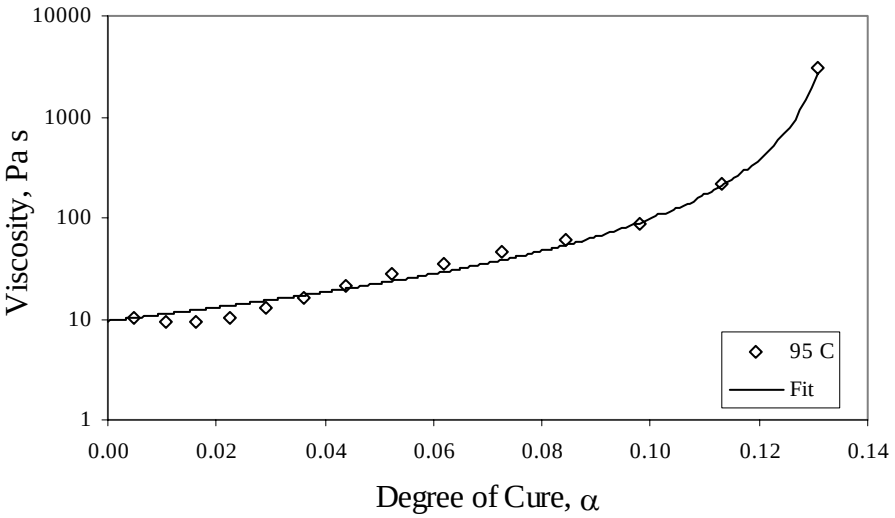

Figure A.3. Overall Viscosity versus Degree of Cure at 95°C

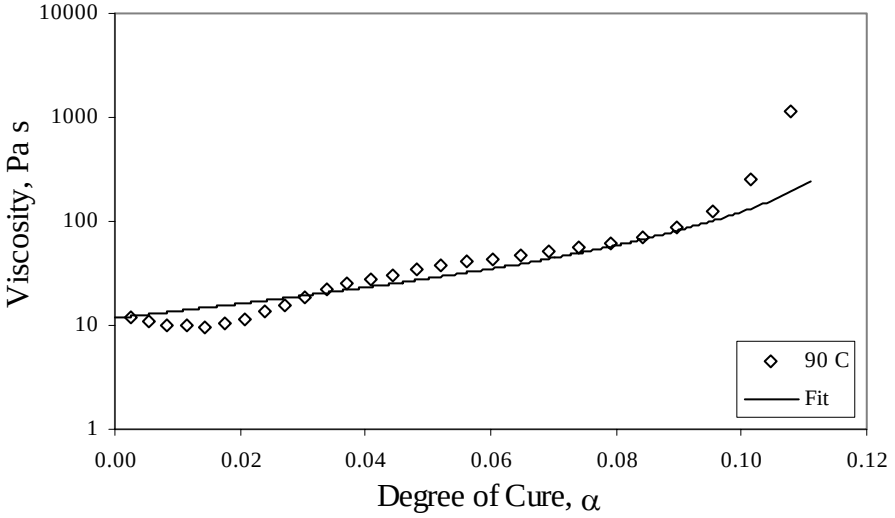

Figure A.4. Overall Viscosity versus Degree of Cure at 90°C

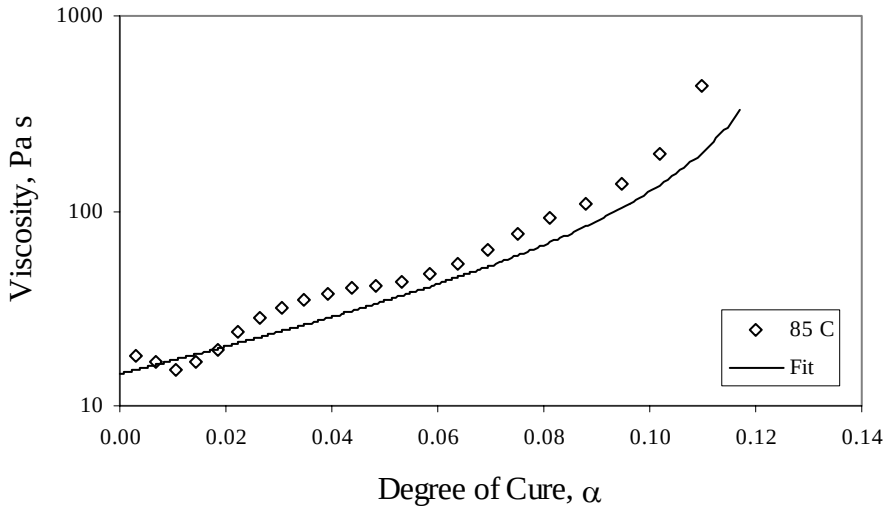

Figure A.5. Overall Viscosity versus Degree of Cure at 85°C

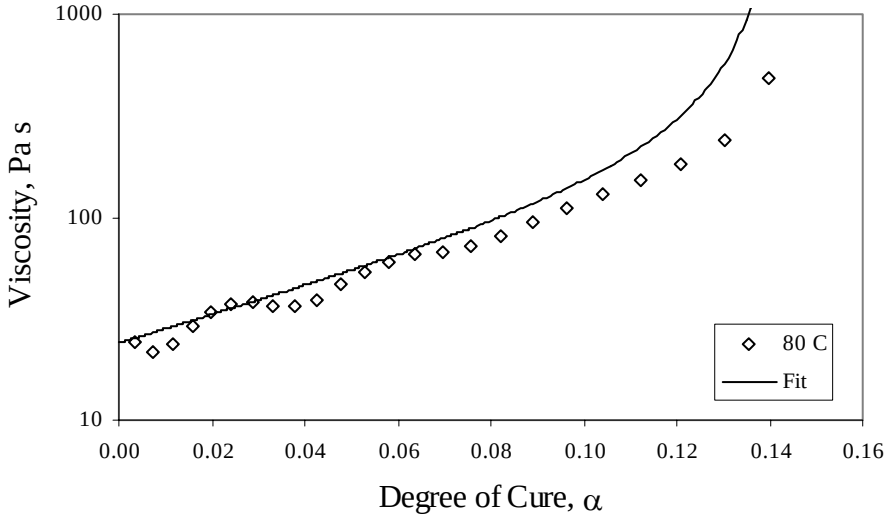

Figure A.6. Overall Viscosity versus Degree of Cure at 80°C

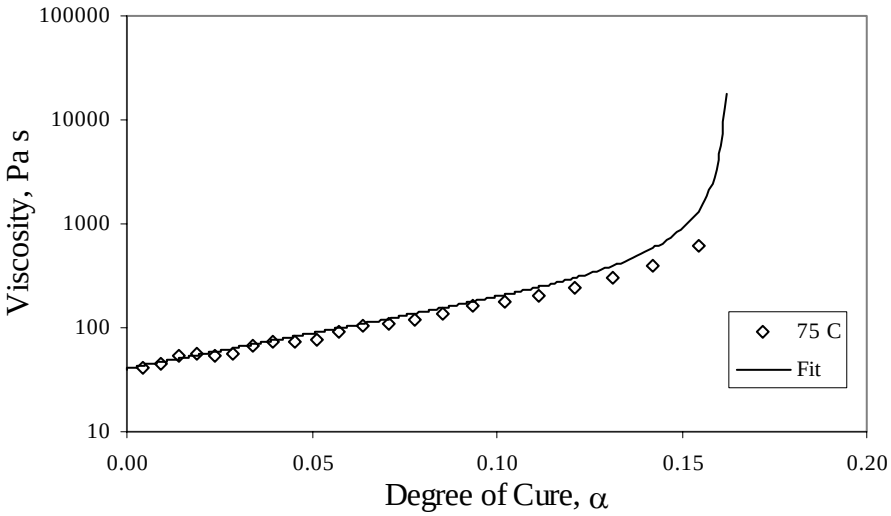

Figure A.7. Overall Viscosity versus Degree of Cure at 75°C

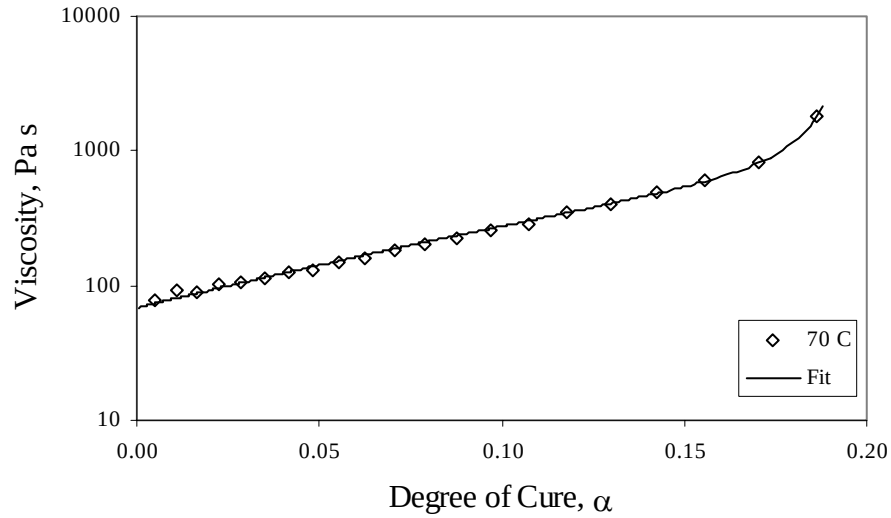

Figure A.8. Overall Viscosity versus Degree of Cure at 70°C

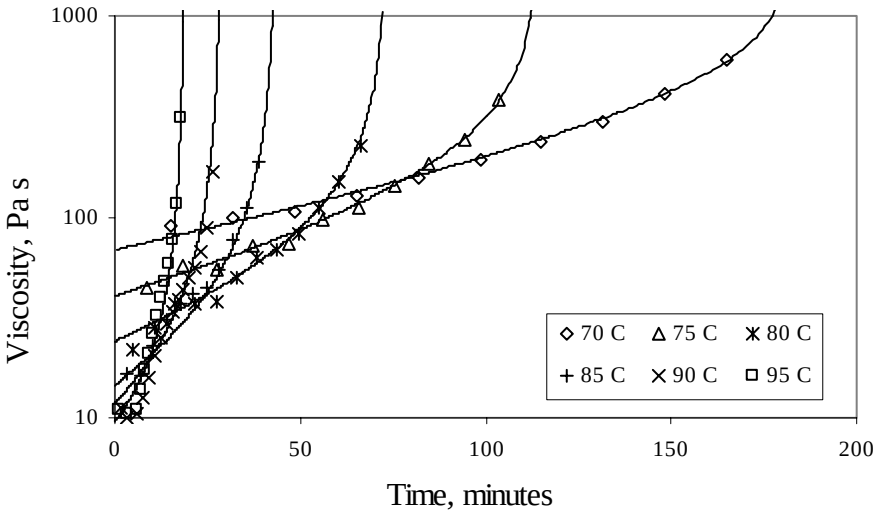

Figure A.9. Viscosity versus Time for all Individual Fits

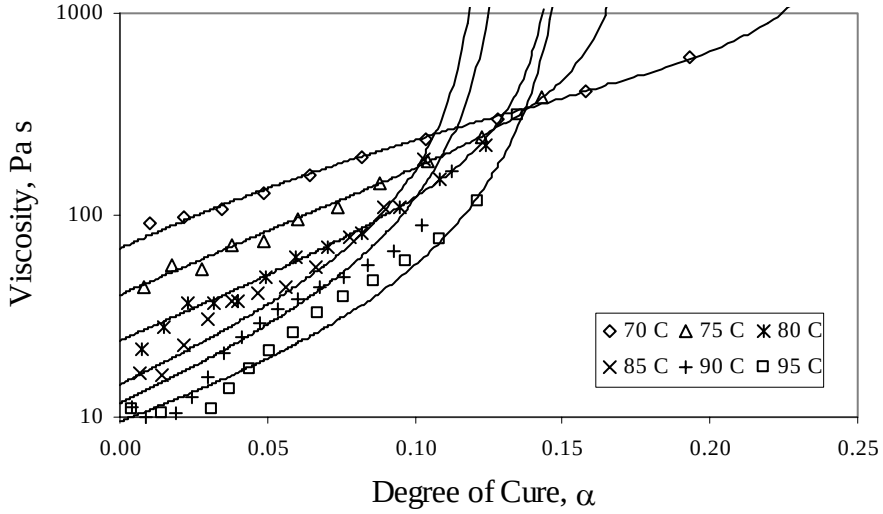

Figure A.10. Viscosity versus Time for all Individual Fits

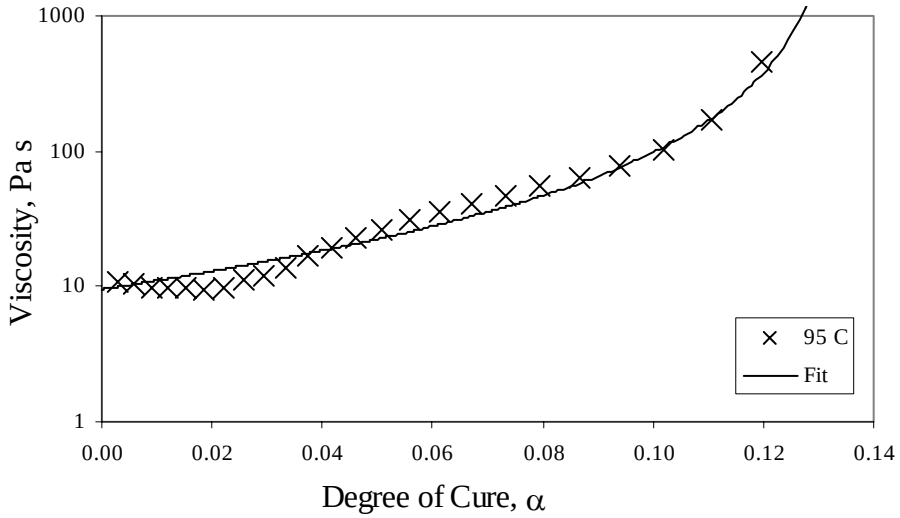

Figure A.11. Viscosity versus Degree of Cure for Individual Fit at 95°C

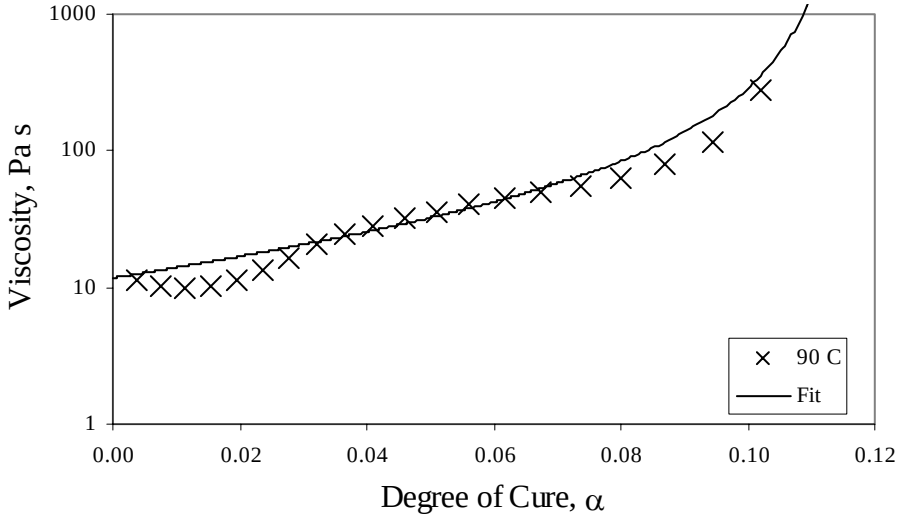

Figure A.12. Viscosity versus Degree of Cure for Individual Fit at 90°C

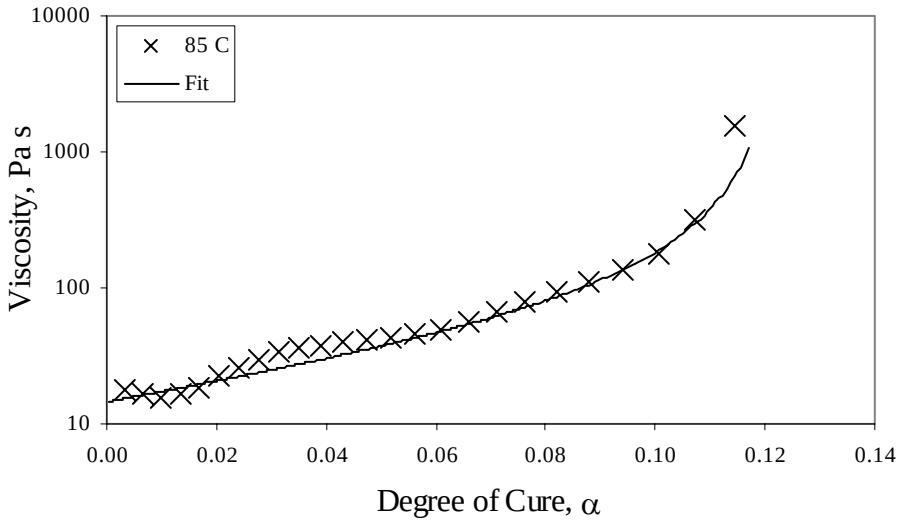

Figure A.13. Viscosity versus Degree of Cure for Individual Fit at 85°C

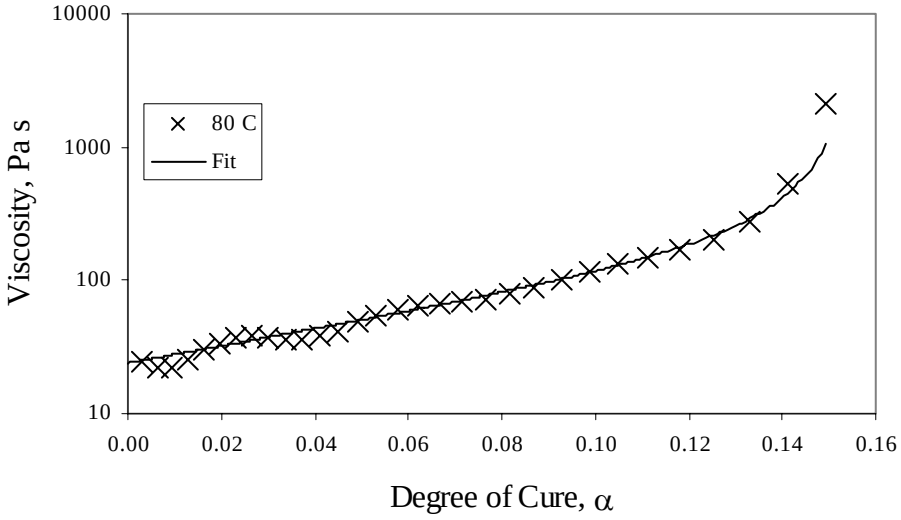

Figure A.14. Viscosity versus Degree of Cure for Individual Fit at 80°C

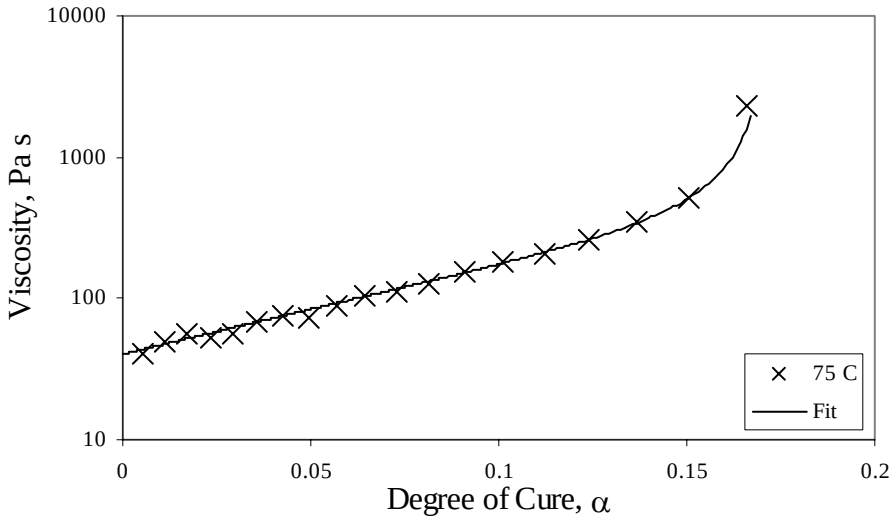

Figure A.15. Viscosity versus Degree of Cure for Individual Fit at 75°C

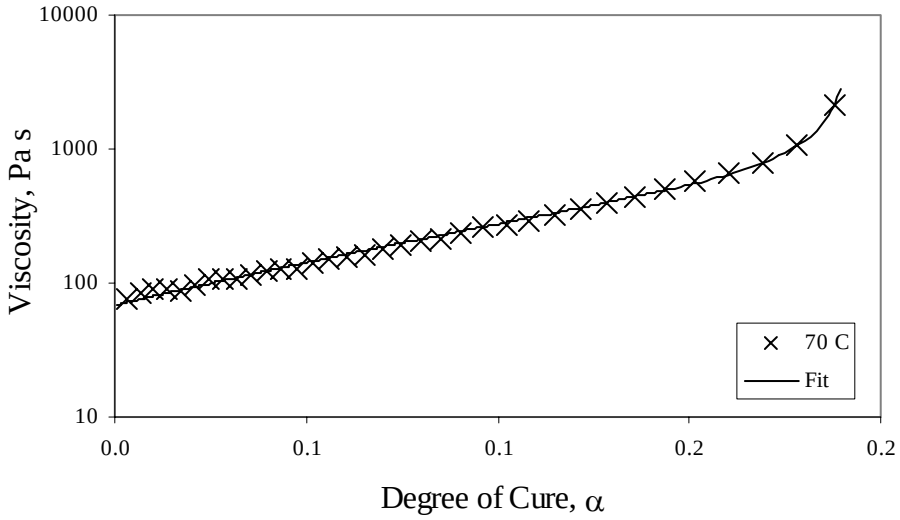

Figure A.16. Viscosity versus Degree of Cure for Individual Fit at 70°C

Appendix B

Experimental Data and Least Squares Fits for Kinetics Relation

Contained in this appendix are the data and fits at for each test conducted in the fitting process of the kinetics model, as detailed in Section 4.2. The data is presented in the following order: (1) Isothermal tests, overall fits. (2) Isothermal tests, individual fits. (3) Dynamic tests, overall fits. (4) Dynamic tests, individual fits. Each type of test describes the data being presented. Each stage of fitting, overall or individual, describes the type of fit being presented. For details on the types of tests, testing technique, fitting technique, or form of the model, refer to Section 4.1. It may be noted that R.O.C. is an abbreviation for Rate Of Cure and that D.O.C. is an abbreviation for Degree Of Cure.

Isothermal Tests, Overall Fits

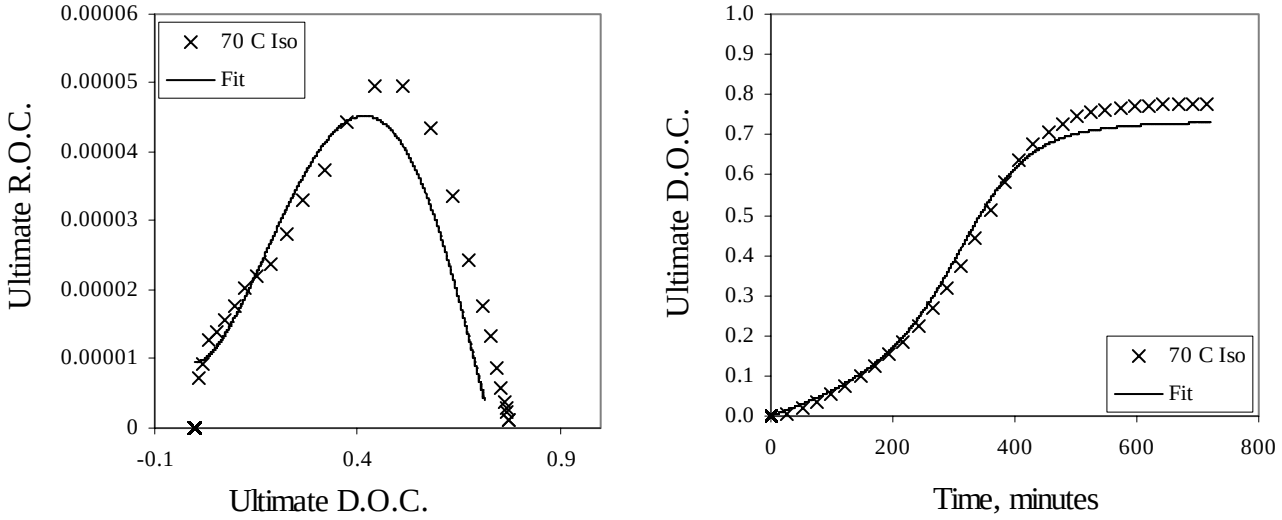

Figure B.1. Ultimate R.O.C. versus Ultimate D.O.C. and Ultimate D.O.C. versus time for 70°C Isothermal Test, Overall Fits

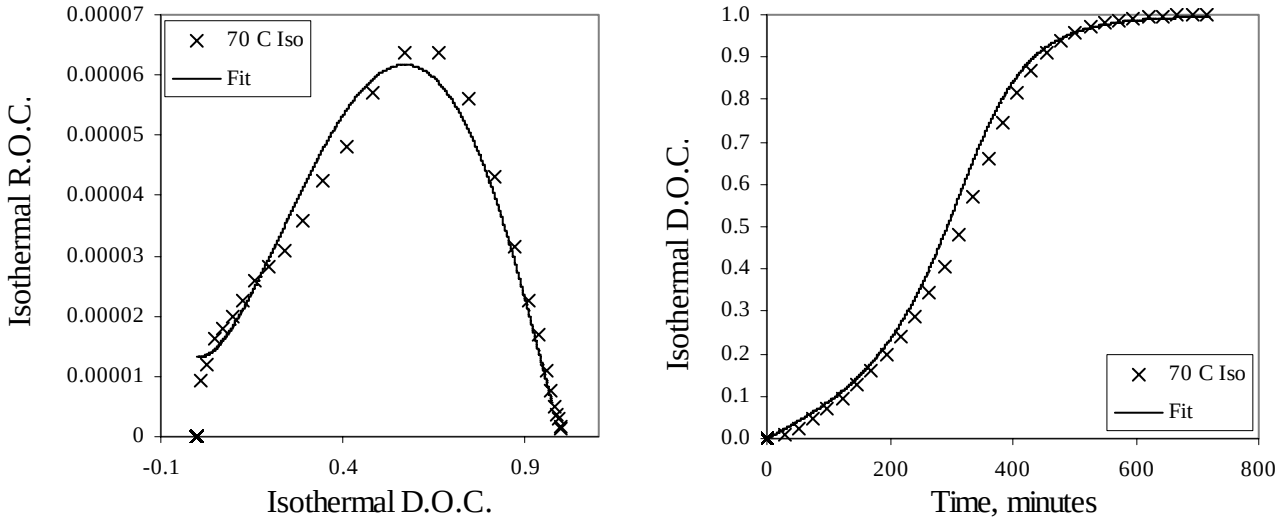

Figure B.2. Isothermal R.O.C. versus Isothermal D.O.C. and Isothermal D.O.C. versus time for 70°C Isothermal Test, Overall Fits

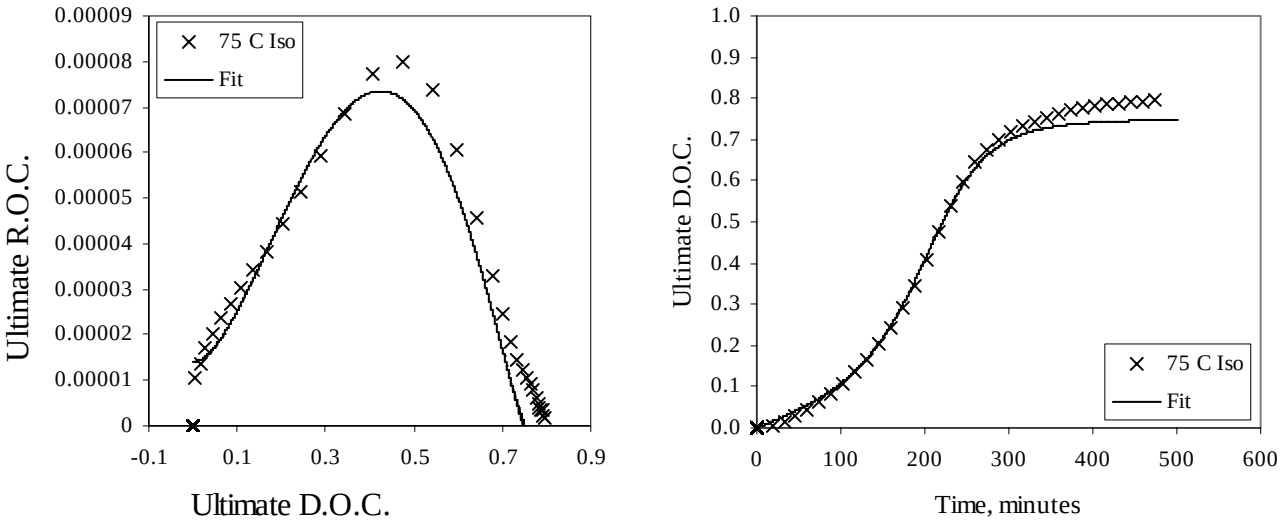

Figure B.3. Ultimate R.O.C. versus Ultimate D.O.C. and Ultimate D.O.C. versus time for 75°C Isothermal Test, Overall Fits

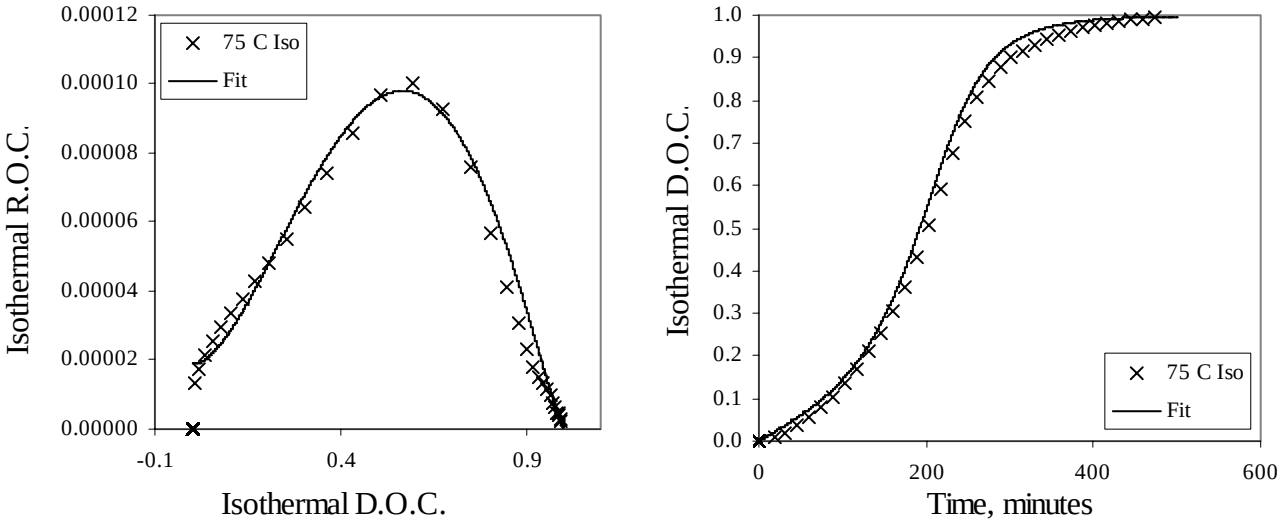

Figure B.4. Isothermal R.O.C. versus Isothermal D.O.C. and Isothermal D.O.C. versus time for 75°C Isothermal Test, Overall Fits

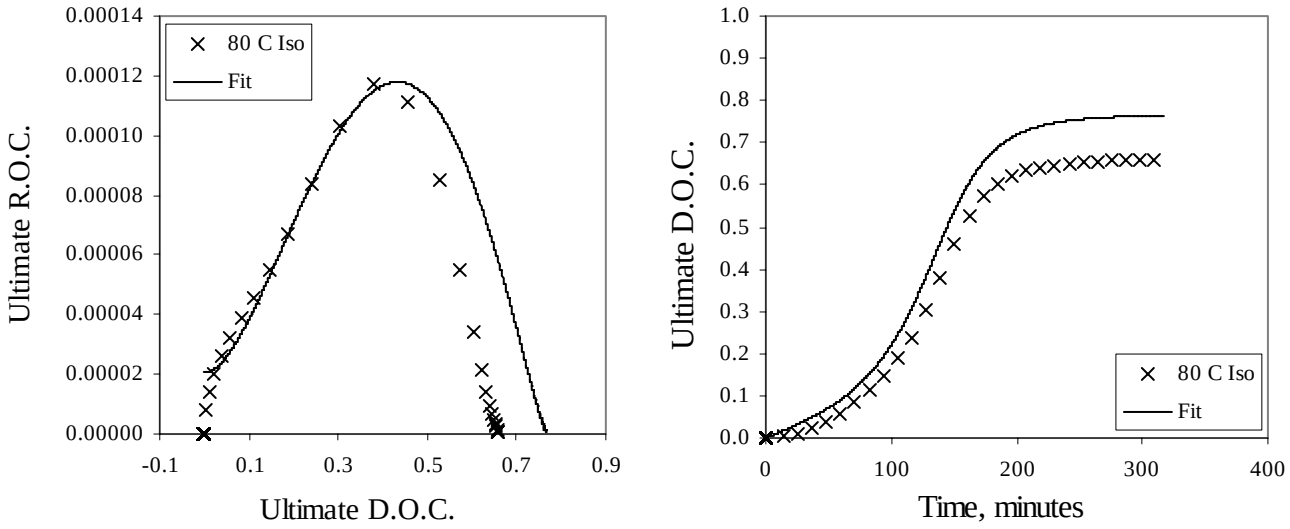

Figure B.5. Ultimate R.O.C. versus Ultimate D.O.C. and Ultimate D.O.C. versus time for 80°C Isothermal Test, Overall Fits

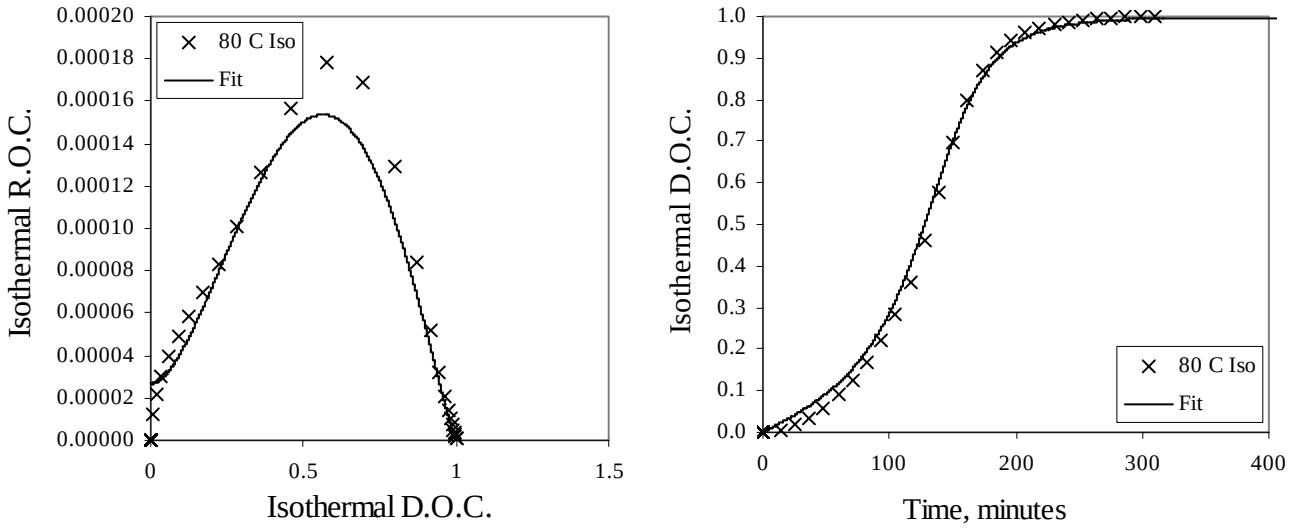

Figure B.6. Isothermal R.O.C. versus Isothermal D.O.C. and Isothermal D.O.C. versus time for 80°C Isothermal Test, Overall Fits

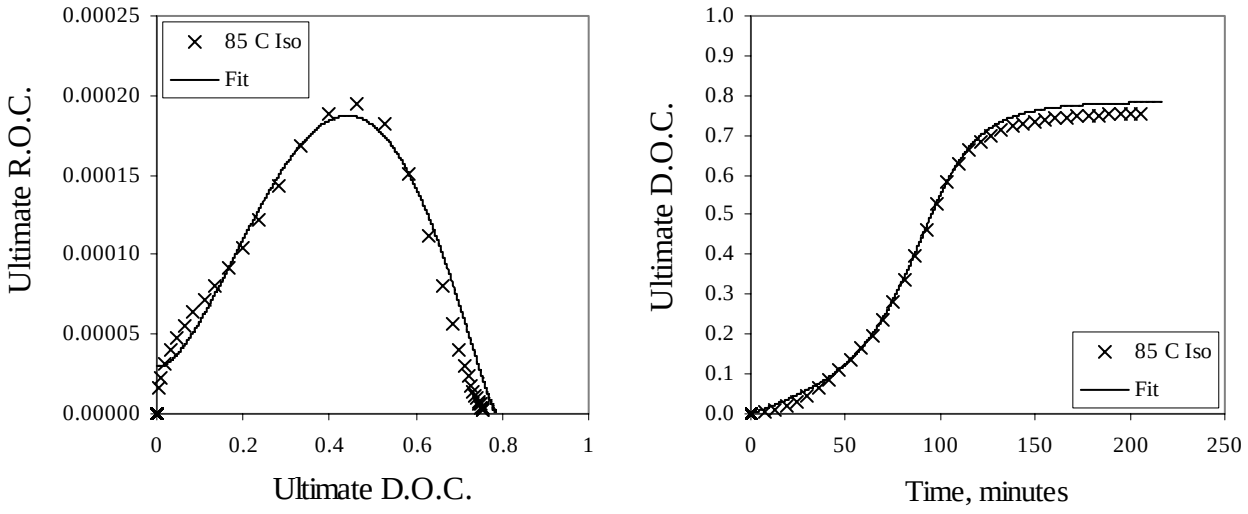

Figure B.7. Ultimate R.O.C. versus Ultimate D.O.C. and Ultimate D.O.C. versus time for 85°C Isothermal Test, Overall Fits

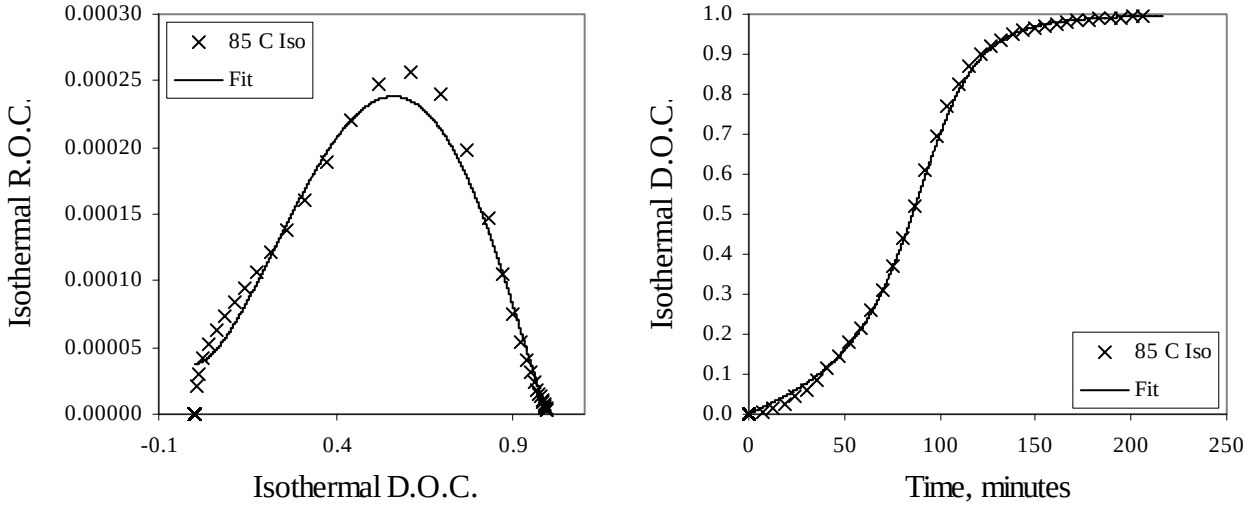

Figure B.8. Isothermal R.O.C. versus Isothermal D.O.C. and Isothermal D.O.C. versus time for 85°C Isothermal Test, Overall Fits

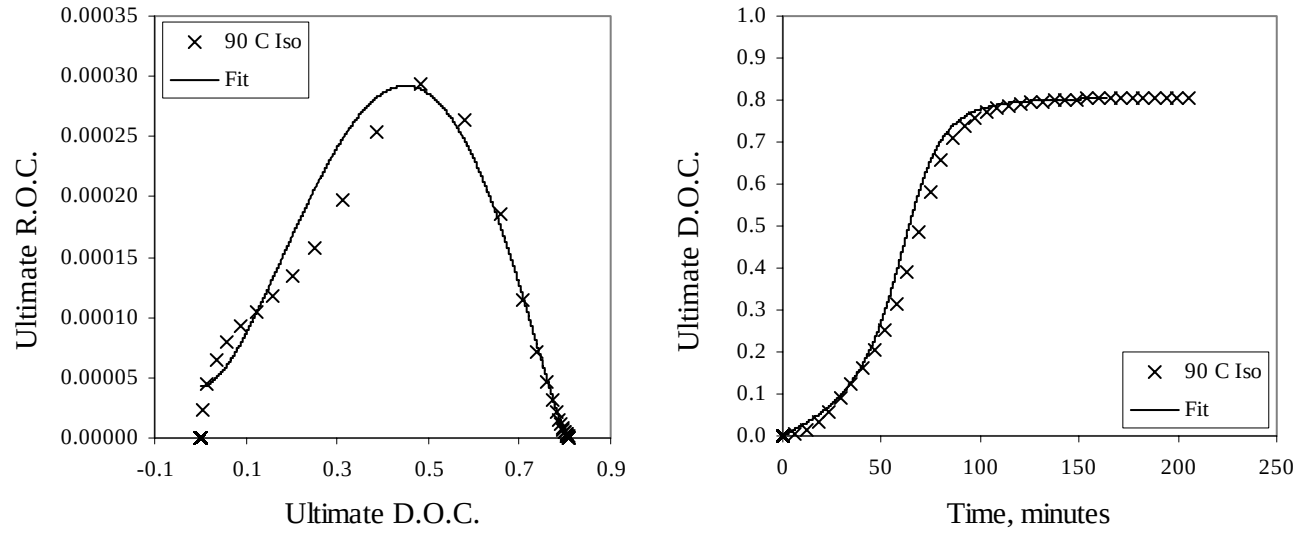

Figure B.9. Ultimate R.O.C. versus Ultimate D.O.C. and Ultimate D.O.C. versus time for 90°C Isothermal Test, Overall Fits

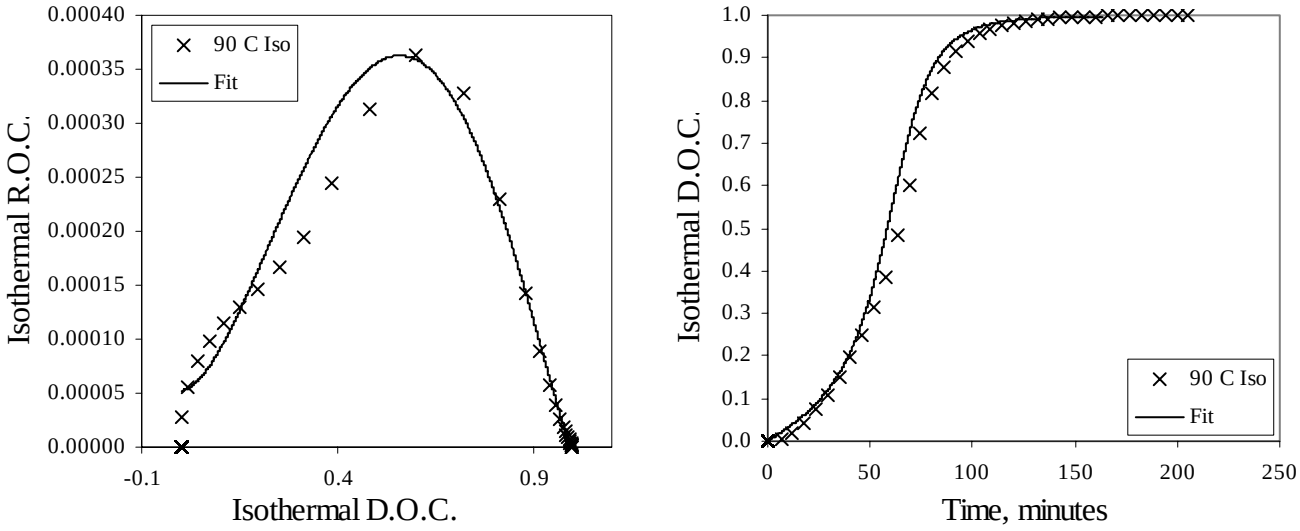

Figure B.10. Isothermal R.O.C. versus Isothermal D.O.C. and Isothermal D.O.C. versus time for 90°C Isothermal Test, Overall Fits

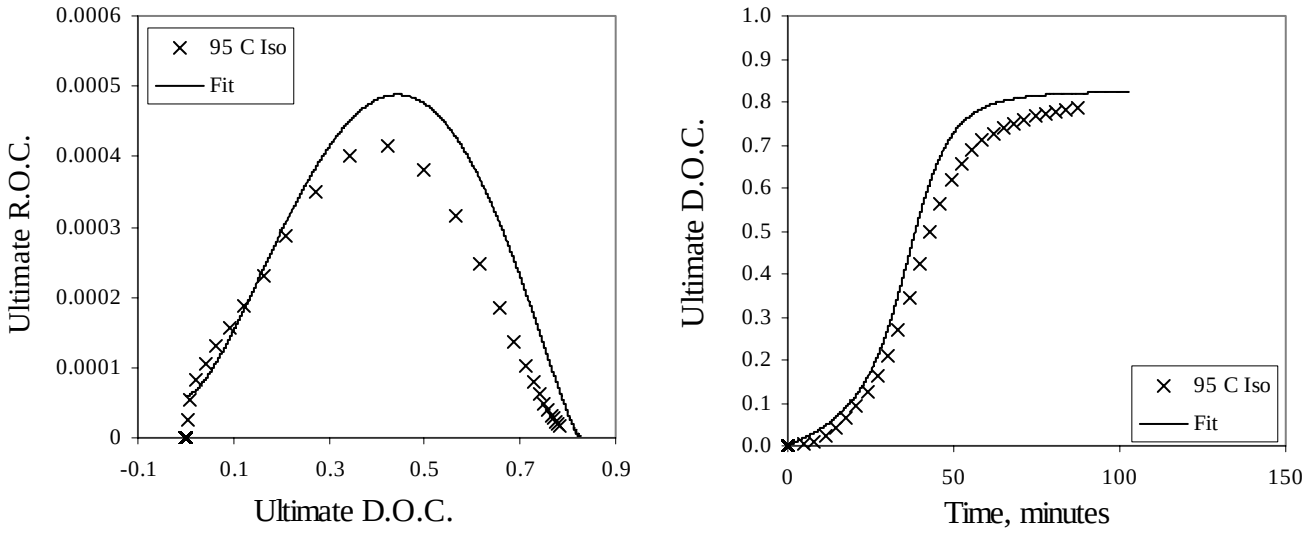

Figure B.11. Ultimate R.O.C. versus Ultimate D.O.C. and Ultimate D.O.C. versus time for 95°C Isothermal Test, Overall Fits

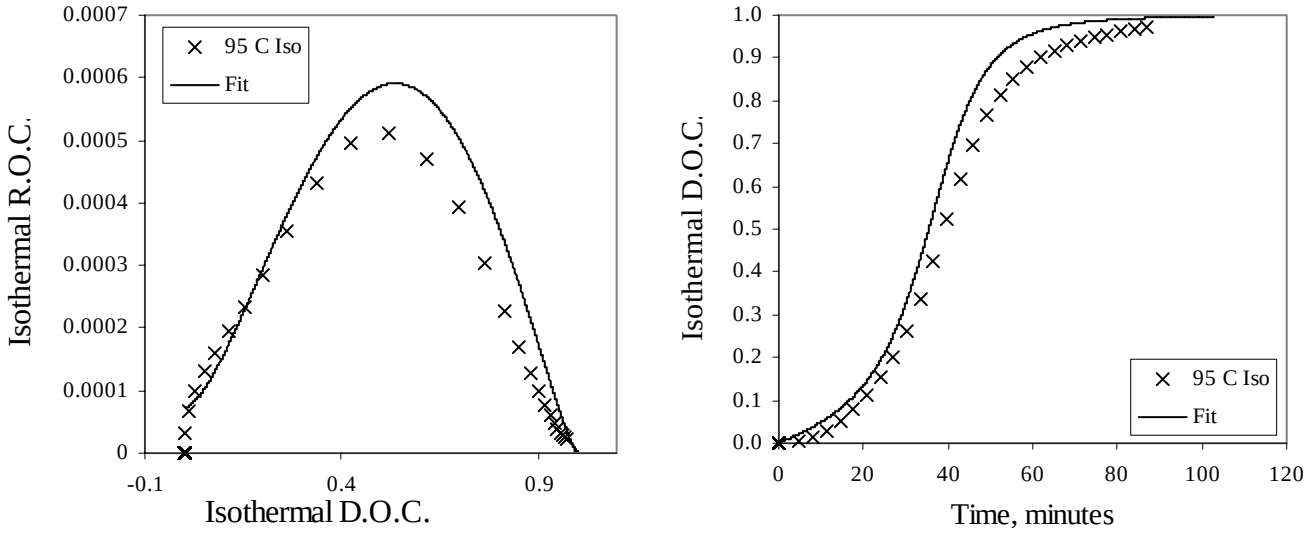

Figure B.12. Isothermal R.O.C. versus Isothermal D.O.C. and Isothermal D.O.C. versus time for 95°C Isothermal Test, Overall Fits

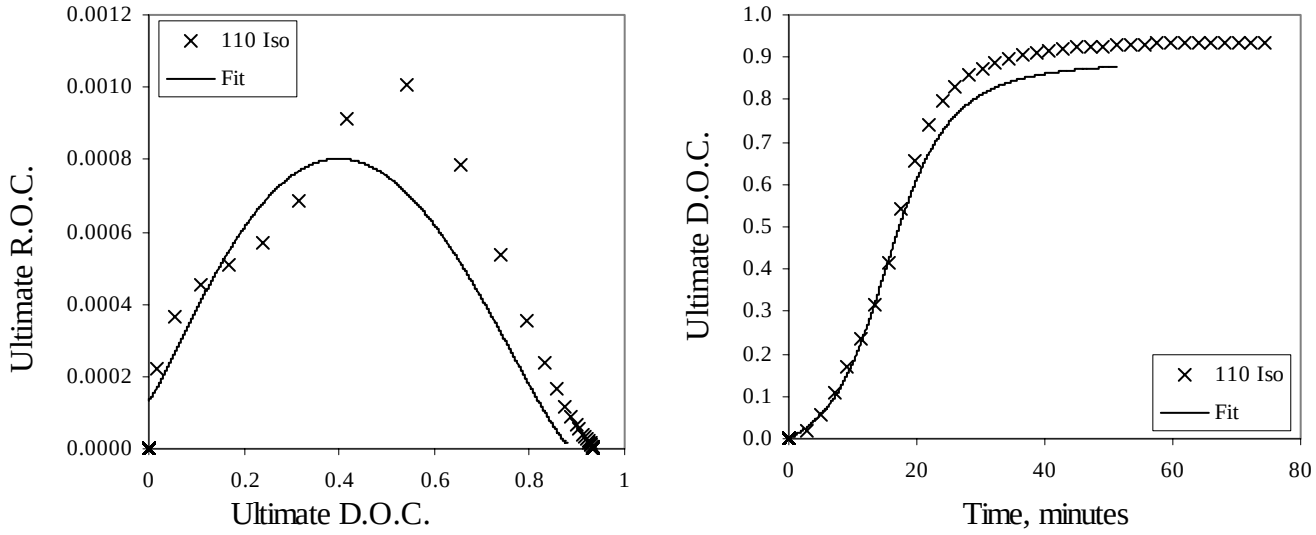

Figure B.13. Ultimate R.O.C. versus Ultimate D.O.C. and Ultimate D.O.C. versus time for 110°C Isothermal Test, Overall Fits

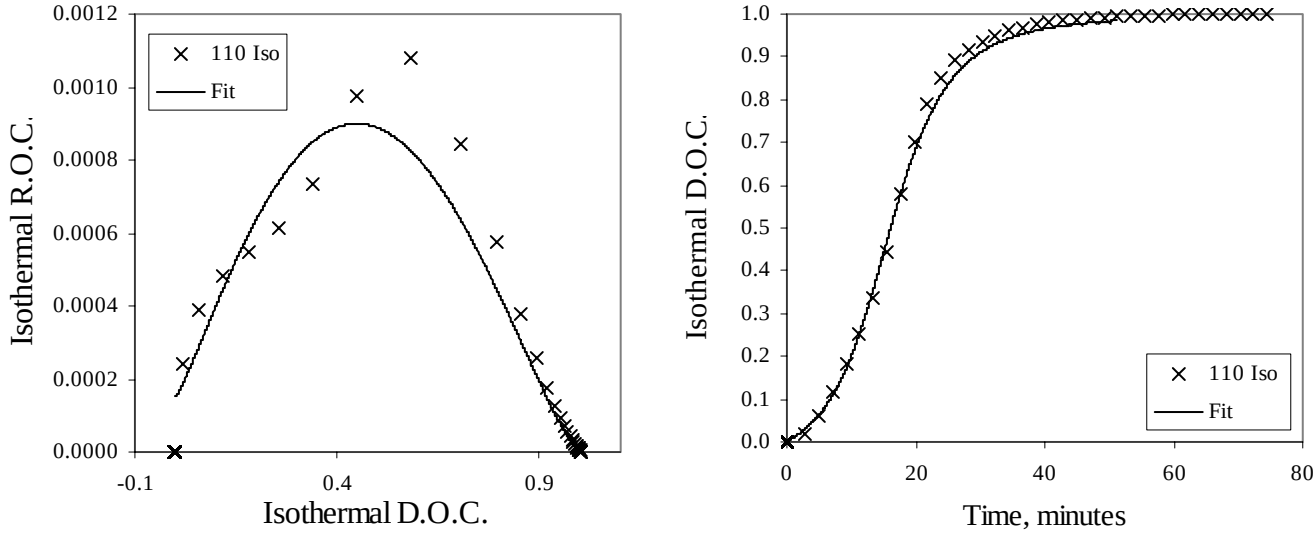

Figure B.14. Isothermal R.O.C. versus Isothermal D.O.C. and Isothermal D.O.C. versus time for 110°C Isothermal Test, Overall Fits

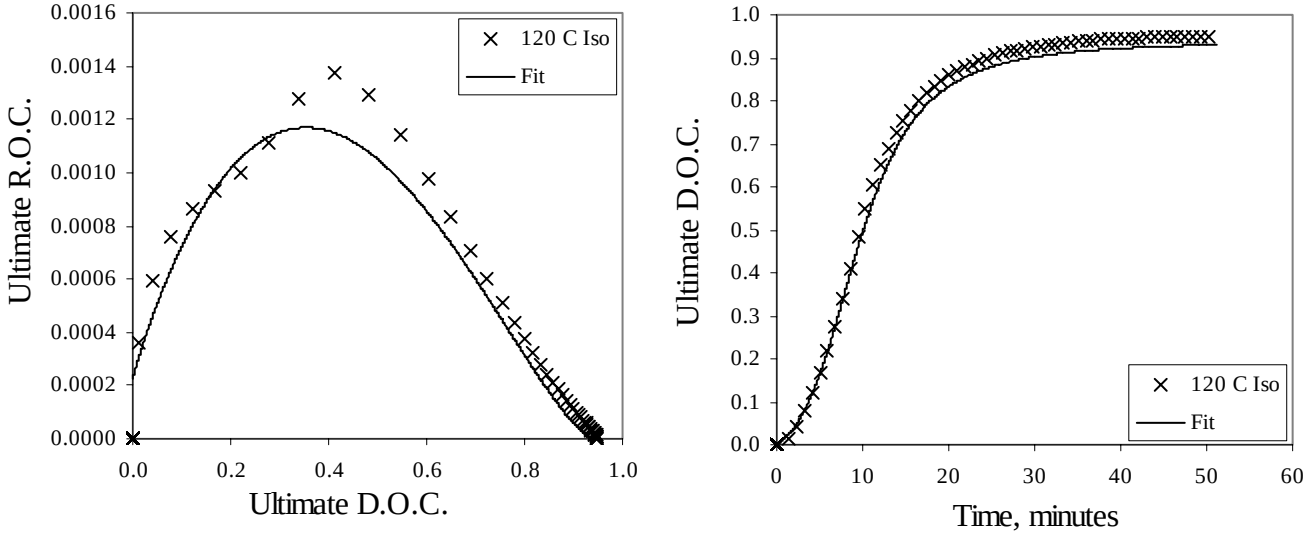

Figure B.15. Ultimate R.O.C. versus Ultimate D.O.C. and Ultimate D.O.C. versus time for 120°C Isothermal Test, Overall Fits

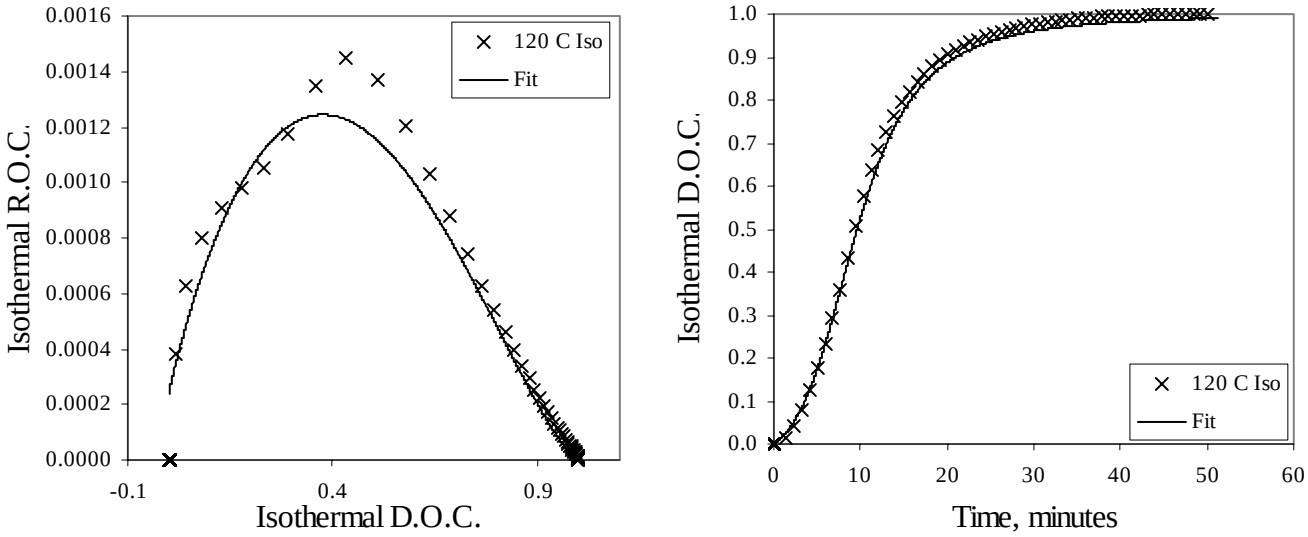

Figure B.16. Isothermal R.O.C. versus Isothermal D.O.C. and Isothermal D.O.C. versus time for 120°C Isothermal Test, Overall Fits

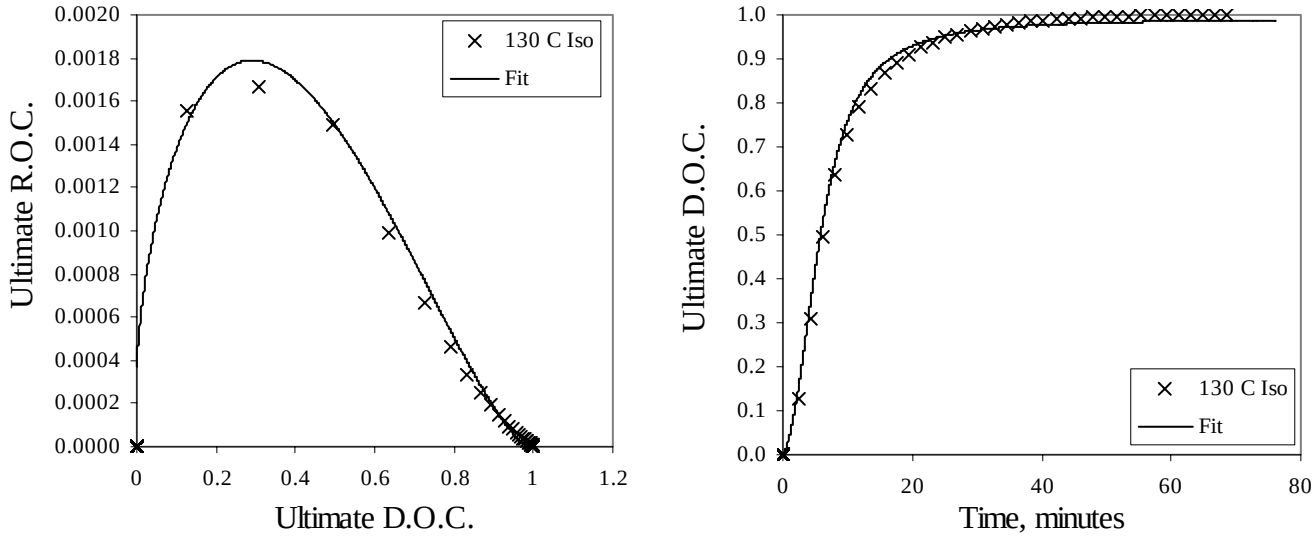

Figure B.17. Ultimate R.O.C. versus Ultimate D.O.C. and Ultimate D.O.C. versus time for 130°C Isothermal Test, Overall Fits

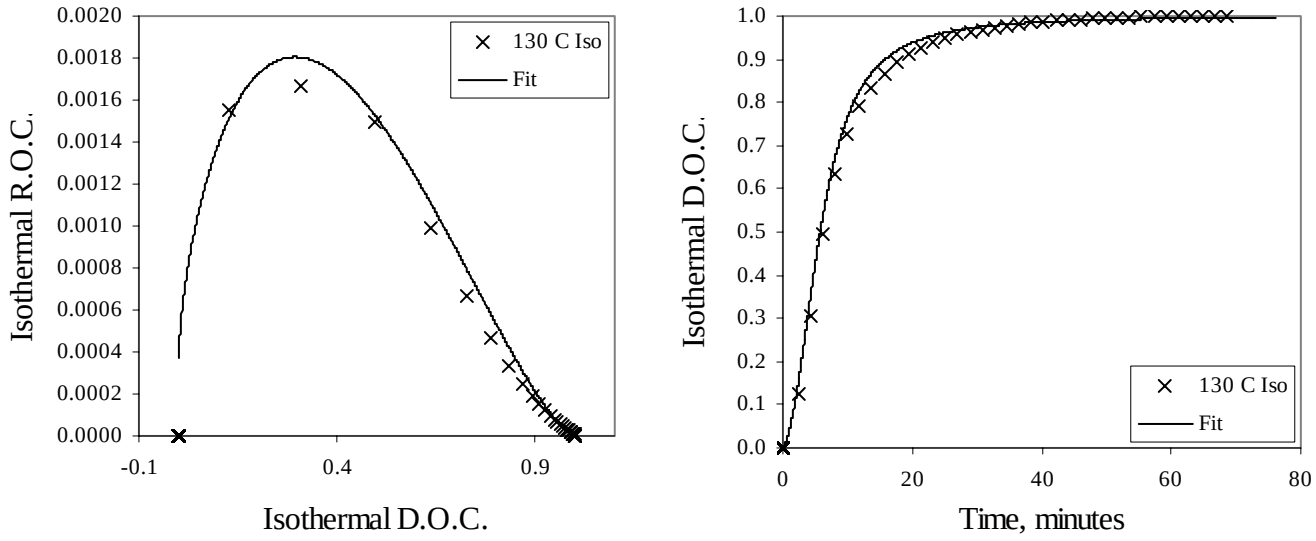

Figure B.18. Isothermal R.O.C. versus Isothermal D.O.C. and Isothermal D.O.C. versus time for 130°C Isothermal Test, Overall Fits

Isothermal Tests, Individual Fits

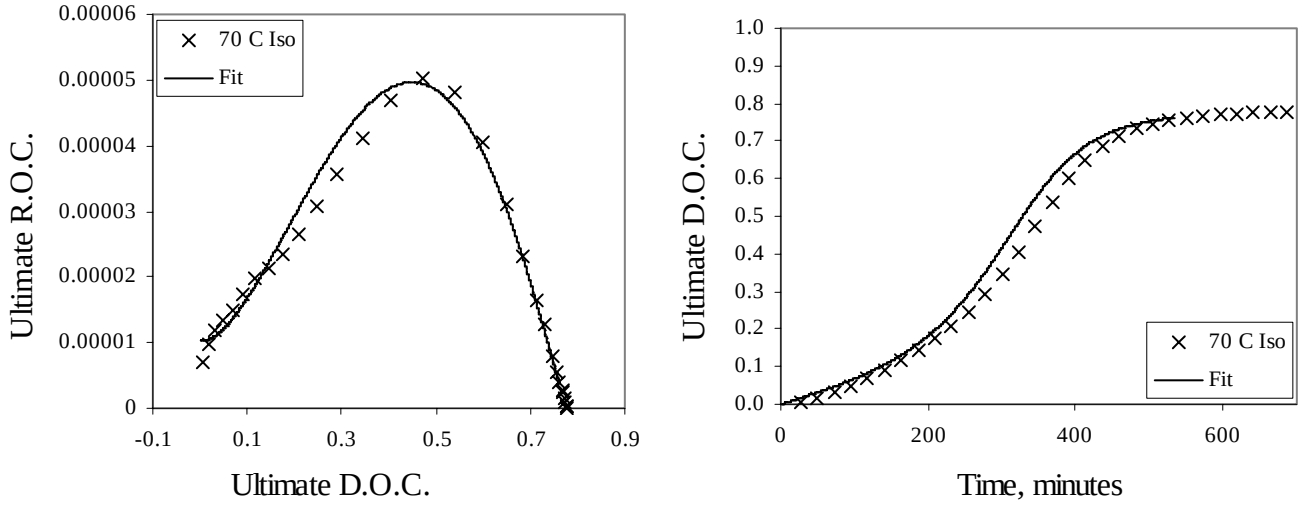

Figure B.19. Ultimate R.O.C. versus Ultimate D.O.C. and Ultimate D.O.C. versus time for 70°C Isothermal Test, Individual Fits

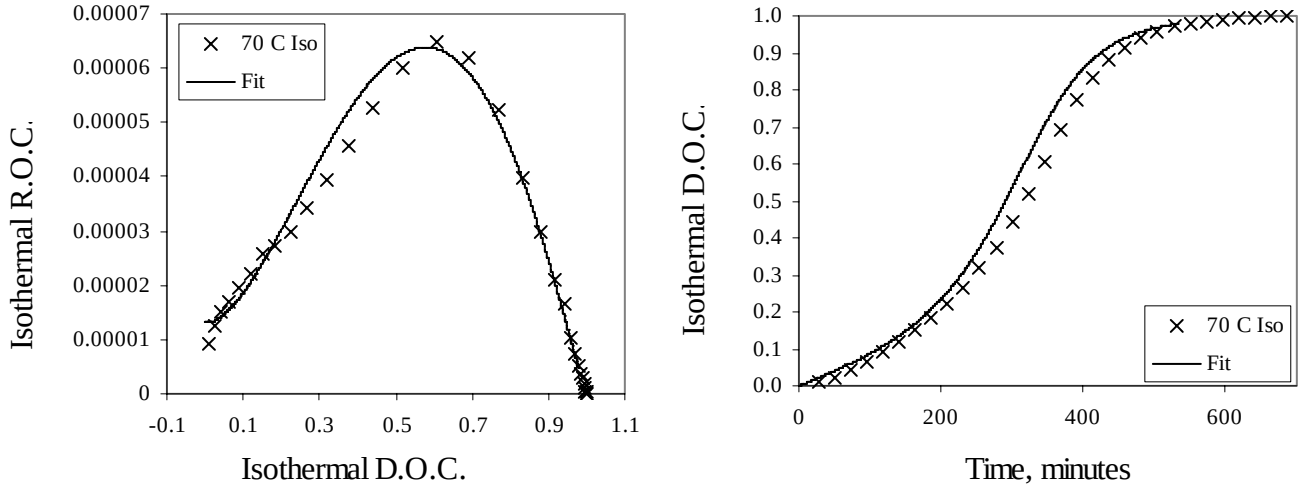

Figure B.20. Isothermal R.O.C. versus Isothermal D.O.C. and Isothermal D.O.C. versus time for 70°C Isothermal Test, Individual Fits

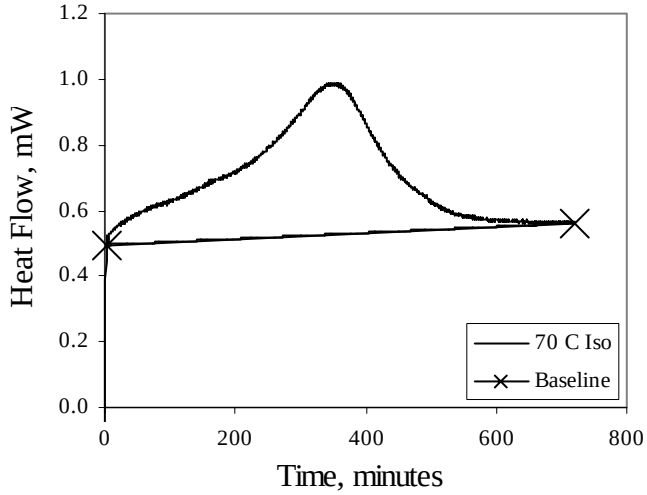

Figure B.21. Heat Flow versus Time for 70°C Isothermal Test

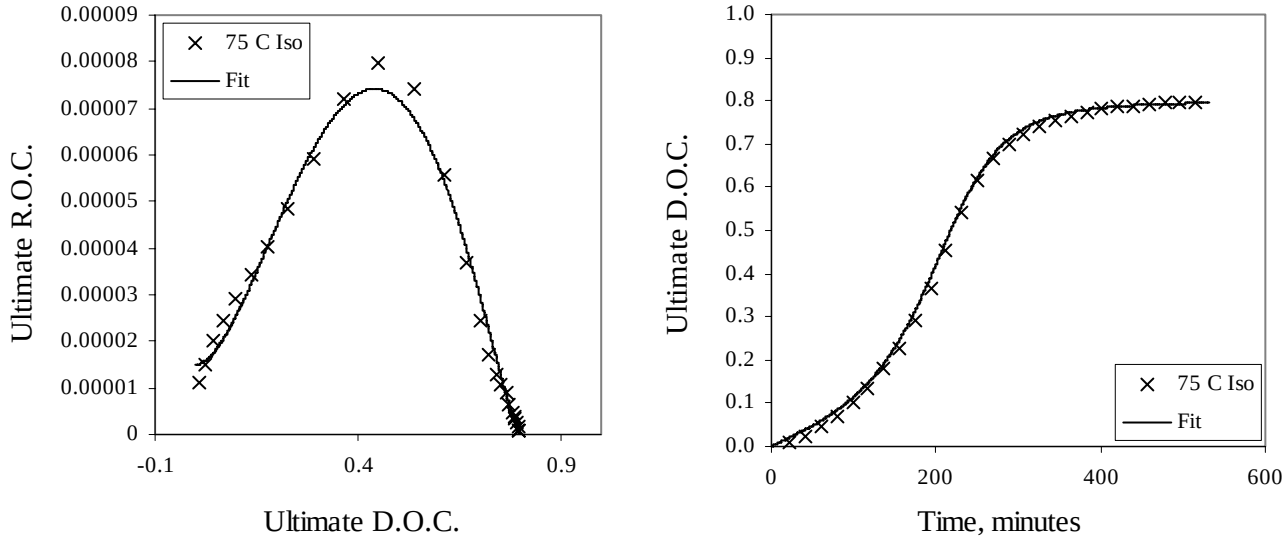

Figure B.22. Ultimate R.O.C. versus Ultimate D.O.C. and Ultimate D.O.C. versus time for 75°C Isothermal Test, Individual Fits

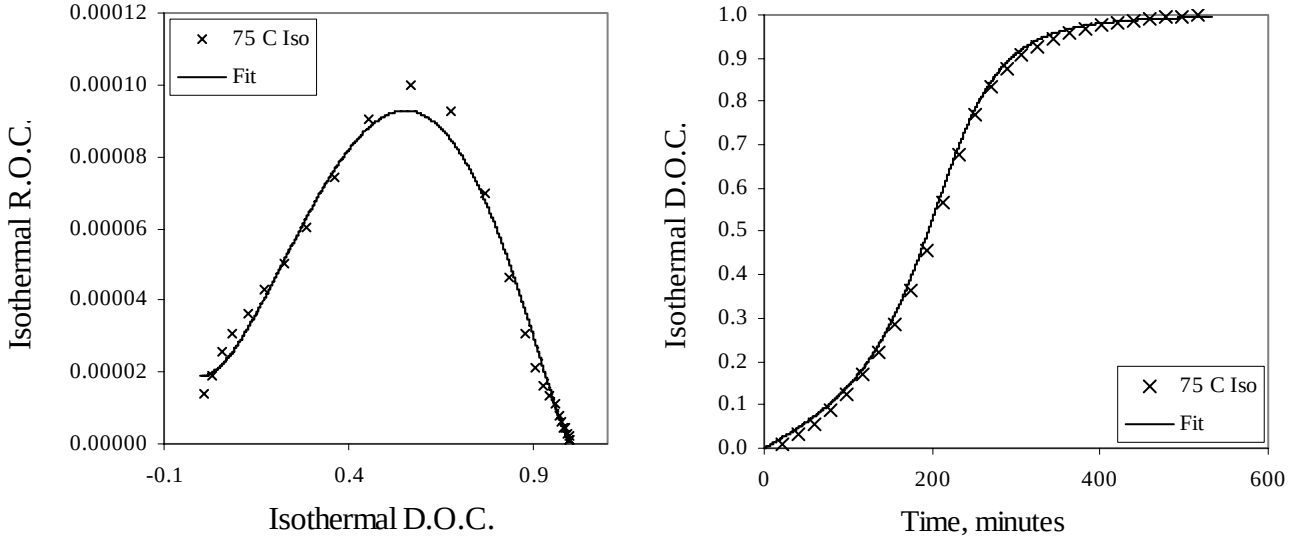

Figure B.23. Isothermal R.O.C. versus Isothermal D.O.C. and Isothermal D.O.C. versus time for 75°C Isothermal Test, Individual Fits

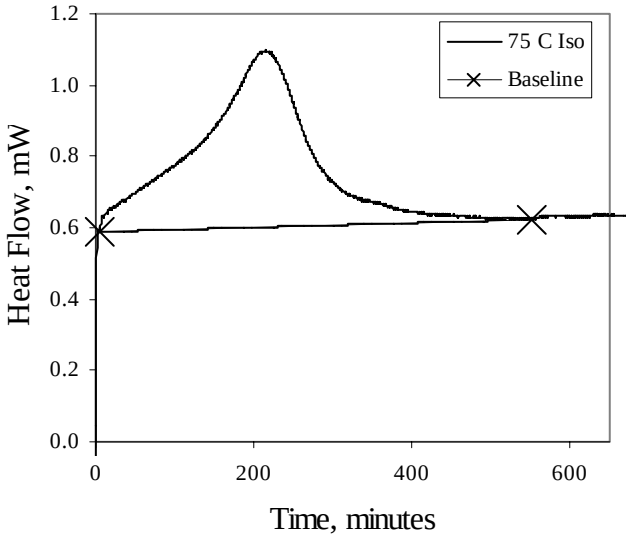

Figure B.24. Heat Flow versus Time for 75°C Isothermal Test

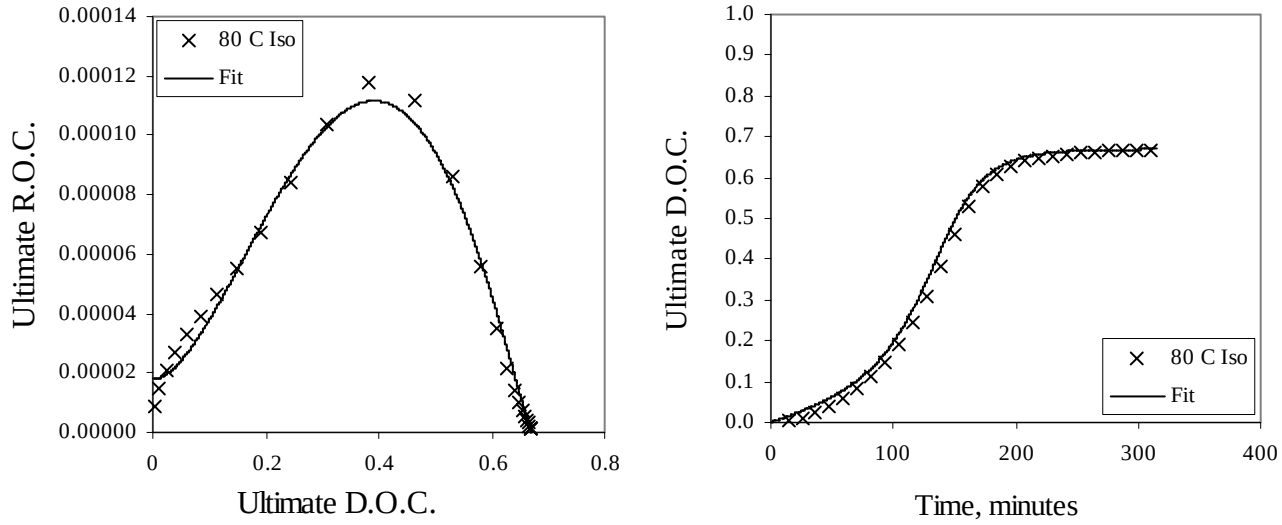

Figure B.25. Ultimate R.O.C. versus Ultimate D.O.C. and Ultimate D.O.C. versus time for 80°C Isothermal Test, Individual Fits

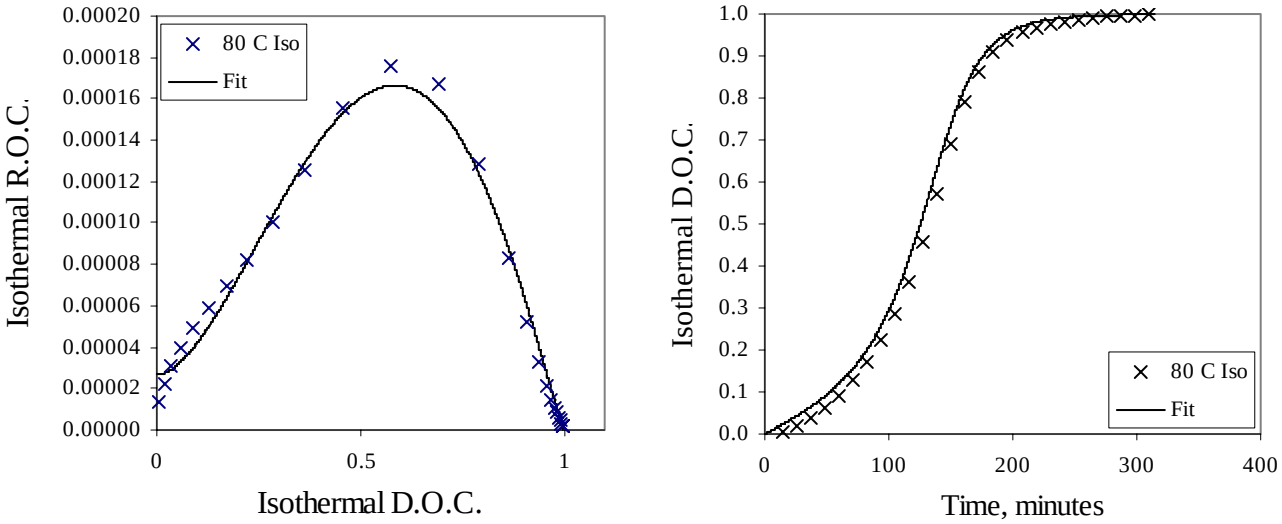

Figure B.26. Isothermal R.O.C. versus Isothermal D.O.C. and Isothermal D.O.C. versus time for 80°C Isothermal Test, Individual Fits

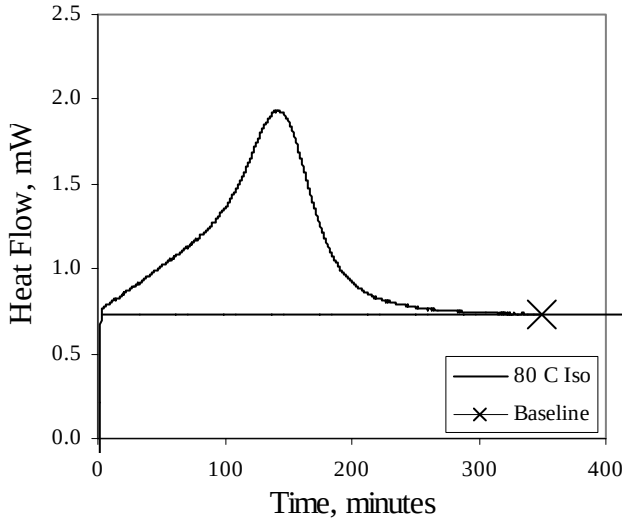

Figure B.27. Heat Flow versus Time for 80°C Isothermal Test

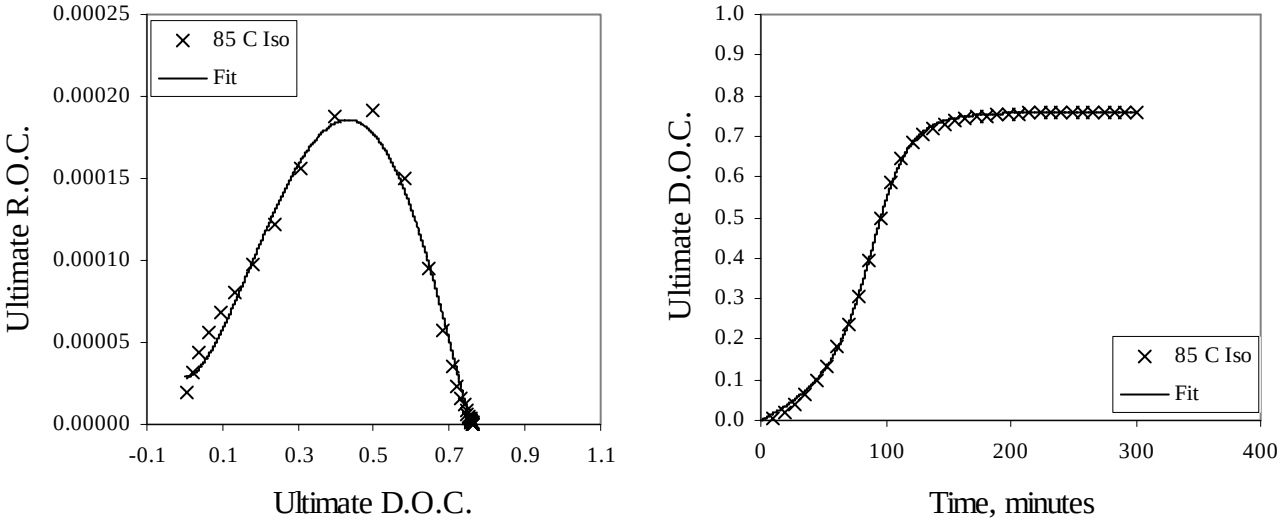

Figure B.28. Ultimate R.O.C. versus Ultimate D.O.C. and Ultimate D.O.C. versus time for 85°C Isothermal Test, Individual Fits

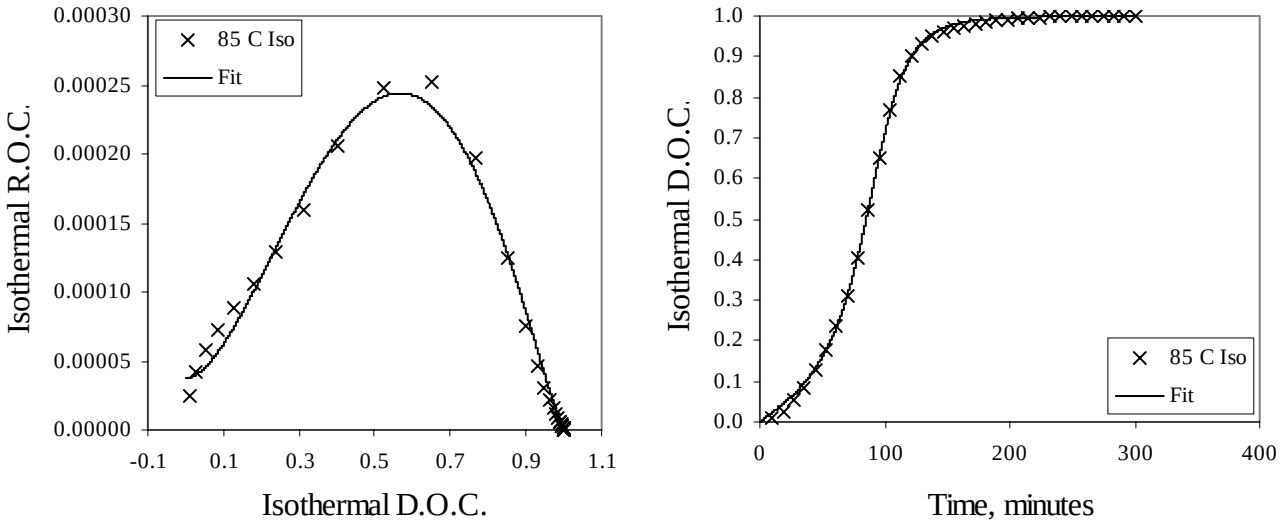

Figure B.29. Isothermal R.O.C. versus Isothermal D.O.C. and Isothermal D.O.C. versus time for 85°C Isothermal Test, Individual Fits

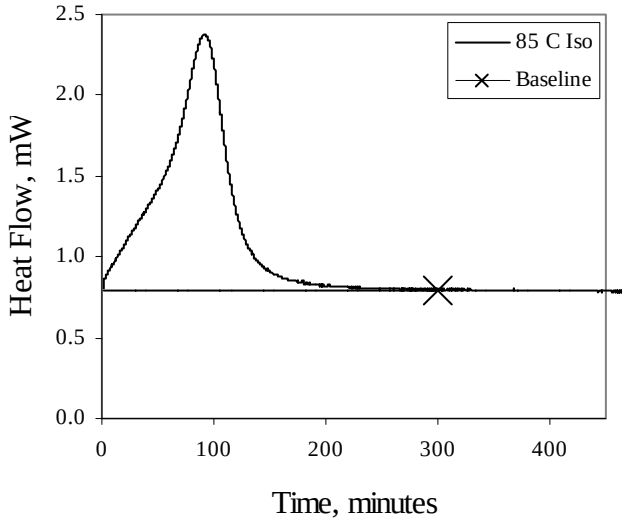

Figure B.30. Heat Flow versus Time for 85°C Isothermal Test

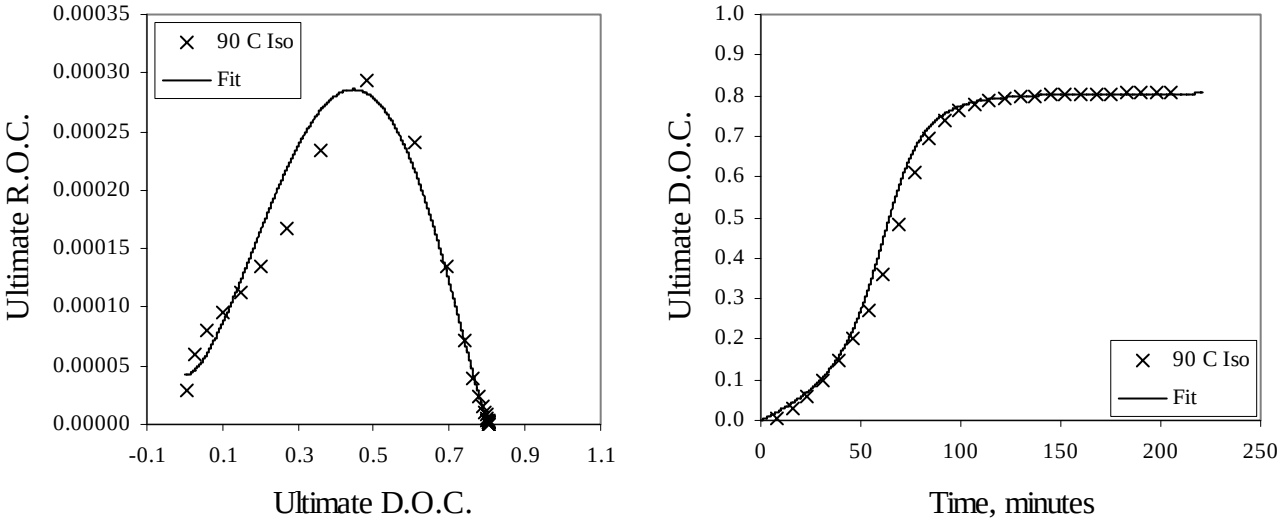

Figure B.31. Ultimate R.O.C. versus Ultimate D.O.C. and Ultimate D.O.C. versus time for 90°C Isothermal Test, Individual Fits

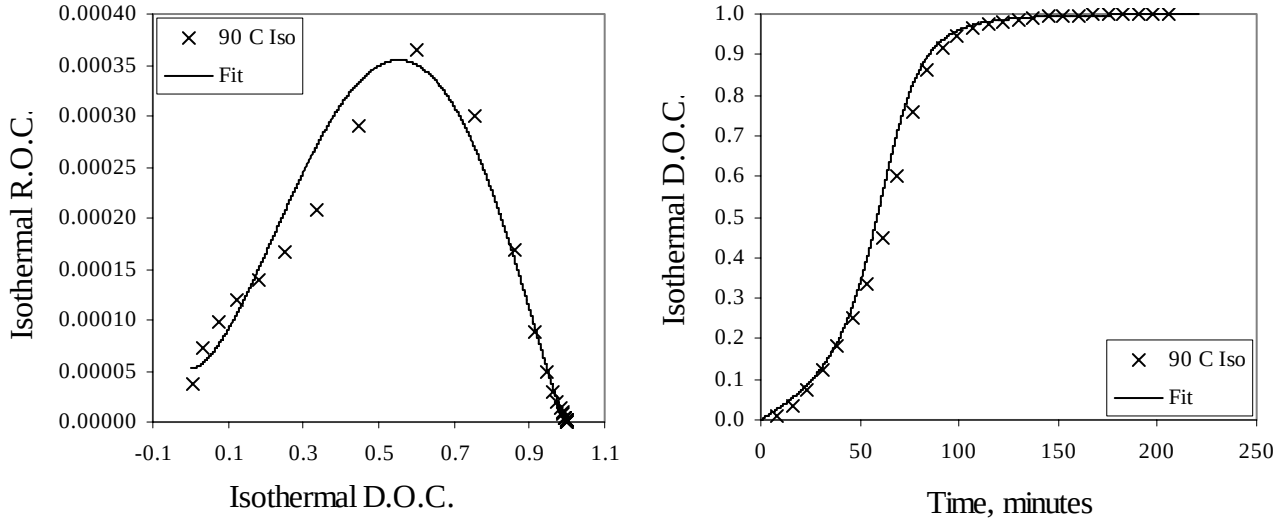

Figure B.32. Isothermal R.O.C. versus Isothermal D.O.C. and Isothermal D.O.C. versus time for 90°C Isothermal Test, Individual Fits

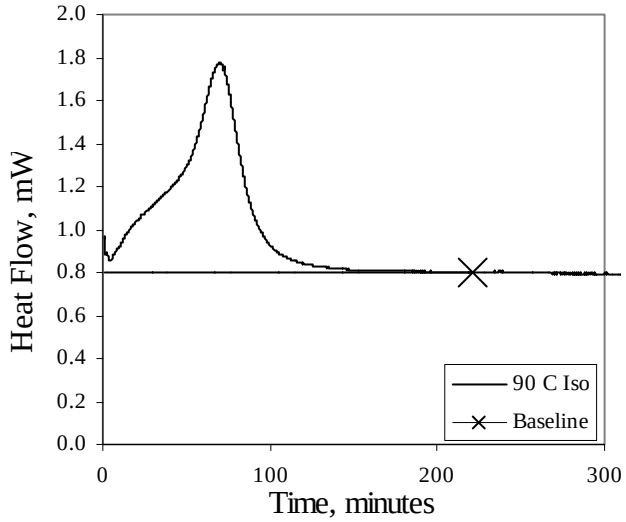

Figure B.33. Heat Flow versus Time for 90°C Isothermal Test

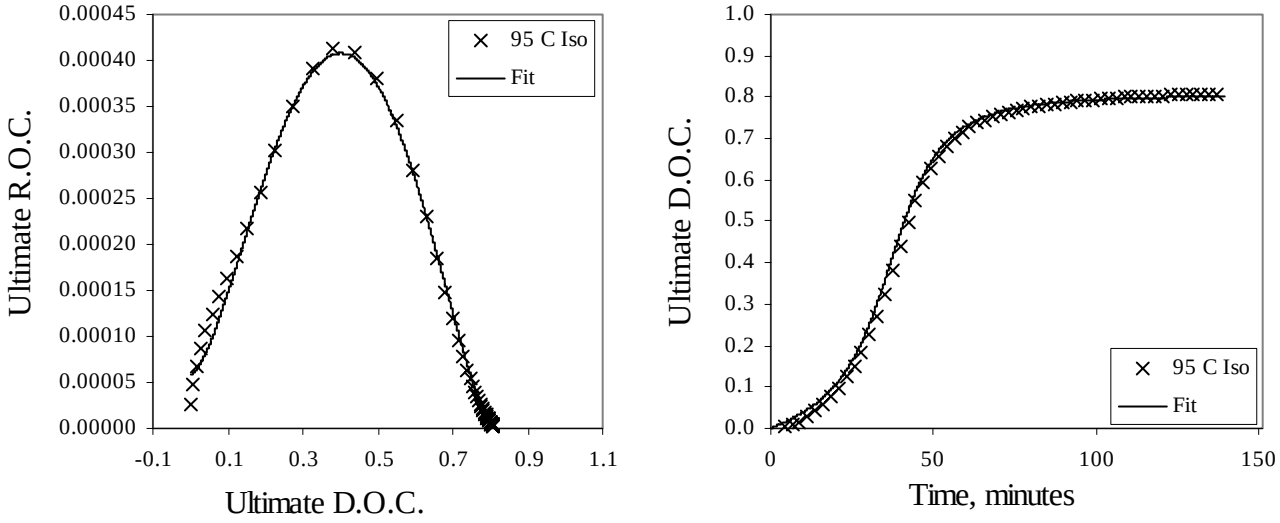

Figure B.34. Ultimate R.O.C. versus Ultimate D.O.C. and Ultimate D.O.C. versus time for 95°C Isothermal Test, Individual Fits

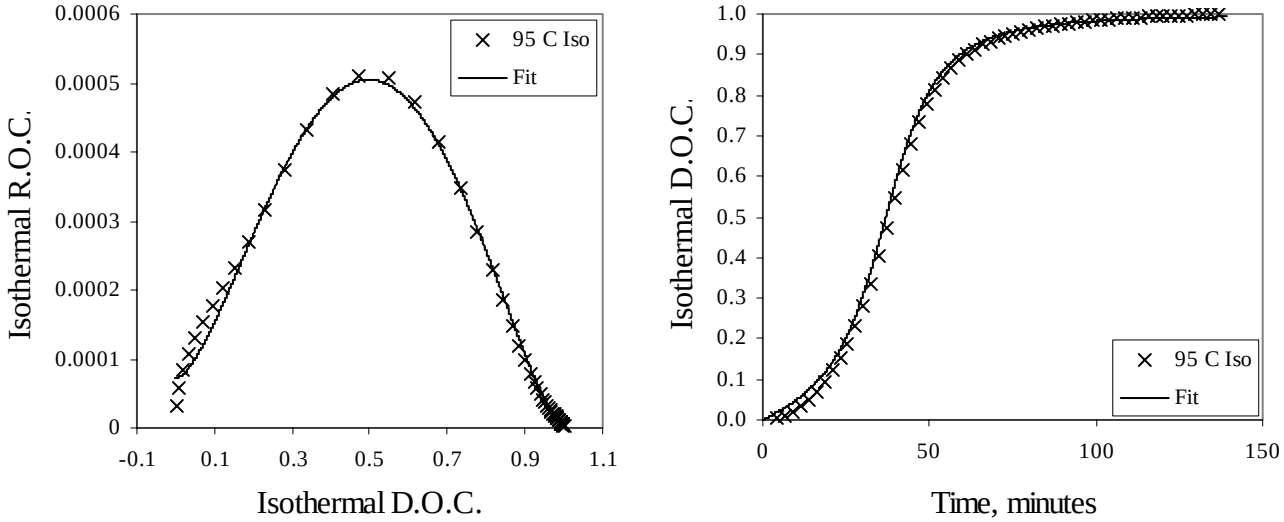

Figure B.35. Isothermal R.O.C. versus Isothermal D.O.C. and Isothermal D.O.C. versus time for 95°C Isothermal Test, Individual Fits

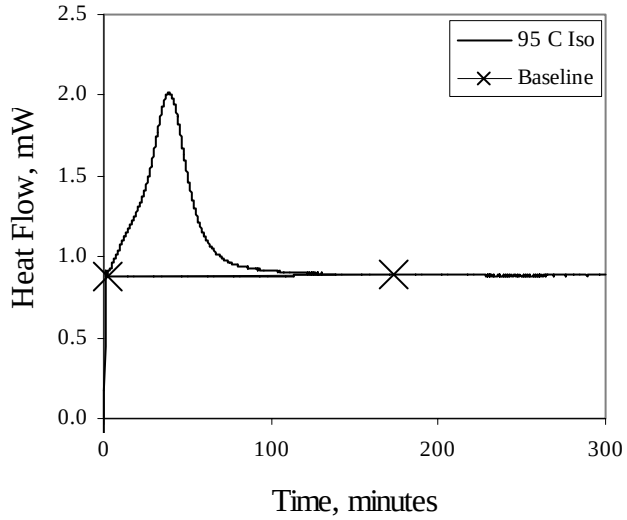

Figure B.36. Heat Flow versus Time for 95°C Isothermal Test

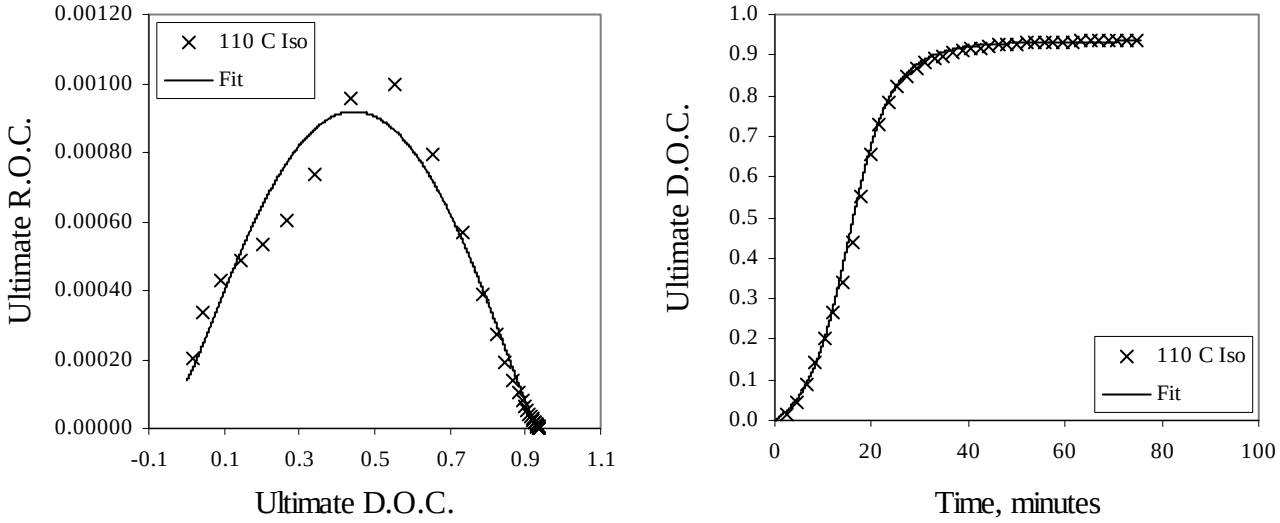

Figure B.37. Ultimate R.O.C. versus Ultimate D.O.C. and Ultimate D.O.C. versus time for 110°C Isothermal Test, Individual Fits

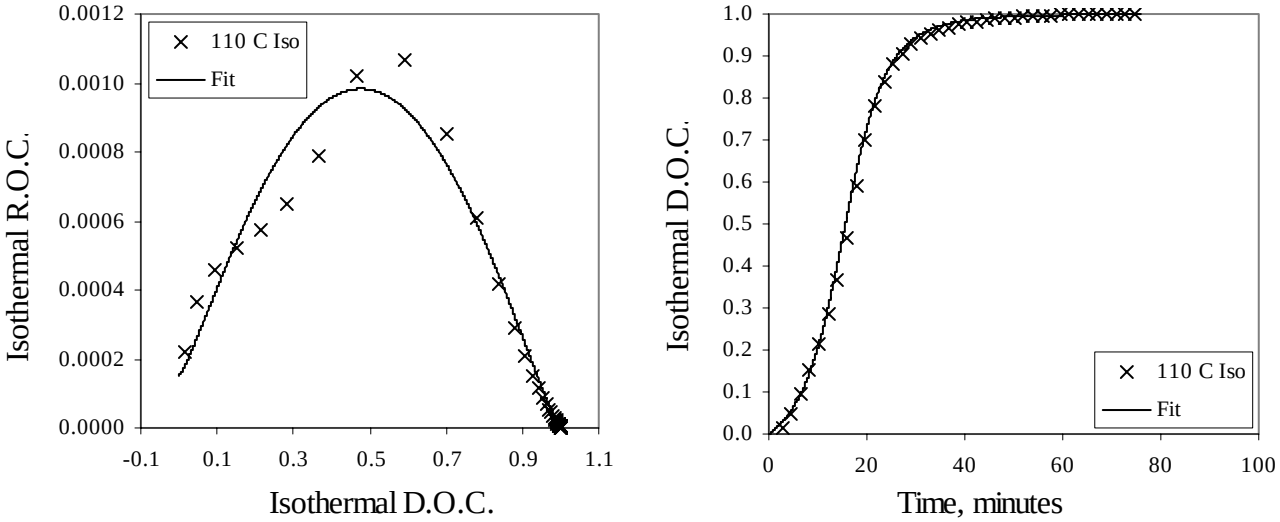

Figure B.38. Isothermal R.O.C. versus Isothermal D.O.C. and Isothermal D.O.C. versus time for 110°C Isothermal Test, Individual Fits

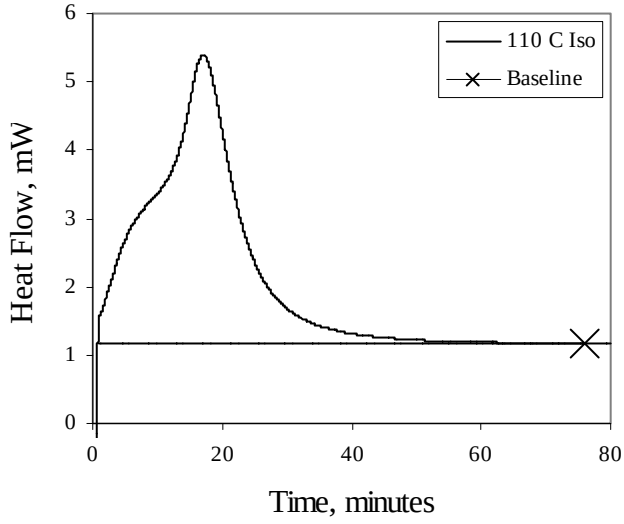

Figure B.39. Heat Flow versus Time for 110°C Isothermal Test

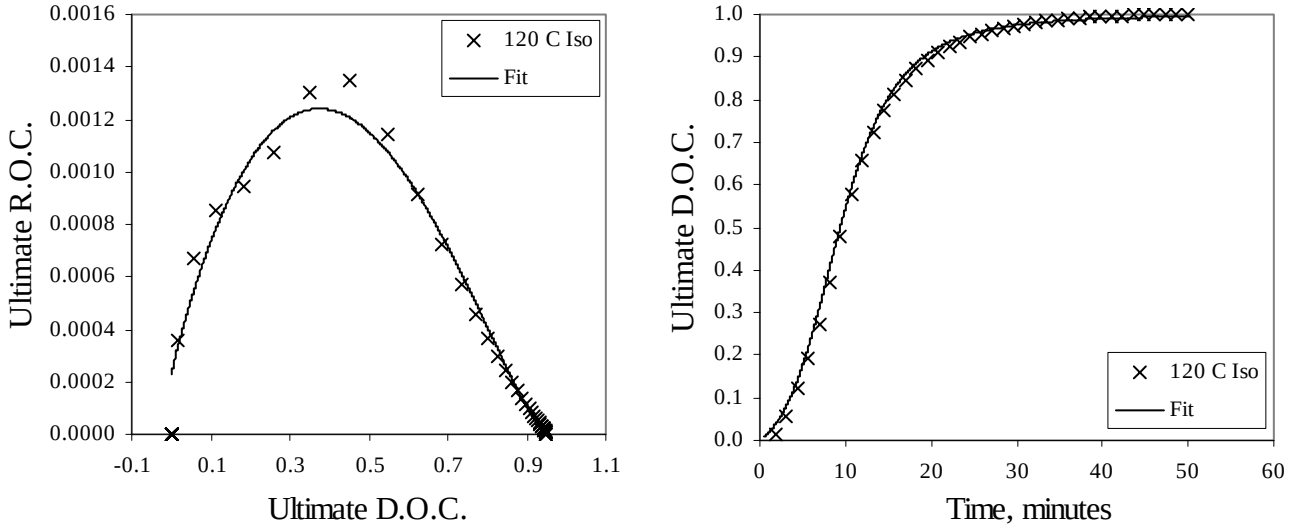

Figure B.40. Ultimate R.O.C. versus Ultimate D.O.C. and Ultimate D.O.C. versus time for 120°C Isothermal Test, Individual Fits

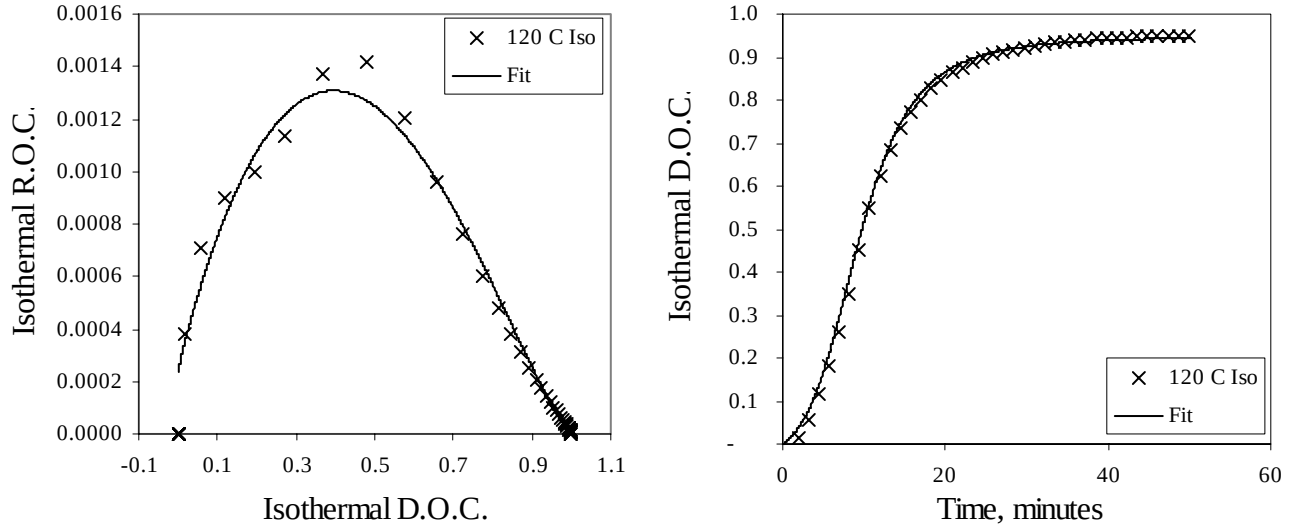

Figure B.41. Isothermal R.O.C. versus Isothermal D.O.C. and Isothermal D.O.C. versus time for 120°C Isothermal Test, Individual Fits

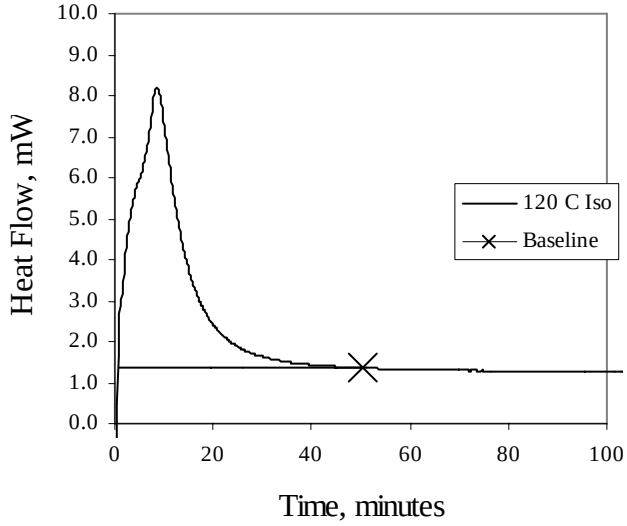

Figure B.42. Heat Flow versus Time for 120°C Isothermal Test

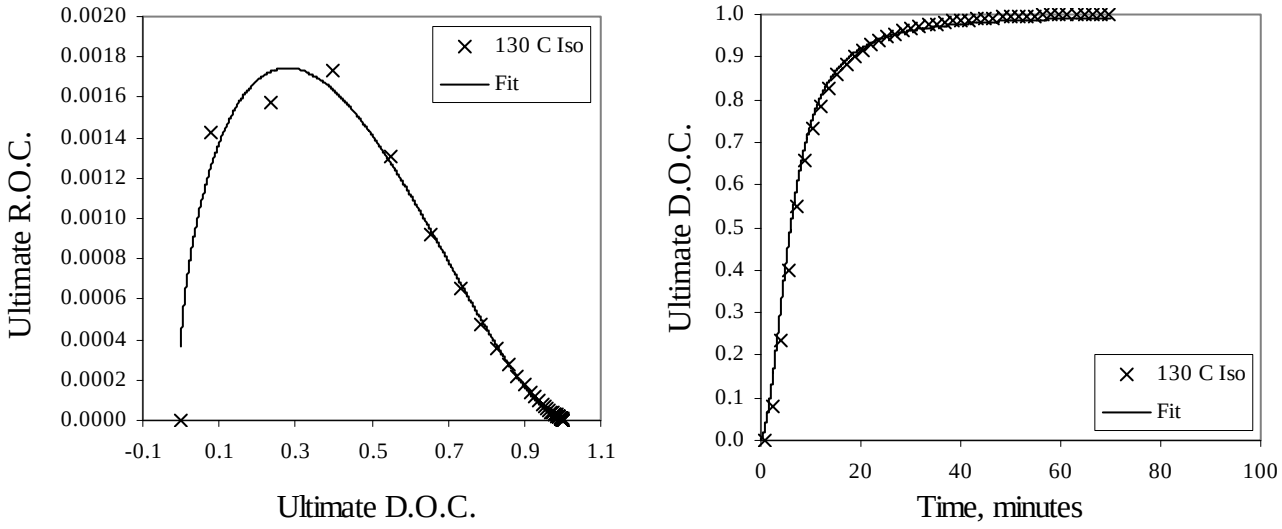

Figure B.43. Ultimate R.O.C. versus Ultimate D.O.C. and Ultimate D.O.C. versus time for 130°C Isothermal Test, Individual Fits

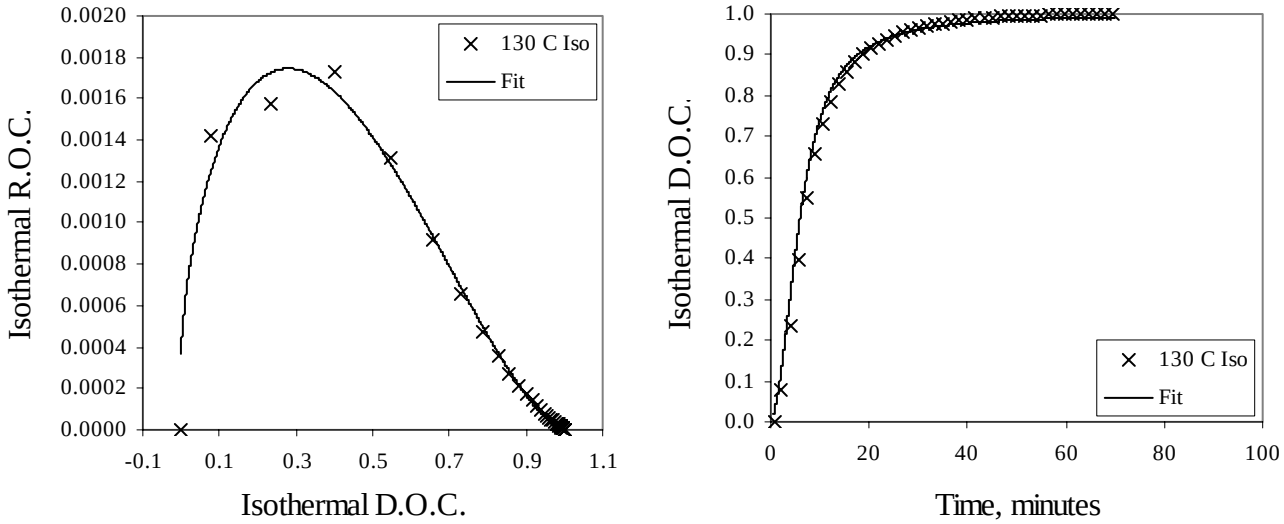

Figure B.44. Isothermal R.O.C. versus Isothermal D.O.C. and Isothermal D.O.C. versus time for 130°C Isothermal Test, Individual Fits

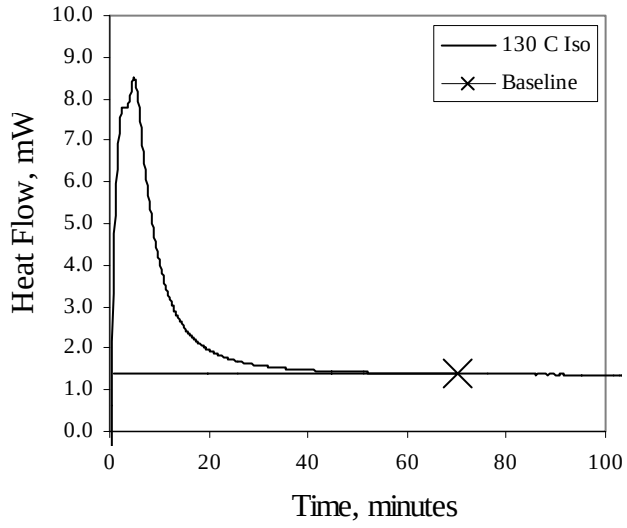

Figure B.45. Heat Flow versus Time for 130°C Isothermal Test

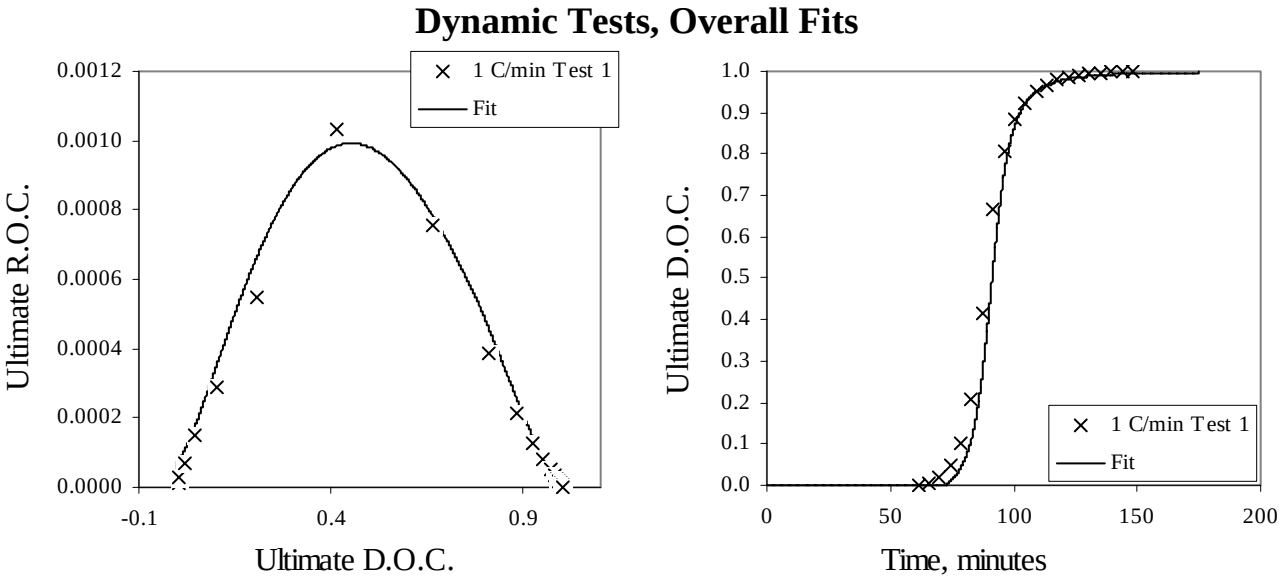

Figure B.46. Ultimate R.O.C. versus Ultimate D.O.C. and Ultimate D.O.C. versus time for 1°C/min Dynamic Test, Overall Fits

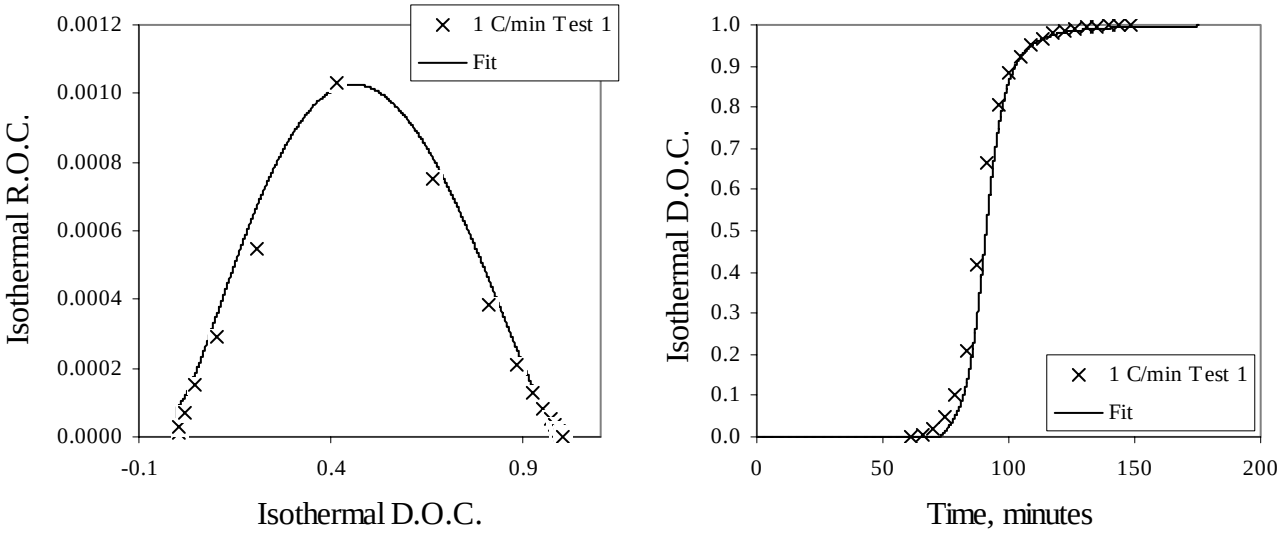

Figure B.47. Isothermal R.O.C. versus Isothermal D.O.C. and Isothermal D.O.C. versus time for 1°C/min Dynamic Test, Overall Fits

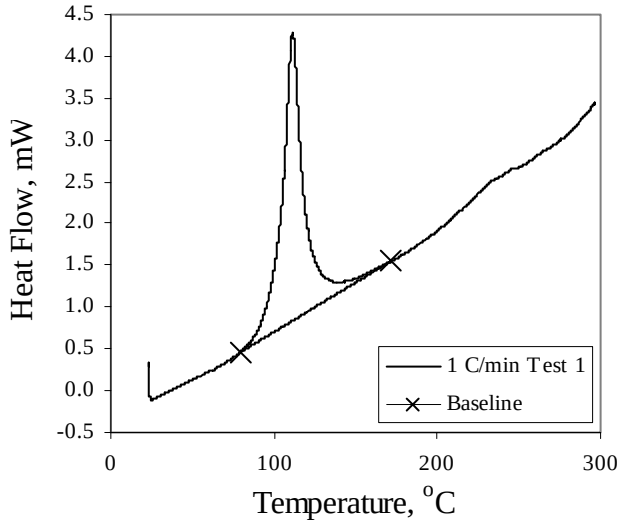

Figure B.48. Heat Flow versus Time for 1°C/min Dynamic Test

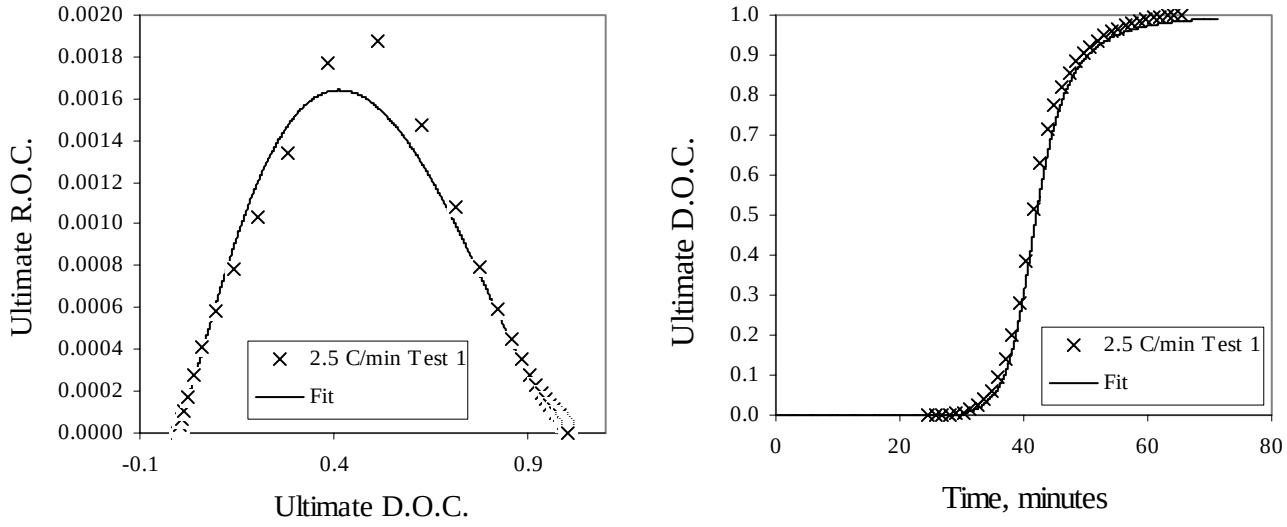

Figure B.49. Ultimate R.O.C. versus Ultimate D.O.C. and Ultimate D.O.C. versus time for 2.5°C/min Dynamic Test 1, Overall Fits

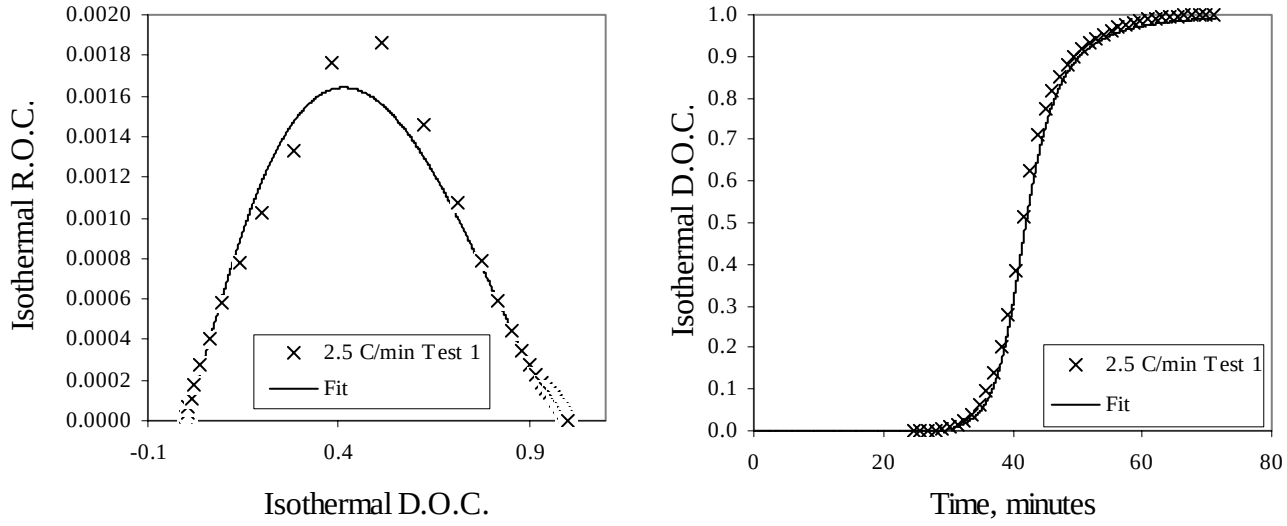

Figure B.50. Isothermal R.O.C. versus Isothermal D.O.C. and Isothermal D.O.C. versus time for 2.5°C/min Dynamic Test 1, Overall Fits

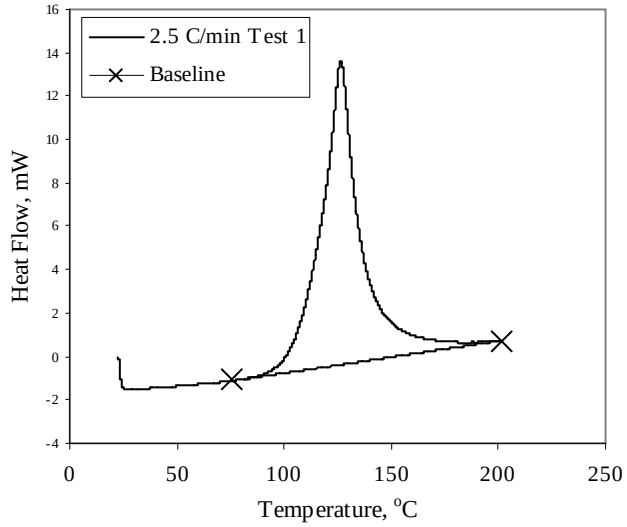

Figure B.51. Heat Flow versus Time for 2.5°C/min Dynamic Test 1

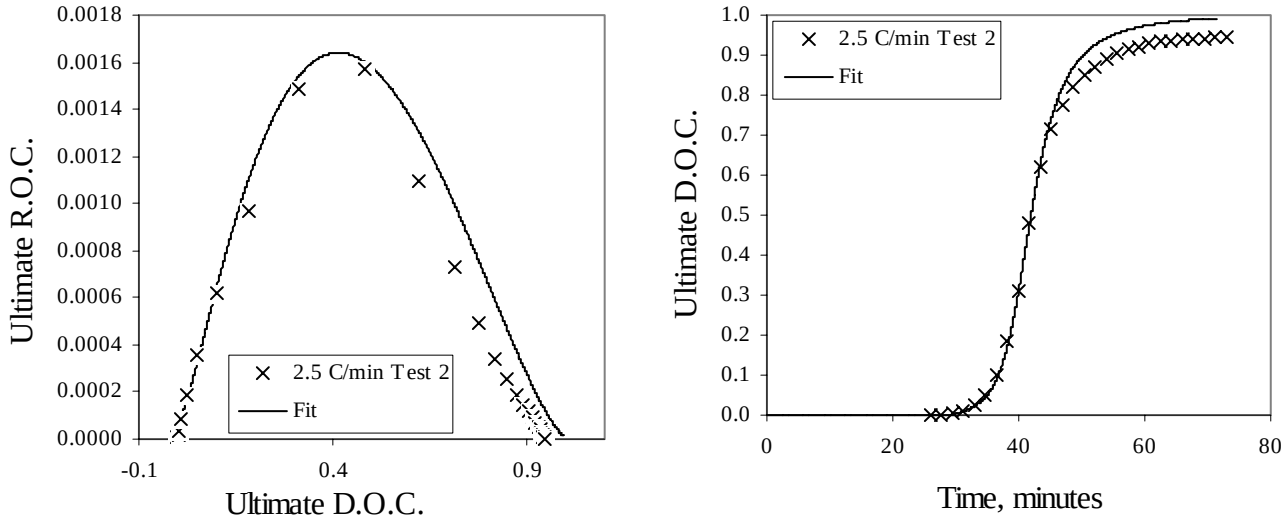

Figure B.52. Ultimate R.O.C. versus Ultimate D.O.C. and Ultimate D.O.C. versus time for 2.5°C/min Dynamic Test 2, Overall Fits

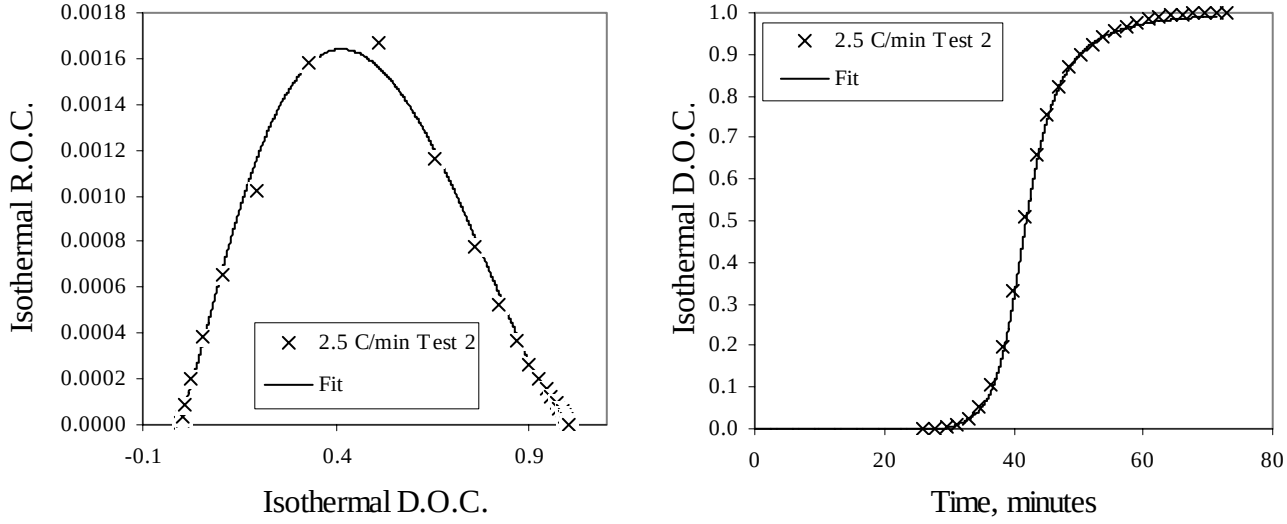

Figure B.53. Isothermal R.O.C. versus Isothermal D.O.C. and Isothermal D.O.C. versus time for 2.5°C/min Dynamic Test 2, Overall Fits

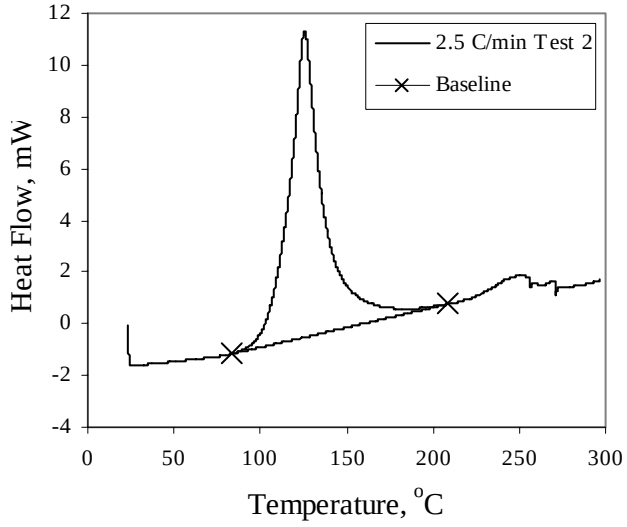

Figure B.54. Heat Flow versus Time for 2.5°C/min Dynamic Test 2

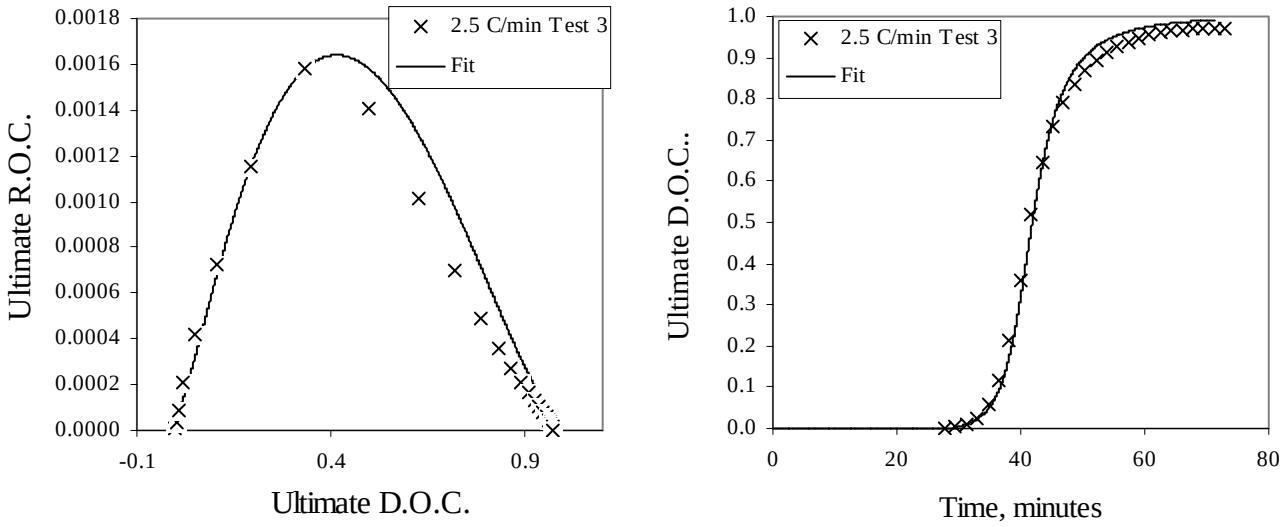

Figure B.55. Ultimate R.O.C. versus Ultimate D.O.C. and Ultimate D.O.C. versus time for 2.5°C/min Dynamic Test 3, Overall Fits

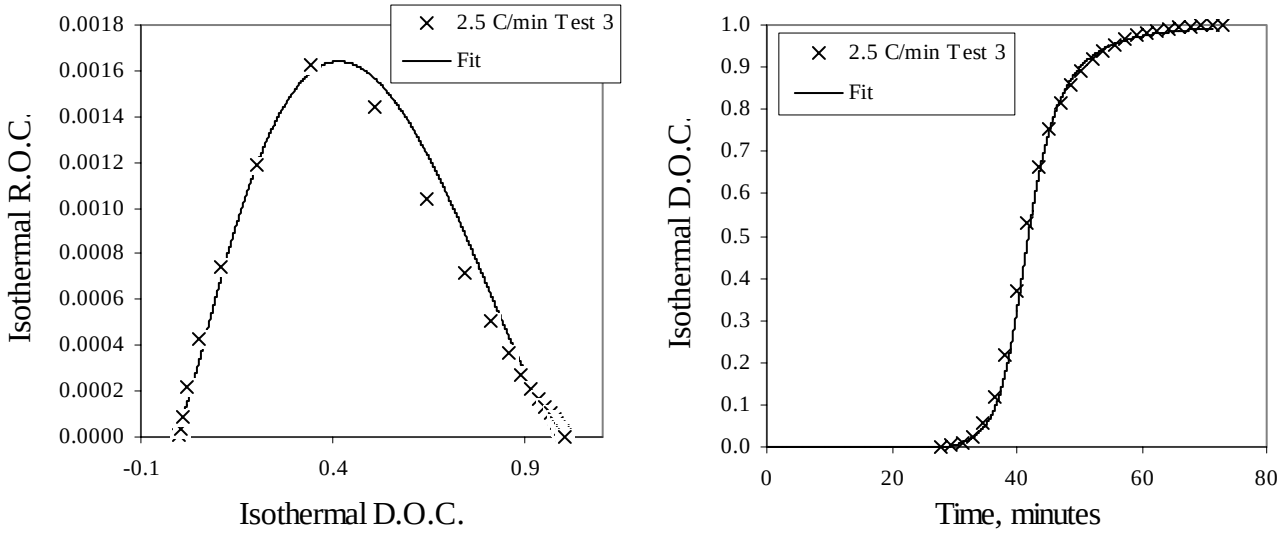

Figure B.56. Isothermal R.O.C. versus Isothermal D.O.C. and Isothermal D.O.C. versus time for 2.5°C/min Dynamic Test 3, Overall Fits

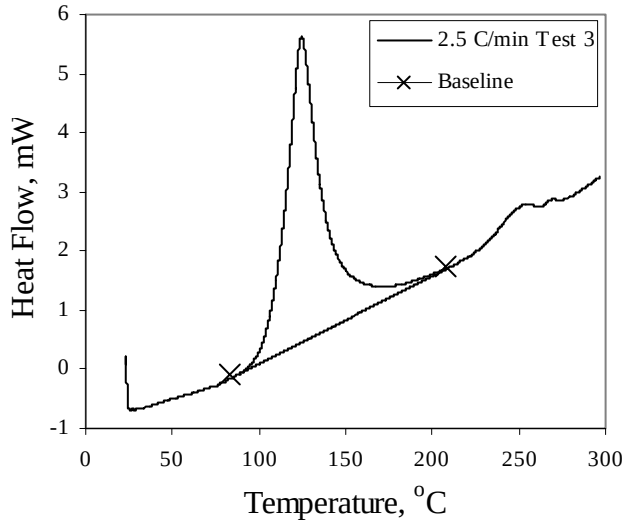

Figure B.57. Heat Flow versus Time for 2.5°C/min Dynamic Test 3

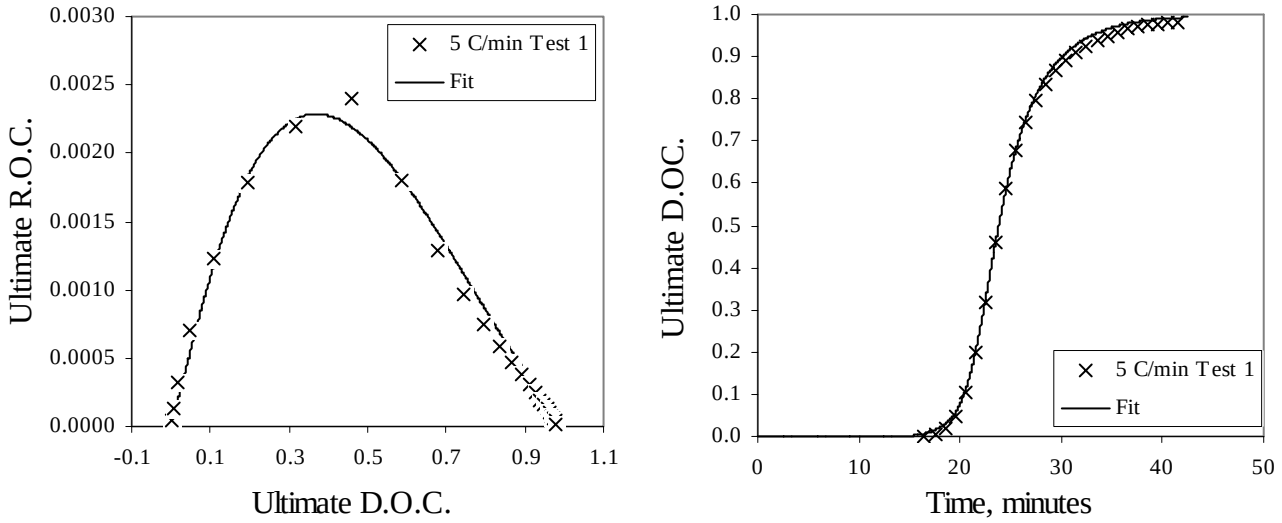

Figure B.58. Ultimate R.O.C. versus Ultimate D.O.C. and Ultimate D.O.C. versus time for 5°C/min Dynamic Test 1, Overall Fits

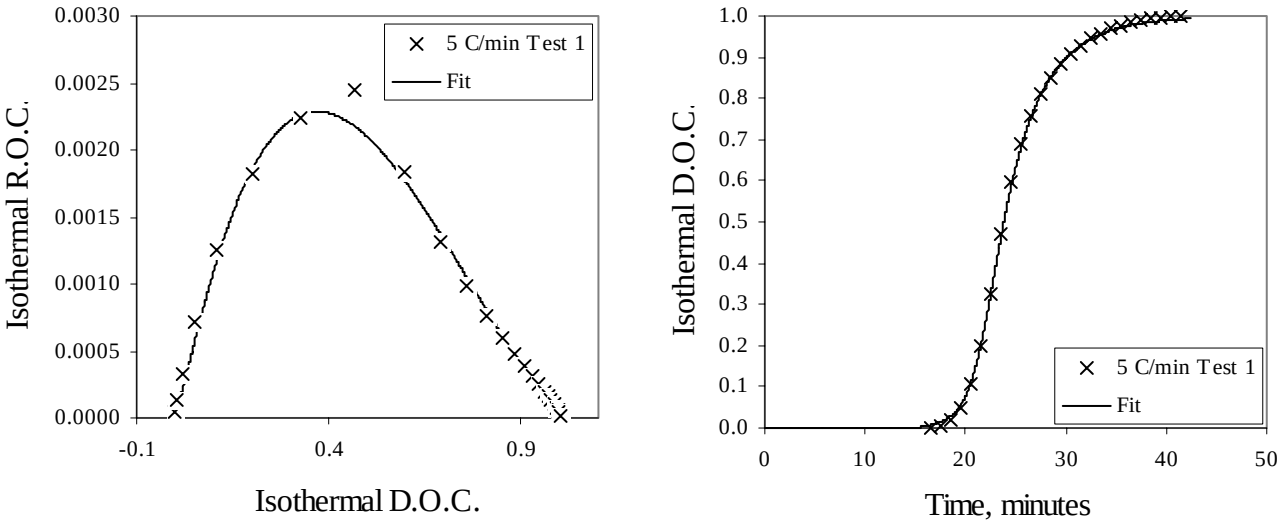

Figure B.59. Isothermal R.O.C. versus Isothermal D.O.C. and Isothermal D.O.C. versus time for 5°C/min Dynamic Test 1, Overall Fits

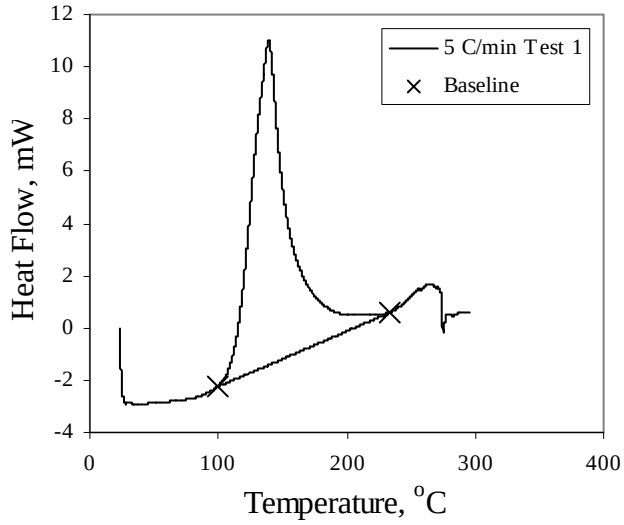

Figure B.60. Heat Flow versus Time for 5°C/min Dynamic Test 1

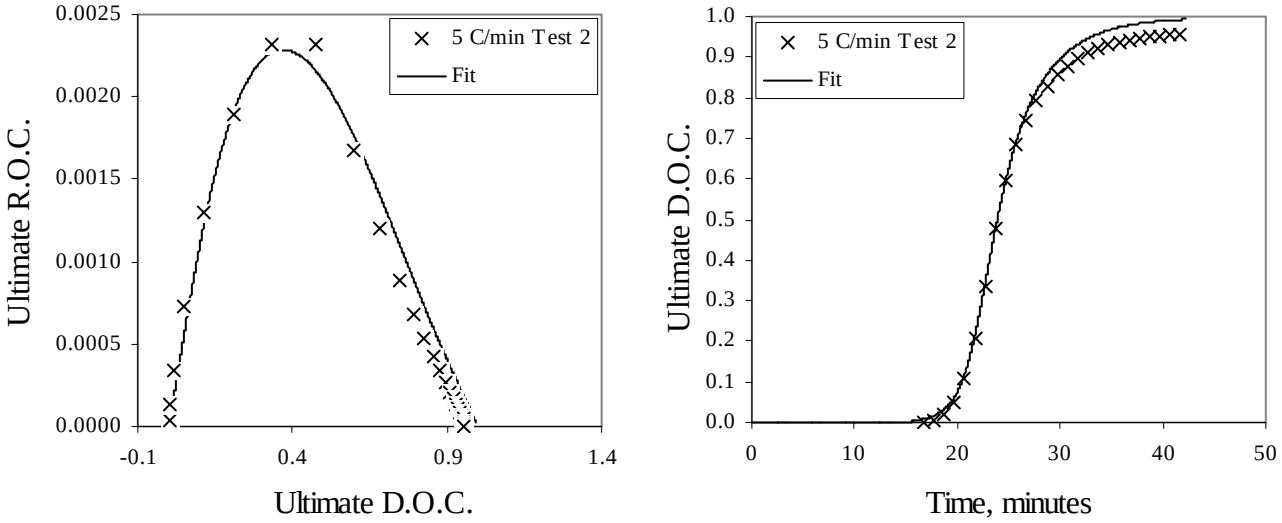

Figure B.61. Ultimate R.O.C. versus Ultimate D.O.C. and Ultimate D.O.C. versus time for 5°C/min Dynamic Test 2, Overall Fits

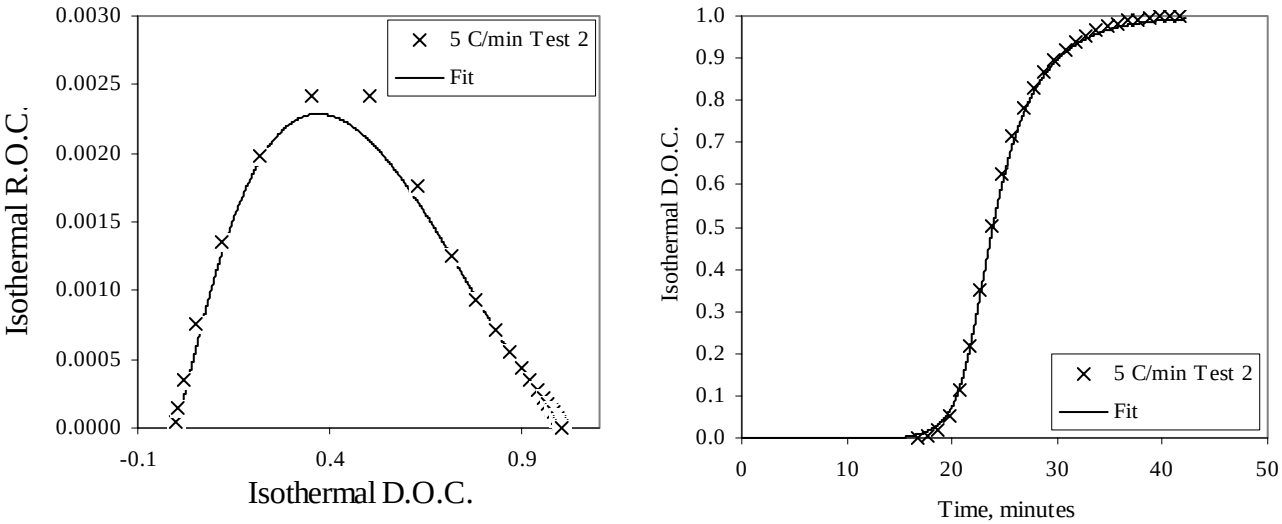

Figure B.62. Isothermal R.O.C. versus Isothermal D.O.C. and Isothermal D.O.C. versus time for 5°C/min Dynamic Test 2, Overall Fits

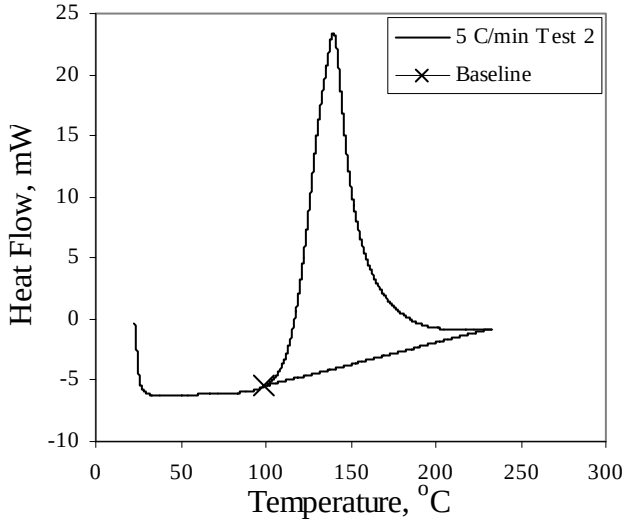

Figure B.63. Heat Flow versus Time for 5°C/min Dynamic Test 2

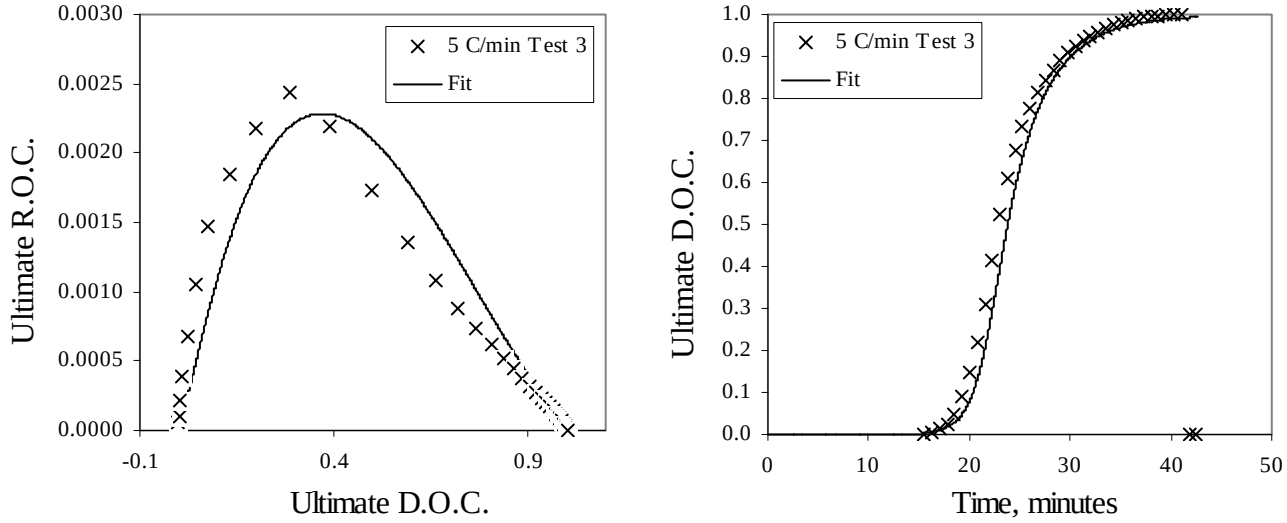

Figure B.64. Ultimate R.O.C. versus Ultimate D.O.C. and Ultimate D.O.C. versus time for 5°C/min Dynamic Test 3, Overall Fits

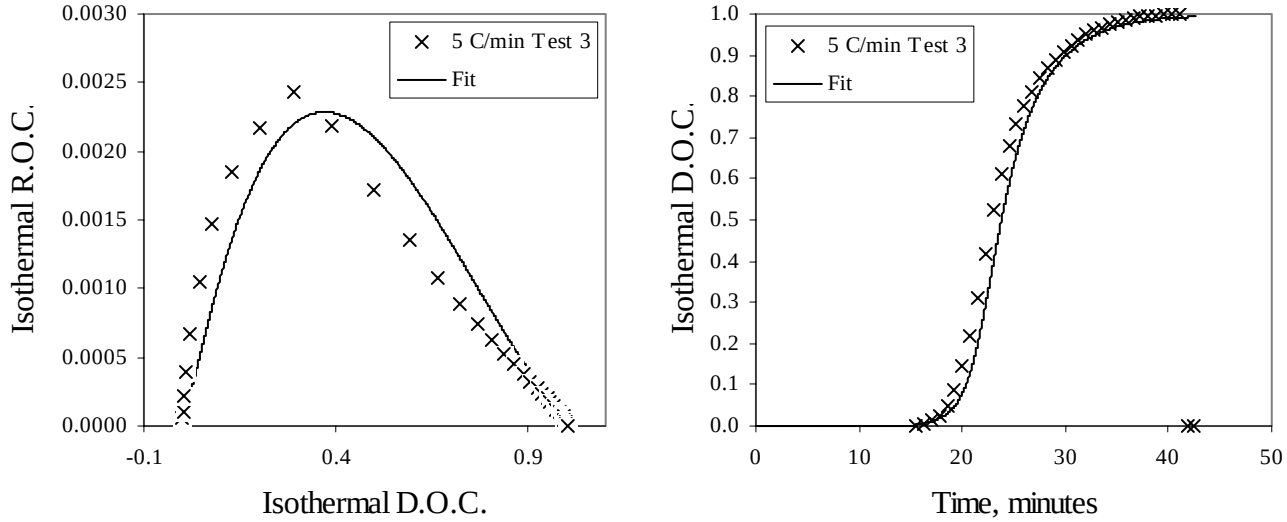

Figure B.65. Isothermal R.O.C. versus Isothermal D.O.C. and Isothermal D.O.C. versus time for 5°C/min Dynamic Test 3, Overall Fits

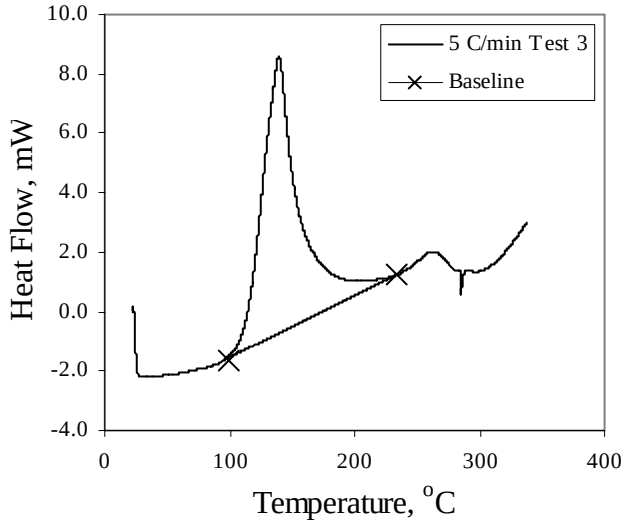

Figure B.66. Heat Flow versus Time for 5°C/min Dynamic Test 2

Dynamic Tests, Individual Fits

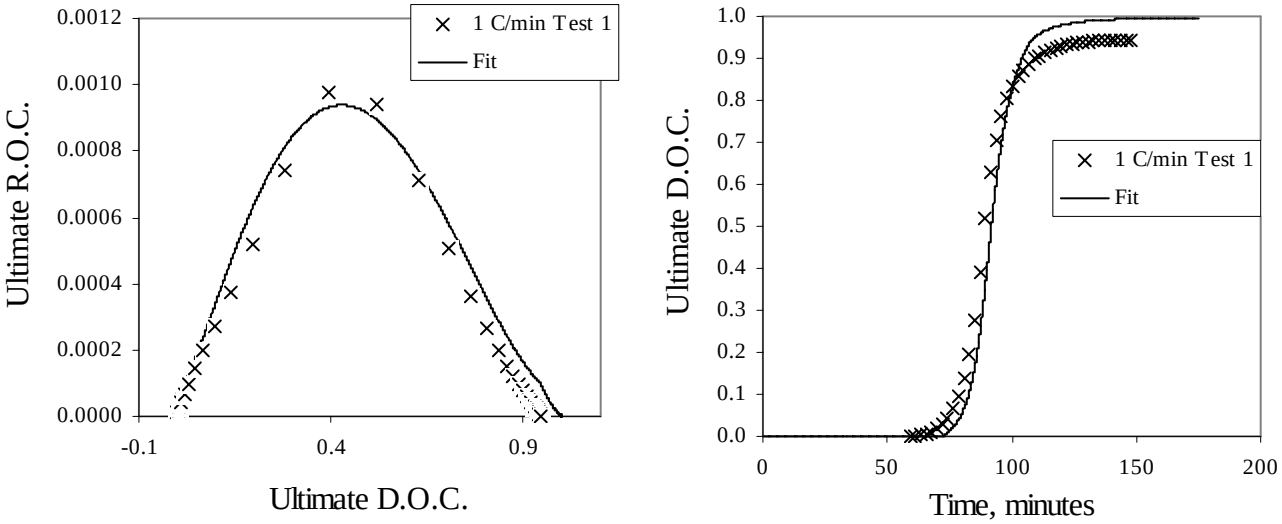

Figure B.67. Ultimate R.O.C. versus Ultimate D.O.C. and Ultimate D.O.C. versus time for 1°C/min Dynamic Test, Individual Fits

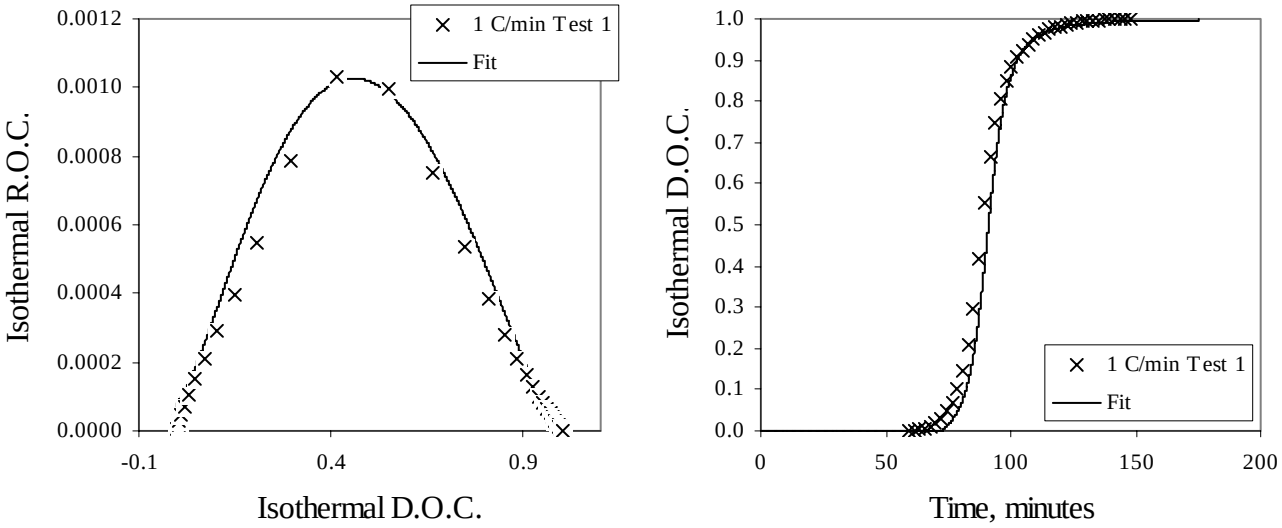

Figure B.68. Isothermal R.O.C. versus Isothermal D.O.C. and Isothermal D.O.C. versus time for 1°C/min Dynamic Test, Individual Fits

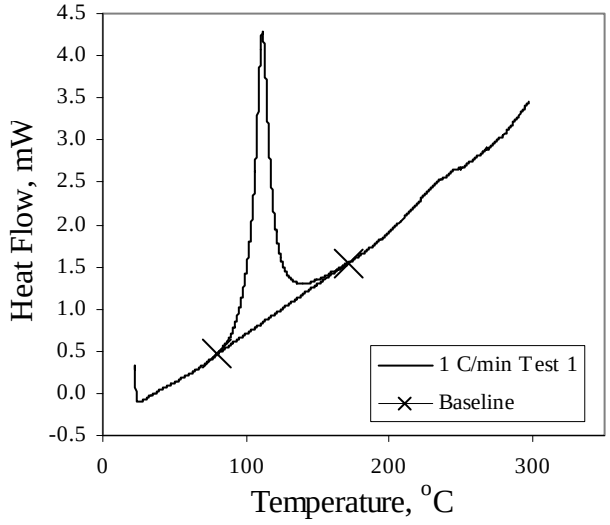

Figure B.69. Heat Flow versus Time for 1°C/min Dynamic Test

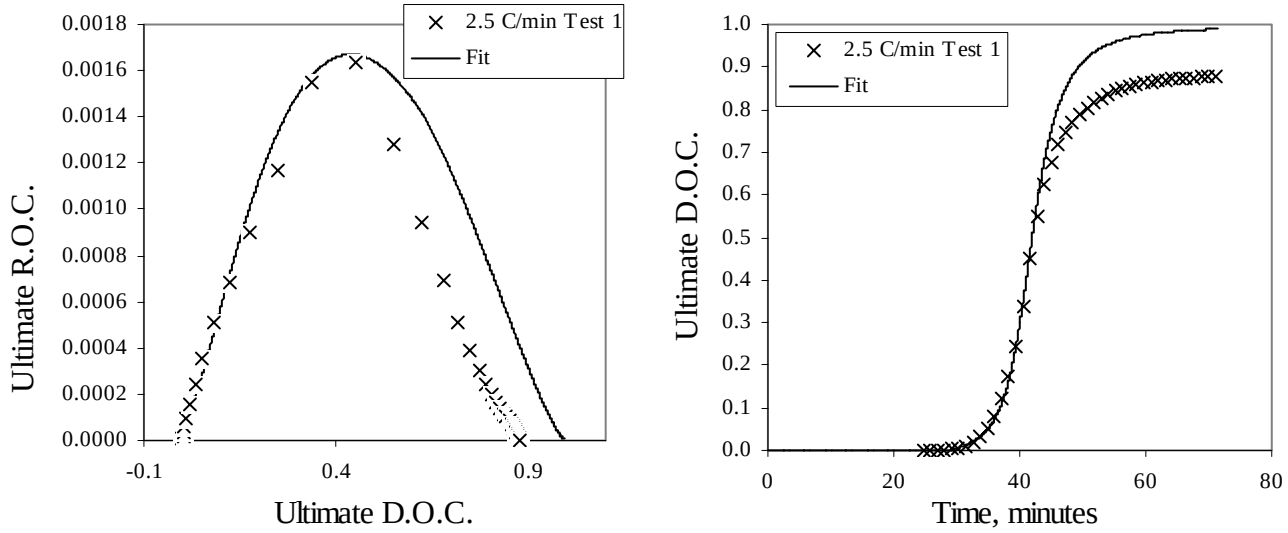

Figure B.70. Ultimate R.O.C. versus Ultimate D.O.C. and Ultimate D.O.C. versus time for 2.5°C/min Dynamic Test 1, Individual Fits

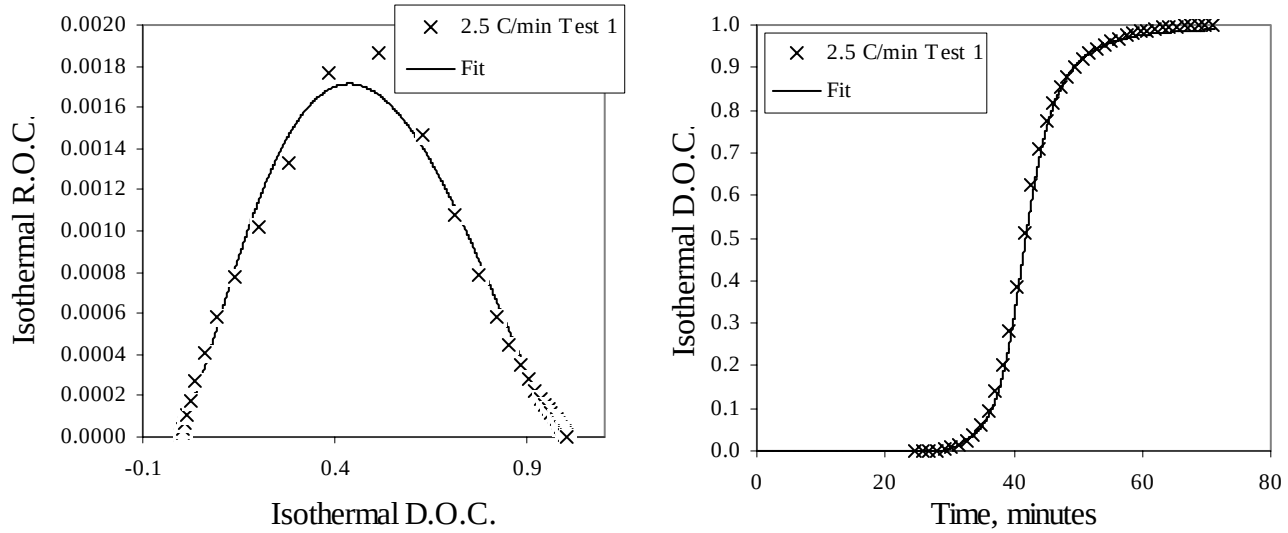

Figure B.71. Isothermal R.O.C. versus Isothermal D.O.C. and Isothermal D.O.C. versus time for 2.5°C/min Dynamic Test 1, Individual Fits

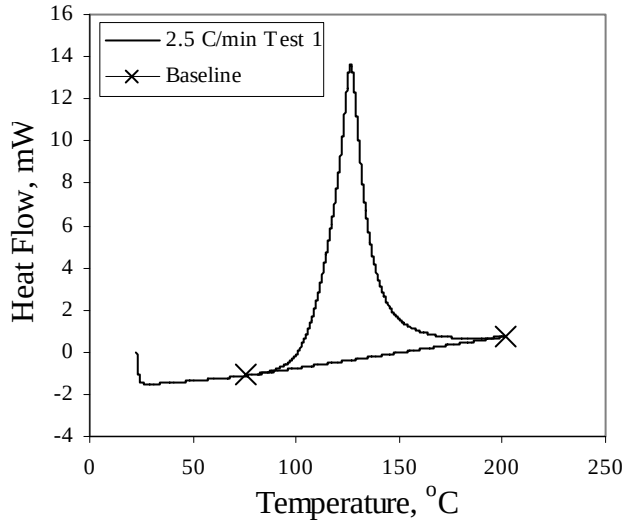

Figure B.72. Heat Flow versus Time for 2.5°C/min Dynamic Test 1

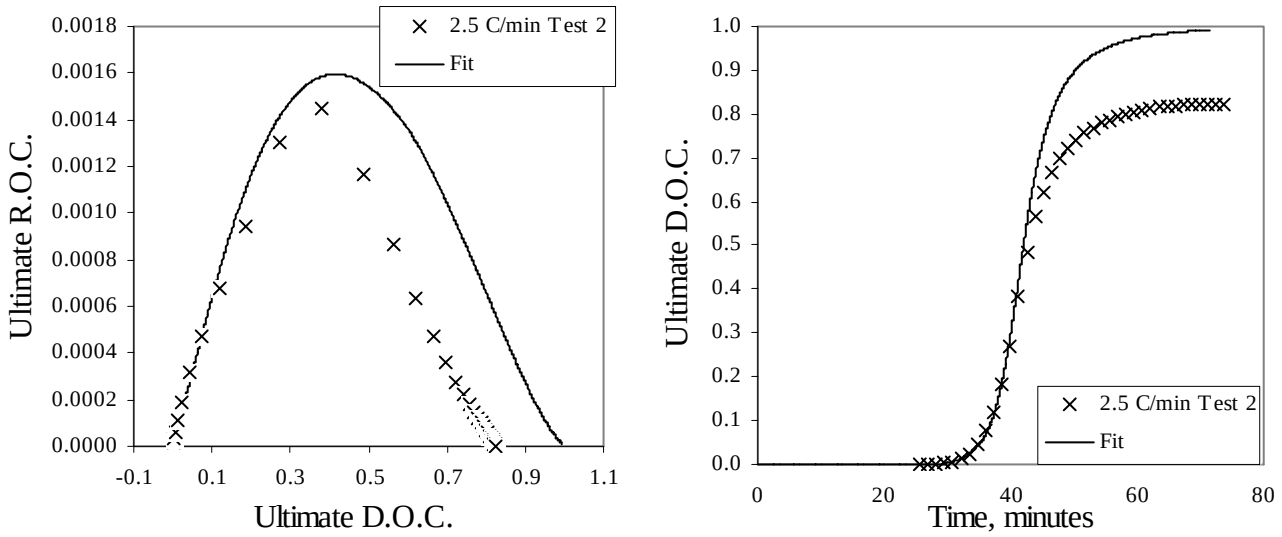

Figure B.73. Ultimate R.O.C. versus Ultimate D.O.C. and Ultimate D.O.C. versus time for 2.5°C/min Dynamic Test 2, Individual Fits

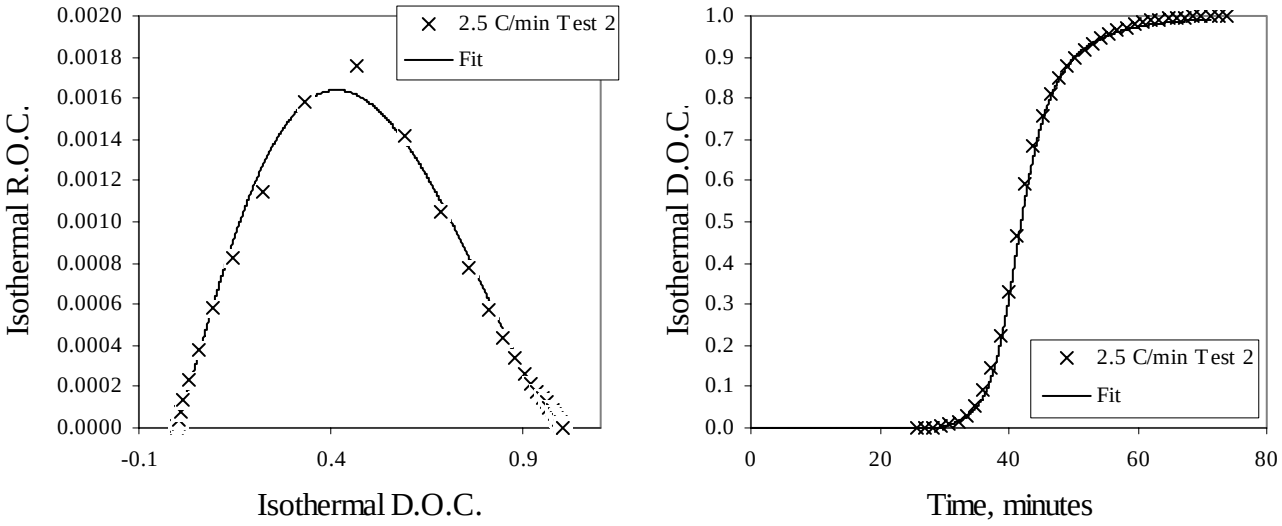

Figure B.74. Isothermal R.O.C. versus Isothermal D.O.C. and Isothermal D.O.C. versus time for 2.5°C/min Dynamic Test 2, Individual Fits

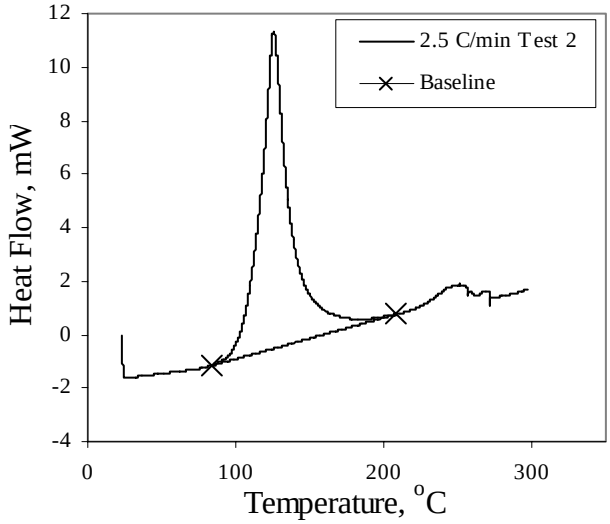

Figure B.75. Heat Flow versus Time for 2.5°C/min Dynamic Test 2

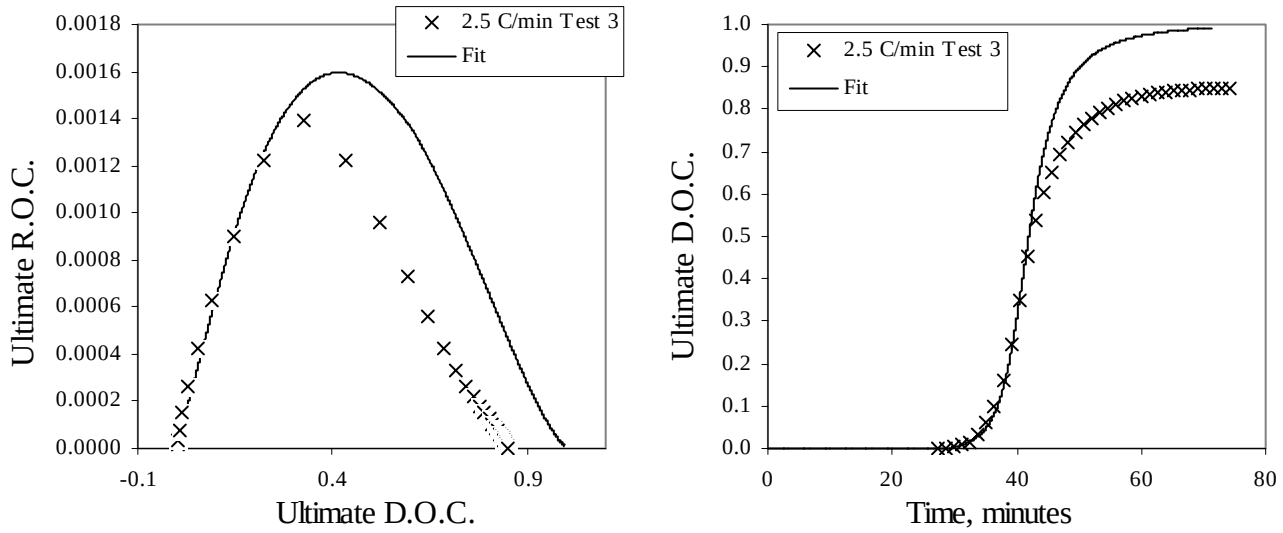

Figure B.76. Ultimate R.O.C. versus Ultimate D.O.C. and Ultimate D.O.C. versus time for 2.5°C/min Dynamic Test 3, Individual Fits

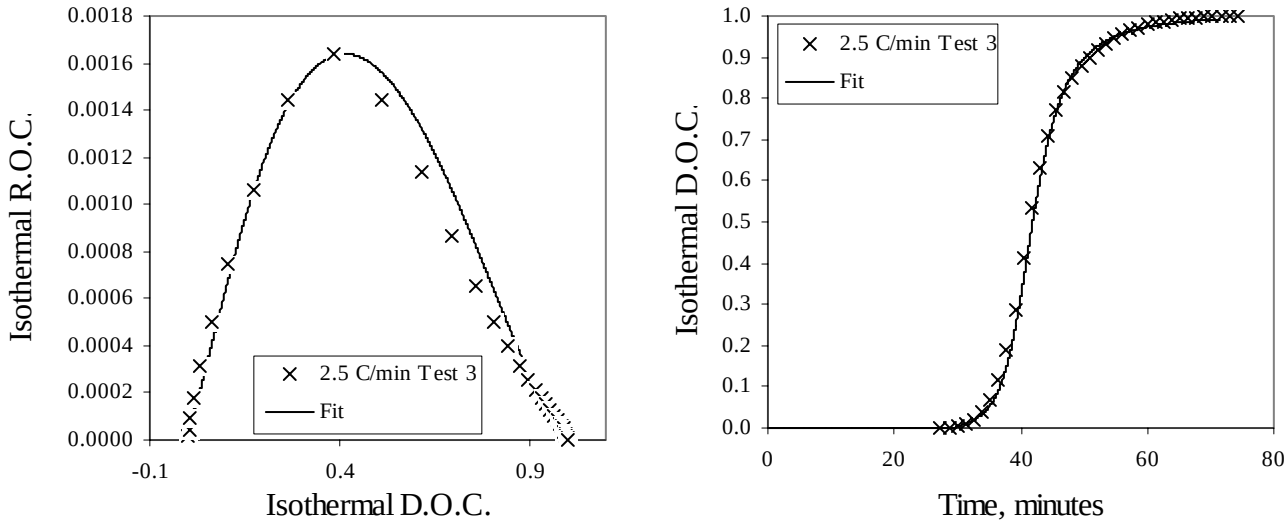

Figure B.77. Isothermal R.O.C. versus Isothermal D.O.C. and Isothermal D.O.C. versus time for 2.5°C/min Dynamic Test 3, Individual Fits

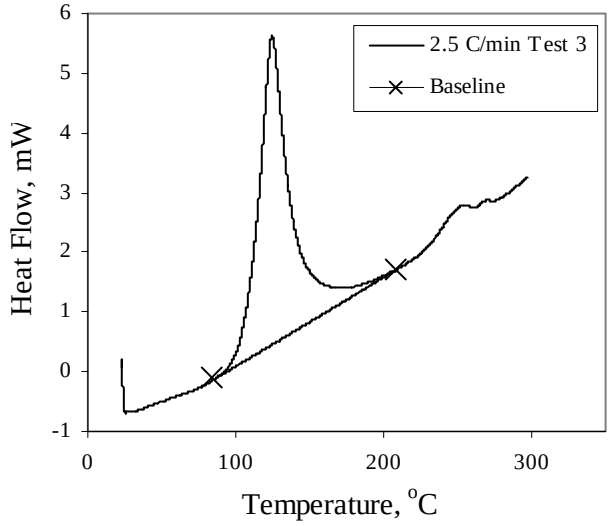

Figure B.78. Heat Flow versus Time for 2.5°C/min Dynamic Test 3

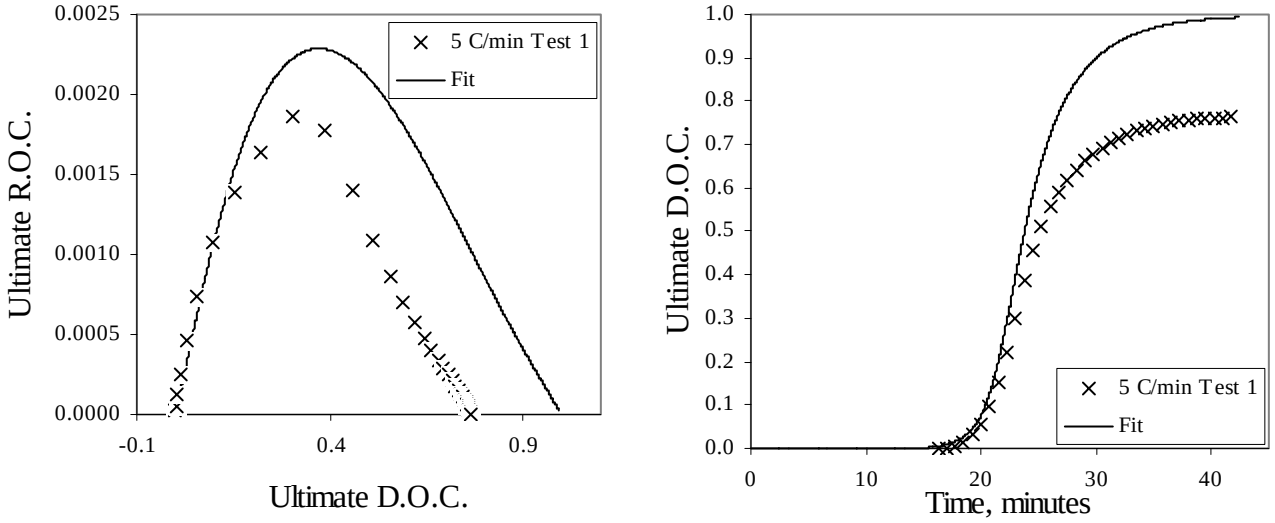

Figure B.79. Ultimate R.O.C. versus Ultimate D.O.C. and Ultimate D.O.C. versus time for 5°C/min Dynamic Test 1, Individual Fits

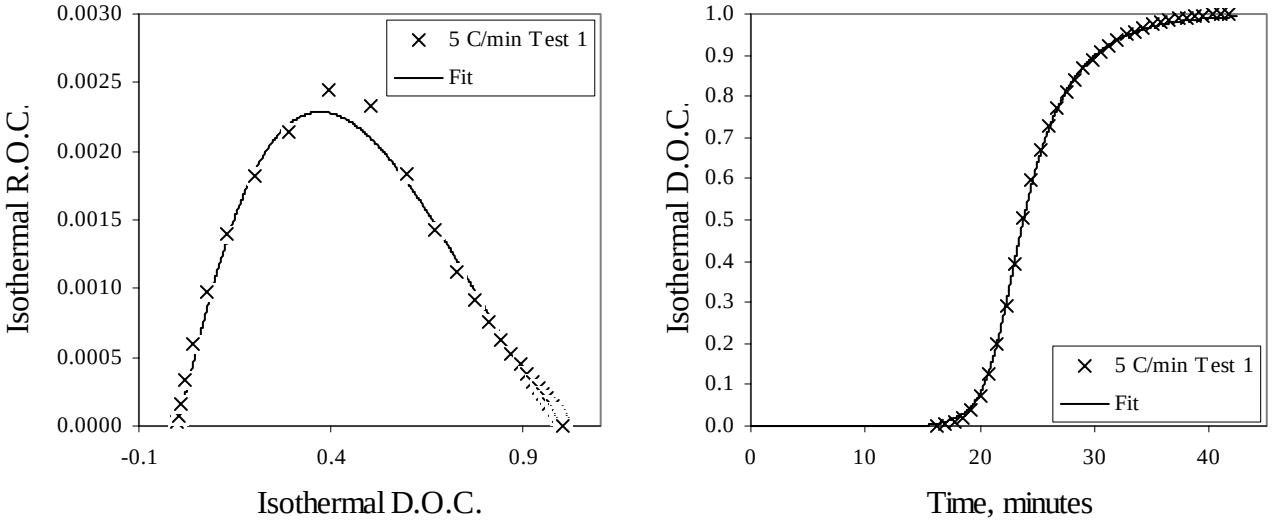

Figure B.80. Isothermal R.O.C. versus Isothermal D.O.C. and Isothermal D.O.C. versus time for 5°C/min Dynamic Test 1, Individual Fits

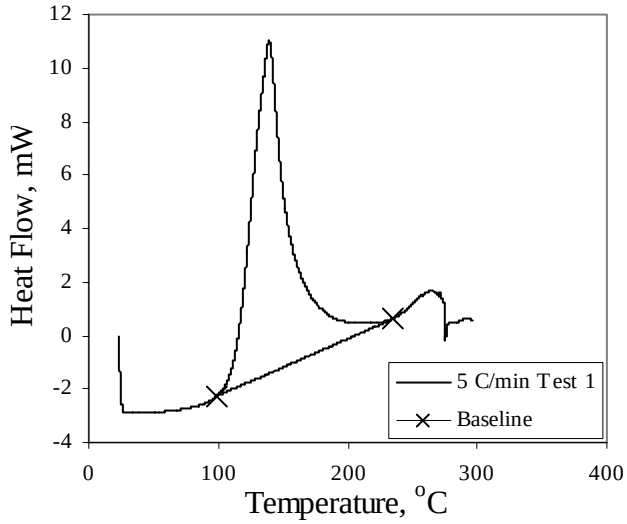

Figure B.81. Heat Flow versus Time for 5°C/min Dynamic Test 1

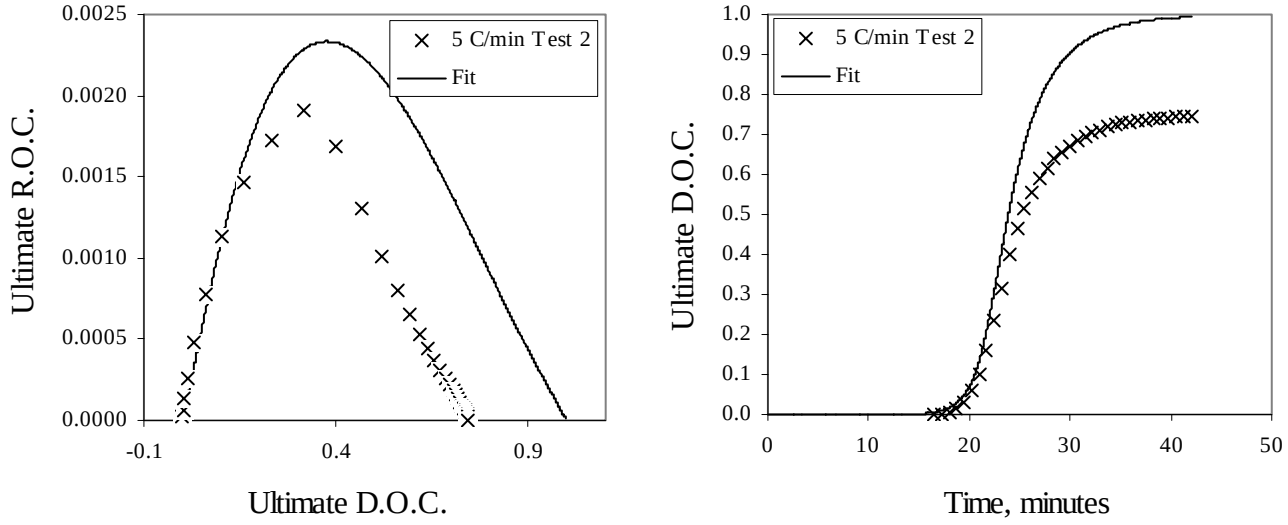

Figure B.82. Ultimate R.O.C. versus Ultimate D.O.C. and Ultimate D.O.C. versus time for 5°C/min Dynamic Test 2, Individual Fits

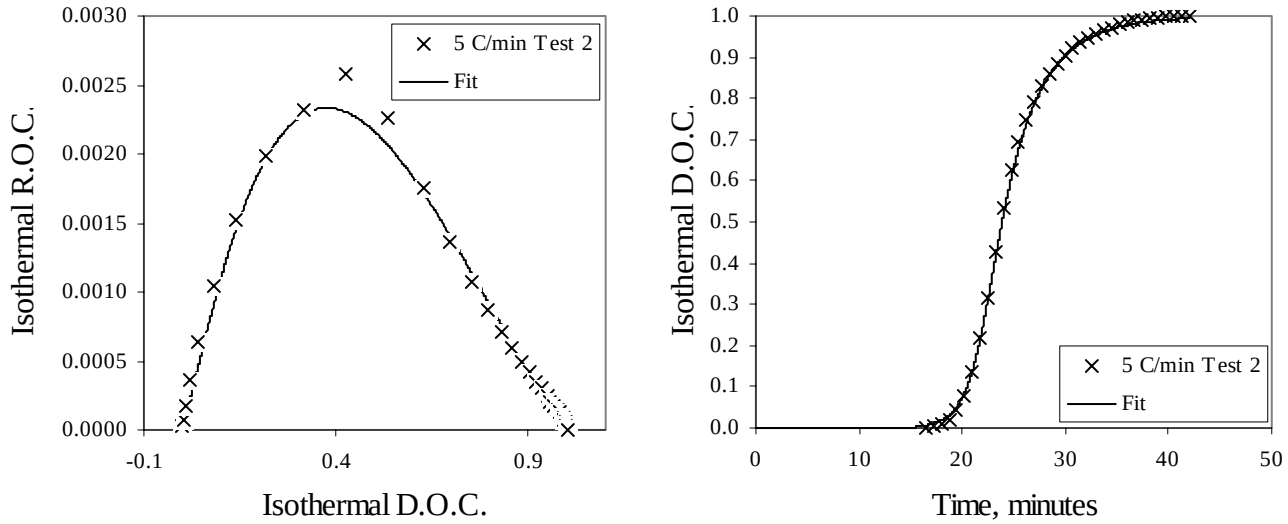

Figure B.83. Isothermal R.O.C. versus Isothermal D.O.C. and Isothermal D.O.C. versus time for 5°C/min Dynamic Test 2, Individual Fits

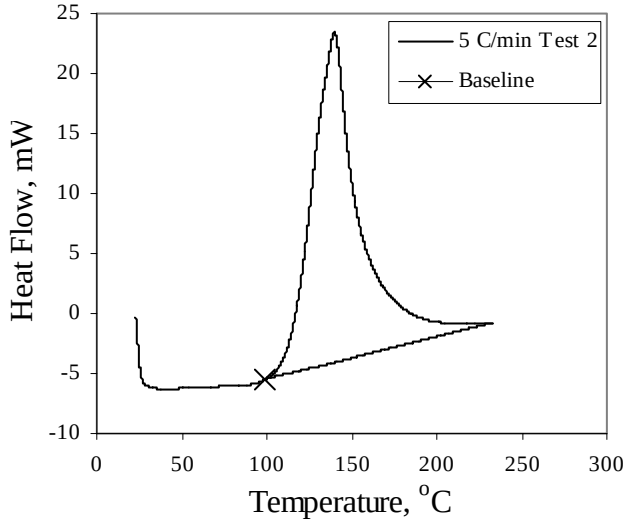

Figure B.84. Heat Flow versus Time for 5°C/min Dynamic Test 2

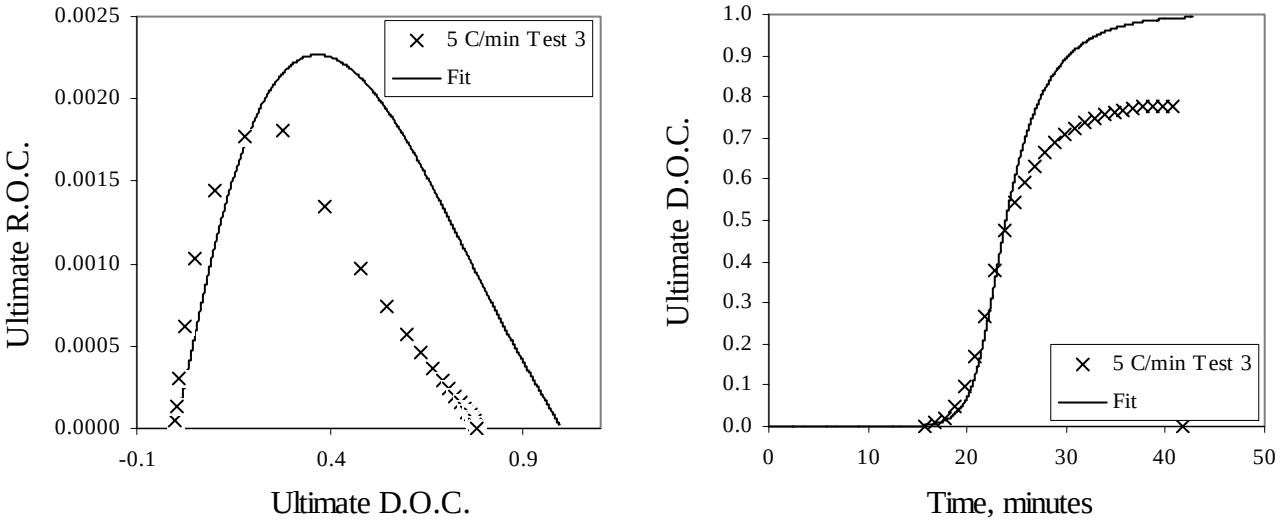

Figure B.85. Ultimate R.O.C. versus Ultimate D.O.C. and Ultimate D.O.C. versus time for 5°C/min Dynamic Test 3, Individual Fits

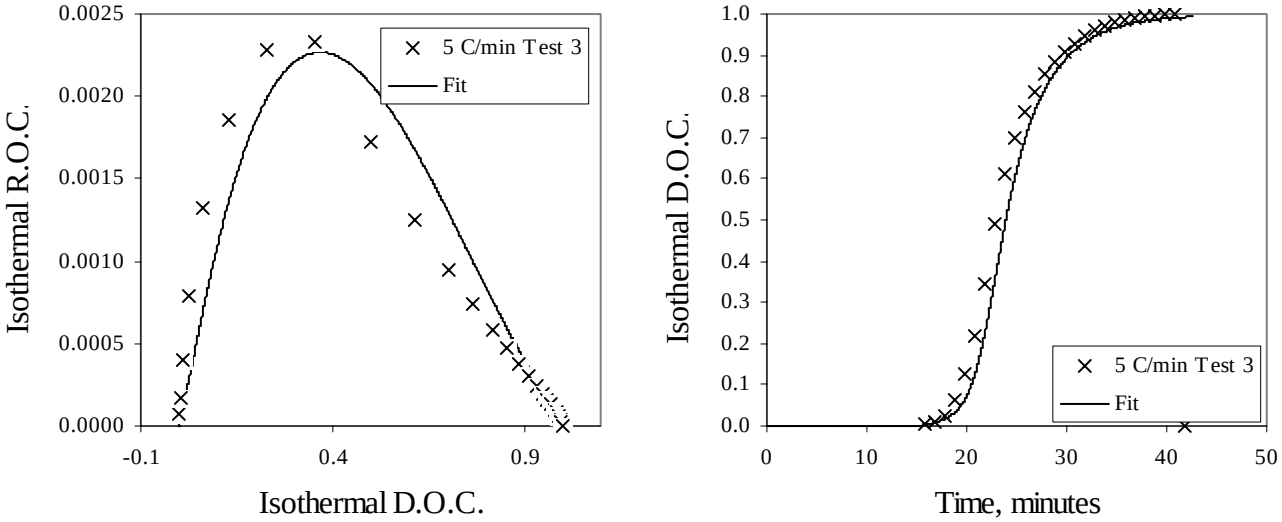

Figure B.86. Isothermal R.O.C. versus Isothermal D.O.C. and Isothermal D.O.C. versus time for 5°C/min Dynamic Test 3, Individual Fits

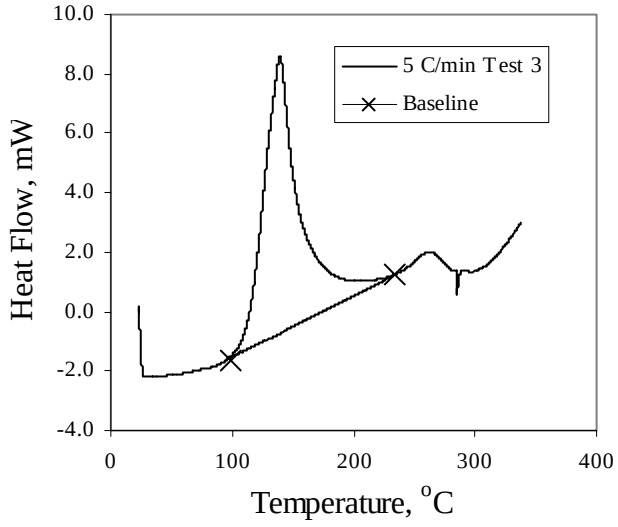

Figure B.87. Heat Flow versus Time for 5°C/min Dynamic Test 3

Appendix C

Experimental Data and Least Squares Fits for the Gutowski Pressure Relation and the Kozeny-Carman Expression for Transverse Permeability

Contained in this appendix are the individual fits of Gutowski's model to glass compaction data found in the literature. As discussed in Chapter 4, data in the literature was given in fitted form. The form of the fits varied, but was usually of the power law form given in Equation 1.2.5. One statistical fit used in the literature was the Kriging model, which has the following form:

$$P(V_f) = C_1 + C_2 V_f + C_3 \left|V_f - X_1\right|^3 + C_4 \left|V_f - X_2\right|^3 + C_5 \left|V_f - X_3\right|^3 + C_6 \left|V_f - X_5\right|^3 + C_7 \left|V_f - X_6\right|^3 \quad \text{(C.1)}$$

The Gutowski model is of the form given by Equation 1.2.3. The original and modified Cozeny-Karman relations are of the forms given in Equations 1.2.1 and 1.2.3. The results of these fits follow.

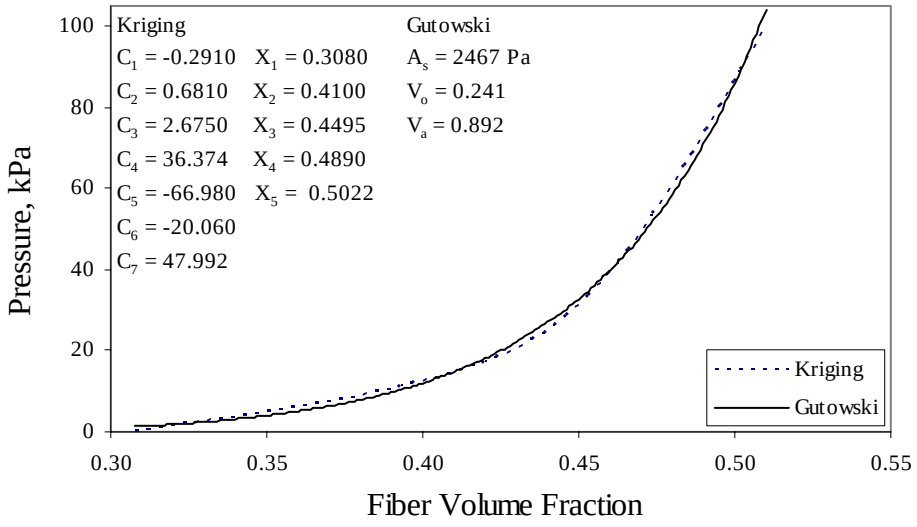

Figure C.1. Kriging and Gutowksi Fits for Data of Hammami and Gebart [10]

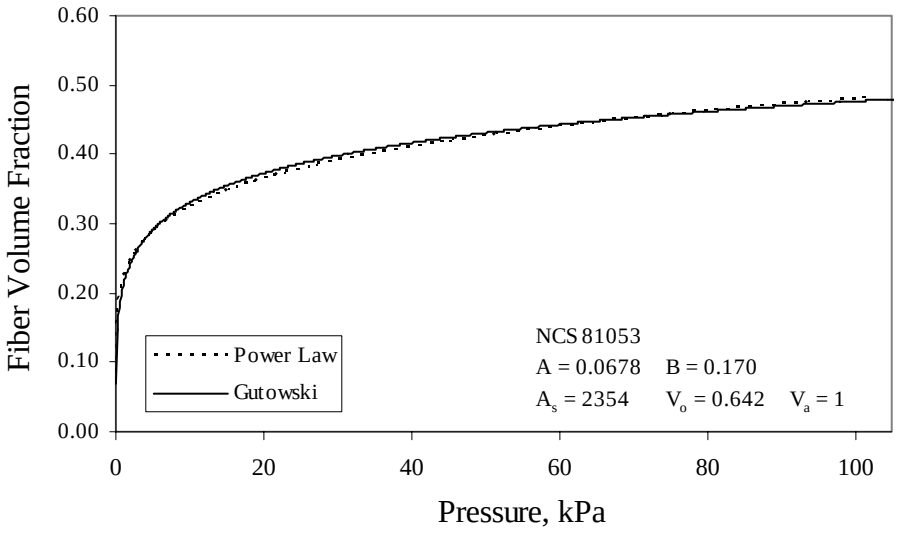

Figure C.2. Power Law and Gutowski Fits to NCS 81053 Data of Gauvin *et al*. [21]

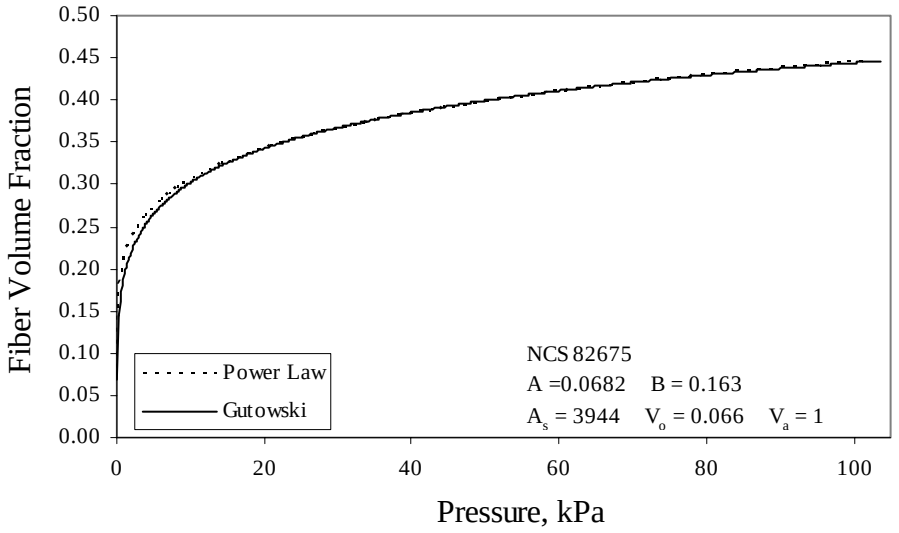

Figure C.3. Power Law and Gutowski Fits to NCS 82675 Data of Gauvin *et al*. [21]

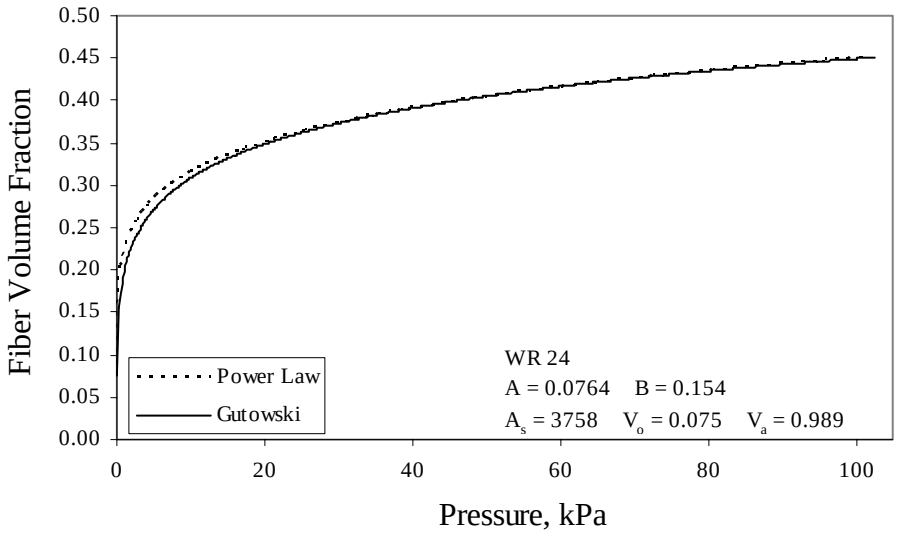

Figure C.4. Power Law and Gutowski Fits to WR 24 Data of Gauvin *et al*. [21]

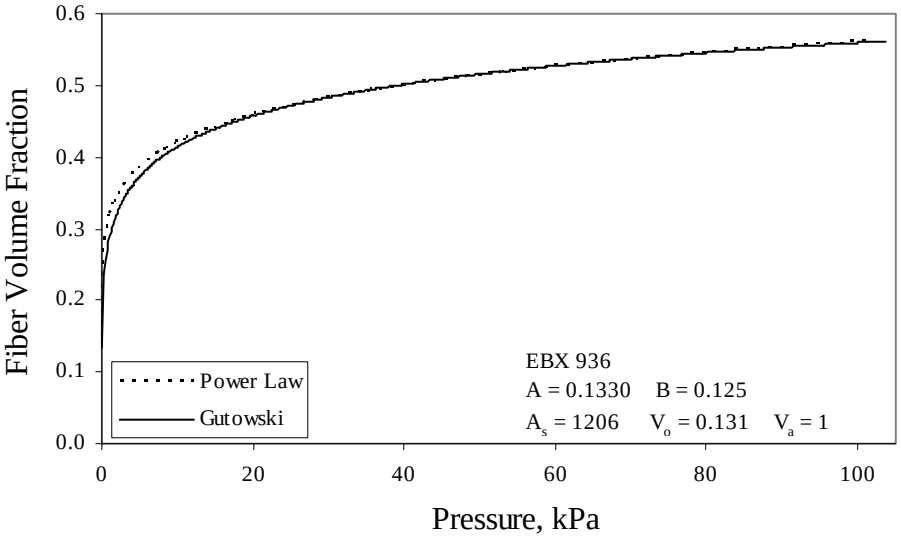

Figure C.5. Power Law and Gutowski Fits to EBX 936 Data of Gauvin *et al*. [21]

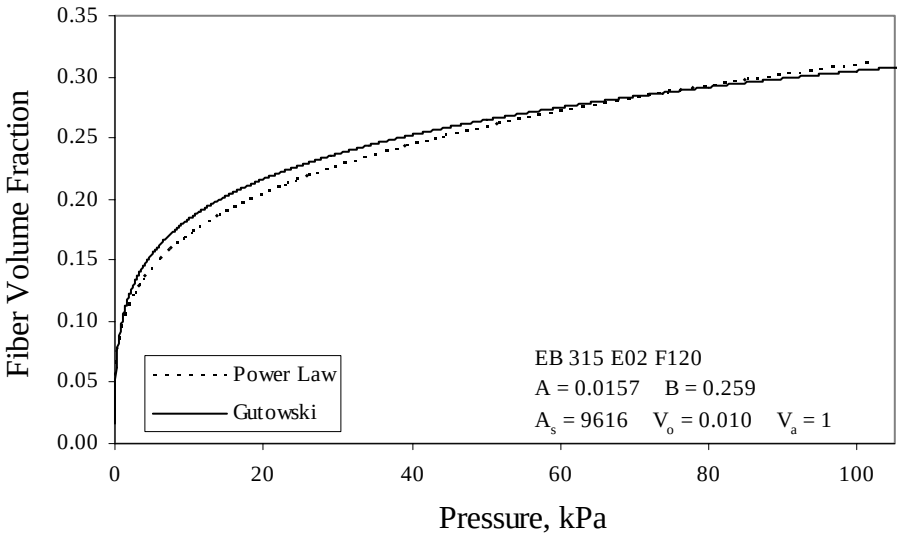

Figure C.6. Power Law and Gutowski Fits to EB 315 E02 F120 Data of Gauvin *et al*. [21]

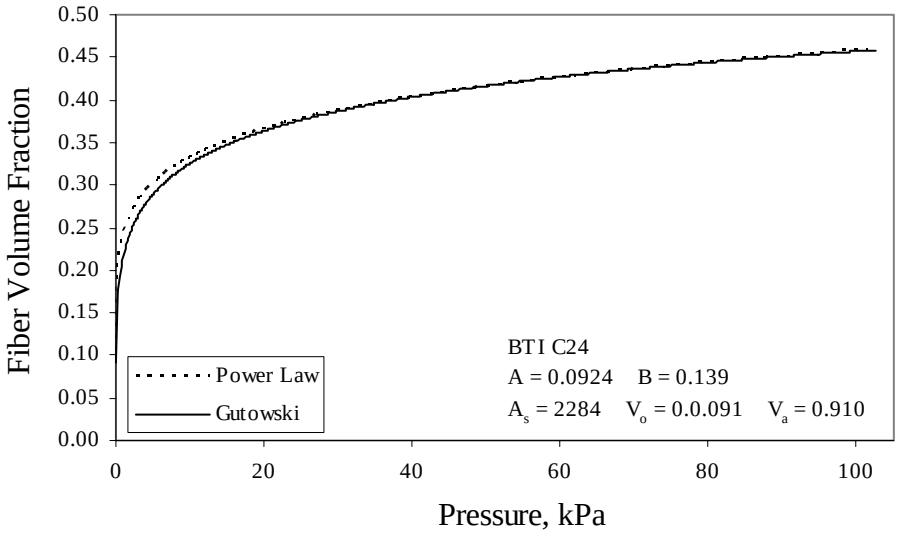

Figure C.7. Power Law and Gutowski Fits to BTI C24 Data of Gauvin *et al*. [21]

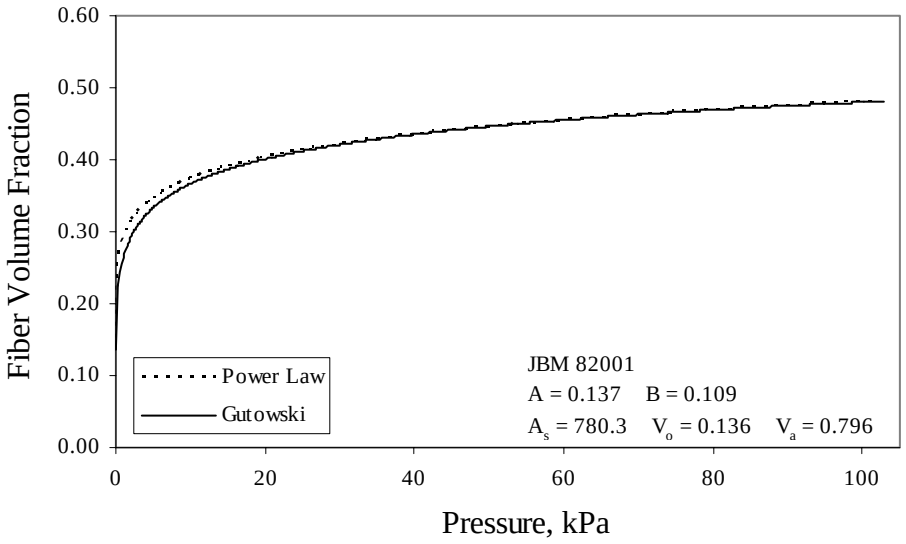

Figure C.8. Power Law and Gutowski Fits to JBM 82001 Data of Gauvin *et al*. [21]

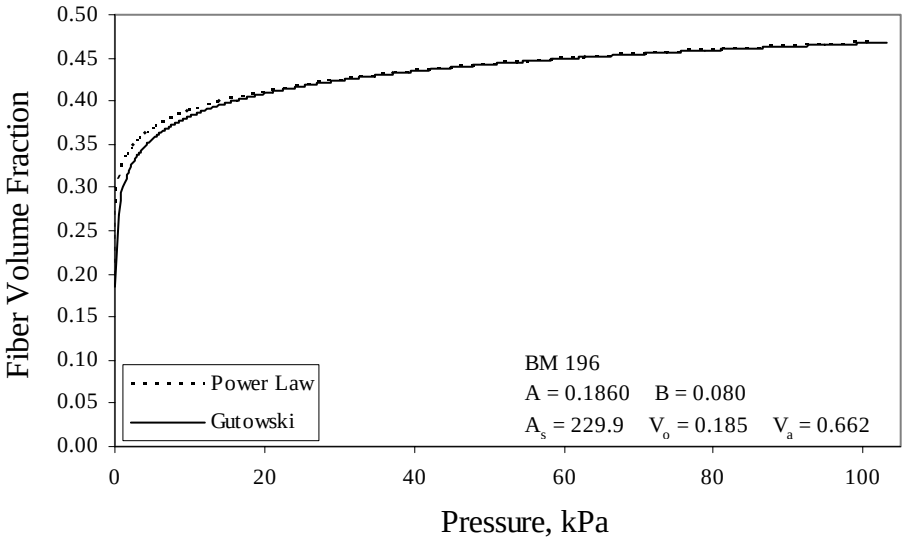

Figure C.9. Power Law and Gutowski Fits to BM 196 Data of Gauvin *et al*. [21]

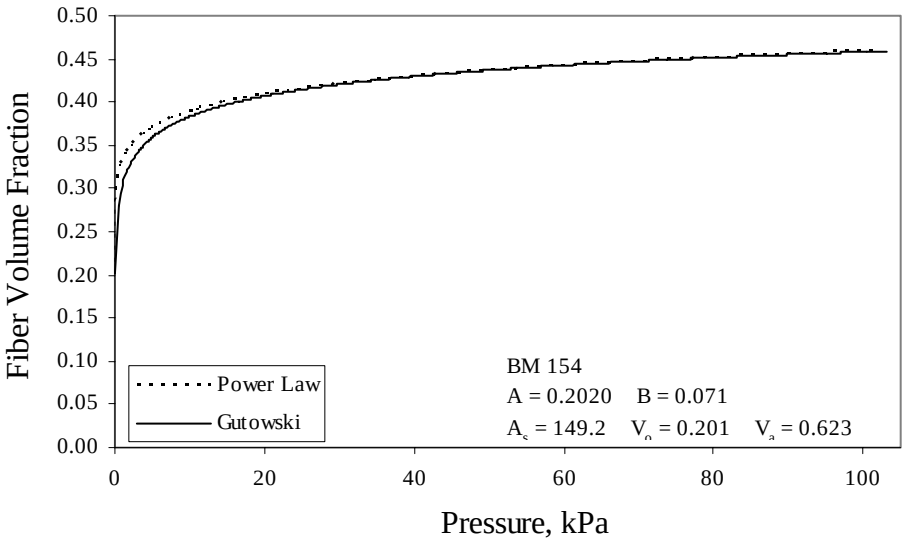

Figure C.10. Power Law and Gutowski Fits to BM 154 Data of Gauvin *et al*. [21]

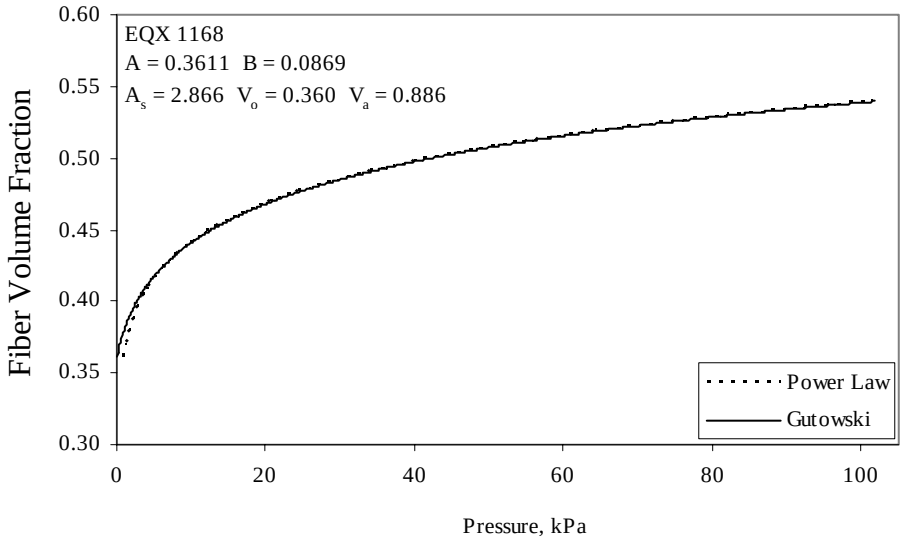

Figure C.11. Power Law and Gutowski Fits to EQX 1168 Data of Liu *et al*. [35]

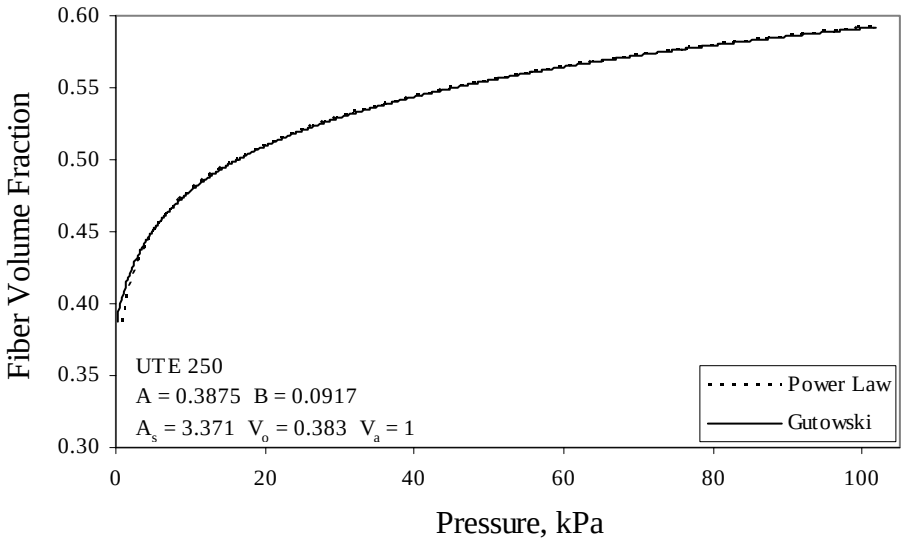

Figure C.12. Power Law and Gutowski Fits to UTE 250 Data of Liu *et al*. [35]

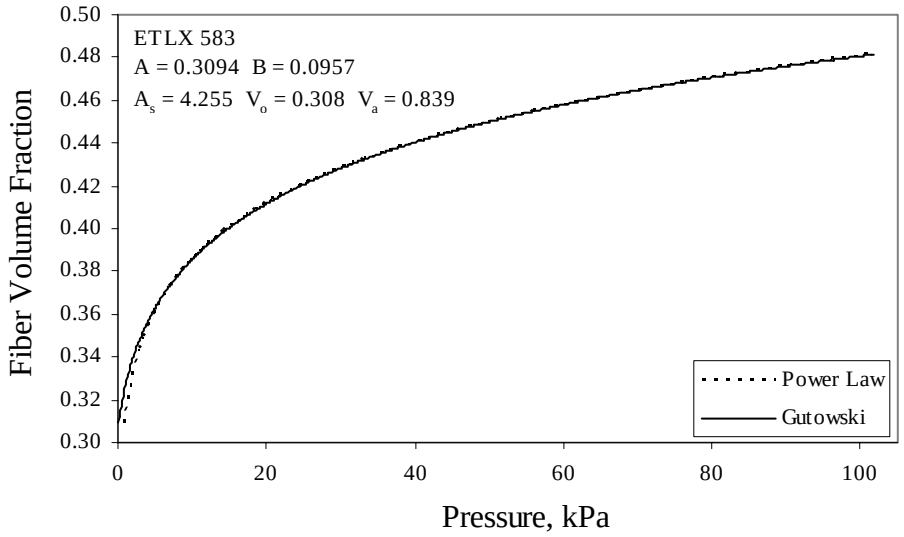

Figure C.13. Power Law and Gutowski Fits to ETLX 583 Data of Liu *et al*. [35]

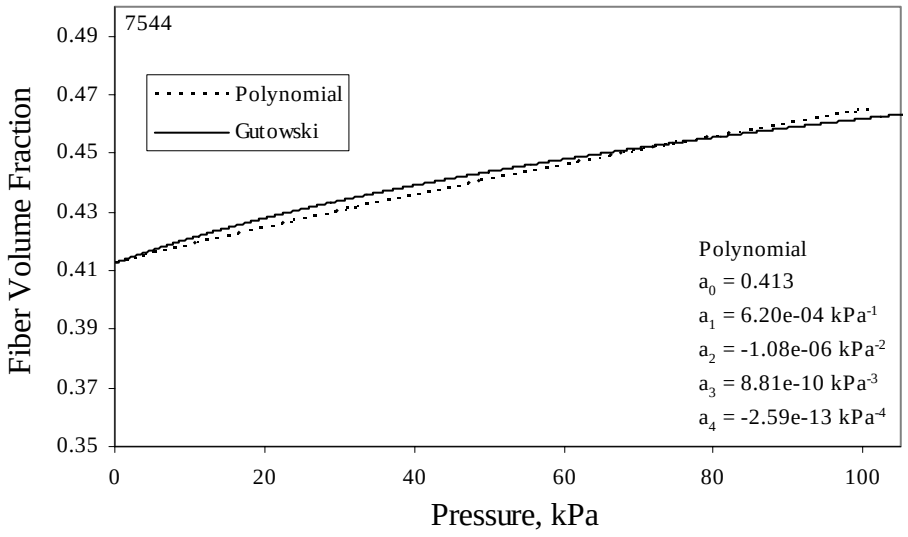

Figure C.14. Polynomial and Gutowski Fits to 7544 Data of Loos *et al*. [24]

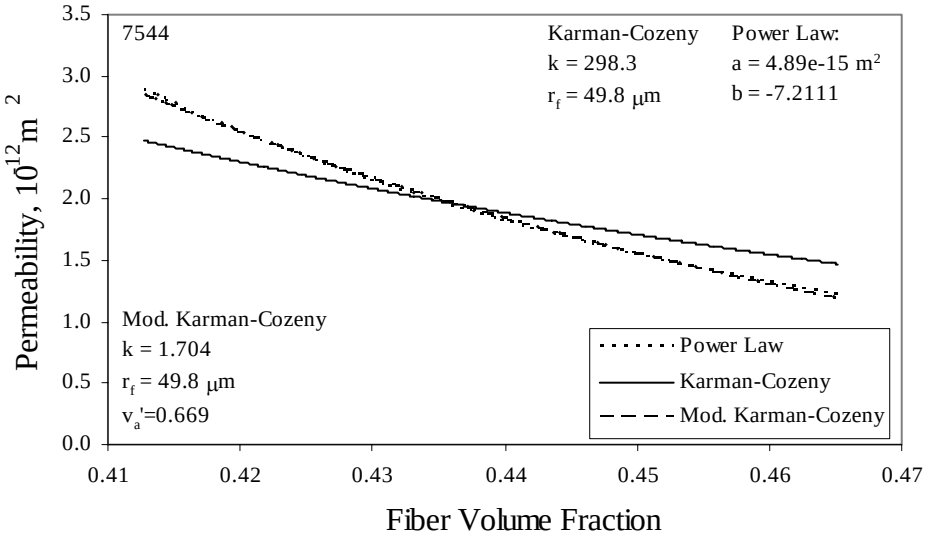

Figure C.15. Power Law and Carman-Kozeny Fits to 7544 Data of Loos *et al*. [24]

Appendix D

Computational Parametric Studies

Contained on the following pages are the results of the computational parametric studies first described in Section 5.3. The data are presented in tabular form. The first table for each test specifies the coordinates of the test points in the respective study. The second table for each test gives the results. Each test was a three dimension Box-Behnkin design, as described in Section 5.3. The parameter α maintains a value of 0.75 for all studies.

Table D.1.1. Parameter Values for Computational Parametric Study 1

Parameter	−1	−α	0	α	1
A_s	2825	2835	2865	2895	2905
$k_{modified}$	1.6	1.625	1.7	1.775	1.8
V_a'	0.659	0.6615	0.669	0.6765	0.679

Table D.1.2 Results of Computational Parametric Study #1

	Results				% Diff. from Experimen		Consolidation	
	Δ Mass, g (%)		Δ Thickness, mm (%)		Mass	Thickness	y / n	Uncons. Layers
1	130.1	(35.4)	7.66	(58.5)	130.1	21.6	n	1
2	149.2	(40.6)	7.89	(60.3)	163.9	25.3	y	0
3	123.1	(33.5)	7.43	(56.8)	117.7	18.0	n	1
4	141.6	(38.5)	7.78	(59.4)	150.4	23.5	y	0
5	130.4	(35.5)	7.64	(58.4)	130.7	21.3	n	1
6	150.3	(40.9)	7.89	(60.3)	165.8	25.3	y	0
7	123.4	(33.6)	7.41	(56.6)	118.2	17.6	n	1
8	143.3	(39.0)	7.81	(59.6)	153.4	23.9	y	0
9	133.3	(36.3)	7.58	(57.9)	135.7	20.4	n	1
10	132.8	(36.1)	7.57	(57.8)	134.8	20.2	n	1
11	133.8	(36.4)	7.60	(58.0)	136.6	20.6	n	1
12	136.4	(37.1)	7.69	(58.7)	141.2	22.1	n	1
13	130.4	(35.5)	7.48	(57.2)	130.7	18.8	n	1
14	127.3	(34.6)	7.49	(57.2)	125.2	18.9	n	1
15	143.1	(38.9)	7.81	(59.7)	153.0	24.0	y	0

Table D.2.1. Parameter Values for Computational Parametric Study 2

Parameter	−1	−α	0	α	1
A_s	2765	2775	2805	2835	2845
$k_{modified}$	1.75	1.775	1.85	1.925	1.95
V_a'	0.66	0.6625	0.67	0.6775	0.68

Table D.2.2 Results of Computational Parametric Study #2

	Results				% Diff. from Experiment		Consolidation	
	Δ Mass, g (%)		Δ Thickness, mm (%)		Mass	Thickness	y / n	Uncons. Layers
1	124.7	(33.9)	7.51	(57.3)	120.4	19.2	n	1
2	142.4	(38.7)	7.80	(59.6)	151.7	23.8	y	0
3	118.4	(32.2)	7.31	(55.8)	109.4	16.0	n	1
4	134.5	(36.6)	7.57	(57.8)	137.9	20.1	n	1
5	119.8	(32.6)	7.48	(57.1)	111.9	18.7	n	1
6	144.1	(39.2)	7.83	(59.8)	154.8	24.2	y	0
7	118.5	(32.3)	7.28	(55.6)	109.6	15.6	n	1
8	136.2	(37.1)	7.62	(58.2)	140.8	21.0	n	1
9	126.8	(34.5)	7.37	(56.3)	124.3	17.0	n	1
10	126.4	(34.4)	7.36	(56.2)	123.5	16.8	n	1
11	127.3	(34.6)	7.38	(56.4)	125.1	17.2	n	1
12	129.5	(35.2)	7.46	(57.0)	129.0	18.4	n	1
13	124.4	(33.8)	7.28	(55.6)	119.9	15.6	n	1
14	121.9	(33.2)	7.34	(56.0)	115.5	16.4	n	1
15	135.7	(36.9)	7.62	(58.2)	139.9	20.9	n	1

Table D.3.1. Parameter Values for Computational Parametric Study 3

Parameter	−1	−α	0	α	1
A_s	2705	2715	2745	2775	2785
$k_{modified}$	1.95	1.975	2.05	2.125	2.15
V_a'	0.66	0.66125	0.665	0.66875	0.67

Table D.3.2 Results of Computational Parametric Study 3

	Results				% Diff. from Experiment		Consolidation	
	Δ Mass, g (%)		Δ Thickness, mm (%)		Mass	Thickness	y / n	Uncons. Layers
1	118.4	(32.2)	7.33	(56.0)	109.4	16.4	n	2
2	122.1	(33.2)	7.23	(55.3)	115.9	14.8	n	1
3	113.3	(30.8)	7.16	(54.7)	100.3	13.6	n	2
4	116.2	(31.6)	7.05	(53.9)	105.5	11.9	n	1
5	118.5	(32.2)	7.30	(55.8)	109.5	15.9	n	1
6	123.3	(33.5)	7.26	(55.4)	118.0	15.2	n	1
7	113.2	(30.8)	7.13	(54.4)	100.2	13.1	n	2
8	117.3	(31.9)	7.07	(54.0)	107.4	12.2	n	1
9	116.4	(31.7)	7.13	(54.4)	105.8	13.1	n	2
10	116.2	(31.6)	7.13	(54.4)	105.4	13.1	n	1
11	116.6	(31.7)	7.12	(54.4)	106.1	13.1	n	1
12	118.5	(32.2)	7.19	(55.0)	109.5	14.2	n	1
13	114.3	(31.1)	7.06	(53.9)	102.2	12.0	n	2
14	115.7	(31.5)	7.19	(54.9)	104.5	14.1	n	2
15	118.6	(32.3)	7.13	(54.5)	109.7	13.2	n	1

Table D.4.1. Parameter Values for Computational Parametric Study 4

Parameter	−1	−α	0	α	1
A_s	2665	2675	2705	2735	2745
$k_{modified}$	2.15	2.175	2.25	2.325	2.35
V_a'	0.655	0.65625	0.66	0.66375	0.665

Table D.4.2 Results of Computational Parametric Study 4

	Results				% Diff. from Experiment		Consolidation	
	Δ Mass, g (%)		Δ Thickness, mm (%)		Mass	Thickness	y / n	Uncons. Layers
1	111.8	(30.4)	7.26	(55.5)	97.7	15.3	n	2
2	113.3	(30.8)	7.04	(53.8)	100.3	11.8	n	2
3	107.5	(29.3)	7.13	(54.4)	90.1	13.1	n	2
4	108.6	(29.5)	6.89	(52.6)	92.0	9.4	n	2
5	112.9	(30.7)	7.26	(55.5)	99.6	15.3	n	2
6	113.7	(30.9)	7.03	(53.7)	101.1	11.7	n	2
7	108.6	(29.5)	7.12	(54.4)	92.0	13.1	n	2
8	109.0	(29.6)	6.88	(52.5)	92.7	9.2	n	2
9	110.9	(30.2)	7.08	(54.1)	96.2	12.4	n	2
10	111.0	(30.2)	7.10	(54.2)	96.2	12.6	n	2
11	110.9	(30.2)	7.07	(54.0)	96.2	12.2	n	2
12	112.7	(30.7)	7.14	(54.5)	99.2	13.3	n	2
13	109.3	(29.7)	7.03	(53.7)	93.3	11.6	n	2
14	110.9	(30.2)	7.18	(54.9)	96.2	14.0	n	2
15	110.8	(30.1)	6.98	(53.3)	95.9	10.8	n	2

Table D.5.1. Parameter Values for Computational Parametric Study 5

Parameter	−1	−α	0	α	1
A_s	2605	2630	2705	2780	2805
$k_{modified}$	2.35	2.3875	2.5	2.6125	2.65
V_a'	0.6625	0.66313	0.665	0.66688	0.6675

Table D.5.2 Results of Computational Parametric Study 5

	Results				% Diff. from Experiment		Consolidation	
	Δ Mass, g (%)		Δ Thickness, mm (%)		Mass	Thickness	y / n	Uncons. Layers
1	108.4	(29.5)	6.97	(53.3)	91.8	10.7	n	2
2	108.9	(29.6)	6.87	(52.5)	92.6	9.0	n	3
3	102.4	(27.9)	6.79	(51.8)	81.1	7.7	n	3
4	108.6	(29.5)	6.89	(52.6)	92.0	9.4	n	2
5	108.7	(29.6)	6.90	(52.7)	92.2	9.6	n	2
6	110.6	(30.1)	6.87	(52.5)	95.6	9.1	n	2
7	102.5	(27.9)	6.71	(51.3)	81.2	6.5	n	2
8	104.2	(28.3)	6.67	(50.9)	84.2	5.8	n	2
9	105.5	(28.7)	6.78	(51.8)	86.6	7.6	n	2
10	105.2	(28.6)	6.80	(51.9)	86.1	7.9	n	2
11	105.9	(28.8)	6.77	(51.7)	87.3	7.5	n	2
12	107.9	(29.4)	6.86	(52.4)	90.8	8.8	n	2
13	103.2	(28.1)	6.71	(51.3)	82.5	6.5	n	2
14	110.7	(30.1)	6.99	(53.4)	95.8	11.0	n	2
15	106.1	(28.9)	6.76	(51.7)	87.6	7.3	n	2

Table D.6.1. Parameter Values for Computational Parametric Study 6

Parameter	−1	−α	0	α	1
A_s	2550	2575	2650	2725	2750
$k_{modified}$	2.75	2.8125	3	3.1875	3.25
V_a'	0.6635	0.66413	0.666	0.66788	0.6685

Table D.6.2 Results of Computational Parametric Study 6

	Results				% Diff. from Experiment		Consolidation	
	Δ Mass, g (%)		Δ Thickness, mm (%)		Mass	Thickness	y / n	Uncons. Layers
1	100.5	(27.4)	6.72	(51.3)	77.8	6.6	n	3
2	100.7	(27.4)	6.61	(50.5)	78.0	4.9	n	2
3	93.1	(25.3)	6.47	(49.4)	64.7	2.7	n	3
4	92.8	(25.3)	6.34	(48.5)	64.1	0.7	n	3
5	100.6	(27.4)	6.64	(50.8)	77.9	5.5	n	3
6	102.3	(27.8)	6.61	(50.5)	80.8	4.9	n	2
7	92.9	(25.3)	6.39	(48.8)	64.3	1.4	n	3
8	94.0	(25.6)	6.33	(48.4)	66.3	0.6	n	3
9	96.4	(26.2)	6.48	(49.5)	70.5	2.9	n	3
10	96.3	(26.2)	6.50	(49.7)	70.2	3.2	n	3
11	96.7	(26.3)	6.47	(49.4)	71.0	2.7	n	3
12	99.5	(27.1)	6.59	(50.3)	75.9	4.5	n	3
13	93.7	(25.5)	6.39	(48.8)	65.7	1.4	n	3
14	96.4	(26.2)	6.52	(49.8)	70.4	3.5	n	3
15	96.9	(26.4)	6.46	(49.4)	71.3	2.6	n	3

Table D.7.1. Parameter Values for Computational Parametric Study 7

Parameter	−1	−α	0	α	1
A_s	2600	2625	2700	2775	2800
$k_{modified}$	3.25	3.3125	3.5	3.6875	3.75
V_a'	0.6645	0.66513	0.667	0.66888	0.6695

Table D.7.2 Results of Computational Parametric Study 7

	Results				% Diff. from Experiment		Consolidation	
	Δ Mass, g (%)		Δ Thickness, mm (%)		Mass	Thickness	y / n	Uncons. Layers
1	92.8	(25.3)	6.41	(49.0)	64.1	1.8	n	2
2	93.4	(25.4)	6.33	(48.4)	65.1	0.5	n	2
3	86.5	(23.5)	6.22	(47.5)	53.0	-1.3	n	3
4	86.9	(23.6)	6.13	(46.8)	53.7	-2.7	n	2
5	93.1	(25.3)	6.35	(48.5)	64.6	0.9	n	2
6	95.0	(25.8)	6.35	(48.5)	68.0	0.7	n	2
7	86.7	(23.6)	6.16	(47.0)	53.3	-2.3	n	2
8	88.4	(24.1)	6.13	(46.8)	56.3	-2.7	n	2
9	89.9	(24.4)	6.23	(47.6)	58.9	-1.1	n	2
10	89.5	(24.4)	6.25	(47.7)	58.3	-0.9	n	2
11	90.2	(24.6)	6.23	(47.6)	59.6	-1.2	n	2
12	92.3	(25.1)	6.31	(48.2)	63.3	0.2	n	2
13	87.5	(23.8)	6.16	(47.1)	54.7	-2.2	n	2
14	89.6	(24.4)	6.26	(47.8)	58.4	-0.6	n	2
15	90.5	(24.6)	6.22	(47.5)	60.0	-1.2	n	2

Table D.8.1. Parameter Values for Computational Parametric Study 8

Parameter	−1	−α	0	α	1
A_s	2150	2175	2250	2325	2350
$k_{modified}$	3.55	3.6	3.75	3.9	3.95
V_a'	0.664	0.6645	0.666	0.6675	0.668

Table D.8.2 Results of Computational Parametric Study 8

	Results				% Diff. from Experiment		Consolidation	
	Δ Mass, g (%)		Δ Thickness, mm (%)		Mass	Thickness	y / n	Uncons. Layers
1	89.6	(24.4)	6.52	(49.8)	58.4	3.5	n	3
2	89.3	(24.3)	6.42	(49.0)	58.0	1.9	n	3
3	85.5	(23.3)	6.38	(48.8)	51.2	1.3	n	4
4	85.0	(23.1)	6.27	(47.9)	50.4	-0.4	n	4
5	89.9	(24.5)	6.45	(49.3)	59.0	2.3	n	3
6	88.6	(24.1)	6.30	(48.1)	56.7	0.0	n	3
7	85.6	(23.3)	6.30	(48.2)	51.3	0.1	n	4
8	84.1	(22.9)	6.15	(47.0)	48.7	-2.4	n	4
9	87.4	(23.8)	6.36	(48.6)	54.5	0.9	n	4
10	87.6	(23.8)	6.40	(48.9)	55.0	1.6	n	4
11	87.0	(23.7)	6.31	(48.2)	53.8	0.2	n	4
12	89.0	(24.2)	6.41	(49.0)	57.5	1.8	n	3
13	85.8	(23.3)	6.30	(48.2)	51.7	0.1	n	4
14	87.8	(23.9)	6.41	(49.0)	55.3	1.8	n	4
15	86.8	(23.6)	6.30	(48.1)	53.4	0.0	n	4

Vita

Joseph Earl Thompson

Joseph Earl Thompson was born on December 15, 1977 to Peter Noel and Judy Ingram Thompson in Hagerstown, Maryland. His early years were spent in Braddock Heights, Maryland. After graduating from Middletown High School in 1996 he attended Virginia Polytechnic Institute and State University, majoring in Engineering Science and Mechanics. After receiving his B.S. in 2002, he remained to pursue graduate studies in Engineering Mechanics.